

Advances in Meteorology

Hydrometeorological Observation and Study in High Altitude Area

Guest Editors: Yongjian Ding, Shiqiang Zhang, Fengjing Liu, Daqing Yang
Chansheng He, and Svetlana Stuefer





Hydrometeorological Observation and Study in High Altitude Area

Advances in Meteorology

Hydrometeorological Observation and Study in High Altitude Area

Guest Editors: Yongjian Ding, Shiqiang Zhang, Fengjing Liu, Daqing Yang, Chansheng He, and Svetlana Stuefer



Copyright © 2016 Hindawi Publishing Corporation. All rights reserved.

This is a special issue published in "Advances in Meteorology." All articles are open access articles distributed under the Creative Commons Attribution License, which permits unrestricted use, distribution, and reproduction in any medium, provided the original work is properly cited.

Editorial Board

- José Antonio Adame, Spain
Cesar Azorin-Molina, Spain
Guillermo Baigorria, USA
Marina Baldi, Italy
Abderrahim Bentamy, France
Massimo A. Bollasina, UK
Stefania Bonafoni, Italy
Isabella Bordi, Italy
Alex Cannon, Canada
Claudio Carbone, Italy
Dominique Carrer, France
Charles Chemel, UK
Annalisa Cherchi, Italy
James Cleverly, Australia
Jill S. M. Coleman, USA
Gabriele Curci, Italy
Mladjen Ćurić, Serbia
Maher A. Dayeh, USA
Klaus Dethloff, Germany
Panuganti C. S. Devara, India
Julio Diaz, Spain
Arona Diedhiou, France
Stefano Dietrich, Italy
Eugenio Domínguez Vilches, Spain
Antonio Donateo, Italy
Igor Esau, Norway
Stefano Federico, Italy
Enrico Ferrero, Italy
Rossella Ferretti, Italy
Roberto Fraile, Spain
Charmaine Franklin, Australia
Jan Friesen, Germany
- Maria Ángeles García, Spain
Herminia García Mozo, Spain
Eduardo García-Ortega, Spain
Luis Gimeno, Spain
Jorge E. Gonzalez, USA
Ismail Gultepe, Canada
Rafiq Hamdi, Belgium
Adel Hanna, USA
Hiroyuki Hashiguchi, Japan
Tareq Hussein, Jordan
Bradley G. Illston, USA
Ivar S A Isaksen, Norway
Yasunobu Iwasaka, Japan
Pedro Jiménez-Guerrero, Spain
Kuruville John, USA
Charles Jones, USA
Hann-Ming H. Juang, USA
George Kallos, Greece
Harry D. Kambezidis, Greece
Nir Y. Krakauer, USA
Simon O. Krichak, Israel
Hisayuki Kubota, Japan
Haim Kutiel, Israel
Richard Leitch, Canada
Monique Leclerc, USA
Ilan Levy, Israel
Gwo-Fong Lin, Taiwan
Anthony R. Lupo, USA
Paolo Madonia, Italy
Andreas Matzarakis, Germany
Samantha Melani, Italy
Nicholas Meskhidze, USA
- Christophe Messenger, France
Mario M. Miglietta, Italy
Takashi Mochizuki, Japan
Goro Mouri, Japan
Brian R. Nelson, USA
Efthymios I. Nikolopoulos, USA
Sandip Pal, USA
Giulia Panegrossi, Italy
Giulia Pavese, Italy
Kyaw T. Paw, USA
Olivier P. Prat, USA
Sara C. Pryor, USA
Philippe Ricaud, France
Tomeu Rigo, Spain
Filomena Romano, Italy
Jose Antonio Ruiz-Arias, Spain
Haydee Salmun, USA
Pedro Salvador, Spain
Arturo Sanchez-Lorenzo, Spain
Andres Schmidt, USA
Shraddhanand Shukla, USA
Fiona Smith, UK
Francisco J. Tapiador, Spain
Yoshihiro Tomikawa, Japan
Tomoo Ushio, Japan
Rogier Van Der Velde, Netherlands
Sergio M. Vicente-Serrano, Spain
Francesco Viola, Italy
Alastair Williams, Australia
Olga Zolina, France

Contents

Hydrometeorological Observation and Study in High Altitude Area

Yongjian Ding, Shiqiang Zhang, Fengjing Liu, Daqing Yang, Chansheng He, and Svetlana Stuefer
Volume 2016, Article ID 1372464, 2 pages

Difficulties in Determining Snowpack Sublimation in Complex Terrain at the Macroscale

Bohumil M. Svoma
Volume 2016, Article ID 9695757, 10 pages

Hydrochemical Denudation and Transient Carbon Dioxide Drawdown in the Highly Glacierized, Shrinking Koxkar Basin, China

Jian Wang, Haidong Han, Qiudong Zhao, and Xiaowen Zhang
Volume 2016, Article ID 6791278, 11 pages

Glacial Area Changes in the Ili River Catchment (Northeastern Tian Shan) in Xinjiang, China, from the 1960s to 2009

Junli Xu, Shiyin Liu, Wanqin Guo, Zhen Zhang, Junfeng Wei, and Tong Feng
Volume 2015, Article ID 847257, 12 pages

Hydrograph Separation in the Headwaters of the Shule River Basin: Combining Water Chemistry and Stable Isotopes

Jiaxin Zhou, Jinkui Wu, Shiwei Liu, Guoxiong Zeng, Jia Qin, Xiuna Wang, and Qiudong Zhao
Volume 2015, Article ID 830306, 10 pages

Actual Evapotranspiration in Suli Alpine Meadow in Northeastern Edge of Qinghai-Tibet Plateau, China

Jin-kui Wu, Shi-qiang Zhang, Hao Wu, Shi-wei Liu, Yu Qin, and Jia Qin
Volume 2015, Article ID 593649, 10 pages

Surface Albedo Variation and Its Influencing Factors over Dongkemadi Glacier, Central Tibetan Plateau

Jie Wang, Yuhuan Cui, Xiaobo He, Jian Zhang, and Shijiang Yan
Volume 2015, Article ID 852098, 10 pages

Evaluation of Water Storage Change of Inland Cryosphere in Northwestern China

Min Xu, Shichang Kang, and Jiazhen Li
Volume 2015, Article ID 681634, 12 pages

Validation of the Accuracy of Different Precipitation Datasets over Tianshan Mountainous Area

Chuancheng Zhao, Shuxia Yao, Shiqiang Zhang, Haidong Han, Qiudong Zhao, and Shuhua Yi
Volume 2015, Article ID 617382, 10 pages

Editorial

Hydrometeorological Observation and Study in High Altitude Area

**Yongjian Ding,¹ Shiqiang Zhang,² Fengjing Liu,³
Daqing Yang,⁴ Chansheng He,⁵ and Svetlana Stuefer⁶**

¹*Cold and Arid Regions Environmental and Engineering Research Institute, Chinese Academy of Sciences, Lanzhou 730000, China*

²*College of Urban and Environmental Sciences, Northwest University, No. 1, Xi'an 710027, China*

³*Department of Agriculture and Environmental Science and Cooperative Research Programs, Lincoln University,
207 Foster Hall, Jefferson City, MO 65101, USA*

⁴*National Hydrology Research Centre, University of Saskatchewan, 11 Innovation Boulevard, Saskatoon, SK, Canada S7N 3H5*

⁵*Department of Geography, Western Michigan University, Kalamazoo, MI 49008-5424, USA*

⁶*University of Alaska Fairbanks, AK 99775-5860, USA*

Correspondence should be addressed to Yongjian Ding; djy@lzb.ac.cn

Received 8 September 2015; Accepted 10 September 2015

Copyright © 2016 Yongjian Ding et al. This is an open access article distributed under the Creative Commons Attribution License, which permits unrestricted use, distribution, and reproduction in any medium, provided the original work is properly cited.

The cryosphere in high altitude area plays a major role in the Earth's system through its impact on the surface energy budget, sea level change, water cycle, primary productivity, and surface gas exchange and is thus a fundamental control on physical, biological, and social environment over substantial areas of the Earth's surface. Knowledge and understanding of all the components of the cryosphere have substantially improved our understanding of the specific processes and their impact on climate, hydrology, and economy.

We invite investigators to contribute original research articles as well as review articles that will stimulate the continuing efforts to improve the technology of hydrometeorological observation by different means in high altitude area, the water-heat process in glaciers, snow, or permafrost, the understanding of water cycle in high altitude area, the climate change in high altitude area, and the impact of climate change on hydrological process and water resource in high altitude areas. The accepted papers focus on these topics.

Spatial distribution of precipitation is very complex, and generally very limited observed precipitations are available in high altitude areas. Estimation of the spatial and temporal distribution of precipitation is very important for hydrological analysis and modeling. Included in this special issue is one paper on this aspect. The paper evaluated the accuracy of

different precipitation datasets over Tianshan Mountainous Area by intensified observation data and gives one good example on the method of how to integrate the remote precipitation dataset with the limited observation data.

Glaciers are very sensitive to climate change. Study on glacier change and the albedo on glacier surface will help us to advance understanding of the mechanism of glacier response to climate change. Included in this special issue are two papers on this aspect. One paper estimates the glacier area change and the driving factors in Ili river basin. Another paper analyzed the variation of glacier surface albedo and effecting factors on Dongkemadi glacier. Both papers improve our understanding about the glacier change mechanism in high altitude regions.

Ecosystems in high altitudes are most sensitive and influential to climate change. Process-based studies will help us understand not only how ecosystems respond to climate change but also how climate change is driven by changes in ecosystems. Included in this special issue are two papers on this aspect. One was to understand hydrochemical denudation and transient carbon dioxide drawdown in highly glacierized areas in the Tianshan Mountains, China, and the other was to understand the role of mountain groundwater in hydrologic cycle in the Qilian Mountains, China. Both papers

help improve our understanding of how glaciation affects/is affected by climate change and how groundwater mediates river runoff under a changing climate.

Snow sublimation and grassland evapotranspiration are very important process in high altitude area. The complexities of modelling and measuring sublimation and evapotranspiration limit investigations to smaller scales in complex terrain in previous studies. Included in this special issue are two papers on the aspect. One paper reviews the effects that microscale controls have on sublimation, and the vegetation cover variability in macroscale was considered to be the most important factor to advance understanding of snow sublimation, which improve our understanding of the snow sublimation process in macroscale and how to simulate the sublimation process. Another paper tried to estimate the grassland evapotranspiration at field scale by using different method, which gives interesting results. Both papers help improve our understanding of the evaporation process in high altitude regions.

Water storage in basin scale provides one new clue to the validation of the water balance in inland river basin, where main water resource developed in high altitude regions. Included in this special issue is one paper on the aspect. The paper evaluated the water storage change of inland cryosphere in western China, which improves our understanding on the water balance in western China, where many inland river basins are included.

*Yongjian Ding
Shiqiang Zhang
Fengjing Liu
Daqing Yang
Chansheng He
Svetlana Stuefer*

Review Article

Difficulties in Determining Snowpack Sublimation in Complex Terrain at the Macroscale

Bohumil M. Svoma

Department of Soil, Environmental, and Atmospheric Sciences, University of Missouri, Columbia, MO 65211, USA

Correspondence should be addressed to Bohumil M. Svoma; svomab@missouri.edu

Received 22 December 2014; Revised 12 May 2015; Accepted 21 May 2015

Academic Editor: Shiqiang Zhang

Copyright © 2016 Bohumil M. Svoma. This is an open access article distributed under the Creative Commons Attribution License, which permits unrestricted use, distribution, and reproduction in any medium, provided the original work is properly cited.

In many mountainous regions, snowmelt is an essential component of water resources and ecosystem function and snow sublimation often leads to water loss from the given drainage basin. Previous investigators have developed numerous modeling and measurement techniques to quantify sublimation, illustrating high variability over short distances. The complexities of modeling and measuring sublimation limit investigations to smaller scales in complex terrain and therefore the effects that microscale controls on sublimation have at the macroscale are not well understood. A key component of microscale variability, vegetation cover, can change on short time scales relative to other components (e.g., slope, aspect, and elevation) in response to natural and anthropogenic influences such as land use practice, drought, wildfire, insect infestation, and climate change. Basic vegetation-sublimation relationships may vary within a given drainage basin, by climate type, seasonally, and interannually. It is therefore particularly important to advance understanding of vegetation effects on sublimation at the macroscale.

1. Introduction

In mountainous regions with seasonal snow cover, melting snow is generally the major component of water resources, providing runoff during the late spring and early summer when demands from humans and the local environment are increasing [1–4]. Snow accumulation also affects ecosystem processes with impacts on soil moisture, soil porosity, biogeochemical processes, and wildfire [5]. Snow surface melting can only occur if the surface temperature is equal to the melting point with additional energy required for melting, while sublimation occurs when the vapor pressure near the ice crystal surface is greater than that of the environment [6, 7]. When sublimation occurs, there is a direct loss of water from the drainage basin upon advection out of the basin.

Sublimation can be separated into three categories: (1) canopy sublimation, (2) sublimation from ground snow cover, and (3) sublimation from blowing snow [8]. Canopy sublimation occurs when snowfall intercepted by vegetation sublimates before being unloaded to the ground snowpack [9]. Relatively high above canopy wind speeds along with a high surface area to mass ratio of snow retained in the canopy

lead to increased sublimation relative to snow stored on the ground [8, 10]. Compared to ground snow cover in open areas, the subcanopy environment typically experiences reduced shortwave radiation and wind speeds as well as increased humidity and longwave radiation; therefore, sublimation from ground snow cover is affected by the presence of forest cover [8]. These components of the surface energy budget can be further altered by the presence of snow retained in the forest canopy [9]. Sun and wind crusts reduce sublimation [11] and the canopy modified surface energy budget also influences the surface snow condition and thus sublimation. Last, blowing snow sublimation occurs when saltating or suspended snow particles are surrounded by air subsaturated with respect to ice, which can occur at very rapid rates [8].

In mountainous terrain, there is high microscale variability in vegetation type, density, forest clearing size, and canopy geometry, as well as elevation, slope, aspect, and curvature [12]. Even site specific measurements of sublimation require careful attention to reduce error [13] and detailed observations of wind, temperature, and humidity in the least (which vary greatly in complex terrain) are required to model sublimation [14]. High resolution fields from interpolation

and modeling have been used to produce spatially distributed simulations of sublimation [8, 15–17] yet many such investigations are only hundreds of square kilometers in scale, and large scale studies are restricted to high latitudes (e.g., [6, 18]).

The goal of this review is to highlight the difficulties that arise when studying sublimation at the macroscale in complex terrain and emphasize important advances that can be made in the knowledge of macroscale sublimation. An overview of common techniques used to measure and model snow sublimation is given followed by a summary of results from previous investigations. Impediments to determining macroscale sublimation in complex terrain are then discussed as well as future directions for the study of macroscale sublimation from complex terrain.

2. Measuring and Modeling Sublimation

In this section, overviews of sublimation measurement and modeling techniques are given. More extensive discussions are given by Lundberg and Halldin [13] for canopy sublimation, Mahrt and Vickers [19] and Hood et al. [14] for ground sublimation, and Groot Zwaafink et al. [16] for blowing snow sublimation. Therefore, this section is not meant to be an exhaustive review of techniques; rather, various methods are briefly introduced to illustrate the difficulty in their use for determining sublimation at the macroscale in Section 4. In this review, the term sublimation, unless otherwise specified, refers to a mass loss from the snowpack through latent heat flux over a given time period, with the understanding that deposition, condensation, and evaporation can also occur over the given time period.

2.1. Measurement Techniques. First, it is important to note that there are no measurement techniques to separate blowing snow sublimation from other processes in uncontrolled environments, and therefore blowing snow sublimation in complex terrain is only quantified by simulation [16, 20]. Latent heat flux from a snow covered surface is most often measured with eddy-covariance systems (e.g., [9, 21, 22]) or gravimetrically (e.g., [11, 23–26]). For both methods, latent heat flux is not separated by sublimation, deposition, condensation, evaporation, or transpiration and assumptions must be made about the dominant form of latent heat flux based on season [13, 27]. High frequency observations with a sonic anemometer, an instrument that is not ideal for long-term observations in harsh alpine environments, are required for eddy-covariance measurements [14]. To measure sublimation over long periods that experience precipitation, gravimetric techniques require accurate measurements of precipitation, a difficulty due to undercatch [13]. Snow removal by wind and sampling a snow surface with properties that are not representative of the surrounding environment are additional sources of error with gravimetric techniques [11, 13].

Measurements of ion chemistry and water isotopes can be used to quantify sublimation [28]. Cumulative snowfall solute concentrations and isotopic values can be determined upon regularly sampling snowfall events and measurements from the snowpack can then be used to quantify the depth of sublimation provided there is no significant mass loss from

melting [28]. In a small catchment in Idaho, USA, isotopic values were measured from streamflow by Koeniger et al. [29] suggesting that variation in isotopic enrichment was due to variation in sublimation due to forest cover characteristics.

2.2. Modeling Techniques. There are numerous approaches to modeling sublimation that vary in complexity based on the level of measurement detail for input and the sublimation type of interest (i.e., ground, canopy, or blowing snow sublimation). For ground snow sublimation, the most common method is the bulk aerodynamic method, requiring meteorological observations at only one height. The aerodynamic profile method has the potential to be more accurate than the bulk method but requires observations at multiple heights [14, 30]. As an example of a bulk method, the Alpine Multi-scale Numerical Distributed Simulation Engine (AMUNDSEN) employs the following that is valid for stability, roughness, and wind speeds common over snow surfaces in mountainous terrain [8]:

$$\text{LH} = 32.82 (0.18 + 0.098U) (e - e_s), \quad (1)$$

where LH is the latent heat flux in W m^{-2} (positive downward), e_s is the saturation vapor pressure with respect to ice (hPa), e is the vapor pressure (hPa), and U is the wind speed (m s^{-1}) at typical measurement levels. The snow surface temperature is required to determine e_s and iterative procedures can be used to determine the surface temperature required for energy balance when the measured air temperature is below 273.16 K [8]. The energy budget equation for the snow surface in a simple one-layer model is given by [31]

$$Q + H + \text{LH} + A + B + \text{LM} = 0, \quad (2)$$

where Q is net radiation, H is the sensible heat flux, A is the energy flux from precipitation, B is the soil heat flux, and LM is the energy available for melting. When the measured air temperature ≥ 273.16 K, the snow surface temperature is assumed to be 273.16 K (e.g., [8]).

Canopy and blowing snow sublimation models fundamentally differ from ground sublimation models to account for the higher surface area to mass ratio of snow stored in the canopy and suspended snow particles [10, 16]. Sublimation from an ice-sphere in thermodynamic equilibrium with the environment [32, 33] is given by [10, 34]

$$\frac{dm}{dt} = \frac{2\pi r (\text{RH}/100 - 1) - S_p \Omega}{h_s \Omega + 1/D\rho_v \text{Sh}} \quad (3)$$

with

$$\Omega = \frac{1}{\lambda_t T_a \text{Nu}} \left(\frac{h_s M}{RT_a} - 1 \right), \quad (4)$$

where m is the ice-sphere mass (kg), r is the radius (m), RH is the relative humidity (%) with respect to ice, S_p is absorbed solar radiation (W m^{-2}), h_s is the latent heat of sublimation (J kg^{-1}), D is the diffusivity of water vapor ($\text{m}^2 \text{s}^{-1}$), ρ_v is the saturation vapor density with respect to ice (kg m^{-3}),

TABLE 1: Slightly modified from Jackson and Prowse [26], selected studies of sublimation from snow covered terrain.

Study	Methods	Site type	Sublimation/evaporation
Bernier and Swanson, 1993 [35]	BA, Gr	Forest and open	0.25–1.07 mm dy ⁻¹
Doty and Johnston, 1969 [36]	Gr	Open	0.15 (January)–1.56 (April) mm dy ⁻¹
Fassnacht, 2004 [37]	BA	Various USA sites	0.23–0.67 mm dy ⁻¹
Golding, 1978 [38]	BA	Subalpine forest	1.2 mm dy ⁻¹ (1975), 2.0 mm dy ⁻¹ (1976)
Hood et al., 1999 [14]	AP	Alpine	0.9–1.8 mm dy ⁻¹ (annual 15% max SWE)
Lundberg et al., 1998 [39]	Gr	Forest (Scotland)	Max 3.9 mm in 7 hours (canopy)
Kaitera and Teräsvirta, 1972 [40]	BA	Boreal forest	0.35 (subcanopy)–0.45 (open) mm dy ⁻¹
Kaser, 1982 [41]	Gr	Alpine	Mean 0.25 mm dy ⁻¹ , max 2.0 mm dy ⁻¹
Marks and Dozier, 1992 [42]	BA	Alpine	Mean 2 mm dy ⁻¹
Martinelli, 1960 [43]	Gr	Alpine	±0.67 mm dy ⁻¹
Meiman and Grant, 1974 [44]		Alpine, forest, and open	45–60% snow season precipitation
Molotch et al., 2007 [9]	EC	Subalpine forest	0.41 (subcanopy)–0.71 (canopy) mm dy ⁻¹
Montesi et al., 2004 [7]	Gr	Subalpine forest	Canopy, 20–30% of total snowfall
Nakai et al., 1999 [45]	EC	Boreal forest canopy	1.2 mm dy ⁻¹ (snow covered)
Pomeroy et al., 1998 [10]	BA	Boreal forest	0.41–1.88 mm dy ⁻¹
Pomeroy and Essery, 1999 [21]	EC	Prairie	1.8 mm dy ⁻¹
Rylov, 1969 [46]	Gr	Open (semidesert)	0.08 (January)–0.6 (April) mm dy ⁻¹
Schmidt and Troendle, 1992 [47]		Canadian forest	Annual 46 mm (canopy)
Schmidt et al., 1998 [11]	BA, Gr	Subalpine forest	0.61 (southerly), 0.43 (northerly) mm dy ⁻¹
Storck et al., 2002 [48]	Gr, SC	Subalpine forest	100 mm/winter, <1 mm dy ⁻¹
Suzuki et al., 2006 [49]	BA, model	Taiga, larch forest	1.0 (forest)–2.0 (open) mm dy ⁻¹
West, 1962 [23]	Gr	Forest, subcanopy	50 mm (2.7% of snowfall) annually
Zhang et al., 2003 [50]	BA, Gr	Taiga	0.2–1.0 mm dy ⁻¹
Zhang et al., 2004 [25]	BA, Gr	Taiga, larch forest	0.22–0.32 mm dy ⁻¹

AP: aerodynamic profile; BA: bulk aerodynamic; EC: eddy covariance; Gr: gravimetric, lysimeter; SC: snow course.

Sh and Nu are the Sherwood and Nusselt numbers (nondimensional), respectively, which depend on the wind speed and particle size, λ_t is thermal conductivity of the air ($\text{J m}^{-1} \text{s}^{-1} \text{K}^{-1}$), T_a is the air temperature (K), R is the universal gas constant ($8313 \text{ J kmole}^{-1} \text{K}^{-1}$), and M is the molecular weight of water ($18.01 \text{ kg kmole}^{-1}$). Complete formulae and definitions for all terms in (3) and (4) are given by Pomeroy et al. [10] and Liston and Elder [34]. To get a canopy sublimation rate (mm s^{-1}), (3) can be multiplied by $\text{m}^{-1} (\text{kg}^{-1})$; the intercepted snow load (kg m^{-2}) that is dependent on leaf area index; and a nondimensional coefficient to account for the exposed snow surface area being less than that of the individual snow grains, dependent on snow load and leaf area index [7, 34, 51].

In modeling blowing snow sublimation, an ice-sphere sublimation model (e.g., (3)) is commonly used to determine mass loss from individual particles in a size spectrum of suspended particles [16, 52, 53]. Three-dimensional models are ideal for simulating blowing snow in complex terrain and include SnowTran-3D [34], SYTRON3 [54], and Alpine3D [55]. Of these three commonly used three-dimensional snow transport models, only Alpine3D explicitly implements negative feedback processes involving sublimation (i.e., in a plume of snow particles, sublimation reduces temperature and snow mass concentration and increases humidity [16]).

Valeo et al. [56] developed a method to estimate sublimation by use of a Global Positioning System. Using a relationship between zenith wet delay and specific humidity, a bulk aerodynamic method can be used to estimate sublimation by replacing measurement height humidity observations with Global Positioning System derived precipitable water [56]. Good agreement between observations from sublimation pans and modeled sublimation has been reported with this method [56].

3. Previous Research Efforts

3.1. Ground and Canopy Sublimation. Jackson and Prowse [26] present a table of sublimation estimates derived from 30 previous studies around the world indicating that sublimation varies considerably both spatially and temporally (Table 1). As seen in Table 1, sublimation rates are generally highest in wind exposed high altitude environments (e.g., a mean of 2 mm dy^{-1} from Marks and Dozier [42] and $0.9\text{--}1.8 \text{ mm dy}^{-1}$ from Hood et al. [14]). Ground sublimation from open areas is generally more rapid than adjacent forested areas (e.g., from Table 1, 1.0 versus 2.0 mm dy^{-1} from Suzuki et al. [49] and 0.35 versus 0.45 mm dy^{-1} from Kaitera and Teräsvirta [40]). In mountainous terrain in southwest Idaho, Reba et al. [22] measured sublimation from ground

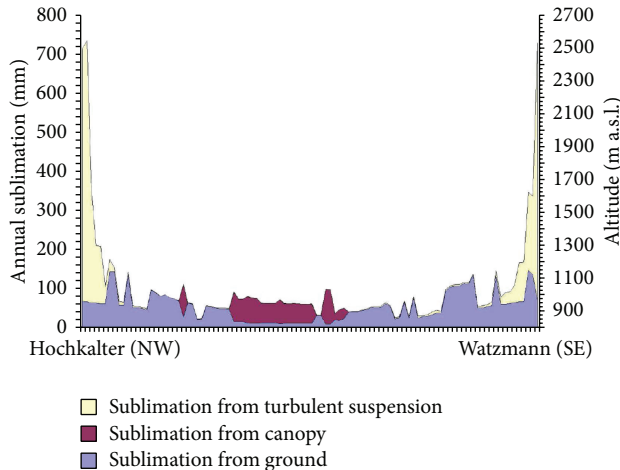


FIGURE 1: Reproduced from Strasser et al. [8], simulated contributions to total annual snow sublimation from ground sublimation, canopy sublimation, and blowing snow sublimation along a ~4 km transect across Wimbach valley in Berchtesgaden National Park, Germany.

snow cover during three winter seasons at a wind sheltered site (aspen forest) and wind exposed site (nonforested). Sublimation was less than 10% of maximum snow water equivalent (SWE) for all three winters at the sheltered site and ranged from 16% to 41% of maximum SWE at the exposed site (with blowing snow sublimation potentially contributing to the high sublimation at the exposed site).

Canopy sublimation rates in boreal forest are considerably larger than ground sublimation rates, from 1.2 mm dy^{-1} by Nakai et al. [45] for canopy sublimation to 0.45 mm dy^{-1} in forest clearings by Kaitera and Teräsvirta [40]. In a subalpine Colorado forest, Molotch et al. [9] measured canopy sublimation rates of 0.71 mm dy^{-1} and subcanopy sublimation rates of 0.41 mm dy^{-1} during March and April. Jackson and Prowse [26] found sublimation rates of 0.4 mm dy^{-1} at open sites during the snowmelt period in a small catchment in the Okanagan River basin in southern British Columbia. On adjacent north and south facing forested slopes in central Colorado, Schmidt et al. [11] found that ground snow cover sublimation is 20% of maximum SWE, with 1.2 times more sublimation on the south facing slope.

In a modeling study, Strasser et al. [8] produced a figure of sublimation totals along a mountain-valley transect in Berchtesgaden National Park, Germany (Figure 1). It can be seen that canopy sublimation is generally the dominant form of sublimation in tree-covered areas although there are portions of the transect with lower leaf area index (not shown) where ground sublimation is larger than canopy sublimation. Strasser et al. [8] report total vapor loss to be as low as 10% of annual snowfall in relatively open canopies with low wind speeds. In addition to leaf area index, the duration of snow cover held within tree canopies greatly influences the prominence of canopy sublimation across a landscape. Yamazaki et al. [57] highlight that solid water storage in the canopy is continuous in Siberian taiga forest

from October through March and note that this contrasts with temperate regions where snow storage in the forest canopy is intermittent except in areas with frequent snowfall.

Cold temperatures can limit sublimation which is evident in Table 1 with low sublimation rates during winter months. This is particularly evident in the values reported by Rylov [46] for an open semidesert area in Kazakhstan with January sublimation rates of 0.08 mm dy^{-1} compared to 0.6 mm dy^{-1} in April. Regions that experience intensely cold winters tend to have little sublimation during the winter [57, 58]. Yamazaki et al. [57] report modeled canopy sublimation rates of $<0.05 \text{ mm dy}^{-1}$ during midwinter in Siberian taiga forest. Zhou et al. [58] report ground sublimation of only $\sim 5 \text{ mm}$ in the Gurbantunggut Desert, China, over ~ 100 -day period. These low sublimation rates in cold regions should not be considered negligible as low winter precipitation results in 23.63% of snowfall sublimated in the Gurbantunggut Desert [58]. This is comparable to relatively high energy subalpine areas of the southwest USA where 17–30% of annual snowfall is lost to sublimation [28]. Of total annual arctic precipitation, 35–50% is thought to be lost to sublimation from tundra [59].

Previous investigators have also noted mass increase through condensation/deposition exceeding sublimation/evaporation, often during warm periods and through entire snowmelt seasons (e.g., [14, 24, 26]). Rates of mass increase as high as 0.75 mm dy^{-1} for March 2007 were measured at a forested site in southern British Columbia by Jackson and Prowse [26]. Subcanopy adjustments to humidity measurements taken at open sites often include setting the relative humidity to 100 percent when the snowpack is melting (e.g., [31]). Strasser et al. [31] simulate nearly equal magnitudes of sublimation and deposition for dense forest cover in Berchtesgaden National Park, Germany, for a single entire snow season (2005/2006). Hood et al. [14] report a May–July mass increase through latent heat flux in 1995 with an increase of 17 mm in May alone at an alpine site in Colorado. Strasser et al. [8] simulated deposition greater than 200 mm in a single year where snow cover persisted into summer in Berchtesgaden National Park, Germany.

Several investigators have highlighted the importance of a few high sublimation events to total seasonal sublimation (e.g., [14, 60]). Sublimation estimates from the aerodynamic profile method in the Front Range of the Rocky Mountains in Colorado, USA, by Hood et al. [14] indicate a two-day period with sublimation that totaled 21% of the monthly total. High sublimation events occur with high wind speeds along with relatively warm temperatures and low specific humidity leading to large vapor pressure deficits (Figure 2). While sublimation is often episodic, there are consistent diurnal patterns as well (Figure 3) with positive net radiation and higher snow surface temperatures, leading to sublimation during the day, and negative net radiation and low snow surface temperatures resulting in latent heat flux to the snowpack (deposition/condensation) at night.

3.2. Blowing Snow Sublimation. Blowing snow sublimation varies greatly in space and time, partly because high wind speeds are required to transport significant amounts of snow

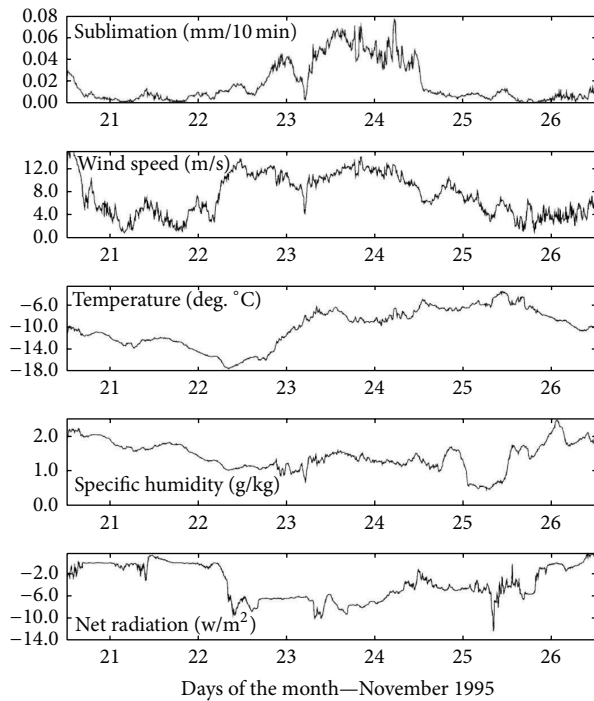


FIGURE 2: Reproduced from Hood et al. [14], ten-minute averages of sublimation, wind speed, temperature, specific humidity, and net radiation from Niwot Ridge, Colorado, USA. Tick marks denote the beginning of the day.

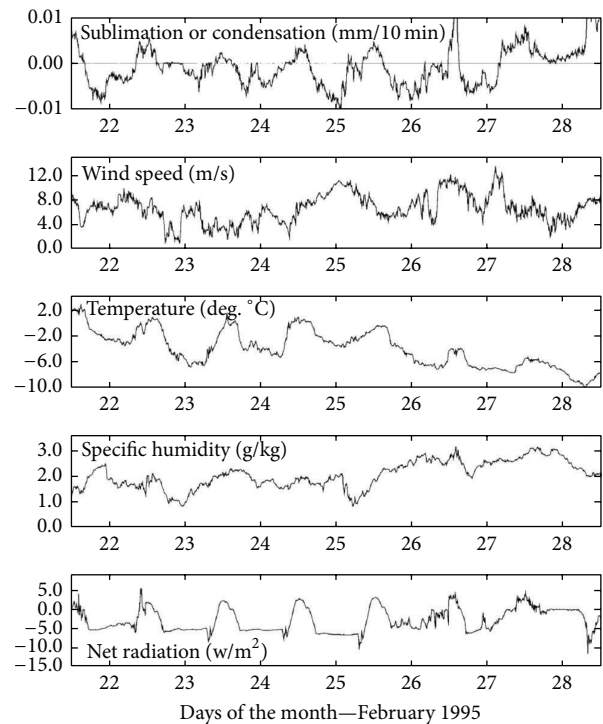


FIGURE 3: Reproduced from Hood et al. [14] as in Figure 2 but for seven days in February. Condensation is represented by negative values in the top panel.

[20, 61]. In a rugged alpine and subalpine region, Strasser et al. [8] show that seasonal totals of blowing snow sublimation can greatly exceed canopy and ground sublimation for exposed alpine ridges (Figure 1) representing a vapor loss that is 90% of total snowfall, but only accounting for a 4.1% loss of snowfall over the entire 210 km² study area in Berchtesgaden National Park, Germany. Bernhardt et al. [17] expanded on the Strasser et al. [8] study by including a gravitational snow transport scheme that resulted in more snow transport from wind exposed areas (e.g., crests and steep terrain) to lower wind sheltered areas. This reduced sublimation, as a percent of total snowfall, to 1.6% [17]. Groot Zwaaftink et al. [20] find even smaller contributions (0.1% of winter snowfall) of blowing snow sublimation to the snow water budget over a 2.4 km² alpine area in the Swiss Alps. The Alpine3D model used by Groot Zwaaftink et al. [20] includes feedback processes that make blowing snow sublimation self-limiting which is one reason why estimates are lower than those of Strasser et al. [8] and Bernhardt et al. [17]. Groot Zwaaftink et al. [20] also find that significant blowing snow sublimation is highly episodic, restricted to short time intervals that often correspond to Föhn storms, and that blowing snow sublimation can increase by an order of magnitude over localized areas of the alpine tundra. In a drier climate than the Swiss Alps, the Canadian Rockies, MacDonald et al. [62] simulated blowing snow sublimation to be between 17 and 19% of seasonal snowfall along a largely treeless ridge. In a relatively windy 65 km² catchment of the low arctic

(e.g., a monthly mean 10-m speed of 7 m s⁻¹) where fetch is longer than most alpine areas, Pomeroy et al. [63] simulated blowing snow sublimation to be 19.5% of annual snowfall.

3.3. Sensitivity to Changes in Forest Cover. While most elements of microscale variability remain constant on short time scales (i.e., slope, aspect, curvature, and elevation) vegetation patterns can vary considerably through natural (wildfire, bark beetle infestation) and anthropogenic (land management practices) processes [5, 64]. Therefore, understanding how changes at the stand scale impact snow sublimation at the macroscale is critical from a future water resources perspective. LaMalfa and Ryle [5] note declining aspen (*Populus tremuloides*) stands in the western USA attributable to fire suppression, ungulate browsing, land use practices, and climate change. LaMalfa and Ryle [5] observed greater water yield for melt driven runoff and groundwater recharge in aspen stands compared to mixed conifer stands and noted the desire for Western USA land managers to restore aspen forests suggesting that the economic benefits from increased water yield could eventually overcome restoration costs.

It is likely that vegetation impacts on sublimation vary by region. Pugh and Small [64] examined sublimation differences among living and dead (from bark beetle infestation) lodgepole pine (*Pinus contorta*) stands in Colorado, USA, concluding more total sublimation loss from live stands. Pugh and Small [64] admit that these results may differ in regions with storm characteristics more conducive to canopy interception and interstorm characteristics less conducive to rapid

sublimation. Similarly, it is possible that the net effect of dense forest cover on sublimation in cold regions is opposite to that in warmer forests due to differences in the length of time during which snow is held in the canopy [57] and differences in the importance of canopy sheltering on the snowpack energy budget. For example, Harpold et al. [65] observed reduced interception in recently burned forest compared to unburned forest in the Jemez Mountains of New Mexico, USA, yet peak snow accumulation was observed to be greater in unburned areas. Harpold et al. [65] speculated that, in a region with high solar elevation angles and frequent cloud-free conditions, ground sublimation may be especially sensitive to increased shortwave radiation following the removal of the forest canopy by fire. Furthermore, if short canopy snow cover duration is a limiting factor for seasonal canopy sublimation in warmer regions, then changes in forest radiation and wind sheltering impacts on ground sublimation may overcome reduced intercepted sublimation upon forest thinning.

4. Challenges in Determining Macroscale Snow Sublimation

The few studies of sublimation across large scales are restricted to high latitude regions. Essery et al. [18] examined canopy sublimation from the Northern Hemisphere boreal forests through coupling a GCM with a canopy snow process model. The fraction of sublimated snow for grid cells was most commonly just greater than one-fifth, with a few grid cells in the continental climates of Asia displaying fractions of one-half [18]. Déry and Yau [6] used the European Centre for Medium Range Weather Forecasts Reanalysis to determine ground snow sublimation through a bulk aerodynamic method and blowing snow sublimation through a double-moment blowing snow model for Antarctica and the Arctic. They found that ground snow sublimation is 7% of annual precipitation over the entire Mackenzie River Basin in Canada and more than 17% of annual precipitation over Antarctica. Van den Broeke [66] used a general circulation model and a bulk aerodynamic method to determine that sublimation over Antarctica represents 10–15% of the annual precipitation.

In mountainous regions of the midlatitudes, terrain is highly complex, with elevation, slope, aspect, curvature, vegetation type, forest density, forest clearing size, and canopy geometry all varying greatly over small spatial scales [12]. It is therefore difficult to scale up results of measured sublimation from specific sites to the basin scale [26]. Similarly, modeling sublimation in complex terrain must be done at high resolution and therefore multiple meteorological variables must be represented at high resolution to do so (e.g., [67]). Interpolated meteorological fields from observations [8, 15, 16, 67] and high resolution fields from mesoscale models [17] can be used to produce spatially distributed simulations of sublimation. Unfortunately, due to the requirement for high resolution modeling, the many investigations concerned with spatially distributed simulations of sublimation in complex terrain are small in scale, only hundreds of square kilometers (e.g., [8, 15–17, 20]).

Isotopic values and solute concentrations of streamflow can provide valuable information on sublimation (e.g., [29]) but seasonal quantification of sublimation at the macroscale would require detailed observations at high resolution as Ohlanders et al. [68] note that snowpack isotopic values vary considerably by elevation and at the microscale with constant elevation. Temperature influences the isotopic variability of precipitation, requiring that samples of precipitation composition be taken in multiple areas of a macroscale study area. Last, isotopic compositions also change during transport as surface and subsurface flow [68], making the contribution from sublimation difficult to isolate.

From a water budget perspective, total macroscale sublimation over time period t can potentially be estimated by considering the following water budget equation:

$$F = P - \text{SUB} - E - T - \Delta\text{ST}, \quad (5)$$

where F is measured river discharge over time period t , P is total precipitation over the contributing basin area, SUB is the total sublimation over the area, E is evaporation, T is transpiration, and ΔST is the increase in water storage over the period t . If t is a long time period (e.g., multiple years), then ΔST will be considerably less than all other terms and errors related to runoff lag will be minimal. Even with large t , errors in sublimation determined from (1) are sensitive to errors in macroscale estimates of P , E , and T in addition to errors in measured river discharge. For short time periods (e.g., t equals several months), ΔST must be determined and errors related to the transport time of water through the basin become significant [69].

5. Future Directions

Strasser et al. [31] simulate sublimation from an idealized mountain with regular patterns of forested and nonforested areas for three consecutive winters. Among many important findings, Strasser et al. [31] concluded that (1) the effects of aspect on snow cover in forests are only apparent for lower values of leaf area index and (2) sublimation losses from the canopy are relatively more dominant during the dry winter, in contrast to the wet winter when more snow accumulated subcanopy. These results from the Strasser et al. [31] experiment highlight important components of spatial and interannual variability in the forest canopy impact on snowpack. Without accurate measurements of sublimation at the macroscale, it is not possible to validate macroscale estimates of sublimation through simulation. Although simulated magnitudes of sublimation at the macroscale cannot presently be taken as truth, advances in the understanding of how microscale variability affects total macroscale sublimation can still be achieved through careful model experiments (e.g., [31]), especially if the sensitivity of results is examined through parameter adjustment and multimodel simulations. For example, examining model output across forest density gradients controlling for topographic characteristics and/or incrementally changing the canopy characteristics between simulations can quantify the impact of forest cover changes (e.g., thinning, insect infestation, and tree species change).

High resolution (e.g., 30-m) terrain and forest cover data and climate reanalysis datasets that provide the necessary variables to determine latent heat flux from (1) to (4) can be used to estimate sublimation at large scales in complex terrain. For example, in the United States, the National Land Cover Database 2011 [70], National Elevation Dataset [71], and the North American Regional Reanalysis by Mesinger et al. [72] can be used in conjunction with established terrain and vegetation adjustments to spatially distribute meteorological observations based on slope, aspect, elevation, terrain curvature, and forest cover (e.g., [31, 34, 67, 73]). With a large study domain and limited computational resources, the terrain and forest cover data can be coarsened, although important features of topography and forest cover (e.g., steep slopes, dense forest cover adjacent to open areas) may be neglected from coarsening. This can be overcome by defining discrete classes, or by using clustering algorithms, to group high resolution cells based on slope, aspect, elevation, terrain curvature, and forest cover characteristics. Snow model systems can be run once for each group, and the results spatially distributed across the domain (e.g., [74]).

To lend confidence to conclusions drawn from seasonal simulations of sublimation at the macroscale, the spatially distributed meteorological observations and modelled sublimation can be compared to measured values reported by the numerous site specific investigations. Multiple years of meteorological observations and eddy-covariance measured latent heat flux over open areas and subcanopy are reported by Reba et al. [22] and Molotch et al. [9] report subcanopy and above canopy eddy-covariance measured latent heat flux for a single spring. Eddy-covariance flux tower reports of latent heat flux measured above canopy and local meteorological observation are presented particularly well by Broxton et al. [27] for more than four years at two sites in the Rocky Mountains of the USA.

Increased confidence in macroscale estimates of snow sublimation through simulation can also be gained by comparisons between modelled and observed macroscale SWE and snow cover extent. Snow cover duration agreement is most critical but when comparisons between sublimation and melt are of interest, peak SWE agreement is also necessary. The seasonal evolution of basin scale SWE and snow cover extent can be quantified from satellite observations (e.g., MODIS on NASA's Terra and Aqua satellites for snow extent and AMSR-E on the Aqua satellite for SWE). Daily true color imagery and the climate-modeling grid-level-3 data (MOD10C1) at 0.05° resolution based on 500 m Terra MODIS observations [75] can be used to control for cloud cover and to quantify snow covered area. The daily resolution of MODIS derived products makes many observations of snow covered area soon after snow events (given cloud-free conditions) and through spring ablation seasons feasible. In complex forested terrain, however, both SWE and snow covered area tend to be underestimated by products derived from satellite observation (e.g., [76–78]). Snow cover may be completely obscured in areas that are more than ~60% forested and simple adjustments to fractional snow covered area based on canopy cover fraction [78] assume that the canopy obscured snow cover fraction is equal to the visible snow cover fraction.

Therefore, automated (e.g., SNOTEL in the USA) or manual (e.g., NRCS snow course or NWS COOP measurements in the USA) ground based measurements should be used to supplement remotely sensed observations. Such observations are often limited in spatial extent and SNOTEL sites are often located in forest openings and in areas favored for snow accumulation [79]. Therefore, when possible, in studies determining macroscale sublimation through simulation, both ground based and remotely sensed snowpack observations should be used to validate the simulated evolution of SWE and snow cover extent.

6. Summary and Conclusion

In this review, an overview of techniques to model and/or measure sublimation from intercepted snow, suspended snow particles, and ground snowpack was given. Previous research efforts were synthesized to further illustrate the controls on, and large variability of, sublimation in complex terrain. Challenges in estimating sublimation in complex terrain were then discussed and, despite an extensive body of literature on the topic, difficulties in measuring and modeling snowpack sublimation limit our understanding of this important water budget component, particularly on larger scales in complex terrain. Without techniques to measure sublimation at the macroscale, model estimates of sublimation cannot be validated directly. The final section of the review highlights datasets, techniques, and previous investigations that may be useful for future studies involving macroscale estimates of sublimation.

If it can be illustrated that the simulated snowpack agrees well with the seasonal evolution of SWE and simulated vapor flux agrees well with numerous previous investigations that report site specific measurements of sublimation, then model experiments have the potential to advance our understanding of sublimation at macroscales. Different model representations of canopy interception, sublimation, unloading, and sheltering may produce substantially different estimates of total macroscale sublimation in forested terrain yet sensitivity tests and ensemble simulations can increase confidence in the insight gained from model experiments that help answer important questions. How do vegetation-sublimation relationships in mountainous terrain vary by climate type, forest class (e.g., deciduous, coniferous, or mixed), healthy versus unhealthy forest, forest clearing size, forest density, intrabasin, seasonally, and interannually?

Snowpack sublimation from mountainous terrain is complex and it has been illustrated in numerous investigations that it is not a negligible component of the snow water balance. With the expectation of a continued global temperature increase, water resource issues in many mountainous regions with seasonal snow cover may develop or intensify. Therefore, advancing knowledge of all water budget components in complex terrain at the macroscale is critically important.

Conflict of Interests

The author declares that there is no conflict of interests regarding the publication of this paper.

References

- [1] T. P. Barnett, J. C. Adam, and D. P. Lettenmaier, "Potential impacts of a warming climate on water availability in snow-dominated regions," *Nature*, vol. 438, no. 7066, pp. 303–309, 2005.
- [2] S. A. Rauscher, J. S. Pal, N. S. Diffenbaugh, and M. M. Benedetti, "Future changes in snowmelt-driven runoff timing over the western US," *Geophysical Research Letters*, vol. 35, no. 16, Article ID L16703, 2008.
- [3] H. G. Hidalgo, T. Das, M. D. Dettinger et al., "Detection and attribution of streamflow timing changes to climate change in the Western United States," *Journal of Climate*, vol. 22, no. 13, pp. 3838–3855, 2009.
- [4] J. R. Minder, "The sensitivity of mountain snowpack accumulation to climate warming," *Journal of Climate*, vol. 23, no. 10, pp. 2634–2650, 2010.
- [5] E. M. LaMalfa and R. Ryle, "Differential snowpack accumulation and water dynamics in aspen and conifer communities: implications for water yield and ecosystem function," *Ecosystems*, vol. 11, no. 4, pp. 569–581, 2008.
- [6] S. J. Déry and M. K. Yau, "Large-scale mass balance effects of blowing snow and surface sublimation," *Journal of Geophysical Research D: Atmospheres*, vol. 107, no. 23, pp. 8-1–8-17, 2002.
- [7] J. Montesi, K. Elder, R. A. Schmidt, and R. E. Davis, "Sublimation of intercepted snow within a subalpine forest canopy at two elevations," *Journal of Hydrometeorology*, vol. 5, no. 5, pp. 763–773, 2004.
- [8] U. Strasser, M. Bernhardt, M. Weber, G. E. Liston, and W. Mauser, "Is snow sublimation important in the alpine water balance?" *Cryosphere*, vol. 2, no. 1, pp. 53–66, 2008.
- [9] N. P. Molotch, P. D. Blanken, M. W. Williams, A. A. Turnipseed, R. K. Monson, and S. A. Margulis, "Estimating sublimation of intercepted and sub-canopy snow using eddy covariance systems," *Hydrological Processes*, vol. 21, no. 12, pp. 1567–1575, 2007.
- [10] J. W. Pomeroy, J. Parviainen, N. Hedstrom, and D. M. Gray, "Coupled modelling of forest snow interception and sublimation," *Hydrological Processes*, vol. 12, no. 15, pp. 2317–2337, 1998.
- [11] R. A. Schmidt, C. A. Troendle, and J. R. Meiman, "Sublimation of snowpacks in subalpine conifer forests," *Canadian Journal of Forest Research*, vol. 28, no. 4, pp. 501–513, 1998.
- [12] A. Varhola, N. C. Coops, M. Weiler, and R. D. Moore, "Forest canopy effects on snow accumulation and ablation: an integrative review of empirical results," *Journal of Hydrology*, vol. 392, no. 3-4, pp. 219–233, 2010.
- [13] A. Lundberg and S. Halldin, "Snow interception evaporation. Review of measurement techniques, processes, and models," *Theoretical and Applied Climatology*, vol. 70, no. 1-4, pp. 117–133, 2001.
- [14] E. Hood, M. Williams, and D. Cline, "Sublimation from a seasonal snowpack at a continental, mid-latitude alpine site," *Hydrological Processes*, vol. 13, no. 12-13, pp. 1781–1797, 1999.
- [15] M. Lehning, I. Völksch Ingo, D. Gustafsson, T. A. Nguyen, M. Stähli, and M. Zappa, "ALPINE3D: a detailed model of mountain surface processes and its application to snow hydrology," *Hydrological Processes*, vol. 20, no. 10, pp. 2111–2128, 2006.
- [16] C. D. Groot Zwaafink, H. Löwe, R. Mott, M. Bavay, and M. Lehning, "Drifting snow sublimation: a high-resolution 3-D model with temperature and moisture feedbacks," *Journal of Geophysical Research D: Atmospheres*, vol. 116, no. 16, 2011.
- [17] M. Bernhardt, K. Schulz, G. E. Liston, and G. Zängl, "The influence of lateral snow redistribution processes on snow melt and sublimation in alpine regions," *Journal of Hydrology*, vol. 424-425, pp. 196–206, 2012.
- [18] R. Essery, J. Pomeroy, J. Parviainen, and P. Storck, "Sublimation of snow from coniferous forests in a climate model," *Journal of Climate*, vol. 16, no. 11, pp. 1855–1864, 2003.
- [19] L. Mahrt and D. Vickers, "Moisture fluxes over snow with and without protruding vegetation," *Quarterly Journal of the Royal Meteorological Society*, vol. 131, no. 607, pp. 1251–1270, 2005.
- [20] C. D. Groot Zwaafink, R. Mott, and M. Lehning, "Seasonal simulation of drifting snow sublimation in Alpine terrain," *Water Resources Research*, vol. 49, no. 3, pp. 1581–1590, 2013.
- [21] J. W. Pomeroy and R. L. H. Essery, "Turbulent fluxes during blowing snow: field tests of model sublimation predictions," *Hydrological Processes*, vol. 13, no. 18, pp. 2963–2975, 1999.
- [22] M. L. Reba, J. Pomeroy, D. Marks, and T. E. Link, "Estimating surface sublimation losses from snowpacks in a mountain catchment using eddy covariance and turbulent transfer calculations," *Hydrological Processes*, vol. 26, no. 24, pp. 3699–3711, 2012.
- [23] A. J. West, "Snow evaporation from a forested watershed in the central Sierra Nevada," *Journal of Forestry*, vol. 60, pp. 481–484, 1962.
- [24] A. N. Gelfan, J. W. Pomeroy, and L. S. Kuchment, "Modeling forest cover influences on snow accumulation, sublimation, and melt," *Journal of Hydrometeorology*, vol. 5, no. 5, pp. 785–803, 2004.
- [25] Y. Zhang, K. Suzuki, T. Kadota, and T. Ohata, "Sublimation from snow surface in southern mountain taiga of eastern Siberia," *Journal of Geophysical Research D: Atmospheres*, vol. 109, Article ID D21103, 2004.
- [26] S. I. Jackson and T. D. Prowse, "Spatial variation of snowmelt and sublimation in a high-elevation semi-desert basin of western Canada," *Hydrological Processes*, vol. 23, no. 18, pp. 2611–2627, 2009.
- [27] P. D. Broxton, A. A. Harpold, J. A. Biederman, P. A. Troch, N. P. Molotch, and P. D. Brooks, "Quantifying the effects of vegetation structure on snow accumulation and ablation in mixed-conifer forests," *Ecology*, 2014.
- [28] J. R. Gustafson, P. D. Brooks, N. P. Molotch, and W. C. Veatch, "Estimating snow sublimation using natural chemical and isotopic tracers across a gradient of solar radiation," *Water Resources Research*, vol. 46, no. 12, Article ID W12511, 2010.
- [29] P. Koeniger, J. A. Hubbart, T. Link, and J. D. Marshall, "Isotopic variation of snow cover and streamflow in response to changes in canopy structure in a snow-dominated mountain catchment," *Hydrological Processes*, vol. 22, no. 4, pp. 557–566, 2008.
- [30] M. Arck and D. Scherer, "Problems in the determination of sensible heat flux over snow," *Geografiska Annaler, Series A: Physical Geography*, vol. 84, no. 3-4, pp. 157–169, 2002.
- [31] U. Strasser, M. Warscher, and G. E. Liston, "Modeling snow-canopy processes on an idealized mountain," *Journal of Hydrometeorology*, vol. 12, no. 4, pp. 663–677, 2011.
- [32] A. D. Thorpe and B. J. Mason, "The evaporation of ice spheres and ice crystals," *British Journal of Applied Physics*, vol. 17, no. 4, pp. 541–548, 1966.
- [33] R. A. Schmidt, "Sublimation of wind-transported snow: a model," USDA Forest Service Research Paper RM-90, Rocky Mountain Forest and Range Experiment Station, Fort Collins, Colo, USA, 1972.

- [34] G. E. Liston and K. Elder, "A distributed snow-evolution modeling system (snowmodel)," *Journal of Hydrometeorology*, vol. 7, no. 6, pp. 1259–1276, 2006.
- [35] P. Y. Bernier and R. H. Swanson, "The influence of opening size on snow evaporation in the forests of the Alberta Foothills," *Canadian Journal of Forest Research*, vol. 23, no. 2, pp. 239–244, 1993.
- [36] R. D. Doty and R. S. Johnston, "Comparison of gravimetric measurements and mass transfer computations of snow evaporation beneath selected vegetation canopies," in *Proceedings of the 37th Western Snow Conference*, pp. 57–62, Fort Collins, Colo, USA, 1969.
- [37] S. R. Fassnacht, "Estimating alter-shielded gauge snowfall undercatch, snowpack sublimation, and blowing snow transport at six sites in the coterminous USA," *Hydrological Processes*, vol. 18, no. 18, pp. 3481–3492, 2004.
- [38] D. L. Golding, "Calculated Snowpack Evaporation during Chinooks along the Eastern Slopes of the Rocky Mountains in Alberta," *Journal of Applied Meteorology*, vol. 17, no. 11, pp. 1647–1651, 1978.
- [39] A. Lundberg, I. Calder, and R. Harding, "Evaporation of intercepted snow: measurement and modelling," *Journal of Hydrology*, vol. 206, no. 3-4, pp. 151–163, 1998.
- [40] P. Kaitera and H. Teräsvirta, "Snow evaporation in South and North Finland 1969/79 and 1970/71," *Aqua Fennica*, vol. 2, pp. 11–19, 1972.
- [41] G. Kaser, "Measurement of evaporation from snow," *Archives for Meteorology, Geophysics, and Bioclimatology*, vol. 30, no. 4, pp. 333–340, 1982.
- [42] D. Marks and J. Dozier, "Climate and energy exchange at the snow surface in the alpine region of the Sierra Nevada. 2. Snow cover energy balance," *Water Resources Research*, vol. 28, no. 11, pp. 3043–3054, 1992.
- [43] M. Martinelli, "Moisture exchange between the atmosphere and alpine snow surfaces under summer conditions (preliminary results)," *Journal of Meteorology*, vol. 17, no. 2, pp. 227–231, 1960.
- [44] J. R. Meiman and L. O. Grant, "Snow-air interactions and management of mountain watershed snowpack," Completion Report 57, Environmental Resources Center, Colorado State University, Fort Collins, Colo, USA, 1974.
- [45] Y. Nakai, T. Sakamoto, T. Terajima, K. Kitamura, and T. Shirai, "The effect of canopy-snow on the energy balance above a coniferous forest," *Hydrological Processes*, vol. 13, no. 14-15, pp. 2371–2382, 1999.
- [46] S. P. Rylov, "Snowcover evaporation in the semi-desert zone of Kazakhstan," *Selected Papers of Soviet Hydrology*, vol. 3, pp. 258–270, 1969.
- [47] R. A. Schmidt and C. A. Troendle, "Sublimation of intercepted snow as a source of global water vapor," in *Proceedings of the 60th Annual Western Snow Conference*, Jackson Hole, Wyo, USA, April 1992.
- [48] P. Storck, D. P. Lettenmaier, and S. M. Bolton, "Measurement of snow interception and canopy effects on snow accumulation and melt in a mountainous maritime climate, Oregon, United States," *Water Resources Research*, vol. 38, no. 11, pp. 51–516, 2002.
- [49] K. Suzuki, J. Kubota, Y. Zhang, T. Kadota, T. Ohata, and V. Vuglinsky, "Snow ablation in an open field and larch forest of the southern mountainous region of eastern Siberia," *Hydrological Sciences Journal*, vol. 51, no. 3, pp. 465–480, 2006.
- [50] Y. Zhang, T. Ohata, K. Ersi, and Y. Tandong, "Observation and estimation of evaporation from the ground surface of the cryosphere in eastern Asia," *Hydrological Processes*, vol. 17, no. 6, pp. 1135–1147, 2003.
- [51] C. R. Ellis, J. W. Pomeroy, T. Brown, and J. MacDonald, "Simulation of snow accumulation and melt in needleleaf forest environments," *Hydrology and Earth System Sciences*, vol. 14, no. 6, pp. 925–940, 2010.
- [52] R. Bintanja, "Modelling snowdrift sublimation and its effect on the moisture budget of the atmospheric boundary layer," *Tellus, Series A: Dynamic Meteorology and Oceanography*, vol. 53, no. 2, pp. 215–232, 2001.
- [53] M. K. MacDonald, J. W. Pomeroy, and A. Pietroniro, "Parameterizing redistribution and sublimation of blowing snow for hydrological models: tests in a mountainous subarctic catchment," *Hydrological Processes*, vol. 23, no. 18, pp. 2570–2583, 2009.
- [54] Y. Durand, G. Guyomarc'h, L. Mérindol, and J. G. Corripio, "Improvement of a numerical snow drift model and field validation," *Cold Regions Science and Technology*, vol. 43, no. 1-2, pp. 93–103, 2005.
- [55] M. Lehning, H. Löwe, M. Ryser, and N. Raderschall, "Inhomogeneous precipitation distribution and snow transport in steep terrain," *Water Resources Research*, vol. 44, no. 7, Article ID W07404, 2008.
- [56] C. Valeo, S. H. Skone, C. L. I. Ho, S. K. M. Poon, and S. M. Shrestha, "Estimating snow evaporation with GPS derived precipitable water vapour," *Journal of Hydrology*, vol. 307, no. 1–4, pp. 196–203, 2005.
- [57] T. Yamazaki, H. Yabuki, and T. Ohata, "Hydrometeorological effects of intercepted snow in an eastern Siberian taiga forest using a land-surface model," *Hydrological Processes*, vol. 21, no. 9, pp. 1148–1156, 2007.
- [58] H.-F. Zhou, X.-J. Zheng, B. Zhou, Q. Dai, and Y. Li, "Sublimation over seasonal snowpack at the southeastern edge of a desert in central Eurasia," *Hydrological Processes*, vol. 26, no. 25, pp. 3911–3920, 2012.
- [59] G. E. Liston and M. Sturm, "The role of winter sublimation in the Arctic moisture budget," *Nordic Hydrology*, vol. 35, no. 4-5, pp. 325–334, 2004.
- [60] Y. Zhang, M. Ishikawa, T. Ohata, and D. Oyunbaatar, "Sublimation from thin snow cover at the edge of the Eurasian cryosphere in Mongolia," *Hydrological Processes*, vol. 22, no. 18, pp. 3564–3575, 2008.
- [61] R. Bintanja, "Snowdrift sublimation in a Katabatic wind region of the Antarctic ice sheet," *Journal of Applied Meteorology*, vol. 40, no. 11, pp. 1952–1966, 2001.
- [62] M. K. MacDonald, J. W. Pomeroy, and A. Pietroniro, "On the importance of sublimation to an alpine snow mass balance in the Canadian Rocky Mountains," *Hydrology and Earth System Sciences*, vol. 14, no. 7, pp. 1401–1415, 2010.
- [63] J. W. Pomeroy, P. Marsh, and D. M. Gray, "Application of a distributed blowing snow model to the arctic," *Hydrological Processes*, vol. 11, no. 11, pp. 1451–1464, 1997.
- [64] E. T. Pugh and E. E. Small, "The impact of beetle-induced conifer death on stand-scale canopy snow interception," *Hydrology Research*, vol. 44, no. 4, pp. 644–657, 2013.
- [65] A. A. Harpold, J. A. Biederman, K. Condon et al., "Changes in snow accumulation and ablation following the Las Conchas Forest Fire, New Mexico, USA," *Ecohydrology*, vol. 7, no. 2, pp. 440–452, 2014.
- [66] M. R. van den Broeke, "Spatial and temporal variation of sublimation on Antarctica: results of a high-resolution general

- circulation model,” *Journal of Geophysical Research D: Atmospheres*, vol. 102, no. 25, pp. 29765–29777, 1997.
- [67] G. E. Liston and K. Elder, “A meteorological distribution system for high-resolution terrestrial modeling (MicroMet),” *Journal of Hydrometeorology*, vol. 7, no. 2, pp. 217–234, 2006.
- [68] N. Ohlanders, M. Rodriguez, and J. McPhee, “Stable water isotope variation in a Central Andean watershed dominated by glacier and snowmelt,” *Hydrology and Earth System Sciences*, vol. 17, no. 3, pp. 1035–1050, 2013.
- [69] A. W. Ellis, T. W. Hawkins, R. C. Balling Jr., and P. Gober, “Estimating future runoff levels for a semi-arid fluvial system in central Arizona, USA,” *Climate Research*, vol. 35, no. 3, pp. 227–239, 2008.
- [70] S. Jin, L. Yang, P. Danielson, C. Homer, J. Fry, and G. Xian, “A comprehensive change detection method for updating the National Land Cover Database to circa 2011,” *Remote Sensing of Environment*, vol. 132, pp. 159–175, 2013.
- [71] D. Gesch, M. Oimoen, S. Greenlee, C. Nelson, M. Steuck, and D. Tyler, “The national elevation dataset,” *Photogrammetric Engineering and Remote Sensing*, vol. 68, no. 1, pp. 5–11, 2002.
- [72] F. Mesinger, G. DiMego, E. Kalnay et al., “North American regional reanalysis,” *Bulletin of the American Meteorological Society*, vol. 87, no. 3, pp. 343–360, 2006.
- [73] B. W. Brock and N. S. Arnold, “A spreadsheet-based (microsoft excel) point surface energy balance model for glacier and snow melt studies,” *Earth Surface Processes and Landforms*, vol. 25, no. 6, pp. 649–658, 2000.
- [74] J. Fiddes and S. Gruber, “TopoSUB: a tool for efficient large area numerical modelling in complex topography at sub-grid scales,” *Geoscientific Model Development*, vol. 5, no. 5, pp. 1245–1257, 2012.
- [75] D. K. Hall, G. A. Riggs, V. V. Salomonson, N. E. DiGirolamo, and K. J. Bayr, “MODIS snow-cover products,” *Remote Sensing of Environment*, vol. 83, no. 1-2, pp. 181–194, 2002.
- [76] M. Tedesco and P. S. Narvekar, “Assessment of the NASA AMSR-E SWE product,” *IEEE Journal of Selected Topics in Applied Earth Observations and Remote Sensing*, vol. 3, no. 1, pp. 141–159, 2010.
- [77] C. L. Moser, G. A. Tootle, A. A. Oubeidillah, and V. Lakshmi, “A comparison of SNOTEL and AMSR-E snow water equivalent data sets in Western US Watersheds,” *International Journal of Remote Sensing*, vol. 32, no. 21, pp. 6611–6629, 2011.
- [78] K. Rittger, T. H. Painter, and J. Dozier, “Assessment of methods for mapping snow cover from MODIS,” *Advances in Water Resources*, vol. 51, pp. 367–380, 2013.
- [79] N. Salzmann and L. O. Mearns, “Assessing the performance of multiple regional climate model simulations for seasonal mountain snow in the Upper Colorado River Basin,” *Journal of Hydrometeorology*, vol. 13, no. 2, pp. 539–556, 2012.

Research Article

Hydrochemical Denudation and Transient Carbon Dioxide Drawdown in the Highly Glacierized, Shrinking Koxkar Basin, China

Jian Wang,^{1,2} Haidong Han,² Qiudong Zhao,² and Xiaowen Zhang³

¹College of Urban and Environmental Sciences, Yancheng Teachers University, Yancheng 224002, China

²State Key Laboratory of Cryosphere Science, Cold and Arid Regions Environmental and Engineering Research Institute, Chinese Academy of Sciences, Lanzhou 730000, China

³College of Urban and Environmental Sciences, Northwest University, Xi'an 710027, China

Correspondence should be addressed to Xiaowen Zhang; zhangsq@nwu.edu.cn

Received 18 December 2014; Revised 29 May 2015; Accepted 16 June 2015

Academic Editor: Fengjing Liu

Copyright © 2016 Jian Wang et al. This is an open access article distributed under the Creative Commons Attribution License, which permits unrestricted use, distribution, and reproduction in any medium, provided the original work is properly cited.

This study considered solute fluxes and the transient CO₂ drawdown process in the highly glacierized Koxkar basin in Central Eurasia, around 70.20% of which is covered by present-day ice. From 27 June to 30 September 2011, the total runoff depth was 671.70 mm, which yielded crustal solute fluxes of $213.65 \pm 10.05 \text{ kg} \cdot (\text{km}^2 \cdot \text{d})^{-1}$ that accounted for 53.59% of the total solute flux of the river water. The solute fluxes derived directly from ice meltwater and precipitation were 70.02 ± 4.68 and $16.57 \pm 1.13 \text{ kg} \cdot (\text{km}^2 \cdot \text{d})^{-1}$, respectively, which accounted for 17.57% and 4.16% of the total solute flux. The carbonation and hydrolysis of carbonate and feldspar minerals occurred because of the presence of H⁺, supplied by sulfide oxidation or CO₂ drawdown. While the H⁺ yielded by sulfide oxidation was insufficient for hydrochemical reactions, atmospheric CO₂ dissolved in the water generated H⁺ that drove follow-up reactions. The total transient drawdown of CO₂ was 804.83 t C, which generated 39.61% of the total HCO₃⁻ and 24.68% of the river water solute. Transient drawdown of CO₂ in the glacier region indicated that change of glacial area and volume could influence atmospheric CO₂ concentration and be important in the long-term global CO₂ cycle.

1. Introduction

From 1880 to 2012, the global mean surface air temperature has increased by 0.85°C and this increase has been especially pronounced since about 1950 [1]. For example, in the extensively glaciated Tarim basin in China, the mean surface air temperature has increased by 0.6°C since the 1980s (i.e., 0.2°C per decade). This rate of warming has had considerable influence on the alpine glaciers and hydrology of such regions. Overall, 82.2% of glaciers have retreated and the total glacial area has reduced by 4.5% [2]. Furthermore, because of climate warming resulting from increased greenhouse gas forcing, the volume of glacial meltwater has increased by about $1.24 \times 10^8 \text{ m}^3 \cdot \text{a}^{-1}$, which accounts for about 15% of the increase in river discharge in the Tarim basin [3]. Increased river discharge increases crustal solute fluxes (or chemical

denudation rates) and CO₂ drawdown rates [4, 5] because of hydrochemical reactions.

A few studies have reported on chemical denudation rates and CO₂ drawdown rates in the glaciers of the Arctic, Alps, and Himalayan mountains [4, 6–13]. These reports suggested that denudation rates in glaciated areas were higher than in nonglaciated regions [7]. In Central Asia, there are many large glaciers (area > 50 km²) covered by supraglacial moraines. Because they are in regions far from the ocean, there is little precipitation and ice/snow meltwater has particular importance as a water resource. However, a review of chemical denudation rates is beyond the scope of the present paper.

The focus of the present study was to examine the fluxes of major ions emanating from a subglacial outlet, to assess the rate of chemical denudation and sequestration of

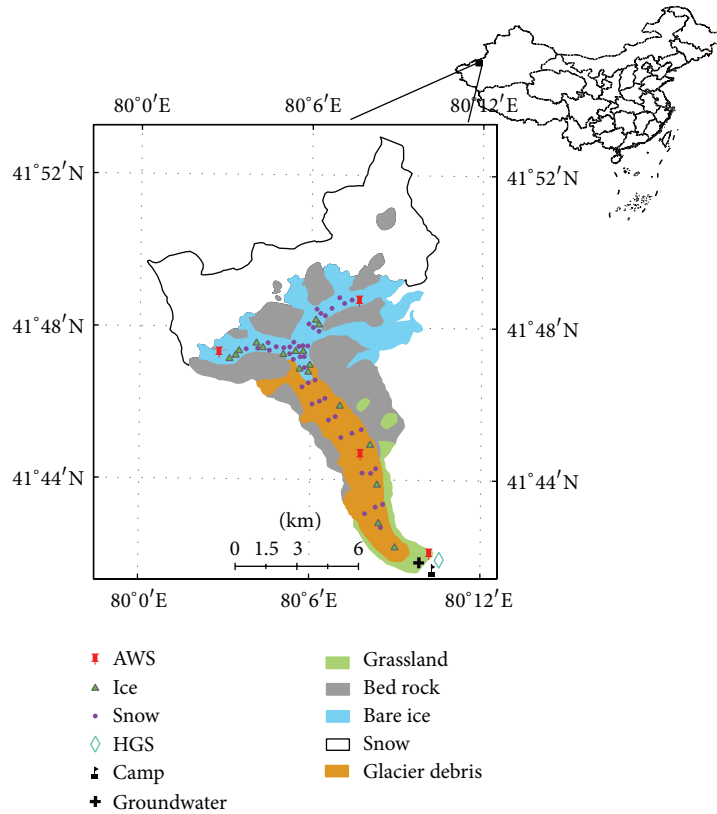


FIGURE 1: Location of study area and positions of sampling sites in the Koxkar glacier region.

atmospheric CO_2 in the glacierized Koxkar basin in Central Asia, based on major ion concentrations in the water. The results provide new data on ion concentrations in large alpine glacierized basins covered by supraglacial moraines, which could be used for modeling and the estimation of CO_2 changes during the last glacial maximum.

2. Study Area

2.1. Site Description. The Koxkar basin is located on the southern side of Mt. Toumuer in Northwest China ($41^\circ 47' \text{N}$, $80^\circ 04' \text{E}$). The watershed covers an area of 118.12 km^2 , of which around 70.20% is covered by present-day ice (Figure 1). There are systems of deep meltwater shafts (moulins) above 3900 m a.s.l. The glacier has a subcontinental regime with subglacial outflow issuing from a conduit at the center of the glacier snout.

The mean annual air temperature observed near the glacier terminus is 0.77°C , and the mean summer (May–September) temperature is 7.74°C [14]. The monthly mean air temperature is $>0^\circ \text{C}$ for about 6 months. The main source of precipitation is water vapor derived from the Atlantic and Arctic oceans [15]. The annual average precipitation is about 630.3 mm at the glacier terminus, 81.24% of which occurs in summer. Precipitation in the glacierized region is mainly solid state (snow or hail).

A field investigation during 2003–2012 suggested that the discharge at the hydrological gauging station (HGS) at

the glacial terminus was $>1.0 \times 10^8 \text{ m}^3 \cdot \text{a}^{-1}$ (Figure 1) and that the runoff flux from May to October accounted for $\sim 94.5\%$ of the annual total [14].

2.2. Geological Setting. Terranes from the Precambrian to Quaternary are exposed in the valleys of the Koxkar basin. Marine terrigenous clastic rocks and carbonates are very important to the regional geology, but their depths are unknown. There is little territorial volcanism [16]. Biotite monzogranite gneiss and augen granite gneiss are exposed above 3900 m a.s.l. in the Koxkar basin. From 3900 to 3400 m a.s.l., marble, shale, and rocks, which enrich the tremolite and biotite of the parametamorphic rock, are distributed on two hillsides, and marine sediment shale is exposed from 3300 to 3400 m a.s.l., supplying large quantities of substances that are important to the carbonation and oxidation processes in the subglacial environment. In other regions of the Koxkar basin, there are tertiary mudstones, siltstones, and glutenite distributed in supraglacial and terminal moraines. The area of the superglacial moraine accounts for $\sim 83\%$ of the total melting area [17].

3. Methods

Four automatic weather stations (AWSs) were established in 2007 (Figure 1). Hourly air temperature, precipitation, wind direction and velocity, and radiation were measured and recorded by the AWS positioned near the camp, while

the other AWSs mainly measured precipitation, air temperature, humidity, and wind speed.

Since 28 June 2011, river water sampling has been conducted at the HGS 200 m downstream of the main subglacial outlet. This sampling site was chosen because of inaccessibility near the subglacial outlet and to avoid sampling before the different water masses were thoroughly mixed [9]. During the sampling period, bulk meltwater samples were taken manually at around 14:00 Beijing time (BT) daily (96 in total). This sampling time was chosen because the specific conductivity (SpC) at 14:00 BT represents 96.72% of the mean of the hourly samples taken during the first 10 days. Additionally, 18 ice samples and 42 precipitation (snow) samples from the ablating area of the Koxkar glacier were collected along the direction of glacial development between 2996 and 4026 m a.s.l. (Figure 1). Furthermore, 9 groundwater samples from a spring located south of the main river bed and 16 rainfall samples from the observation camp were collected.

All samples were collected manually in prerinsed polypropylene bottles containing as little air as possible. Bottles and lids were rinsed in the sampling water before collection and disposable gloves were used to avoid contamination. The ice samples from the ablating region were collected after melting in a disposable polypropylene bag. At the camp, all samples were stored in a dark and cold location. Bottled samples, which were in a frozen state in insulated boxes, were transported to the State Key Laboratory of Cryosphere Science—the Cold and Arid Regions Environmental and Engineering Research Institute, Chinese Academy of Sciences—and kept in a cold room at -20°C . Three blank samples were assessed to ensure that the cumulative contamination was below the baseline for each measured chemical species. After the samples were retrieved, they were immediately analyzed for pH and SpC using a pH meter (PHSJ-4A; measurement range of 0–14, uncertainty within ± 0.005) and a conductivity meter (DDSJ-308A; measurement range of 0–999 $\mu\text{s}\cdot\text{cm}^{-1}$ and uncertainty of less than 5%), respectively. Then, the precipitation, bulk meltwater, groundwater, and ice meltwater samples were gradually warmed to a temperature of 20°C .

Major cations (Na^+ , K^+ , Mg^{2+} , and Ca^{2+}) were analyzed using a Dionex ISC 600 ion chromatograph with 20 mM MSA (methanesulfonic acid) eluent and CSRS suppresser (uncertainty $<0.1\%$). Major anions (Cl^- , NO_3^- , and SO_4^{2-}) were analyzed using a Dionex ISC 300 ion chromatograph with 25 mM KOH eluent and ASRS suppresser (measurement range of 0.5–400 μm , uncertainty $<0.5\%$) [6]. The water samples were analyzed for $\delta^{18}\text{O}$ values using the CO_2 equilibration method with a gas bench, which was interfaced with a MAT-252 isotope ratio mass spectrometer. The $^{18}\text{O}/^{16}\text{O}$ ratio was expressed as the difference in parts per thousand relative to the Vienna Standard Mean Ocean Water. The precision of the $\delta^{18}\text{O}$ measurement was 0.2%.

Notably, the summations of the contents of major cationic (Na^+ , K^+ , Mg^{2+} , and Ca^{2+}) and anionic (F^- , Cl^- , SO_4^{2-} , and NO_3^-) electronic charges appeared unbalanced. Ratios of $\sum(\text{cations})/t(\text{anions})$ for bulk river water, precipitation, groundwater, and glacial ice meltwater were 3.49, 3.07, 3.92,

and 2.81, respectively, implying that there was at least one anion present that was not considered in the experiment. The mean pH of 8.12 and the maximum value of only 8.70 indicated that CO_3^{2-} was not present in the different waters from the study area. Therefore, we determined the HCO_3^- concentration from ionic charge balances [8, 12, 18, 19], that is, the sum of all cationic charges (\sum^+) minus the sum of all anionic charges (\sum^-):

$$\text{Charge}(\text{HCO}_3^-) = \sum^+ - \sum^- \quad (1)$$

To verify the reliability of the HCO_3^- calculation in (1), the 13 river water samples were analyzed using the titrimetric method. The average error was 2.30% and the maximum margin of absolute error was $7.40 \times 10^{-5} \text{ mol}\cdot\text{L}^{-1}$. Unfortunately, most of the sample volumes were not large enough to be measured using the titrimetric method and ultimately, the titrimetric method was not considered because of atmospheric CO_2 contamination to the HCO_3^- at the time of sample collection.

4. Results

4.1. Meteorology and Hydrology. From 27 June to 30 September 2011, the mean daily air temperature was 9.8°C . The highest temperature recorded was 16.1°C on 6 August and the lowest temperature was 2.0°C on 17 September (Figure 2(a)). Contemporaneous, total precipitation was 260.8 mm, which was mostly solid state (i.e., snow, hail, or sleet). The largest precipitation total was 28.0 mm on 12 August (Figure 2(b)).

The minimum and maximum daily discharges at the HGS were 2.94 and 17.00 $\text{m}^3\cdot\text{s}^{-1}$, respectively, and the mean daily discharge was 9.57 $\text{m}^3\cdot\text{s}^{-1}$. The total discharge volume was $7.93 \times 10^7 \text{ m}^3$ (Figure 2(c)). The daily runoff obviously changed with the mean daily temperature, but it showed a clear hysteretic characteristic.

4.2. Hydrochemistry. The mean SpC of the meltwater throughout the entire observation period was 177.98 $\mu\text{s}\cdot\text{cm}^{-1}$ (range 110.00–284.00 $\mu\text{s}\cdot\text{cm}^{-1}$), which is higher than that reported (95.13 $\mu\text{s}\cdot\text{cm}^{-1}$) in 2003 (Table 1) [20]. It is also higher than the electrical conductivities recorded in both the headwaters of the Grümüqi River (118.57 $\mu\text{s}\cdot\text{cm}^{-1}$) [21] and the meltwater of the Kartamak glacier area in Muztag Ata (85.50 $\mu\text{s}\cdot\text{cm}^{-1}$) in Northwest China [22]. However, rainfall, especially continuous rainfall, probably led to lower air temperatures and this would lead to a reduction in the melting of ice. There was an opposite relation between the intensity of the chemical reaction of the water-rock interface and the water flow speed; hence, lower water flow speed indirectly increased the SpC of the river water on a cloudy day.

The mean SpC of the glacial ice (mean 21.73 $\mu\text{s}\cdot\text{cm}^{-1}$, range 8.11–34.10 $\mu\text{s}\cdot\text{cm}^{-1}$) was lower than the mean SpC of the precipitation (mean 30.16 $\mu\text{s}\cdot\text{cm}^{-1}$, range 6.33–151.8 $\mu\text{s}\cdot\text{cm}^{-1}$) in the Koxkar basin. Generally, the SpC of glacial ice should

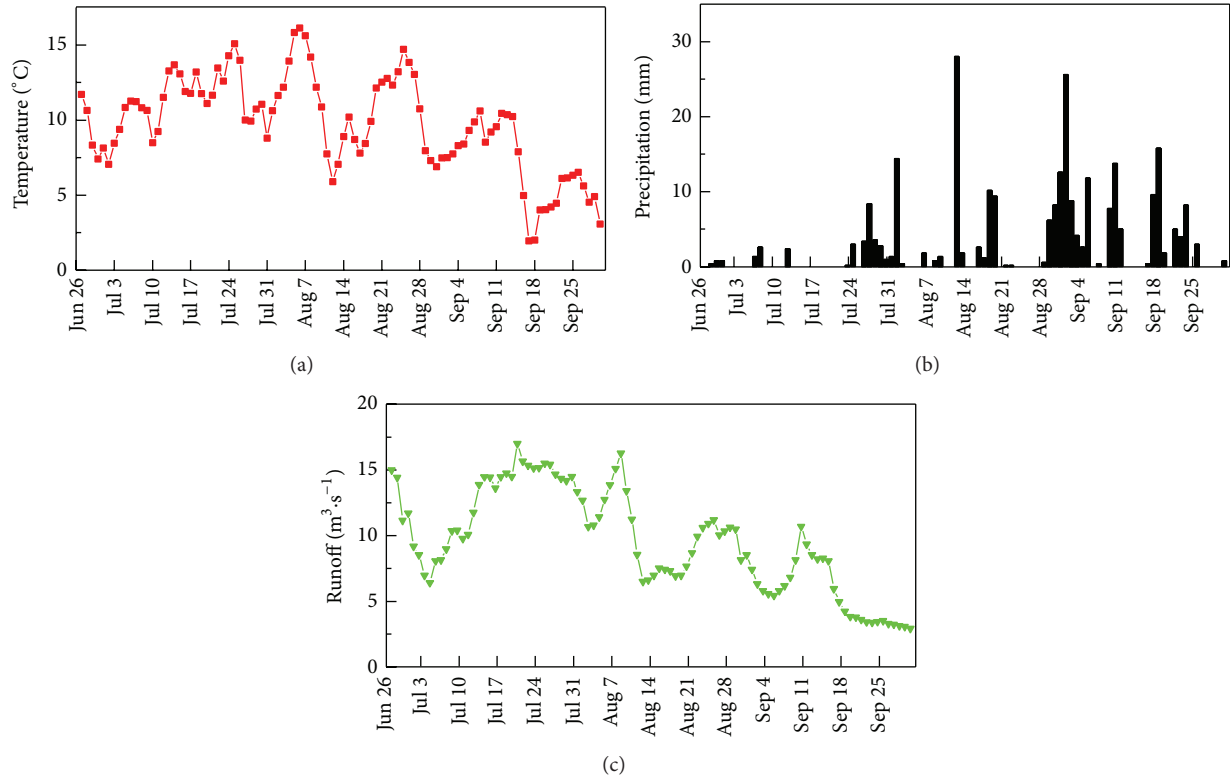


FIGURE 2: Daily average (a) air temperature, (b) precipitation, and (c) discharge in the Koxkar region from 27 June 2011 to 30 September 2011.

TABLE 1: Differences in ion concentrations of different waters in the Koxkar basin ($\times 10^{-6}$ mol·L $^{-1}$).

Item	$N^{(1)}$	Na^+			K^+			Mg^{2+}			Ca^{2+}		
		Mean	Max	Min	Mean	Max	Min	Mean	Max	Min	Mean	Max	Min
Glacial ice	21	9.23	29.00	1.78	1.93	6.92	0.26	12.19	33.92	1.83	63.90	108.25	25.25
Precipitation	58	25.29	226.90	1.44	2.71	10.57	0.15	13.86	55.01	0.31	63.01	148.03	2.50
Groundwater	9	353.85	372.74	332.56	111.44	115.35	108.24	269.95	301.20	233.17	240.99	297.72	172.33
River water	96	139.00	403.20	27.51	50.27	121.87	11.04	76.64	170.33	10.19	210.33	436.50	72.44
Item	N	F^-			Cl^-			SO_4^{2-}			NO_3^-		
		Mean	Max	Min	Mean	Max	Min	Mean	Max	Min	Mean	Max	Min
Glacial ice	21	1.72	4.32	0.48	3.92	11.69	0.93	3.91	10.73	0.56	—	—	—
Precipitation	58	0.86	2.22	0.23	19.07	117.07	1.29	11.26	37.00	1.69	3.44	18.95	1.04
Groundwater	9	25.69	28.74	23.10	96.41	110.53	75.40	120.49	188.52	95.80	14.52	17.21	11.25
River water	96	15.80	26.89	4.32	34.48	61.55	6.19	80.08	146.71	11.44	9.24	16.50	16.50
Item	N	HCO_3^-			$\delta^{18}\text{O}$			SpC			pH		
		Mean	Max	Min	Mean	Max	Min	Mean	Max	Min	Mean	Max	Min
Glacial ice	21	149.89	284.55	54.82	-10.73	-9.63	-11.99	21.73	34.10	8.11	8.07	8.96	7.02
Precipitation	58	136.38	389.66	0.00	-9.97	-0.55	-18.75	30.16	151.80	6.33	6.88	8.12	6.31
Groundwater	9	1109.59	1290.12	903.10	-11.04	-10.36	-11.01	225.80	274.00	204.00	8.16	8.40	7.86
River water	96	543.53	1107.85	126.49	-10.50	-9.59	-11.38	177.98	284.00	110.00	8.13	8.70	7.55

⁽¹⁾ N is the number of samples.

be higher than that of precipitation because of soluble material exchange during the formation of the ice. However, the difference here is probably because the ice samples reflected the accumulated historical precipitation in the Koxkar basin. The average SpC of the water samples decreased in the

following order: groundwater > river water > precipitation > glacial ice.

The river water was alkaline (pH 7.55–8.70). The order of $\delta^{18}\text{O}$ of the different water samples was as follows: precipitation > river water > glacial ice > groundwater

(Table 1). It is important to note that an average value of $\delta^{18}\text{O}$ for groundwater was adopted when calculating the volumes of different waters in the river discharge because systematic groundwater sampling had not been performed. Concentrations of NO_3^- in some samples (especially ice meltwater) are probably lower than the lower limit of the Dionex ISC 300 ion chromatograph. Thereby, the anionic concentrations of both groundwater and river water were in the following order: $\text{HCO}_3^- > \text{SO}_4^{2-} > \text{Cl}^- > \text{F}^- > \text{NO}_3^-$, whereas precipitation had the following order: $\text{HCO}_3^- > \text{Cl}^- > \text{SO}_4^{2-} > \text{NO}_3^- > \text{F}^-$, and ice had the following order: $\text{HCO}_3^- > \text{Cl}^- > \text{SO}_4^{2-} > \text{F}^- > \text{NO}_3^-$ (Table 1). The HCO_3^- of the different types of water played a predominant role and accounted for 94.01%, 81.19%, 79.57%, and 79.75% of the anion concentrations of ice meltwater, groundwater, river water, and precipitation, respectively. The reason for this phenomenon was carbonation with river water and groundwater because of widespread marble, shale, and marine sediment shale [16]. The HCO_3^- of precipitation and ice meltwater mainly originated from regional Asian dust [23].

The order of the cationic concentrations of glacial ice ($\text{Ca}^{2+} > \text{Mg}^{2+} > \text{Na}^+ > \text{K}^+$) differed from that of river water and precipitation ($\text{Ca}^{2+} > \text{Na}^+ > \text{Mg}^{2+} > \text{K}^+$). The specific reasons for this are as follows. First, there was an interchange of material between raindrops and aerosols during ice formation after the precipitation reached the surface [24–26]. Second, the dry/wet sedimentation of atmospheric dust affected the chemical composition of river water and ice meltwater [24–27]. Third, the ice samples were collected from the area of glacial ablation and thus they were related to historical precipitation/snow. Fourth, sulfide oxidation and carbonate hydrolysis affected the river water composition, which made it distinguishable from the ice composition [6–8, 11]. In addition, the higher Ca^{2+} and lower K^+ concentrations of the different water samples were consistent with the geochemical composition of the marine deposit [28]; this also reflected the function of the regional geological setting. The transformation of $\text{Mg}^{2+} > \text{Na}^+$ of the glacial ice into $\text{Na}^+ > \text{Mg}^{2+}$ of the river water was controlled largely by the hydrochemical denudation rate and the chemical composition of the groundwater and precipitation in the Koxkar glacier basin [11, 24].

5. Discussion

5.1. Water Origin

5.1.1. Oxygen Isotope Provenance Model. Hydrograph separation of bulk meltwater has been described in attempts to quantify the recharge of different water sources [29–32]. The $\delta^{18}\text{O}$ has been chosen as one indicator. First, seasonal variations in the development of the inner drainage system of the glacier influence the residence time of water within the glacial area and thus cause variations in the chemical composition of the water sources [33, 34]. Second, the ion species used are not conservative and are exposed to chemical reactions after the components have mixed.

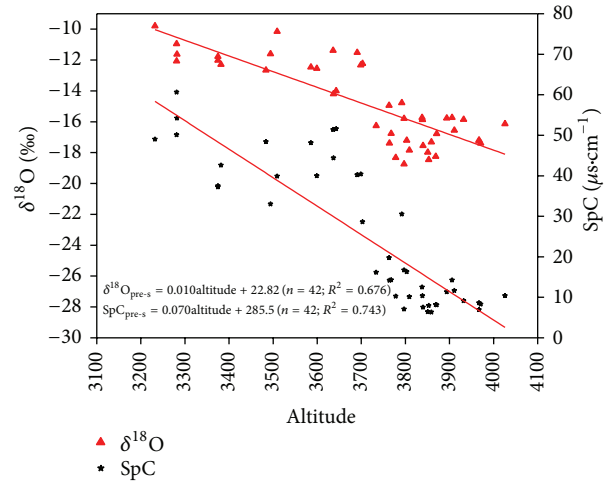


FIGURE 3: Relationship between $\delta^{18}\text{O}$ and SpC of spatial precipitation and altitude in melting area of the Koxkar glacier.

Although some degree of isotopic fractionation can be expected at the water-ice and water-air interfaces in the drainage system, stable isotopes are assumed more conservative than major ions [35, 36]. The water flow and oxygen isotopes issuing through the hydrographic section of the Koxkar River at any specific time can be divided into three provenances as follows:

$$Q_{\text{bulk}} = Q_{\text{ice}} + Q_{\text{pre}} + Q_{\text{ground}}, \quad (2)$$

$$Q_{\text{bulk}}\delta_{\text{bulk}} = Q_{\text{ice}}\delta_{\text{ice}} + Q_{\text{pre}}\delta_{\text{pre}} + Q_{\text{ground}}\delta_{\text{ground}},$$

where Q is discharge, δ is the $\delta^{18}\text{O}$ value, and the subscripts denote river water (bulk), ice meltwater (ice), precipitation (pre: including liquid water, snow, and hailstone), and underground water (ground).

The hydrograph separation was performed using the $\delta^{18}\text{O}$ value of each precipitation event. The $\delta^{18}\text{O}$ value of precipitation varied on both spatial and temporal scales and in addition, its dependence on altitude was considered. The relationship between altitude and the $\delta^{18}\text{O}$ value of precipitation (snow) was established (Figure 3):

$$\delta^{18}\text{O}_{\text{pre-s-i}} = 0.01 * \text{Altitude}_i + 22.82. \quad (3)$$

Actually, precipitation was extremely spatially inhomogeneous; it decreased by 7.00% from 3000 to 3700 m a.s.l. and increased by 46.60% from 3700 to 4200 m a.s.l. in the Koxkar basin [14]. Considering the dependence of precipitation volume on altitude, the following equation was derived for the corrected value of $\delta^{18}\text{O}$ of precipitation in the ablating region:

$$\delta^{18}\text{O}_{\text{c-pre}} = \frac{\sum (\delta^{18}\text{O}_{\text{pre-s-i}} * P_i A_i)}{\sum (P_i A_i)}, \quad (4)$$

where $\delta^{18}\text{O}_{\text{pre-s-i}}$ is the $\delta^{18}\text{O}$ value of precipitation at altitude i (m), $\delta^{18}\text{O}_{\text{c-pre}}$ is corrected $\delta^{18}\text{O}$ value of precipitation in

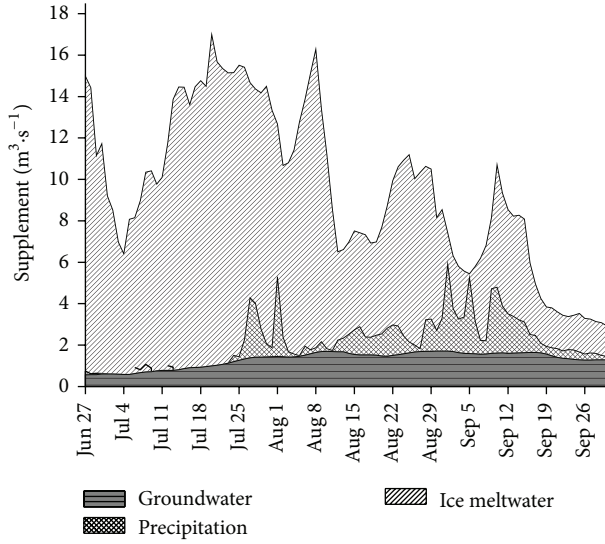


FIGURE 4: Supplement of precipitation, groundwater, and ice meltwater to river water in the Koxkar glacier region.

the melting area, and P_i and A_i are the total precipitation and the area, respectively, at altitude i .

To determine the relative amounts of supply of the three provenances, another indicator is required to solve the equation set. The relationship between the $\delta^{18}\text{O}$, SpC, and all soluble ionic concentrations of the river water was tested. The relationship between the $\delta^{18}\text{O}$ and SpC was poor ($R = -0.118$), which indicated that SpC was an independent parameter that could be used as one indicator to separate the river water [37–39]. The SpC of precipitation, which was referred to during the calculation, was similarly corrected as the precipitation $\delta^{18}\text{O}$.

5.1.2. Hydrological Separation. The results of the hydrograph separation using $\delta^{18}\text{O}$ and SpC suggested that glacial ice meltwater dominated the streamflow, accounting for $76.49 \pm 4.58\%$ of the total discharge from 27 June to 30 September 2011. This was followed by groundwater, which accounted for $13.71 \pm 3.06\%$ of the total discharges. The least influential was precipitation, which accounted for $9.79 \pm 1.64\%$ of the total discharge (Figure 4). The ratio of ice meltwater supplied to river runoff was 80%, as calculated by applying a degree-day model from Zhang et al. [40], which suggested that the result of the hydrological separation was reliable.

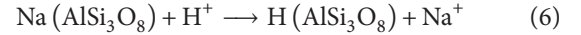
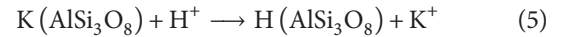
5.2. Hydrochemical Erosion

5.2.1. Solute Provenance during Erosion. The results of empirical orthogonal functions (EOFs) might be accepted for soluble ions of river water in Koxkar basin [23] (Table 2). Four feature vectors accounted for 94.2% of the cumulative variance. EOF1 which was strongly related to Na^+ , K^+ , Mg^{2+} , Cl^- , SO_4^{2-} , and HCO_3^- describes the main ion yield variance and accounted for 35.7% of the total ionic variance. In general, sources and quantities of Na^+ and Cl^- are connected with the

TABLE 2: Joint empirical orthogonal function analysis of the major ion concentrations of the river samples collected in the Koxkar basin.

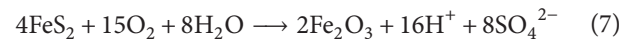
Item	EOF1	EOF2	EOF3	EOF4
Na^+	0.811	-0.560	-0.273	0.073
K^+	0.829	-0.535	-0.215	0.087
Mg^{2+}	0.832	-0.541	-0.114	0.108
Ca^{2+}	0.676	0.024	0.722	-0.129
F^-	0.574	0.655	0.188	0.407
Cl^-	0.833	0.615	-0.258	-0.142
SO_4^{2-}	0.850	0.582	-0.086	0.096
NO_3^-	0.795	0.418	-0.155	-0.672
HCO_3^-	0.775	-0.486	0.599	0.046
Total variance explained (%)	35.67	26.02	17.66	14.81

transport intension of marine aerosols. However, the Koxkar basin is in Central Eurasia and is far from any sea or ocean. Fan [41] reported that bedrock in the Koxkar basin is chiefly Mesozoic sedimentary rock and metasediment with flesh-red alkali-feldspar granite intruding into off-white monzonitic granite. Thus, Na^+ and K^+ are likely provided by chemical erosion during the runoff of precipitation and snow/ice meltwater. The main reactions are represented by



Although there was little olivine or pyroxene, the marine clastic rocks and carbonates of the Paleozoic era were massively distributed along the upper lateral ridge and in debris of the Koxkar glacier region. However, these were not only an important Mg^{2+} source but also sources of Cl^- and Na^+ [42–44]. Therefore, EOF1 mainly represents the hydrolysis of the feldspar and carbonate of the metamorphic rock, which supplies soluble matter to the river water.

EOF2 accounted for 26.0% of the total ion variance and it related greatly to F^- , Cl^- , and SO_4^{2-} and partially to Na^+ and K^+ . The ratio of $[\text{Na}^+ + \text{K}^+]/[\text{F}^- + \text{Cl}^- + 2\text{SO}_4^{2-}]$ was 0.94, which implies that hydrochemical exchange reactions existed. There was some pyrite (FeS_2) in the debris on the glacier surface and a coal seam on the glacial lateral ridge, which probably supplied abundant material for the oxidation of sulfides:



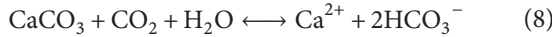
This reaction yields H^+ , which promotes the hydrolysis of K/Na-feldspar and sedimentary rock minerals and increases Na^+ , K^+ , and Cl^- concentrations. Therefore, EOF2 represents chemical erosion involving the sulfide oxidation of acidic materials. However, the ratio of $[\text{Na}^+ + \text{K}^+]/[\text{F}^- + \text{Cl}^- + 2\text{SO}_4^{2-}]$ was $0.94 < 1.00$, which also suggested that there might be another chemical reaction.

EOF3 accounted for 17.7% of the total ion variance relating to Ca^{2+} and HCO_3^- in the glacial runoff, which suggests that

TABLE 3: Solute provenances and amounts of chemical denudation in the Koxkar region [$\text{kg}\cdot(\text{km}^2\cdot\text{d})^{-1}$].

Item	Na^+	K^+	Mg^{2+}	Ca^{2+}	F^-	Cl^-	SO_4^{2-}	NO_3^-	HCO_3^-
Chemical denudation	18.89	12.46	9.80	42.94	1.94	7.05	48.46	3.56	166.94
Ice meltwater	1.16	0.41	1.60	13.95	0.18	0.76	2.05	0.01	49.91
Precipitation	0.91	0.25	0.37	2.78	0.04	0.62	1.49	0.43	9.69
Solute of river water	20.96	13.13	11.77	59.68	2.16	8.42	52.00	4.00	226.54

the sources were alike, that is, calcium salt carbonation, as described by



The ratio of $[\text{Ca}^{2+}]/[\text{HCO}_3^-]$ was $0.80 > 0.50$; therefore, the H^+ of carbonation was beyond that of atmospheric CO_2 drawdown. Furthermore, this also explained why the ratio of $[\text{Na}^+ + \text{K}^+]/[\text{F}^- + \text{Cl}^- + 2\text{SO}_4^{2-}]$ was < 1.00 .

EOF4 described 14.8% of the total ion variance, relating mostly to NO_3^- . However, the NO_3^- concentration for river water only accounted for 0.82% of the total ion concentration in the Koxkar basin. The NO_3^- concentration is the main factor governing the abundance of subglacial anaerobes, and it is affected by human activities such as industry, agriculture, and the herding of cattle and sheep [45]. Because nitrate in the natural world is present as an easily soluble salt, it is nearly impossible for it to be in the form of a solid in a glacierized basin. Hence, the NO_3^- in river water was likely due to the presence of aerosols in dry/wet deposition and material exchange at the atmosphere-hydrosphere interface during precipitation events and the formation of runoff.

5.2.2. Evaluation of Hydrochemical Denudation Rates. The crustal component of chemical denudation rates (CDRs) is equal to the total solute flux of river water minus the solute fluxes of precipitation, ice meltwater, dry/wet sedimentation of atmospheric dust, and exchange at the gas-liquid interface (see (9)). As little of the crustal component was supplied by dry/wet sedimentation of atmospheric dust and exchange at the air-liquid interface, these processes can be ignored in the analysis of basin erosion [46–48]. Table 3 presents the results according to ionic equilibrium. From 27 June to 30 September 2011, the total solute flux of chemical erosion was $312.05 \pm 17.42 \text{ kg}\cdot(\text{km}^2\cdot\text{d})^{-1}$ ($3.54 \pm 0.22 \times 10^6 \text{ kg}$ gross) (Table 3), which implies that chemical erosion for a continental glacier in the Koxkar glacier region is more intense than for some oceanic glaciers [4, 9, 49] and nonglacier regions [50–52]. In contrast, HCO_3^- erosion was strongest with a flux of $166.94 \pm 9.31 \text{ kg}\cdot(\text{km}^2\cdot\text{d})^{-1}$. The second strongest fluxes were the erosions of sulfide oxidation (SO_4^{2-}) and Ca^{2+} with values of 48.46 ± 2.70 and $42.94 \pm 2.16 \text{ kg}\cdot(\text{km}^2\cdot\text{d})^{-1}$, respectively. The erosions of Na^+ , K^+ , Mg^{2+} , Cl^- , and NO_3^- were weaker with fluxes of 18.89 ± 1.05 , 12.46 ± 0.69 , 9.80 ± 0.55 , 7.05 ± 0.39 , and $3.56 \pm 0.47 \text{ kg}\cdot(\text{km}^2\cdot\text{d})^{-1}$, respectively. The F^- erosion was the least intense with a flux of only $1.94 \pm 0.26 \text{ kg}\cdot(\text{km}^2\cdot\text{d})^{-1}$. In total, the solute fluxes of river water supplied by precipitation and ice meltwater were only 16.57 ± 1.13 and $70.02 \pm 4.68 \text{ kg}\cdot(\text{km}^2\cdot\text{d})^{-1}$, respectively, accounting

for 4.16% and 17.57% of the total flux. The CDR accounted for 78.28% of the total flux:

$$\text{CDR} = 3600 * 24 * 10^{-6}$$

$$* \frac{(Q_{\text{bulk}} * C_{\text{bulk}-j} - Q_{\text{pre}} * C_{\text{pre}-j} - Q_{\text{ice}} * C_{\text{ice}-j} - D)}{(A * I_j)}, \quad (9)$$

where CDR is the crustal component of the CDRs [$\text{kg}\cdot(\text{km}^2\cdot\text{d})^{-1}$]; Q_{bulk} , Q_{pre} , and Q_{ice} are the bulk river water, precipitation, and ice meltwater supplements, respectively ($\text{m}^3\cdot\text{S}^{-1}$); C_{bulk} , C_{pre} , and C_{ice} are the ion concentrations of river water, precipitation, and ice meltwater, respectively ($\times 10^{-6} \text{ mol}\cdot\text{L}^{-1}$); I is molecular weight; j represents the ion species; and D is the dry/wet sedimentation of atmospheric dust, which was ignored.

5.3. Carbon Dioxide Drawdown during the Ablation Period

5.3.1. Sulfide Provenance. The reason for considering sulfide provenance is because, in nature, most reactions of chemical denudation need abundant H^+ , the provenance of which is not limited to transient CO_2 drawdown (8) but includes sulfide oxidation processes (7). Thus, when calculating H^+ processes, crustal sulfate ($^{\text{cru}}\text{SO}_4^{2-}$) flux is equal to the total sulfate flux minus the sulfate flux of precipitation and ice meltwater:

$$^{\text{cru}}\text{SO}_4^{2-} = ^{\text{tot}}\text{SO}_4^{2-} - ^{\text{pre}}\text{SO}_4^{2-} - ^{\text{ice}}\text{SO}_4^{2-} \quad (10)$$

The SO_4^{2-} fluxes of river water (total), precipitation, ice meltwater, and crustal chemical erosion are depicted in Figure 5. The total SO_4^{2-} flux of river water was $\sim 52.00 \pm 2.47 \text{ kg}\cdot(\text{km}^2\cdot\text{d})^{-1}$ and crustal chemical erosion accounted for about 93.21% of the total SO_4^{2-} flux. The second largest contribution was that supplied by ice melting, which accounted for $\sim 3.94\%$. The mean SO_4^{2-} recharge attributed to precipitation was $\sim 1.49 \pm 0.88 \text{ kg}\cdot(\text{km}^2\cdot\text{d})^{-1}$, which accounted for only $\sim 2.86\%$ of the total flux. As with SpC, the SO_4^{2-} flux of river water also decreased with increasing precipitation in the Koxkar basin, as observed on 1 and 12 August 2011 (Figure 5).

5.3.2. CO_2 Drawdown. There is considerable Paleozoic marine terrigenous clastic rock, carbonatite, and Quaternary moraine debris in the Koxkar basin, and the amount of crustal bicarbonate (HCO_3^-) released during hydrochemical erosion mainly depended on the carbonation of carbonate and aluminosilicate (silicate). The second largest source was the hydrolysis of limestone and dolomite, induced by the oxidation of sulfides. As the Koxkar basin is in Central Eurasia

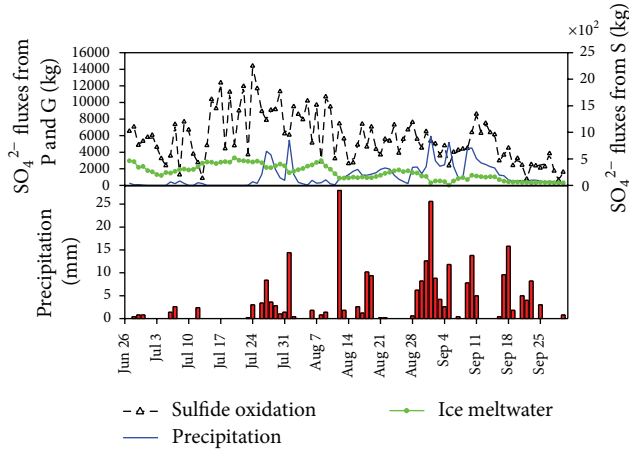
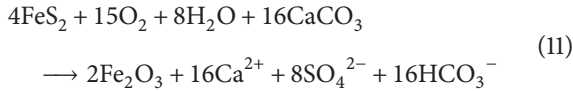


FIGURE 5: SO_4^{2-} daily fluxes for different sources and river water in the Koxkar region from 27 June to 30 September 2011 (P: precipitation; G: ice meltwater; S: sulfide oxidation).

and is largely unaffected by human activity, the main supply of SO_4^{2-} was the oxidation of pyrite [11, 53]. This process yields H^+ , as seen in (7). This provision of H^+ accelerates the hydrolysis of highly charged ions, such as Mg^{2+} and Ca^{2+} :



The case for Mg^{2+} is similar. The total mass of crustal Ca^{2+} and Mg^{2+} was $1.68 \pm 0.31 \times 10^7$ mol, which is more than twice the SO_4^{2-} mass of $0.57 \pm 0.07 \times 10^7$ mol in the Koxkar basin. This implies that some of the Mg^{2+} and Ca^{2+} yield is due to atmospheric CO_2 drawdown, according to (8). Hence, the amounts of Mg^{2+} and Ca^{2+} yielded by the oxidation of pyrite and calculated by (11) should be equal to twice the amount of SO_4^{2-} [53].

The mass of Ca^{2+} and Mg^{2+} in the chemical erosion due to carbonate hydrolysis resulting from atmospheric CO_2 drawdown [$\text{Ca}^{2+} + \text{Mg}^{2+}$]_{hydro} can be calculated by subtracting twice the value of the SO_4^{2-} mass from the total crustal Ca^{2+} and Mg^{2+} mass. Based on (8), the actual numerical value of atmospheric CO_2 drawdown [CO_2]_{car-hydro} during the carbonate hydrolytic process can be obtained using

$$\text{CO}_2^{\text{car-hydro}} = \text{cru}(\text{Ca}^{2+} + \text{Mg}^{2+}) - 2\text{SO}_4^{2-} \quad (12)$$

In nature, K/Na-feldspar takes the form of an unstable mineral substance, and atmospheric CO_2 , which may be soluble in water, could yield H^+ to accelerate the hydrolysis of K/Na-feldspar [11, 54]. Hence, according to (5) and (6), the amount of atmospheric CO_2 drawdown during K/Na-feldspar hydrolysis should equal the sum of the crustal Na^+ and K^+ contents:

$$\text{CO}_2^{\text{K/Na}} = \text{cru}(\text{K}^+ + \text{Na}^+) \quad (13)$$

Figure 6 shows that the total atmospheric CO_2 drawdown for the Koxkar basin during the melting season of 2011

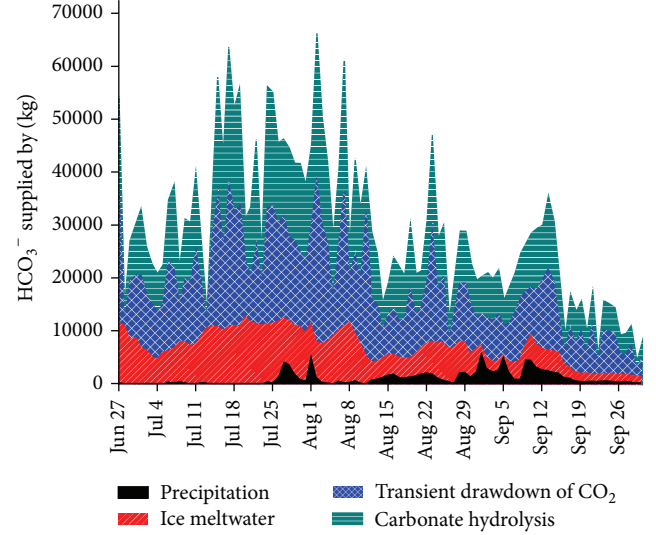


FIGURE 6: Daily flux of HCO_3^- originating from precipitation, ice meltwater, carbonate hydrolysis, and transient drawdown of CO_2 in the Koxkar region during the sampling period.

was about $70.98 \pm 5.30 \text{ kg}\cdot\text{C}\cdot(\text{km}^2\cdot\text{d})^{-1}$ (i.e., $8.05 \pm 0.60 \times 10^5 \text{ kg C}$, yield HCO_3^- was $\sim 98.40 \pm 7.35 \text{ kg}\cdot(\text{km}^2\cdot\text{d})^{-1}$). This was well below the $336.34 \text{ kg}\cdot\text{C}\cdot(\text{km}^2\cdot\text{d})^{-1}$ for the Scottbreen basin (3397 $\text{kg}\cdot\text{C}\cdot\text{km}^{-2}$ from 8 July to 5 September 2002) on Svalbard [4] but greater than the fluxes of CO_2 sinks in the Rhône and Oberaar catchments [7] and far more than that in nonglacierized zones [10, 13, 55]. This implies that variation in glacial melting, particularly within the context of climate change, is an important factor in the global CO_2 cycle [56–58].

Globally, runoff HCO_3^- originates from precipitation, ice meltwater, carbonate hydrolysis, and transient drawdown of atmospheric CO_2 . The different sources of HCO_3^- were calculated through a detailed analysis of the transient drawdown of CO_2 [4, 11, 52]. Figure 6 shows the HCO_3^- obtained for the Koxkar basin in the above analysis. It can be seen that HCO_3^- was mainly (39.61%) supplied by transient drawdown of CO_2 . The secondary source (36.39%) was carbonate hydrolysis, in accordance with the abundance of Paleozoic marine terrigenous clastic rocks, carbonates, and Quaternary moraine debris in the Koxkar basin. Only small quantities of HCO_3^- were supplied by ice meltwater and precipitation (20.09% and 3.90%, resp.).

5.4. Revising Hydrochemical Erosion. The transient drawdown of atmospheric CO_2 is an important source of HCO_3^- in the river water of the Koxkar basin. Therefore, the assessment of HCO_3^- from crustal chemical erosion needs to be revised. Crustal HCO_3^- chemical erosion should equal the results obtained in Section 5.2.2 ($166.94 \pm 9.31 \text{ kg}\cdot(\text{km}^2\cdot\text{d})^{-1}$) minus the HCO_3^- flux that originated from the transient drawdown CO_2 ($\sim 98.40 \pm 7.35 \text{ kg}\cdot(\text{km}^2\cdot\text{d})^{-1}$). Ultimately, the total crustal solute fluxes for hydrochemical erosion should

be about $213.65 \pm 10.05 \text{ kg}\cdot(\text{km}^2\cdot\text{d})^{-1}$ during the sampling period.

6. Conclusions

The CDRs and transient CO_2 drawdown during the melting season of 2011 in a highly glacierized basin at the heart of the Eurasian continent were investigated and the following conclusions drawn:

- (1) Streamflow was dominated by glacial ice meltwater, which accounted for $76.49 \pm 4.58\%$ of the total discharge in the Koxkar basin. The secondary contributors were groundwater and precipitation, which accounted for $13.71 \pm 3.06\%$ and $9.79 \pm 1.64\%$, respectively, from 27 June to 30 September 2011.
- (2) CO_2 flux from chemical erosion was $70.98 \pm 5.30 \text{ kg}\cdot\text{C}\cdot(\text{km}^2\cdot\text{d})^{-1}$ during the sampling period, which was significantly higher than that in other glacierized regions and nonglacierized regions.
- (3) The CDR during the sampling period, derived from the crustal solute flux, was $213.65 \pm 10.05 \text{ kg}\cdot(\text{km}^2\cdot\text{d})^{-1}$, which accounted for 53.59% of the total solute flux of the river water. The solute flux yielded by transient drawdown of CO_2 was $98.40 \pm 7.35 \text{ kg}\cdot(\text{km}^2\cdot\text{d})^{-1}$, which accounted for 24.68% of the total solute of the river water. The solute fluxes from ice meltwater and precipitation were lower: about $70.02 \pm 4.68 \text{ kg}\cdot(\text{km}^2\cdot\text{d})^{-1}$ and $16.57 \pm 1.13 \text{ kg}\cdot(\text{km}^2\cdot\text{d})^{-1}$, respectively, which accounted for 17.57% and 4.16% of the total solute flux.

Conflict of Interests

The authors declare that there is no conflict of interests regarding the publication of this paper.

Acknowledgments

This study was funded by the National Basic Research Program of China (no. 2013CBA01808) and the National Natural Science Foundation of China (nos. 41471060, 4130638, 41271078, and 41201025). The authors appreciate the comments of anonymous reviewers.

References

- [1] J. W. Ren, "Updating assessment results of global cryospheric change from SPM of IPCC WGI Fifth Assessment Report," *Journal of Glaciology and Geocryology*, vol. 35, no. 5, pp. 1065–1067, 2013.
- [2] Y. J. Ding, S. Y. Liu, J. Li, and D. H. Shangguan, "The retreat of glaciers in response to recent climate warming in western China," *Annals of Glaciology*, vol. 43, pp. 97–105, 2006.
- [3] S. Y. Liu, Y. J. Ding, Y. Zhang et al., "Impact of the glacial change on water resources in the Tarim River Basin," *Acta Geographica Sinica*, vol. 61, no. 5, pp. 482–490, 2006.
- [4] W. E. Krawczyk and S. A. Bartoszewski, "Crustal solute fluxes and transient carbon dioxide drawdown in the Scottbreen Basin, Svalbard in 2002," *Journal of Hydrology*, vol. 362, no. 3–4, pp. 206–219, 2008.
- [5] G. H. Brown, "Glacier meltwater hydrochemistry," *Applied Geochemistry*, vol. 17, no. 7, pp. 855–883, 2002.
- [6] G. Dongarrà, E. Manno, G. Sabatino, and D. Varrica, "Geochemical characteristics of waters in mineralised area of Peloritani Mountains (Sicily, Italy)," *Applied Geochemistry*, vol. 24, no. 5, pp. 900–914, 2009.
- [7] R. Hosein, K. Arn, P. Steinmann, T. Adatte, and K. B. Föllmi, "Carbonate and silicate weathering in two presently glaciated, crystalline catchments in the Swiss Alps," *Geochimica et Cosmochimica Acta*, vol. 68, no. 5, pp. 1021–1033, 2004.
- [8] T. D. L. Irvine-Fynn and A. J. Hodson, "Biogeochemistry and dissolved oxygen dynamics at a subglacial upwelling, Midtre Lovénbreen, Svalbard," *Annals of Glaciology*, vol. 51, no. 56, pp. 41–46, 2010.
- [9] J. C. Yde, N. T. Knudsen, and O. B. Nielsen, "Glacier hydrochemistry, solute provenance, and chemical denudation at a surge-type glacier in Kuannersuit Kuussuat, Disko Island, West Greenland," *Journal of Hydrology*, vol. 300, no. 1–4, pp. 172–187, 2005.
- [10] P. K. Jha, J. Tiwari, U. K. Singh, M. Kumar, and V. Subramanian, "Chemical weathering and associated CO_2 consumption in the Godavari river basin, India," *Chemical Geology*, vol. 264, no. 1–4, pp. 364–374, 2009.
- [11] V. B. Singh, A. L. Ramanathan, J. G. Pottakkal, and M. Kumar, "Seasonal variation of the solute and suspended sediment load in Gangotri glacier meltwater, central Himalaya, India," *Journal of Asian Earth Sciences*, vol. 79, pp. 224–234, 2014.
- [12] K. Kumar, M. S. Miral, S. Joshi, N. Pant, V. Joshi, and L. M. Joshi, "Solute dynamics of meltwater of Gangotri glacier, Garhwal Himalaya, India," *Environmental Geology*, vol. 58, no. 6, pp. 1151–1159, 2009.
- [13] D. Wolff-Boenisch, E. J. Gabet, D. W. Burbank, H. Langner, and J. Putkonen, "Spatial variations in chemical weathering and CO_2 consumption in Nepalese High Himalayan catchments during the monsoon season," *Geochimica et Cosmochimica Acta*, vol. 73, no. 11, pp. 3148–3170, 2009.
- [14] H. D. Han, S. Y. Liu, Y. J. Ding et al., "Near-surface meteorological characteristics on the Koxkar Baxi Glacier, Tianshan," *Journal of Glaciology and Geocryology*, vol. 30, no. 6, pp. 967–975, 2008.
- [15] E. S. Kang, S. S. Zhu, and M. M. Huang, "The characteristics of glacier hydrology in the Tumuer region. Glacier and Meteorology in Mt. Tumuer Region, Tianshan," *Urumqi: People's Publishing House of Xinjiang*, pp. 99–119, 1985.
- [16] Scientific Expedition Team on Mountaineering of the Chinese Academy of Sciences, *Geology and Paleontology in Tumur Peak Region, Tianshan Mountains*, Xinjiang People's Publishing House, Ürümqi, China, 1985.
- [17] H. D. Han, J. Wang, J. F. Wei, and S. Liu, "Backwasting rate on debris-covered Koxkar glacier, Tuomuer mountain, China," *Journal of Glaciology*, vol. 56, no. 196, pp. 287–296, 2010.
- [18] E. L. Williams, K. J. Szramek, L. X. Jin, T. C. W. Ku, and L. M. Walter, "The carbonate system geochemistry of shallow groundwater-surface water systems in temperate glaciated watersheds (Michigan, USA): significance of open-system dolomite weathering," *Bulletin of the Geological Society of America*, vol. 119, no. 5–6, pp. 515–528, 2007.
- [19] B. G. Mark, J. M. McKenzie, and J. Gómez, "Hydrochemical evaluation of changing glacier meltwater contribution to stream

- discharge: Callejon de Huaylas, Peru,” *Hydrological Sciences Journal*, vol. 50, no. 6, pp. 975–988, 2005.
- [20] J. Wang, Y.-J. Ding, J.-L. Xu, and H.-D. Han, “Hydrochemical characteristic analysis of melting water flow in Keqikaer Glacier, Tianshan (west) Mountains,” *Environmental Science*, vol. 27, no. 7, pp. 1305–1311, 2006.
- [21] C. L. Li, S. G. Hou, and D. H. Qin, “Spatial differences of hydrochemical and its control factors of the headwater runoff in the Ürümqi River, Tianshan Mountains,” *Journal of Glaciology and Geocryology*, vol. 25, no. 1, pp. 72–76, 2003.
- [22] H. B. Zhao, T. D. Yao, and B. Q. Xu, “Hydrological and hydrochemical features of fartamak glacier area in Muztag Ata,” *Journal of Glaciology and Geocryology*, vol. 28, no. 1, pp. 269–275, 2006.
- [23] S. G. Hou, “Chemical characteristics of precipitation at the headwaters of the Ürümqi River in the Tianshan Mountains,” *Journal of Glaciology and Geocryology*, vol. 23, no. 1, pp. 80–84, 2001.
- [24] K. Yalcin, C. P. Wake, J. E. Dibb, and S. I. Whitlow, “Relationships between aerosol and snow chemistry at King Col, Mt. Logan Massif, Yukon, Canada,” *Atmospheric Environment*, vol. 40, no. 37, pp. 7152–7163, 2006.
- [25] X. Li, Z. Li, Y. Ding et al., “Seasonal variations of pH and electrical conductivity in a snow-firn pack on Glacier No. 1, eastern Tianshan, China,” *Cold Regions Science and Technology*, vol. 48, no. 1, pp. 55–63, 2007.
- [26] L. Krnavek, W. R. Simpson, D. Carlson, F. Domine, T. A. Douglas, and M. Sturm, “The chemical composition of surface snow in the Arctic: examining marine, terrestrial, and atmospheric influences,” *Atmospheric Environment*, vol. 50, pp. 349–359, 2012.
- [27] R. S. Hindshaw, E. T. Tipper, B. C. Reynolds et al., “Hydrological control of stream water chemistry in a glacial catchment (Damma Glacier, Switzerland),” *Chemical Geology*, vol. 285, no. 1–4, pp. 215–230, 2011.
- [28] S. Y. Yang, H. S. Jung, D. I. Lim, and S. Y. Yang, “A review on the provenance discrimination of sediments in the Yellow Sea,” *Earth-Science Reviews*, vol. 63, no. 1-2, pp. 93–120, 2003.
- [29] D. N. Collins, “Hydrology of an alpine glacier as indicated by the chemical composition of meltwater,” *Zeitschrift für Gletscherkunde und Glazialgeologie*, vol. 13, pp. 219–238, 1978.
- [30] D. N. Collins, “Quantitative determination of the subglacial hydrology of two Alpine glaciers,” *Journal of Glaciology*, vol. 22, no. 89, pp. 347–362, 1979.
- [31] M. Tranter and R. Raiswell, “The composition of the englacial and subglacial component in bulk meltwaters draining the Gornergletscher, Switzerland,” *Journal of Glaciology*, vol. 37, no. 125, pp. 59–66, 1991.
- [32] M. Tranter, G. Brown, R. Raiswell, M. Sharp, and A. Gurnell, “A conceptual model of solute acquisition by Alpine glacial meltwaters,” *Journal of Glaciology*, vol. 39, no. 133, pp. 573–581, 1993.
- [33] G. H. Brown and M. Tranter, “Hydrograph and chemograph separation of bulk meltwaters draining the upper Arolla Glacier, Valais, Switzerland,” in *Hydrology in Mountainous Regions I*, H. Lang and A. Musy, Eds., no. 193, pp. 429–437, IAHS Press, 1990.
- [34] F. J. Liu, M. Williams, J. Y. Sun et al., “Hydrochemical process and hydrological separation at the headwaters of the Ürümqi River, Tianshan Mountains, China,” *Journal of Glaciology and Geocryology*, vol. 21, no. 4, pp. 362–370, 1999.
- [35] C. Gazis and X. H. Feng, “A stable isotope study of soil water: evidence for mixing and preferential flow paths,” *Geoderma*, vol. 119, no. 1-2, pp. 97–111, 2004.
- [36] I. Braud, T. Bariac, J. P. Gaudet, and M. Vauclin, “SiSPAT-Isotope, a coupled heat, water and stable isotope (HDO and H₂¹⁸O) transport model for bare soil. Part I. Model description and first verifications,” *Journal of Hydrology*, vol. 309, no. 1–4, pp. 277–300, 2005.
- [37] D. W. Ostendorf, “Hydrograph and chloride pollutograph analysis of Hobbs Brook reservoir subbasin in eastern Massachusetts,” *Journal of Hydrology*, vol. 503, pp. 123–134, 2013.
- [38] J. L. McCallum, P. G. Cook, D. Berhane, C. Rumpf, and G. A. McMahon, “Quantifying groundwater flows to streams using differential flow gaugings and water chemistry,” *Journal of Hydrology*, vol. 416–417, pp. 118–132, 2012.
- [39] K. J. Dinsmore, M. F. Billett, K. E. Dyson et al., “Stream water hydrochemistry as an indicator of carbon flow paths in Finnish peatland catchments during a spring snowmelt event,” *Science of the Total Environment*, vol. 409, no. 22, pp. 4858–4867, 2011.
- [40] Y. Zhang, S. Y. Liu, Y. J. Ding et al., “Preliminary study of mass balance on the Keqicar Baxi Glacier on the south slopes of Tianshan Mountains,” *Journal of Glaciology and Geocryology*, vol. 28, no. 4, pp. 477–484, 2006.
- [41] Y. X. Fan, *Granide. Geology and Paleontology in Tuomur Peak Region, Tianshan Mountains*, Xinjiang People’s Publishing House, Ürümqi, China, 1985.
- [42] T. G. Churikova, B. N. Gordeychik, B. V. Ivanov, and G. Wörner, “Relationship between Kamen Volcano and the Klyuchevskaya group of volcanoes (Kamchatka),” *Journal of Volcanology and Geothermal Research*, vol. 263, pp. 3–21, 2013.
- [43] I. González-Álvarez and R. Kerrich, “Trace element mobility in dolomitic argillites of the Mesoproterozoic Belt-Purcell Supergroup, Western North America,” *Geochimica et Cosmochimica Acta*, vol. 75, no. 7, pp. 1733–1756, 2011.
- [44] C. Cordier, L. Folco, and S. Taylor, “Vestoid cosmic spherules from the South Pole Water Well and Transantarctic Mountains (Antarctica): a major and trace element study,” *Geochimica et Cosmochimica Acta*, vol. 75, no. 5, pp. 1199–1215, 2011.
- [45] J. N. Galloway, Z. Dianwu, X. Jiling, and G. E. Likens, “Acid rain: China, United States, and a remote area,” *Science*, vol. 236, no. 4808, pp. 1559–1562, 1987.
- [46] B. Bookhagen and M. R. Strecker, “Spatiotemporal trends in erosion rates across a pronounced rainfall gradient: examples from the southern central Andes,” *Earth and Planetary Science Letters*, vol. 327–328, pp. 97–110, 2012.
- [47] A. R. Stumpf, M. E. E. Madden, G. S. Soreghan, B. L. Hall, L. J. Keiser, and K. R. Marra, “Glacier meltwater stream chemistry in Wright and Taylor Valleys, Antarctica: significant roles of drift, dust and biological processes in chemical weathering in a polar climate,” *Chemical Geology*, vol. 322–323, pp. 79–90, 2012.
- [48] B. Delmonte, C. Baroni, P. S. Andersson et al., “Modern and Holocene aeolian dust variability from Talos Dome (Northern Victoria Land) to the interior of the Antarctic ice sheet,” *Quaternary Science Reviews*, vol. 64, pp. 76–89, 2013.
- [49] A. Hodson, P. Porter, A. Lowe, and P. Mumford, “Chemical denudation and silicate weathering in Himalayan glacier basins: Batura Glacier, Pakistan,” *Journal of Hydrology*, vol. 262, no. 1–4, pp. 193–208, 2002.
- [50] K. L. Ferrier and J. W. Kirchner, “Effects of physical erosion on chemical denudation rates: a numerical modeling study of soil-mantled hillslopes,” *Earth and Planetary Science Letters*, vol. 272, no. 3–4, pp. 591–599, 2008.

- [51] P. Louvat and C. J. Allègre, "Present denudation rates on the island of réunion determined by river geochemistry: basalt weathering and mass budget between chemical and mechanical erosions," *Geochimica et Cosmochimica Acta*, vol. 61, no. 17, pp. 3645–3669, 1997.
- [52] D. P. Dethier and E. D. Lazarus, "Geomorphic inferences from regolith thickness, chemical denudation and CRN erosion rates near the glacial limit, Boulder Creek catchment and vicinity, Colorado," *Geomorphology*, vol. 75, no. 3-4, pp. 384–399, 2006.
- [53] D. J. Hercod, P. V. Brady, and R. T. Gregory, "Catchment-scale coupling between pyrite oxidation and calcite weathering," *Chemical Geology*, vol. 151, no. 1-4, pp. 259–276, 1998.
- [54] J. R. Price, C. R. Hardy, K. S. Tefend, and D. W. Szymanski, "Solute geochemical mass-balances and mineral weathering rates in small watersheds II: biomass nutrient uptake, more equations in more unknowns, and land use/land cover effects," *Applied Geochemistry*, vol. 27, no. 6, pp. 1247–1265, 2012.
- [55] J. Gaillardet, B. Dupré, P. Louvat, and C. J. Allègre, "Global silicate weathering and CO₂ consumption rates deduced from the chemistry of large rivers," *Chemical Geology*, vol. 159, no. 1-4, pp. 3–30, 1999.
- [56] S. P. Anderson, J. I. Drever, C. D. Frost, and P. Holden, "Chemical weathering in the foreland of a retreating glacier," *Geochimica et Cosmochimica Acta*, vol. 64, no. 7, pp. 1173–1189, 2000.
- [57] W. Ludwig, P. Amiotte-Suchet, and J.-L. Probst, "Enhanced chemical weathering of rocks during the last glacial maximum: a sink for atmospheric CO₂?" *Chemical Geology*, vol. 159, no. 1-4, pp. 147–161, 1999.
- [58] K. B. Föllmi, R. Hosein, K. Arn, and P. Steinmann, "Weathering and the mobility of phosphorus in the catchments and forefields of the Rhône and Oberaar glaciers, central Switzerland: implications for the global phosphorus cycle on glacial–interglacial timescales," *Geochimica et Cosmochimica Acta*, vol. 73, no. 8, pp. 2252–2282, 2009.

Research Article

Glacial Area Changes in the Ili River Catchment (Northeastern Tian Shan) in Xinjiang, China, from the 1960s to 2009

Junli Xu,^{1,2} Shiyin Liu,¹ Wanqin Guo,¹ Zhen Zhang,^{1,2} Junfeng Wei,^{1,2} and Tong Feng^{1,2}

¹State Key Laboratory of Cryospheric Sciences, Cold and Arid Regions Environmental and Engineering Research Institute (CAREERI), Chinese Academy of Sciences, Lanzhou 730000, China

²University of Chinese Academy of Sciences, Beijing 100049, China

Correspondence should be addressed to Junli Xu; xujunli05@lzb.ac.cn and Shiyin Liu; liusy@lzb.ac.cn

Received 18 December 2014; Revised 27 April 2015; Accepted 30 April 2015

Academic Editor: Charles Jones

Copyright © 2015 Junli Xu et al. This is an open access article distributed under the Creative Commons Attribution License, which permits unrestricted use, distribution, and reproduction in any medium, provided the original work is properly cited.

The Ili River originates in the Tian Shan Mountains of Northwest China before flowing into Kazakhstan and Lake Balkash. Melting snow and ice are its major contributors. We analyzed glacial changes in the upper Ili River basin between the 1960s and 2007/2009 using topographic maps and satellite imagery from a Landsat TM. The relationships between glacial changes and glacial size, topographic factors, and debris cover were examined. Our results found that total glacial area decreased by $485 \pm 177.3 \text{ km}^2$ (24.2% \pm 8.8%) during the study period, and there were no advancing glaciers. Additionally, 331 glaciers disappeared and 18 disintegrated into two or three smaller glaciers. This study demonstrated a linear relationship between glacial area change and elevation. Changes in glaciers smaller than 1 km^2 were affected by both glacial size and topographic factors, while larger ones were affected by size only. Area losses in debris-covered glaciers were smaller by 2.5% to 7.5% compared to clean ice of the same size in this basin. As in other glaciated regions, glacial retreat in the Ili River basin is attributed to global warming. The slightly increasing precipitation over the study period could not offset the ice melting.

1. Introduction

The Intergovernmental Panel on Climate Change (IPCC) reported that alpine glaciers respond to regional climate over a period of decades and thus serve as indicators of regional climate change [1]. Most alpine glaciers in the world have shown shrinkage in area since the later part of the 19th century, as did the glaciers in the Tian Shan Mountains [1–3]. However, advancing or surging glaciers were found in the Karakoram Himalaya, northwestern Himalaya, and Qilian mountains during the same period [4–6].

Global-warming-induced snow and ice losses from the cryosphere impact socioeconomic development because rising sea levels cause coastal flooding, melting glaciers cause flooding from rapid melting and glacial lake outburst, and glacial shrinkage reduces a dependable irrigation supply [7–10]. Cryosphere-related disasters such as glacier/snow melt floods, glacial lake outburst floods, ice jam floods, and avalanches have frequently been observed in the Tian Shan region [11]. In these mountains, hazards related to drifting

snow, avalanches, ice jam floods, and glacial melt floods have occurred [11, 12]. There were no reports of glacial lake outburst floods in the study area, and many glacial lakes continue to expand in the Ili River basin as a result of glacial melting [13]. Thus, it is important to know how glaciers have changed in this area. However, there has been little research to quantify the actual changes to glaciers [14, 15].

Changes in length, area, thickness, and volume in response to temperature and precipitation changes are not uniform across the glaciers over periods of years to decades [6, 16–19]. This variable pattern of responses to climate changes is expected to be affected by glacial size and topographic factors. Glaciers that are smaller in area experience greater shrinkage [16–18]. However, there is no information about the relationship between glacial changes and topographic factors. In addition, there is seemingly conflicting research regarding the influence that debris cover plays on changes to glacial surface elevation, area, and length [20, 21]. There are debris-covered glaciers with no visible or only little area changes but significant mass changes.

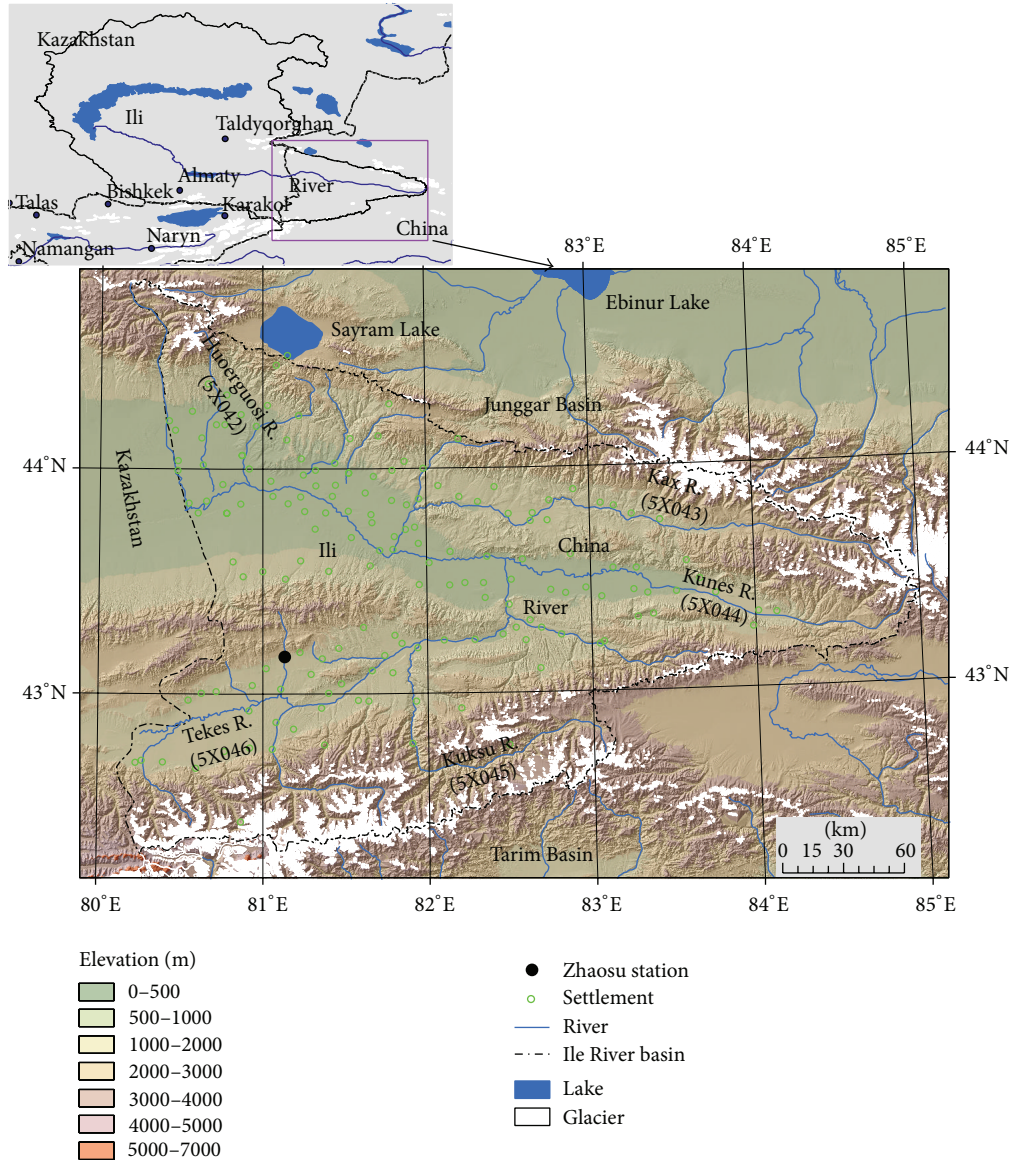


FIGURE 1: Glaciated areas in the Ili River basin.

Glaciers in the Ili River watershed have a wide range of surface areas, elevations, and debris covers. This examination of changes in the Ili River basin's glaciers, from the 1960s to 2009, used topographic maps and satellite imagery from the Landsat Thematic Mapper (TM) to document glacial size, topographic factors affecting glacial area changes, and the amount of debris cover.

2. Study Area

The Ili River, originating in the central northwest Tian Shan Mountains and flowing from China into Kazakhstan (Lake Balkhash), is fed by melting snow and ice [22]. Its total drainage area is $4.2 \times 10^5 \text{ km}^2$, including both the Chinese and Kazakhstan sections. Because this region lies on

the west side of the mountains, it receives more precipitation than other parts of the Tian Shan Mountains; its westward opening allows westerly uplift [22]. Precipitation at the year-round snow line is around 800–1000 mm per year. Snowfall, during the winter and spring, accounts for 40%–50% of the annual precipitation [22]. This is different from other glaciated areas in the Tian Shan Mountains where most of the precipitation occurs during summer. Although the Ili River is mostly in Kazakhstan, 77.5% of the glaciers that feed it are in China [23]. Our study focused on the glaciers within China (Figure 1). The World Glacier Inventory (http://nsidc.org/data/docs/noaa/g01130_glacier_inventory/) has coded the Ili River basin as 5X04 with five tributary basins originating in China (5X042, 5X043, 5X044, 5X045, and 5X046). The first Ili River basin glacier inventory, performed in the 1960s, found 2373 glaciers totaling 2022.66 km^2 and occupying

TABLE 1: Topographic maps list for the study area.

Sources	Year	Quantity
1:50,000 topographic maps	1959	2
	1962	2
	1964	12
	1966	2
1:100,000 topographic maps	1959	2
	1962	2
	1964	1
	1966	3
	1968	1

an estimated 127.96 km³ in China [24]. Snow line elevations ranged from 3630 to 3840 m above sea level (m asl).

3. Dataset and Methodology

3.1. Glaciers in the 1960s. The first Chinese inventory of glaciers (FCI) was compiled using primarily topographic maps scaled at 1:50,000 or 1:100,000. There were few glaciers from maps scaled at 1:1,000,000 because of the data quality [22]. Although glacier boundaries were manually corrected using 1:43,000 and 1:60,000 aerial photographs and analytic photogrammetric methods [22], notable errors remained in the mapped delineation of glaciers. No vectorized glacier boundaries were included in this inventory compilation. Instead, glacier boundaries were determined from attribute tables or by manually measuring the areas on maps. We reexamined the early maps depicting the glaciers at scales of 1:50,000 and 1:100,000 (Table 1). Where the first Chinese inventory used maps scaled at 1:1,000,000, we employed three Landsat Multispectral Scanner (MSS) satellite images instead. These early maps, from between 1959 and 1968, were produced with photogrammetric methods by the Chinese Military Geodetic Service. The MSS images were acquired by the United States Geological Survey (USGS) in 1972 and 1977 from the National Aeronautics and Space Administration, orthorectified at level 1T. During this study, these maps were first scanned at a resolution of 300 dots per inch and then two-dimension georeferenced and rectified using a global coordinate grid to remove the geometric distortion acquired during long-term storage. Using ERDAS Imagine 9.1 software, these maps were georeferenced to the mapping coordinates of the 1954 Beijing Geodetic Coordinate System geoid, known as BJ54, and the datum level was the Yellow Sea mean sea level at Qingdao Tidal Observatory. These maps were then transposed into the Universal Transverse Mercator coordinate system referenced to the World Geodetic System 1984 ellipsoidal elevation (WGS84) using a seven-parameter transformation. Shifts and deformations occurred between BJ54 and the WGS84 coordinate systems in both the east-west direction and north-south direction [25]. Detailed information from the seven-parameter transformation was shown by Wang et al. [26]. The seven parameters of each map were calculated utilizing national trigonometric reference

points. Errors introduced by this method were shown to be no greater than 0.5 meters [6, 27, 28]. The Landsat MSS images were orthorectified by USGS using the Universal Transverse Mercator coordinate system referenced to the WGS84 ellipsoidal elevation. Finally, glacier boundaries on maps and MSS images were digitized manually into a shape file format using ArcMap software. Glaciers were white and easy to distinguish from other surface features in bands 4, 3, and 2 of the composite MSS images. Glaciers that measured at least 0.01 km² were included in this study. Detailed information was found in 1:50,000 topographic maps for 30% of the glaciers, in 1:100,000 maps for 35% of the glaciers, and in MSS images for the remaining 35% of the glaciers, which were larger than 2 km². These glaciers formed the basic data for the changes in glaciers in the source region of the Ili River.

3.2. Glaciers in 2007 and 2009. To develop new glacier inventories and up-to-date satellite images of the Ili River watershed, this study acquired eight Landsat TM scenes from the USGS (https://lpdaac.usgs.gov/get_data/) that had spatial resolutions of 30 meters (Table 1). All Landsat scenes were orthorectified in level 1T by the USGS using global ground control points (GCPs) from Global Land Survey 2005 datasets. The GCP report files for TM images were available, but those for MSS images were not. Table 2 shows the GCP residuals, which have a maximum of 4.6 m and a mean of 4.1 m. Where there were no GCP files for MSS data, we compared tie points of MSS images with TM images to assess the accuracy. The mean error was 13.2 m.

Methods for glacier mapping using Landsat data include (1) manual delineation of glacier outlines on false color image composites [16, 29], (2) segmentation of ratio images with reflectance thresholds [30], (3) the normalized-difference snow index (NDSI) [31, 32], and (4) supervised classification techniques [33]. In this study, ratio images of the raw digital numbers from TM band 3 and TM band 5 with a threshold of 2.1 were used to obtain a surface mask for the glaciers in the Ili River basin. This thematic method has been commonly used and proven to be effective for extracting glacial information [30–32, 34]. The drawbacks of this method are its inability to identify glacier debris cover and its inability to determine portions of the glaciers covered by debris, which must be done by manual digitizing. Current automatic methods for delineating glacier debris cover continue to need manual modifications [35–38]. For the 80 glaciers in the Ili watershed that had debris covering their terminus areas, manual delineation with Landsat TM was applied to extract debris boundaries. Manual digitization of debris-covered glaciers was based mainly on the recognition of distinctive surface features such as supraglacial lakes and differences in colors and textures of the glacial surface in various red-green-blue composites of Landsat images. These special features made it easier to differentiate debris from surrounding periglacial landforms [39]. This manual digitization was performed by experienced glaciologists. The debris terminal ended at the outlets of subglacial streams near glacial termini. Finally, the resultant contiguous ice coverage was further divided into individual glacier polygons,

TABLE 2: Landsat images list for the study area.

Satellite	Path	Row	Acquisition date (yy-mm-dd)	Tie points/GCP residual (m)
Landsat MSS	156	30	1972-10-8	15.2
	157	30	1977-8-18	13.1
	158	30	1977-8-18	11.2
Landsat 5 TM	144	30	2009-8-8	4.0
	145	29	2007-9-11	4.0
	145	30	2007-9-11	4.2
	146	30	2007-9-18	4.6
	146	31	2007-9-18	4.1
	147	29	2009-8-13	4.2
	147	30	2007-9-25	3.9
	147	31	2007-8-24	4.6
	148	29	2007-9-16	3.5

based on topographical ridgelines, using ASTER GDEM data (<http://gdem.ersdac.jspacesystems.or.jp/>) [40].

The debris cover percentage used hereinafter was calculated based on current glaciers. Our purpose was not to study the changes of debris cover; thus the debris cover area in the 1960s was not extracted.

4. Error Assessment

Two methods are used to assess the error in measurements of glacial changes: one based primarily on image resolutions and coregistration accuracies of multi-images [41] and the other on calculating the uncertainty of glacial data using given buffers [42, 43]. The latter was applied in this study because the former lacks assessment of errors in the debris-covered areas.

The 1960s glaciers were extracted from topographic maps and Landsat MSS images. Thus, the uncertainty which arises during glacial boundary delineation needed to be assessed in terms of the accuracy of both map data and MSS images. In topographic maps, the accuracy of glacial boundary delineation is dependent on scanning resolution, map quality, and map scales. Previous research demonstrated that the accuracy of these maps can be further confirmed using data from a global positioning satellite (GPS) [25, 44]. However, instead of using GPS data, we used the root mean square of geometrical corrections and the digitizing accuracy to confirm glacier boundaries. The root mean square for each map was calculated from ground control points (GCPs), and mean errors of 4.2 m and 9.8 m were found for the 1:50,000 and 1:100,000 maps, respectively. When digitizing maps, the error is around one pixel, or 5 m and 10 m for the 1:50,000 and 1:100,000 maps, respectively [45]. We applied the law of error (1) and found that the total errors were 6.5 m and 14.2 m for the 1:50,000 and 1:100,000 maps, respectively

$$\sigma = \sqrt{\sigma_1^2 + \sigma_2^2}. \quad (1)$$

In satellite images, the main factors that cause uncertainty in glacier delineation include cloud and snow cover, the sensor

spatial resolution, and mountain shadows [6, 43, 46]. Moreover, extracting glacier boundaries also brings about errors [34, 47]. No images with clouds and seasonal snow were used in our study except for one MSS image that showed a 1% cover of seasonal snow. We modified the shadow areas using images from Google Earth by the Export to KML tool. In addition, the method of segmentation using TM band 3 and TM band 5 could also partially discern shadows [32]. After we performed these corrections, hindrances from clouds, snow, and shadows became negligible. Accuracy of less than one-half pixel was usually achievable for glaciers without debris, cloud, and seasonal snow cover [42]. Thus, we determined the uncertainty to be 28.5 m for Landsat MSS images and 14.3 m for TM images in clean ice areas. However, the error caused by debris cover was larger [39]. Our partner compared the debris boundary with GPS points and found that the error in debris-covered ice was 31.3 m in Landsat TM images [48], which is nearly one pixel. Thus, a one-pixel buffer was used for debris-covered glaciers in TM images and 57 m for glaciers in MSS data. This analysis determined an uncertainty of 7.6% for glaciers mapped using data from the 1960s and 6% for glaciers mapped using TM data from 2007 and 2009.

5. Results

5.1. Glaciers in the 1960s. The first inventory of glaciers, which took place in the 1960s, found 2373 glaciers with a total glacial area of 2022.7 km². Our more accurate study of the 1960s maps resulted in identification of 2119 glaciers with a total area of 2002.9 ± 152.2 km². Details of the differences are shown in Table 3. The large difference in both glacier numbers and areas as a result of this update is probably a consequence of error in the 1:1,000,000 maps that were used by the FCI. Some glacial areas were likely missed while some seasonal snow was mistaken for glacier ice. There are no other data available to validate the accuracy of the FCI, and we used both the topographic maps and MSS to cross-validate the glaciers found in the 1960s. The biggest difference was found in the area of glacier 5X046G0048, which had originally been inaccurately measured to be 36.5 km² using the 1:1,000,000

TABLE 3: The differences in glaciers before and after update.

Area (km ²)	Glacier before update		Glacier after update	
	Quantity	Area	Quantity	Area
<0.5	1662	317.16	1420	281.53
0.5~1	316	219.06	321	229.35
1~2	194	271.1	185	266.46
2~5	130	390.46	123	375.54
5~10	48	329.61	48	339.37
10~40	21	402.35	20	371.05
>40	2	92.92	2	139.64
Total	2373	2022.66	2119	2002.94

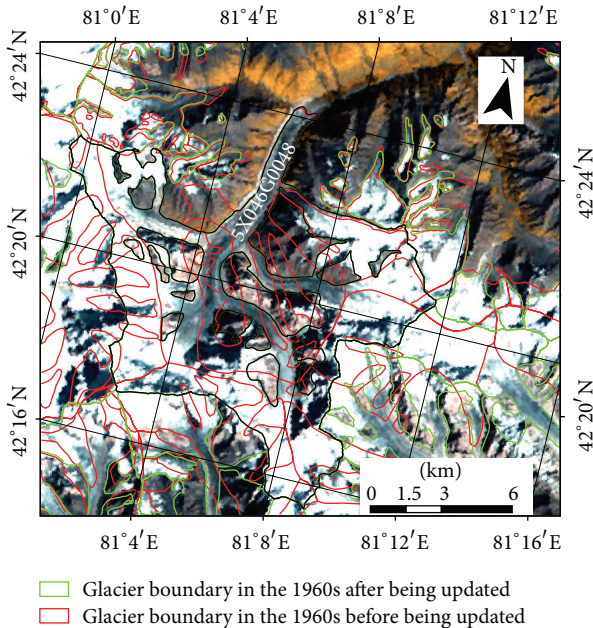


FIGURE 2: Glaciers in the 1960s before and after update. Glacier 5X046G0048 was in the black boundary after update.

scale maps. Using the MSS image, its area was found to be 88.9 km² (Figure 2), making it the largest glacier in the study area. Another problem identified in the 1960s inventory was that 33.5 km² was originally described as glacier ice, but it was actually seasonal snow. In addition, 9.3 km² was not recognized as glacier ice.

The corrected 1960s maps showed that median glacial elevation ranged from 3158 to 4567 m asl (Figure 3), and the lowest elevation of a glacier’s terminus was 2635 m asl; 97% of the total glacial area was located between 3500 and 4200 m asl.

In the 1960s, there were 23 glaciers in the Ili River basin larger than 10 km². Although 96.7% of the glaciers in the basin would be considered small (≤ 5 km²), these made up 57.6% of the total glacial area in the basin (Table 3). There were only 80 debris-covered glaciers in the basin, but these glaciers accounted for 34% of the total glacial area (686.7 km²) and included the two largest glaciers in the basin. The surfaces of individual glaciers were 1.3% to 26.4% covered in debris.

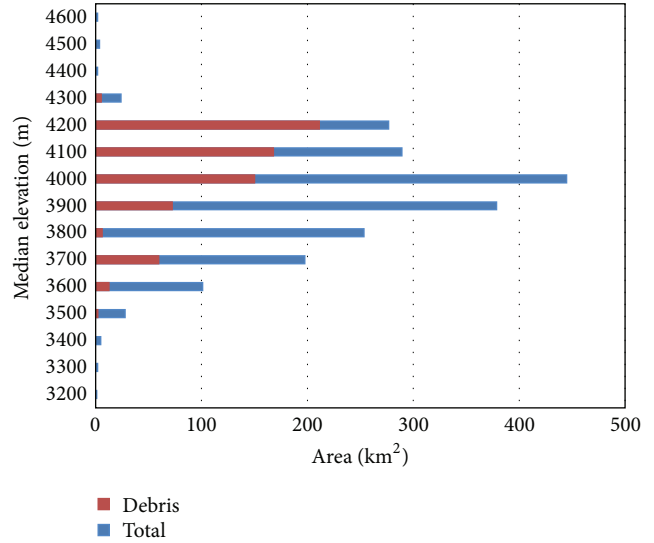


FIGURE 3: Proportion of glacial area covered by debris at varying elevations per 2007/2009 mapping data.

Debris covered 16.2% of the surfaces of the two largest glaciers. Most of the debris cover was found between 3500 m and 4300 m asl (Figure 3), and the peak debris area was found between 3900 and 4000 m asl.

5.2. *Glacial Changes.* When comparing glacial area from the 1960s to 2007 and 2009, we found that almost all those in the Ili River basin were receding; three small glaciers remained stable. During the same time period, the total glacial area decreased by 485 ± 177.3 km², or $24.2\% \pm 8.8\%$ ($\sim 0.6\% \cdot a^{-1}$). The number of glaciers decreased from 2119 in the 1960s to 1813 in the late 2000s. During the same period, the mean glacial size decreased from 0.94 km² to 0.72 km². The speed of glacial retreat appeared to be dependent on the subbasin in which it was located (Table 4). The most drastic shrinkages were $47.2\% \pm 5.7\%$ in the Kunes river subbasin and $42.6\% \pm 9.4\%$ in the Huoerguosi River. Glaciers in the Kax River and Kuksu River subbasins experienced moderate recession rates of $27.5\% \pm 5.0\%$ and $29.2\% \pm 9.0\%$, respectively. The least amount of shrinkage, found in the Tekes River subbasin, was $18.3\% \pm 10.8\%$.

Between the 1960s and the late 2000s, 331 glaciers disappeared completely, and 18 glaciers disintegrated into two or three smaller glaciers. All those that disappeared were debris-free. The area of these glaciers was 34.8 km², accounting for 1.7% of the total glacial area in the Ili River basin. Of those that disappeared, 59.4% were smaller than 0.1 km², 30.3% were between 0.1 km² and 0.2 km², and the remaining 10% were larger than 0.2 km². A scatter plot of the median altitude versus glacial area of the disappearing glaciers is shown in Figure 4. Most were at around 3100 to 4200 m asl, and the median altitude decreased linearly with glacial area. Furthermore, nearly 60% of them were smaller than 0.1 km², independent of their locations or altitudes. However, the larger ones (>0.3 km²) were generally at very low altitudes

TABLE 4: Glacial area changes in five tributary subbasins of the Ili River.

Drainage name (code)	Quantity	Area in the 1960s (km ²)	Area in 2007 and 2009 (km ²)	Mean area (km ²)	Area change (%)
Huerguosi R. (5X042)	112	53.17 ± 4.7	30.54 ± 1.7	0.47	-42.6 ± 9.4
Kax R. (5X043)	502	413.86 ± 11.4	300.03 ± 17.1	0.82	-27.5 ± 5.0
Kunes R. (5X044)	222	80.81 ± 3.9	42.68 ± 2.4	0.36	-47.2 ± 5.7
Kuksu R. (5X045)	510	405.60 ± 32.4	287.09 ± 16.4	0.80	-29.2 ± 9.0
Tekes R. (5X046)	773	1049.50 ± 99.8	857.61 ± 53.5	1.36	-18.3 ± 10.8
Total	2119	2002.94 ± 152.2	1517.95 ± 91.1	0.95	-24.2 ± 8.8

TABLE 5: Details regarding the 18 glaciers that disintegrated.

Drainage basin name	Glacial area (km ²)	Altitude of disintegration (m)	Area change (%)
Huerguosi R.	2.02	3447	-15.96
	0.74	3429	-52.77
	4.04	3405	-33.40
	1.44	3474	-51.77
Kax R.	18.79	3172	-19.06
	6.89	3385	-21.17
	6.45	3418	-13.22
	1.96	3466	-31.77
Kuksu R.	3.91	3872	-26.95
	5.79	3804	-13.78
	1.86	3970	-30.31
	2.49	3889	-31.44
Tekes R.	35.07	3015	-8.86
	2.38	3434	-28.61
	8.87	3527	-16.31
	9.70	3800	-11.58
	14.44	3665	-10.14
	88.93	3102	-5.25
		3860	

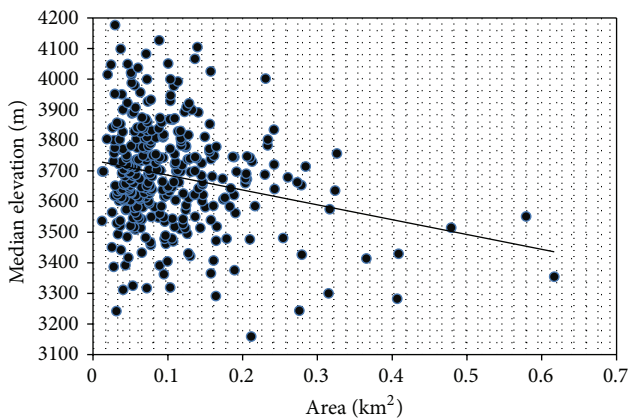


FIGURE 4: Scatter plot showing the median altitude versus area of disappearing glaciers.

(lower than 3600 m asl), indicating that these glaciers disappeared because of warming temperatures.

Disintegrated glaciers (Table 5), those that broke up into smaller pieces, existed in all subbasins except for the Kunes River basin. Seventeen broke up into two glaciers, and one broke up into three glaciers. Disintegration occurred at elevations between 3015 m and 3970 m, at the glacier terminal or in the upper branch joints. Most (14) of them disintegrated between 3400 and 3800 m elevation.

5.3. Changes in Glacial Area Related to Topographic Variables.

To analyze the effect of topography on changes in surface area, the median elevation and mean surface slope of each glacier in the basin were calculated using SRTM DEM. It is necessary to point out that ASTER GDEM is not suited for topographic factor extraction on a changing glacial surface because its obtained date is uncertain. Figure 5(a) shows the results of comparing glacial shrinkage by dividing all glaciers into one of eight groups according to mean surface slope. The groups were divided by five-degree increments (e.g., one division might represent glaciers with 5° to 10° mean surface slope). Figure 5(b) compares glacial elevation to shrinkage. Glaciers

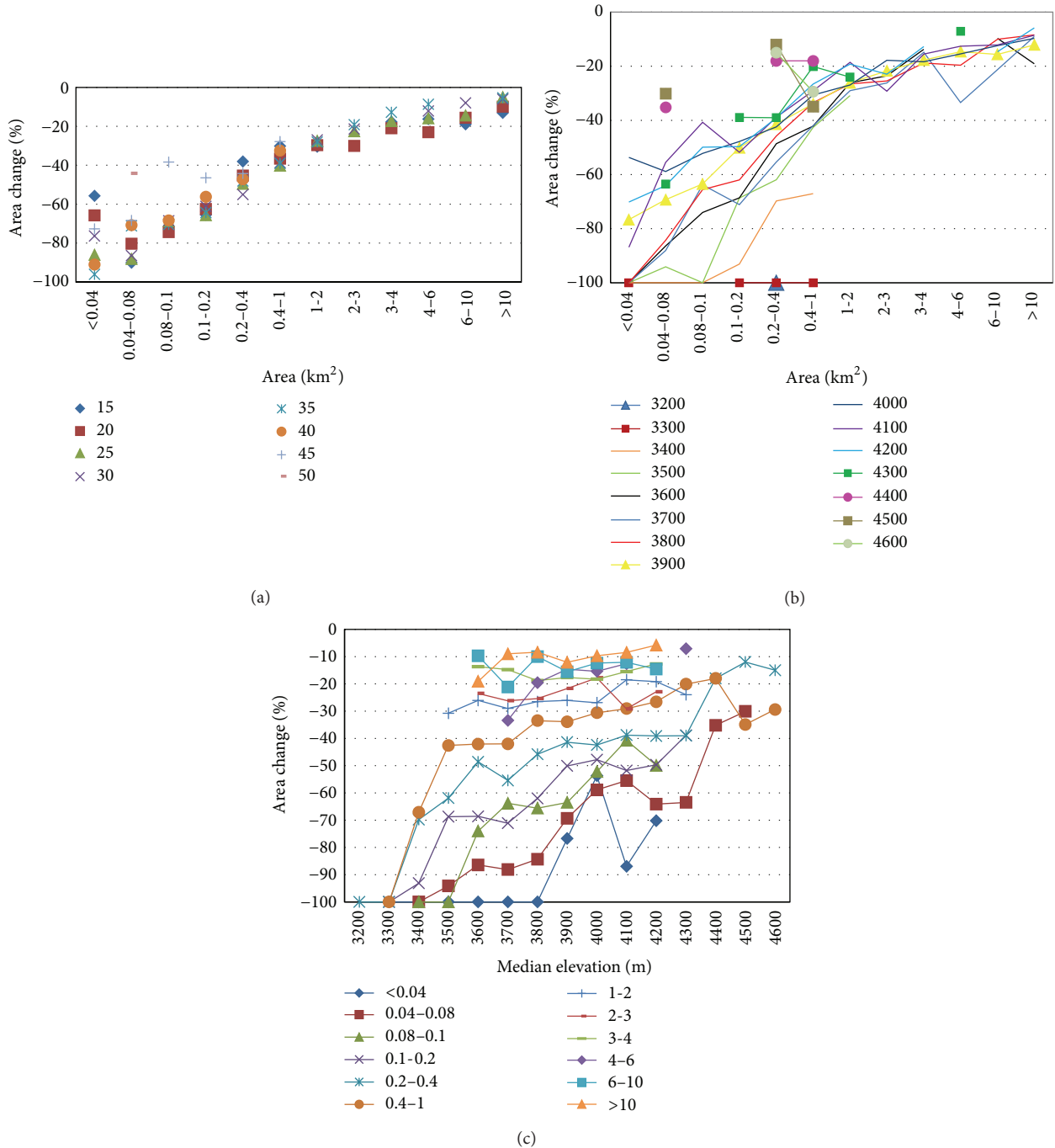


FIGURE 5: Glacial change in area (%) versus mean slope, median elevation, and glacial area. (a) Glacial mean slope plotted as a function of glacial shrinkage and area, (b) glacial median elevation plotted as a function of glacial shrinkage and area, and (c) glacial area plotted as a function of glacial shrinkage and median elevation.

were divided into 15 100-meter elevation groups. For example, all glaciers with a median surface elevation between 2900 and 3000 m were grouped together in the 3000 m division. Figure 5(c) groups glaciers of similar size to compare glacial size to shrinkage.

Figure 5(a) shows that shrinkage was greater for glaciers smaller than 0.08 km². It also shows that the slopes of

large glaciers (>0.08 km²) had nearly no effect on shrinkage. Glaciers smaller than 0.08 km² showed no relationship between glacial area and shrinkage.

Figure 5(b) shows a logarithmic relationship between shrinkage and area for glaciers at similar median elevations. For example, at 3700 m median elevation, large (>1 km²) glaciers experienced less shrinkage than smaller ones.

TABLE 6: Area percentage of each area group in all subbasins in the 1960s.

Area (km ²)	5X042	5X043	5X044	5X045	5X046
<0.05	0.7	0.33	0.47	0.21	0.06
0.05–0.1	1.9	1.53	3.76	1.25	0.47
0.1–0.5	29.74	13.52	33.85	14.27	9.48
0.5–1	22.36	10.37	30.04	14.3	8.69
1–5	45.3	36.62	31.88	44.67	24.92
5–10		16.72		17.9	17.87
>10		20.91		7.4	38.51

Figure 5(c) shows that the relationship between glacial shrinkage and area is more pronounced for those larger than 1 km². It also indicates that shrinkage in small glaciers (<1 km²) was greater at lower elevations whereas shrinkage in larger glaciers was less affected by elevation. Our results concur with previous research which found that lower median elevation resulted in relatively more loss in area [42]. Bolch's study did not remove the impact of glacial size, and the exact relationship was not as distinct as was found in our study [42].

In summary, in glaciers smaller than 0.08 km², glacial recession appeared to be primarily controlled by median elevation (Figures 5(a) and 5(c)). Those between 0.08 km² and 1 km² showed a linear relationship between size and median elevation (Figures 5(b) and 5(c)). Shrinkage was not affected by median elevation for glaciers larger than 1 km² (Figures 5(b) and 5(c)).

Table 6 shows that the majority of overall glacial area is concentrated in glaciers larger than 1 km². Glaciers larger than 5 km² accounted for over half the total glacial area in the Tekes River subbasin. Glaciers larger than 1 km² accounted for 74.3% of the total glacial area in the Kax River subbasin and 70% of the total glacial area in the Kuksu River subbasin. Of the five subbasins, the Kunes River basin held the smallest glaciers. The distribution of glacial area in the five subbasins was consistent with their glacial changes. The larger the proportion of large glaciers (>10 km²), the smaller the glacial area loss. For example, glaciers in the Tekes River basin, with the largest proportion of glaciers larger than 10 km², had the smallest area shrinkage. Consequently, the distribution of glacial area is probably one of the main factors of change for the basin scale.

Most glaciers at lower elevations disappeared during the study period. For example, 80% of those at a median elevation of less than 3400 m disappeared (Figure 6). Through regression analysis, Figure 6 demonstrates an exponential relationship between the percentage of disappearing glaciers and median glacial elevation. All glaciers below 3300 m asl disappeared, and 38% of those between 3300 m and 3400 m disappeared. Only 1% of the glaciers at a median elevation of 3800 m disappeared. As expected, smaller glaciers at lower elevations were the most likely to lose area or disappear.

5.4. Changes in Glacial Area Related to Debris Cover. The 2007 and 2009 maps showed that 80 glaciers were covered

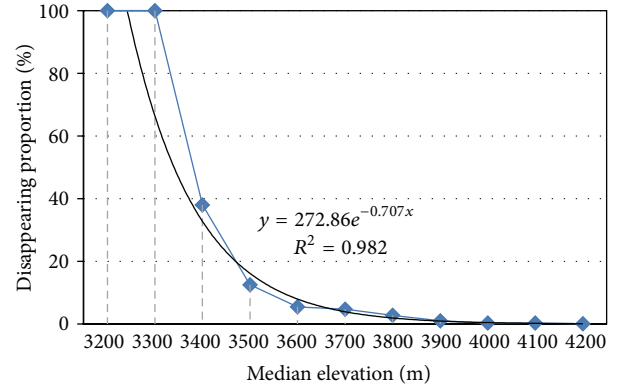


FIGURE 6: Percentage of glacial area lost by glaciers that disappeared as a function of median glacial elevation.

with debris. Compared with debris-free glaciers, these shrunk less (Figure 7(a)). The area lost from debris-covered glaciers was between 7.5% and 20%, significantly less than the area lost from debris-free glaciers. Area loss by debris-covered glaciers is smaller by 2.5% to 7.5% than clean ice of the same size. This difference becomes smaller in large glaciers. The general result is that glaciers with debris cover greater than 25% lost less surface area than the others (Figure 7(b)).

6. Discussion

There were no advancing or surging glaciers in the Ili River basin during the measurement periods. It is different from the Aksu catchment in the central Tian Shan Mountains where 10 advancing glaciers were found between 1990 and 2010 [49]. Our results are similar to those found for glaciers in the western Nyainqentanglha Range and the Nam Co Basin, Tibet, where also no advancing/surging was found from 1976 to 2009 [42]. Sorg et al. reported that, of the entire Tian Shan range, the outer ranges had the strongest annual area shrinkage rates since the middle of the twentieth century; they were between 0.38% and 0.76% a⁻¹ [50]. Thus, glaciers in the Ili River basin should show the greatest area shrinkage (0.6% a⁻¹) of the range, the same as in the glaciers of Big Naryn basin (central Tian Shan), where the area shrinkage was 23.4% (0.6% a⁻¹) from the mid-20th century to 2007.

In many mountainous regions, various glaciers grow and shrink at different rates, and some glaciers will advance or surge while others shrink [6, 20, 31]. Some studies pointed out that glaciers of different sizes respond to climate change differently because of the time lag [17, 42, 51]. Previous studies found that larger glaciers tended to shrink less, as a percentage of total area, than smaller glaciers [42, 51, 52]; our results agree. These studies also implied that small glaciers (<0.4 km²) were easily affected by topography, and glaciers that shrank in area or disappeared had lower mean elevations [53]. However, this research showed only the relationship between topographic settings and glaciers smaller than 0.4 km². Our results not only showed that changes in small glaciers (<1 km²) are affected by topography

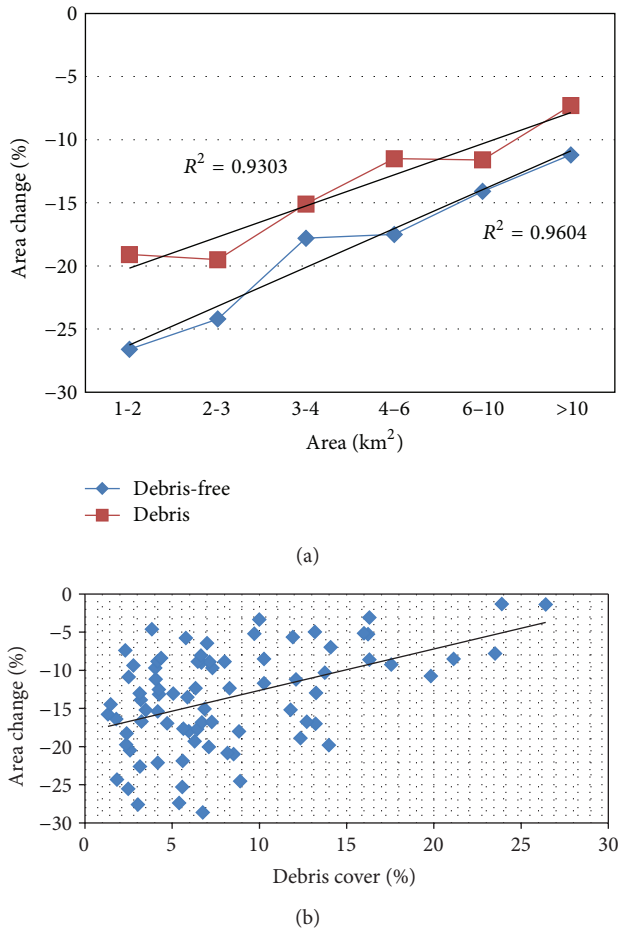


FIGURE 7: Area change (%) of debris-covered glaciers. (a) Percent area shrinkage of glaciers of various sizes, debris-covered and debris-free, and (b) percent decrease in glacial area as a function of the percentage of the glacier covered in debris.

and size together, but also showed that larger glaciers were less affected by topographic factors. These diverse factors result in a real world situation that is difficult to simulate with hydrological or land surface models.

Debris cover affects the response of glaciers to climate change by altering surface ablation rates [54, 55]. Previous research pointed out that heavily debris-covered glaciers, with stagnant low-gradient terminus regions, typically had stable fronts in the Himalayas [20]. Our results agree that debris-covered glaciers have less shrinkage than debris-free glaciers. Thus, we suggest that the vast debris cover of glaciers in the Tekes River basin is one factor that was responsible for the lower shrinkage seen there rather than in other basins. However, previous studies of debris-covered glaciers on Tomur Peak showed that thinning of debris-covered ice was not statistically different from that of debris-free ice [19, 56]. This should not conflict with our results. Studies have shown that ice cliffs and supraglacial lakes always develop in debris-covered areas, and these cliffs result in 69% of the melting of debris-covered areas in the Himalayas [57]. These quick ablation ice cliffs could cause extensive thinning of

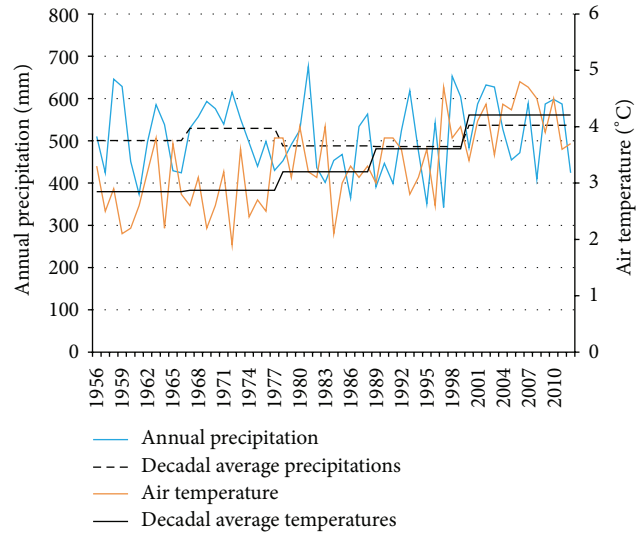


FIGURE 8: Changes in annual air temperature and precipitation between 1956 and 2012.

debris-covered ice, but the percentage of ice cliffs is small, and they can not affect the overall area shrinkage seen in debris-covered glaciers. This calls for studies of ice thickness changes in debris-covered and debris-free glaciers while observing ice cliff distribution in debris areas.

Research suggests that glacial recession is mainly influenced by global warming [42, 44, 49, 52]. Meteorological data obtained from the Zhaosu weather station (43.15°N, 81.133°E; 1851 m asl) were used to analyze the drivers of change to the glaciers in the Ili River basin (Figure 8). This station recorded a significant temperature increase between 1956 and 2012. Temperature has risen by 1.4°C in the past 56 years and the warming tendency has accelerated, as evidenced by the decadal average temperatures. Precipitation has slightly increased during the same period but decreased between 1978 and 1998. Thus, we suggest that glacial recession between the 1960s and 2007/2009 can be attributed primarily to air-temperature increases, even though precipitation slightly increased at the same time. This greater precipitation could not offset ice losses resulting from surface melting driven by higher temperatures.

7. Summary and Conclusions

This study used multitemporal remote sensing and historical topographic maps to analyze glacial changes in the area of the Ili River. Our results updated the first glacier inventory from the 1960s by employing additional sources of data and enhanced analytical methods. The use of satellite data revealed that glaciers in the study area shrunk by $24.2\% \pm 8.8\%$ between the 1960s and 2007/2009. No expanding or advancing glaciers were identified in the study area during the same time period. The greatest glacial shrinkage occurred in the Kunes River basin, which contained most of the smaller glaciers. During the 40-year study period, 331 glaciers disappeared, and 18 disintegrated into two or three glaciers.

Rising temperatures resulting from global climate change are considered to be the main reason for glacial recession. Glacial sizes and elevations were determined to be control factors which determined the magnitude of response that glaciers had to climate change. The mean glacier slope showed no relationship with glacial recession and disappearance. Increases in the debris cover appeared to have a minor influence on the melting of glaciers, an effect that was more pronounced in smaller glaciers. We found that smaller glaciers lost a higher percentage of their surface area as a result of melting.

Conflict of Interests

The authors declare that there is no conflict of interests regarding the publication of this paper.

Acknowledgments

This work was supported by the Key Research Program of the Chinese Academy of Sciences (Grant no. KZZD-EW-12-1), the China National Natural Science Foundation (Grant no. 41401084), the Ministry of Science and Technology of China (MOST; Grant nos. 2010DFA92720-23 and 2013FY111400), and the Strategic Priority Research Program-Climatic Change: Carbon Budget and Relevant Issues (Grant no. XDA05090302). The data applied resulted from an immediate past project from the MOST (Grant no. 2006FY110200). The authors' appreciation is also extended to NASA for the provision of the Landsat TM data and SRTM data, as well as China Meteorological Administration for climate data.

References

- [1] Intergovernmental Panel on Climate Change, *Climate Change 2013—The Physical Science Basis. Contribution of Working Group I to the Fifth Assessment Report of the Intergovernmental Panel on Climate Change*, T. F. Stocker, D. Qin, G.-K. Plattner, Eds., Cambridge University Press, Cambridge, UK, 2013.
- [2] R. G. Barry, "The status of research on glaciers and global glacier recession: a review," *Progress in Physical Geography*, vol. 30, no. 3, pp. 285–306, 2006.
- [3] World Glacier Monitoring Service, *Global Glacier Changes: Facts and Figures*, 2008, <http://www.grid.unep.ch/glaciers/>.
- [4] K. Hewitt, "Glacier change, concentration, and elevation effects in the Karakoram Himalaya, upper Indus basin," *Mountain Research and Development*, vol. 31, no. 3, pp. 188–200, 2011.
- [5] T. Bolch, A. Kulkarni, A. Kääb et al., "The state and fate of Himalayan glaciers," *Science*, vol. 336, no. 6079, pp. 310–314, 2012.
- [6] J. L. Xu, S. Y. Liu, S. Zhang, W. Guo, and J. Wang, "Recent changes in glacial area and volume on Tuanjiefeng Peak Region of Qilian Mountains, China," *PLoS ONE*, vol. 8, no. 8, Article ID e70574, 2013.
- [7] A. S. Trupin, M. F. Meier, and J. M. Wahr, "Effect of melting glaciers on the Earth's rotation and gravitational field: 1965–1984," *Geophysical Journal International*, vol. 108, no. 1, pp. 1–15, 1992.
- [8] S. G. Evans and J. J. Clague, "Recent climatic change and catastrophic geomorphic processes in mountain environments," *Geomorphology*, vol. 10, no. 1–4, pp. 107–128, 1994.
- [9] W. Haeberli and M. Beniston, "Climate change and its impacts on glaciers and permafrost in the Alps," *Ambio*, vol. 27, no. 4, pp. 258–265, 1998.
- [10] J. M. Reynolds, A. Dolecki, and C. Portocarrero, "The construction of a drainage tunnel as part of glacial lake hazard mitigation at Hualcan, Cordillera Blanca, Peru," in *Geohazards in Engineering Geology*, vol. 15, pp. 41–48, 1998.
- [11] Y. P. Sheng, H. C. Su, G. Y. Wang et al., "The response of glaciers and snow cover to climate change in Xinjiang (II): hazards effects," *Journal of Glaciology and Geocryology*, vol. 35, no. 6, pp. 1355–1370, 2013.
- [12] W. D. Gao, M. Z. Liu, W. S. Wei et al., "The occurrence and mitigation of drifting snow and avalanche hazard in the mountains along the Jinghe-Yining railway, Tianshan, China," *Journal of Mountain Science*, vol. 23, no. 1, pp. 43–52, 2005.
- [13] X. Wang, K. P. Wu, H. L. Jiang et al., "Wide expansion of glacial lakes in Tianshan Mountains during 1990–2010," *Acta Geographica Sinica*, vol. 68, no. 7, pp. 983–993, 2013.
- [14] Y. He, T. B. Yang, H. Z. Tian et al., "Response of glacier area variation to climate change in northern Tianshan Mountains in the past 23 years," *Journal of Arid Land Resources and Environment*, vol. 27, no. 3, pp. 53–60, 2013.
- [15] I. V. Severskiy, A. L. Kokarev, S. Severskiy et al., *Contemporary and Prognostic Changes of Glaciation in Balkhash Lake Basin*, VAC Publishing House, Almaty, Kazakhstan, 2006.
- [16] R. Jin, X. Li, T. Che, L. Wu, and P. Mool, "Glacier area changes in the Pumqu river basin, Tibetan Plateau, between the 1970s and 2001," *Journal of Glaciology*, vol. 51, no. 175, pp. 607–610, 2005.
- [17] D. Shangguan, S. Liu, Y. Ding, L. Ding, J. Xu, and L. Jing, "Glacier changes during the last forty years in the Tarim Interior River basin, northwest China," *Progress in Natural Science*, vol. 19, no. 6, pp. 727–732, 2009.
- [18] C. Narama, A. Kääb, M. Duishonakunov, and K. Abdrakhmatov, "Spatial variability of recent glacier area changes in the Tien Shan Mountains, Central Asia, using Corona (~1970), Landsat (~2000), and ALOS (~2007) satellite data," *Global and Planetary Change*, vol. 71, no. 1–2, pp. 42–54, 2010.
- [19] T. Pieczonka, T. Bolch, W. Junfeng, and L. Shiyin, "Heterogeneous mass loss of glaciers in the Aksu-Tarim Catchment (Central Tien Shan) revealed by 1976 KH-9 Hexagon and 2009 SPOT-5 stereo imagery," *Remote Sensing of Environment*, vol. 130, pp. 233–244, 2013.
- [20] D. Scherler, B. Bookhagen, and M. R. Strecker, "Spatially variable response of Himalayan glaciers to climate change affected by debris cover," *Nature Geoscience*, vol. 4, no. 3, pp. 156–159, 2011.
- [21] A. Kääb, E. Berthier, C. Nuth, J. Gardelle, and Y. Arnaud, "Contrasting patterns of early twenty-first-century glacier mass change in the Himalayas," *Nature*, vol. 488, no. 7412, pp. 495–498, 2012.
- [22] C. H. Liu and L. F. Ding, "Some comments on the glacier inventory of Ili river drainage basin in Tianshan mountains," in *Glacier Inventory of China III, Tian Shan Mountains (Ili River Drainage Basin)*, C.A.O.S. Lanzhou Institute of Glaciology and Geocryology, Ed., pp. 1–7, Science Press, Peking, China, 1986.
- [23] C. H. Liu, Z. C. Xie, and M. B. Dyurgerov, *Glaciation in Tianshan Mountains*, Science Press, Beijing, China, 1998.

- [24] Y. F. Shi, *Concise Glacier Inventory in China*, Shanghai Popular Science Press, 2005.
- [25] Y. Zhang, K. Fujita, S. Liu, Q. Liu, and X. Wang, "Multi-decadal ice-velocity and elevation Changes of a monsoonal maritime glacier: hailuogou glacier, China," *Journal of Glaciology*, vol. 56, no. 195, pp. 65–74, 2010.
- [26] J. X. Wang, J. Wang, and C. P. Lu, "Problem of coordinate transformation between WGS-84 and BEIJING 54," *Journal of Geodesy of Geodynamic*, vol. 23, no. 3, pp. 70–73, 2003.
- [27] Y. J. Gao and D. F. Zhang, "The conversion method and accuracy analysis between WGS-84 coordinate system and Xi'an 80 coordinate system," *Engineering of Surveying and Mapping*, vol. 18, pp. 55–57, 2009.
- [28] G. D. Liu, Y. Q. Zhao, Z. L. Wang et al., "The conversion method and accuracy analysis between Xi'an 1980 and WGS-84 coordinate system," *Geomatics & Spatial Information Technology*, vol. 29, pp. 40–41, 2006.
- [29] R. S. Williams Jr., D. K. Hall, O. Sigurbsson, and J. Y. L. Chien, "Comparison of satellite-derived with ground-based measurements of the fluctuations of the margins of Vatnajökull, Iceland, 1973–92," *Annals of Glaciology*, vol. 24, pp. 72–80, 1997.
- [30] H. Rott, "Thematic studies in alpine areas by means of polarimetric SAR and optical imagery," *Advances in Space Research*, vol. 14, no. 3, pp. 217–226, 1994.
- [31] D. Shangguan, S. Liu, Y. Ding, L. Ding, and G. Li, "Glacier changes at the head of Yurungkax River in the West Kunlun Mountains in the past 32 years," *Acta Geographica Sinica*, vol. 59, no. 6, pp. 855–862, 2004.
- [32] J. L. Xu, S. Y. Liu, S. Q. Zhang et al., "Glaciers fluctuations in the Karamilan-Keriya River Watershed in the past 30 years," *Journal of Glaciology and Geocryology*, vol. 28, no. 3, pp. 312–318, 2006.
- [33] Z. Li, W. Sun, and Q. Z. Zeng, "Measurements of glacier variation in the Tibetan Plateau using landsat data," *Remote Sensing of Environment*, vol. 63, no. 3, pp. 258–264, 1998.
- [34] F. Paul, "Changes in glacier area in Tyrol, Austria, between 1969 and 1992 derived from Landsat 5 thematic mapper and Austrian Glacier Inventory data," *International Journal of Remote Sensing*, vol. 23, no. 4, pp. 787–799, 2002.
- [35] R. Bhambri, T. Bolch, and R. K. Chaujar, "Mapping of debris-covered glaciers in the Garhwal Himalayas using ASTER DEMs and thermal data," *International Journal of Remote Sensing*, vol. 32, no. 23, pp. 8095–8119, 2011.
- [36] F. Paul, C. Huggel, and A. Kääb, "Combining satellite multi-spectral image data and a digital elevation model for mapping debris-covered glaciers," *Remote Sensing of Environment*, vol. 89, no. 4, pp. 510–518, 2004.
- [37] R. Ranzi, G. Grossi, L. Iacovelli, and S. Taschner, "Use of multi-spectral ASTER images for mapping debris-covered glaciers within the GLIMS project," in *Proceedings of the IEEE International Geoscience and Remote Sensing Symposium (IGARSS '04)*, vol. 2, pp. 1144–1147, Anchorage, Alaska, USA, September 2004.
- [38] A. Shukla, M. K. Arora, and R. P. Gupta, "Synergistic approach for mapping debris-covered glaciers using optical-thermal remote sensing data with inputs from geomorphometric parameters," *Remote Sensing of Environment*, vol. 114, no. 7, pp. 1378–1387, 2010.
- [39] M. Shahgedanova, G. Nosenko, S. Kutuzov, O. Rototaeva, and T. Khromova, "Deglaciation of the Caucasus Mountains, Russia/Georgia, in the 21st century observed with ASTER satellite imagery and aerial photography," *The Cryosphere*, vol. 8, no. 6, pp. 2367–2379, 2014.
- [40] W. Q. Guo, S. Y. Liu, P. C. Yu et al., "Automatic extraction of ridgelines using on drainage boundaries and aspect difference," *Science of Surveying and Mapping*, vol. 36, no. 6, pp. 210–212, 2011.
- [41] D. K. Hall, K. J. Bayr, W. Schöner, R. A. Bindschadler, and J. Y. L. Chien, "Consideration of the errors inherent in mapping historical glacier positions in Austria from the ground and space (1893–2001)," *Remote Sensing of Environment*, vol. 86, no. 4, pp. 566–577, 2003.
- [42] T. Bolch, T. Yao, S. Kang et al., "A glacier inventory for the western Nyainqentanglha range and the Nam Co Basin, Tibet, and glacier changes 1976–2009," *Cryosphere*, vol. 4, no. 3, pp. 419–433, 2010.
- [43] D. H. Shangguan, S. Y. Liu, Y. J. Ding et al., "Glacier changes in the Koshi River basin, central Himalaya, from 1976 to 2009, derived from remote-sensing imagery," *Annals of Glaciology*, vol. 55, no. 66, pp. 61–68, 2014.
- [44] G. L. Zhang, B. T. Pan, J. Wang et al., "Research on the glacier change in the Gongga Mountain based on remote-sensing and GPS from 1966 to 2008," *Journal of Glaciology and Geocryology*, vol. 32, no. 3, pp. 454–460, 2010.
- [45] Y. W. Zeng, "Accuracy analysis of map scanning digitization," *Surveying and Mapping of Sichuan Province*, vol. 26, no. 3, pp. 82–85, 2003.
- [46] A. E. Racoviteanu, F. Paul, B. Raup, S. J. S. Khalsa, and R. Armstrong, "Challenges and recommendations in mapping of glacier parameters from space: results of the 2008 global land ice measurements from space (GLIMS) workshop, Boulder, Colorado, USA," *Annals of Glaciology*, vol. 50, no. 53, pp. 53–69, 2009.
- [47] T. Bolch, B. Menounos, and R. Wheate, "Landsat-based inventory of glaciers in western Canada, 1985–2005," *Remote Sensing of Environment*, vol. 114, no. 1, pp. 127–137, 2010.
- [48] W. Q. Guo, S. Y. Liu, J. L. Xu, and et al., "The second Chinese glacier inventory: data, methods and results," *Journal of Glaciology*, vol. 61, no. 226, pp. 357–372, 2015.
- [49] A. Osmonov, T. Bolch, C. Xi, A. Kurban, and W. Guo, "Glacier characteristics and changes in the Sary-Jaz River Basin (Central Tien Shan, Kyrgyzstan)—1990–2010," *Remote Sensing Letters*, vol. 4, no. 8, pp. 725–734, 2013.
- [50] A. Sorg, T. Bolch, M. Stoffel, O. Solomina, and M. Beniston, "Climate change impacts on glaciers and runoff in Tien Shan (Central Asia)," *Nature Climate Change*, vol. 2, no. 10, pp. 725–731, 2012.
- [51] J. L. Xu, S. Q. Zhang, and D. H. Shangguan, "Glacier change in head water of the Yangze river in recent three decades," *Arid Zone Research*, vol. 35, no. 5, pp. 919–926, 2013.
- [52] D. H. Shangguan, S. Y. Liu, Y. J. Ding et al., "Changes in the elevation and extent of two glaciers along the Yanglonghe river, Qilian Shan, China," *Journal of Glaciology*, vol. 56, no. 196, pp. 309–317, 2010.
- [53] C. M. DeBeer and M. J. Sharp, "Topographic influences on recent changes of very small glaciers in the monashee mountains, British Columbia, Canada," *Journal of Glaciology*, vol. 55, no. 192, pp. 691–700, 2009.
- [54] M. Nakawo, H. Yabuki, and A. Sakai, "Characteristics of Khumbu Glacier, Nepal Himalaya: recent change in the debris-covered area," *Annals of Glaciology*, vol. 28, pp. 118–122, 1999.
- [55] Y. Takeuchi, R. B. Kayastha, and M. Nakawo, "Characteristics of ablation and heat balance in debris-free and debris-covered areas on Khumbu Glacier, Nepal Himalayas, in the pre-monsoon season," *Debris-Covered Glaciers*, no. 264, pp. 53–61, 2000.

- [56] G. X. Ding, C. P. Chen, C. W. Xie et al., "Study of the ice tongue ablation features of a large glacier in the south slopes of the Mt. Tuomuer in the Tianshan mountains," *Journal of Glaciology and Geocryology*, vol. 36, no. 1, pp. 20–29, 2014.
- [57] A. Sakai, M. Nakawo, and K. Fujita, "Melt rate of ice cliffs on the Lirung glacier, Nepal Himalayas, 1996," *Bulletin of Glacier Research*, vol. 16, pp. 57–66, 1998.

Research Article

Hydrograph Separation in the Headwaters of the Shule River Basin: Combining Water Chemistry and Stable Isotopes

Jiaxin Zhou,^{1,2} Jinkui Wu,^{1,2} Shiwei Liu,^{1,2} Guoxiong Zeng,³
Jia Qin,^{1,2} Xiuna Wang,^{1,2} and Qiudong Zhao^{1,2}

¹Laboratory of Watershed Hydrology and Ecology, Cold and Arid Regions Environmental and Engineering Research Institute, Chinese Academy of Sciences, Lanzhou 730000, China

²State Key Laboratory of Cryospheric Science, Cold and Arid Regions Environmental and Engineering Research Institute, Chinese Academy of Sciences, Lanzhou 730000, China

³Shule River Basin Water Resources Administration of Gansu Province, Yumen 735200, China

Correspondence should be addressed to Jinkui Wu; jkwu@lzb.ac.cn

Received 25 December 2014; Revised 20 April 2015; Accepted 28 April 2015

Academic Editor: Fengjing Liu

Copyright © 2015 Jiaxin Zhou et al. This is an open access article distributed under the Creative Commons Attribution License, which permits unrestricted use, distribution, and reproduction in any medium, provided the original work is properly cited.

The runoff components were identified in the headwater area of Shule River Basin, using isotopic and chemical tracing with particular focus on the temporal variations of catchment sources. A total of 95 samples, including precipitation, groundwater, and glacial meltwater, were collected and analyzed for stable water isotopes (^{18}O and ^2H) and major chemical ion parameters (potassium, sodium, calcium, magnesium, sulfate, chloride, and bicarbonate). Based on the isotope and water chemistry data, we applied end member mixing analysis (EMMA) to identify and quantify the major runoff generating sources and their contributions. The contributions of groundwater, precipitation, and glacial meltwater were 66.7%, 19.9%, and 13.4%, respectively. The study indicated that groundwater dominated runoff in the headwater area of Shule River Basin. The roles of glacier meltwater should be remarkable in water resource management in this basin. The uncertainties of the EMMA method were summarized and estimated via a classical Gaussian error propagation technique. Analyses suggested that the uncertainty in the measurement method was less important than that in the temporal and spatial variations of tracer concentrations. The uncertainty was sensitive when the difference between mixing components was small. Therefore, the variation of tracers and the difference of mixing components should be considered when hydrograph separation was applied in the basin.

1. Introduction

The quantification of catchment response to rainfall or snowmelt events in terms of water fluxes and chemical composition is an important issue in catchment hydrology. In particular, during flooding periods, different interacting processes occur that are spatially distributed within the catchment [1, 2]. These processes are defined by physiographic characteristics. In addition, runoff generation depends on the initial state of the various hydrological reservoirs and on the characteristics of the hydrological input (precipitation or snowmelt). Due to these factors, it is difficult to identify the dominant runoff generation processes [3].

The water shortage and low use efficiency make china thirsty, and the loss of glacier and wetland in the western plateau will exaggerate this thirst in the future [4], while the same situation happens in other places of the world [5]. Therefore, it is important to understand the runoff generation mechanism. In arid or semiarid regions, water is a key factor affecting the biomass production. A better understanding of runoff generation processes as well as catchment function is important for improved water resources management [6]. The hydrograph separation technique using natural tracers, in which different runoff components are quantified according to their chemical signature, is a widely used method for investigating runoff generation processes at

the catchment scale [7]. Isotopes were used to quantify the interaction of different end member in glaciated catchments for longer time periods (monthly) and/or larger catchment areas ($>1000 \text{ km}^2$) [8–10]. Isotope techniques can be easily and successfully used to study the origin and dynamics of surface water and groundwater, evaporation of water bodies, and mixing processes between various water sources [11–13]. To obtain both temporal and spatial origins, some investigations using stable isotopes associated with chemical tracers have been undertaken in several different basins [14, 15]. Hydrochemical tracers, such as PH, electrical conductivity, or the concentration of different anions and cations [16], have been used to determine the origin of runoff components. In recent years, geochemical methods and environmental isotope techniques have been used increasingly to determine runoff components in various catchments under different environmental conditions [17, 18]. In the arid and semiarid areas, a combination of hydrologic and environmental isotope methods (^{18}O , D) has been proved to be a valuable tool for studying processes within the water cycle and in isotope hydrology [19–21].

One common tool to identify runoff sources and flux components and calculate their contributions to the stream discharge is end member mixing analysis (EMMA) [22]. EMMA techniques have been applied in varieties of studies, at both the plot and the catchment scales. Only few studies have applied EMMA in the arid or semiarid regions [23]. It has been applied in many studies to identify end members at small catchment scales that describe the vertical sequence of water storages to flow contribution. These vertical end members are, for example, rain, soil water, and groundwater [24] or overland flow, soil water, and hillslope water. Fewer studies have applied EMMA at larger catchment scales of hundreds or even thousands of square kilometers [25]. This approach is based on three mass conservations: one for water, one for isotopic tracer, and one for geochemical tracer. It allows separating the relative contribution of the different components, which correspond to different reservoirs or different contributive areas. The use of isotopic tracers allows separating the runoff hydrograph into preevent water and event water while the use of geochemical tracers allows identifying the three origins of the runoff components [26, 27].

There is a clear need to develop predictive capabilities related to the identification of runoff generating sources in large ungauged basins, particularly in emergent countries such as China [28]. Runoff generation and dynamics is an important issue in watershed and water resource management. On the one hand, knowledge about runoff generation processes and flow pathways is crucial for evaluating the vulnerability of surface and groundwater system [29]. On the other hand, such knowledge helps to develop and validate hydrological models. Since arid and semiarid basins usually have more severe natural conditions and scarcities of observation data, the application of isotope techniques in catchment hydrology study seems to be a more economic and helpful tool [30]. Understanding hydrological processes will significantly add our ability to evaluate potential tradeoffs

between social development and water availability. We expect that scientific results will provide an insight for water resource and watershed management in a large-area.

In this study, we applied the EMMA method to identify and quantify the major runoff generating sources in a three end members' system. The objectives of this study are (1) to identify runoff producing sources using ^{18}O and chloride ion as tracers in the headwater area of the Shule River Basin, (2) to investigate the applicability of the EMMA method in semiarid catchments, (3) to calculate the contributions of the three components of runoff. We developed a conceptual hydrograph separation technique, namely, three components' mixing model. It is based on the steady-state mass balance equations of water and tracer fluxes in a catchment. In addition, uncertainties analyses were performed for the hydrograph separation.

2. Study Areas

The Shule River, the third largest inland rivers basin with the whole catchment area of approximately $14.21 \times 10^4 \text{ km}^2$, is located in the Western Qilian Mountains. The upstream of the Shule River (Figure 1), at $96.6^\circ\text{E}\sim 99.0^\circ\text{E}$ and $38.2^\circ\text{N}\sim 40.0^\circ\text{N}$, with the area of $1.14 \times 10^4 \text{ km}^2$ and the mean elevation of 3885 m, is located in the Tianjun, Qinghai Province, Northeastern margin of the Tibetan Plateau. The mainstream annual runoff varying significantly during different years is $10.83 \times 10^8 \text{ m}^3$. The 53% of the total annual runoff concentrated between July and September. However, the runoff distributed unevenly over time. The runoff in spring and winter only makes up for 8.5% and 10%, respectively. According to nearly 40 years' hydrological data of Changmabao gauge station, the annual runoff of dry years and wet years is $5.36 \times 10^8 \text{ m}^3$ and $15.07 \times 10^8 \text{ m}^3$, respectively.

In the headwater area of Shule River Basin, our study area, Gahe, at $96.49^\circ\text{E}\sim 98.58^\circ\text{E}$ and $38.02^\circ\text{N}\sim 39.12^\circ\text{N}$, with the area 4096 km^2 , there are 347 glaciers and the area of glaciers is 29.45 km^2 , which accounts for 0.72% of the headwater area (Figure 2). Glaciers are mainly distributed above elevation 4500 m, which is located in Shule Nanshan and Tuolai Nanshan [31]. Annual sunshine time is 3033–3246 hours. The mean annual elevation is 4000–4500 m. The mean annual air temperature is approximately -5°C , the annual precipitation is 100–300 mm and mainly falling between May and September, and annual evaporation is about 1200 mm [32]. The temperatures of the hottest month (July) and the coldest month (January) are 7.5°C and -17.5°C , respectively. The study area belongs to the continental arid desert climate region which is characterized by cold, dry winters and relative warm, wet summers [33]. In the growing season of May through September, the plentiful sunshine and rainfall (80% of annual total precipitation) allows plants to grow efficiently.

The Quaternary sediments, comprising diluvial-alluvial, aeolian, and lacustrine deposits, form the main aquifers in the basin. These sediments are enriched in calcite, gypsum, and mirabilite in parts of the middle reaches, and soil salinization occurs widely in the middle and lower reaches. The depth to the water table is 5–10 m. There formed

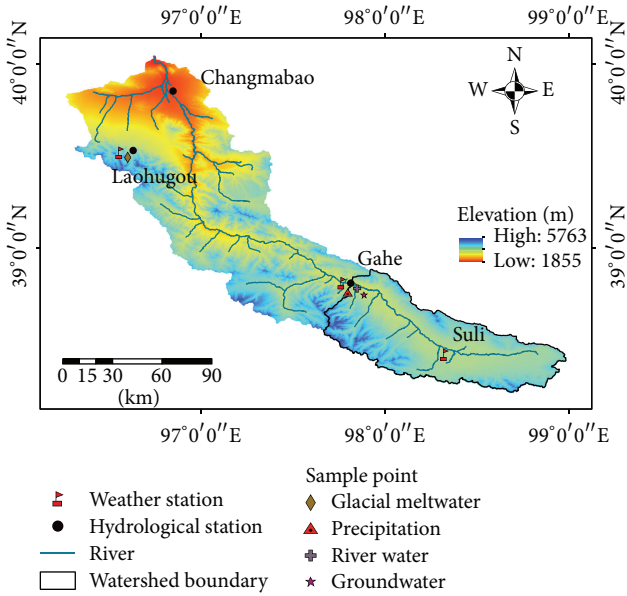


FIGURE 1: Site map showing the upstream of Shule River catchment and sampling sites.

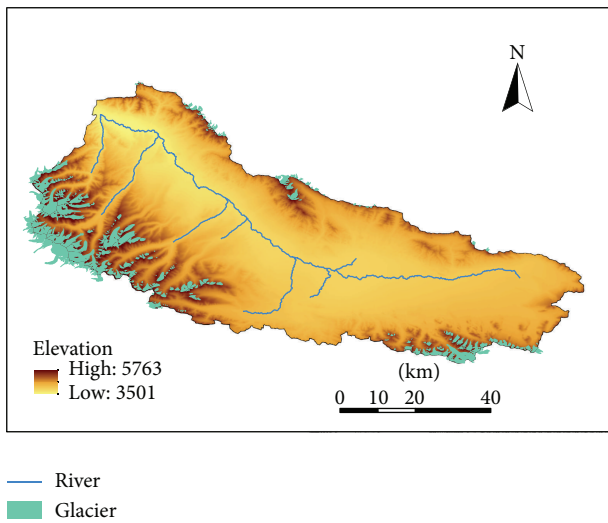


FIGURE 2: Glacier distribution of Gage region.

a large area of swamp in the source places. The aquifer system includes a thick unconfined zone consisting of coarse-grained gravel, sand and a confined part consisting of medium to fine and silty sand. The landscape is characterized by large mountain ranges with steep valleys and gorges interspersed with relatively level and wide intermountain grassland basins [34].

3. Material and Methods

3.1. Field Sampling. Intensive synoptic sampling was carried out between April and September 2009 in Gage, the headwater area of the Shule River, consisting of 95 samples.

Precipitation, glacial meltwater, groundwater, and river water were sampled. The number of four kinds of samples is precipitation 15, river water 30, groundwater 31, and glacial meltwater 19, respectively. Precipitation, glacial meltwater, groundwater, and river water were sampled and analyzed for stable water isotopes (^{18}O and ^2H), major ion chemistry parameters as well. Samples were collected in polyethylene bottles and filtered through 0.45 mm Millipore membrane for major element analyses. Meteorological parameters and hydrology data were measured continuously by means of an automatic weather station and gauge station.

Precipitation samples were collected immediately after each precipitation event in order to minimize the alteration of heavy isotopes by evaporation with plastic basin sets. River water and groundwater samples were collected once a week. Due to the limitations of some nature conditions, we cannot get to glaciers distributed around Gage. Hence, we collected the glacial meltwater samples in Laohugou Glacier number 12. Due to the background of the same atmospheric circulation, the moisture of the two sites comes from the same source. We considered the substitute is feasible.

3.2. Laboratory Analyses. All samples were kept in near-frozen condition and transported to the State Key Laboratory of Cryospheric Science, Cold and Arid Regions Environmental and Engineering Research Institute, Chinese Academy of Sciences, for test.

Concentration of anions (Cl^- , SO_4^{2-}) was analyzed by Ion Chromatography (IC, DX-120, Dionex, Germany) while HCO_3^- and CO_3^{2-} were analyzed by the titration method. Cations, K^+ , Na^+ , Ca^{2+} , and Mg^{2+} were analyzed by using Atomic Absorption Spectroscopy (AAS) method. Every sample value represents the mean of two consecutive measurements. Measurement errors were less than 1%. The detection limits of all ions were lower than 0.1 mg/L. Chloride ion and ^{18}O were finally selected to assess the different contributing sources using mass balance equations and end member mixing diagrams.

The δD and $\delta^{18}\text{O}$ composition of all water samples were analyzed by Liquid-Water Isotope Analyzer (DLT 100, Los Gatos, USA) based on off-axis integrated cavity output spectroscopy (OA-ICOS). Each sample is injected six times to avoid memory effect between samples. The isotopic ratios were expressed in per mil (‰) units relative to Vienna Standard Mean Ocean Water (V-SMOW):

$$\delta = \left(\frac{R_{\text{sample}}}{R_{\text{SMOW}}} - 1 \right) \times 10^3, \quad (1)$$

where R is the ration $^{18}\text{O}/^{16}\text{O}$ or $^2\text{H}/^1\text{H}$. Precision of δD and $\delta^{18}\text{O}$ was $\pm 0.6\text{‰}$ and $\pm 0.2\text{‰}$, respectively.

3.3. Hydrograph Separation Method and Uncertainties Analysis. In general, hydrograph separations are based on

the steady-state mass balance equations of water and tracer fluxes in a catchment [34]. Following are the equations:

$$\begin{aligned} Q_s &= Q_g + Q_p + Q_m, \\ Q_s \delta_s &= Q_g \delta_g + Q_p \delta_p + Q_m \delta_m, \\ Q_s C_s &= Q_g C_g + Q_p C_p + Q_m C_m. \end{aligned} \quad (2)$$

We converted the equations to vector form:

$$\begin{bmatrix} Q_g \\ Q_p \\ Q_m \end{bmatrix} = \begin{bmatrix} 1 & 1 & 1 \\ \delta_g & \delta_p & \delta_m \\ C_g & C_p & C_m \end{bmatrix}^{-1} \begin{bmatrix} 1 \\ \delta_s \\ C_s \end{bmatrix} Q_s. \quad (3)$$

Then the right side equations are divided by Q_s :

$$\begin{bmatrix} \frac{Q_g}{Q_s} \\ \frac{Q_p}{Q_s} \\ \frac{Q_m}{Q_s} \end{bmatrix} = \begin{bmatrix} 1 & 1 & 1 \\ \delta_g & \delta_p & \delta_m \\ C_g & C_p & C_m \end{bmatrix}^{-1} \begin{bmatrix} 1 \\ \delta_s \\ C_s \end{bmatrix}, \quad (4)$$

where Q is the discharge and C and δ are the concentration of tracer chloride ion and ^{18}O , respectively. Subscripts s , g , p , and m refer to river water, groundwater, precipitation, and glacial meltwater, respectively. The application of these equations is based on certain assumptions, which are discussed, for instance, by Hinton et al. [35], Buttle [1], or Rodhe [36]:

- (1) there is a significant difference between the tracer concentrations of the different components;
- (2) the tracer concentrations are constant in space and time, or any variations can be accounted for;
- (3) contributions of an additional component must be negligible, or the tracer concentrations must be similar to that of another component;
- (4) the tracers must mix conservatively;
- (5) the tracer concentrations of the components are not collinear.

Recent focus of hydrograph separation has been on uncertainty analysis. Several approaches are available for calculating uncertainty. Genereux (1998) suggested a general uncertainty propagation technique using Gaussian error estimators for two- and three-component separations [37]. However, an extensive overview of all possible causes of hydrograph separation uncertainties during different periods of a given event is still lacking. A classical Gaussian error propagation technique was applied to quantify the uncertainty of tracer-based hydrograph separations. This technique is generally used in other scientific and engineering problems. Errors of all separation equation variables are considered. Assuming that the uncertainty in each variable is independent of the uncertainty in the others, the relative error W_f of the contribution of a specific runoff component is related to the uncertainty in each of the variables by the following [37]:

$$\begin{aligned} w_y &= \sqrt{\left(\frac{\partial y}{\partial x_1} w_{x_1}\right)^2 + \left(\frac{\partial y}{\partial x_2} w_{x_2}\right)^2 + \dots + \left(\frac{\partial y}{\partial x_n} w_{x_n}\right)^2}, \\ w_{f_p} &= \sqrt{\left[\frac{C_e - C_s}{(C_e - C_p)^2} w_{C_p}\right]^2 + \left[\frac{C_s - C_p}{(C_e - C_p)^2} w_{C_e}\right]^2 + \left[\frac{-1}{(C_e - C_p)} w_{C_s}\right]^2}, \end{aligned} \quad (5)$$

where w represents the uncertainty in the variable specified in the subscript, c is the concentration of corresponding tracer, e represents the event water, and p represents the preevent water. In the results the relative error is given as percentage value.

It is demonstrated that large relative uncertainties must be considered for the quantification of runoff components. Uncertainties are caused by (1) tracer analysis and discharge measurement; (2) intrastorm variability of ^{18}O ; (3) elevation effect of ^{18}O and chloride; (4) solution of minerals during runoff formation; and (5) general spatial heterogeneity of tracer concentrations. The last source of error was the most significant. An investigation on the dominating runoff generation processes in the catchment, before a model is set up, would reduce such uncertainties.

4. Results

4.1. Temporal Variance of Runoff. The temporal variance of runoff is showed in Figure 3. The runoff showed a significant seasonal variation. The runoff varied in the range of 3.82~338.09 m³/s with an average of 71.57 m³/s. There is a minor peak in April since the snowmelt peak usually occurs in spring. We could see from the figure that most of peak flows were corresponding with the big rainfall events between June and September. It means the significant increase of runoff is the results of precipitation event. The average runoff is dominated by a snowmelt peak in spring followed by a decline in discharge over the growing season. From June to September, when most rainstorms occur, there is a considerable increase in discharge, followed by an again declining hydrograph until October, when the river itself freezes.

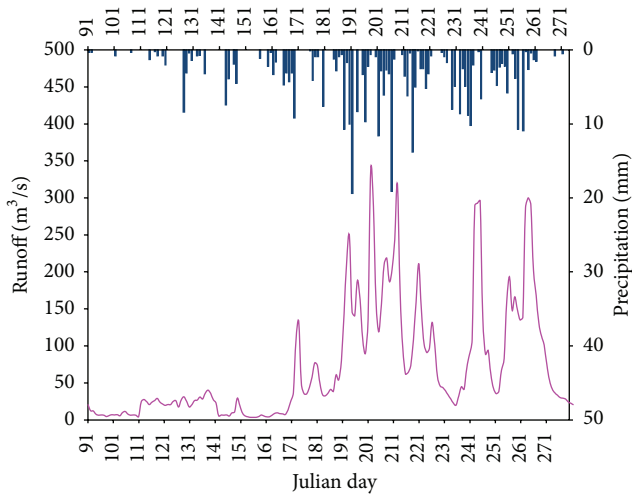


FIGURE 3: Runoff and rainfall from April to October 2009.

4.2. Isotopic Composition

4.2.1. Isotopic Composition of River Water. The isotopic composition of river water during April and September in the Gahé station shows a steady variability, ranging from -9.9 to -8.5‰ in $\delta^{18}\text{O}$ and from -68.9 to -58.2‰ in δD , respectively. The possibility of differential isotopic evaporation of samples can be analyzed by comparing the samples to the meteoric water line which is formed by plotting δD against $\delta^{18}\text{O}$ [38]. The local meteoric water line (LMWL) is commonly used as indicators of water vapor source, source of the humidity, and kinetic conditions in a number of fields including isotope hydrology [39]. The relationship between river water and the local meteoric water line (LMWL) was displayed by bivariate plot of $\delta^{18}\text{O}$ versus δD (Figure 4). According to the distribution of river water in the space of $\delta^{18}\text{O}$ versus δD , most of the river water sample points were located approaching the local meteoric water line (LMWL) ($\delta\text{D} = 8.11\delta^{18}\text{O} + 11.40$, $R^2 = 0.97$, $n = 30$). Also, the slope of the regression line was fairly close to the multiple-year observed values in Northwest China (7.88) and in Heihe River Basin, an inland river basin neighboring the study area (7.82) [40].

4.2.2. Isotopic Signature of Precipitation, Groundwater, and Glacial Meltwater. The isotopic composition of precipitation shows a relative significant variance. The values of $\delta^{18}\text{O}$ fluctuate in -13.0‰ ~ -8.3‰ and -95.1‰ ~ -54.2‰ in δD . The equation between $\delta^{18}\text{O}$ and δD ($\delta\text{D} = 7.68\delta^{18}\text{O} + 9.29$, $R^2 = 0.97$, $n = 15$) (Figure 5(a)). The temporal and spatial variability of ^{18}O in precipitation are relatively high. This is caused by fractionation during evapotranspiration and condensation due to lower saturated vapor pressure of water molecules containing the heavier ^{18}O isotope than that of water molecules containing the lighter ^{16}O isotope. As a result, the $\delta^{18}\text{O}$ in precipitation decreases with decreasing air temperature, increasing elevation, increasing latitude, increasing distance of vapor transport through the atmosphere, and increasing precipitation amounts.

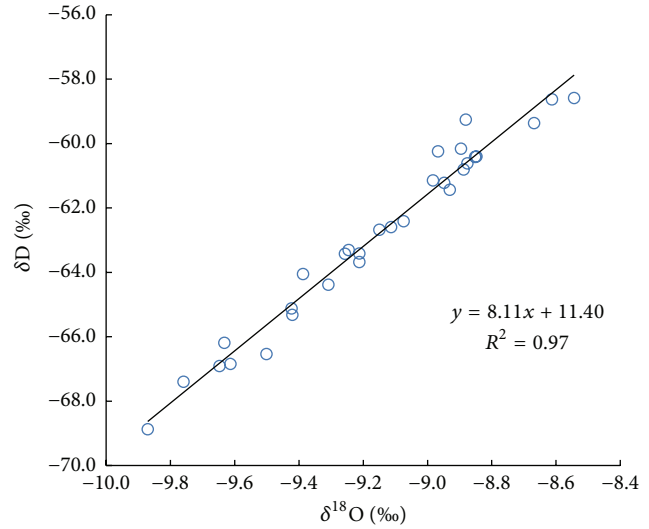


FIGURE 4: Stable isotope (δD and $\delta^{18}\text{O}$) compositions of river water.

The isotopic composition of groundwater ranges in -9.5‰ ~ -6.7‰ (in $\delta^{18}\text{O}$) and -68.2‰ ~ -45.3‰ (in δD). The equation between $\delta^{18}\text{O}$ and δD ($\delta\text{D} = 8.28\delta^{18}\text{O} + 10.74$, $R^2 = 0.96$, $n = 31$) (Figure 5(b)). It is fairly close to that of river water. The value of $\delta^{18}\text{O}$ ranges in -14.7‰ ~ -12.3‰ and δD in -105.0‰ ~ -85.1‰ in glacial meltwater. The equation between $\delta^{18}\text{O}$ and δD ($\delta\text{D} = 7.55\delta^{18}\text{O} + 7.34$, $R^2 = 0.96$, $n = 19$) (Figure 5(c)). The stable isotope ratios of hydrogen and oxygen of water samples can provide essential information about water dynamics within a given watershed. In general, this is from isotope fractionation by evaporation, altitude effects, and different water sources they received [23]. The slope and the intercept of LMWL were slightly lower, showing drier and stronger local evaporation conditions. Evaporation caused a differential increase in the δD and $\delta^{18}\text{O}$ values of the remaining water, resulting in a lower slope for the linear relationship between δD and $\delta^{18}\text{O}$ values [41].

4.3. Temporal Variance of Cl^- . It can be assumed that mixing processes in the catchment determine the isotopic concentration of total runoff. However, the hydrochemical composition of water is essentially changed as a result of interactions with organic and inorganic material during its passage through the unsaturated and saturated zones. The concentration of Cl^- in river water fluctuates in $9.4\text{--}13.4\text{ mg}\cdot\text{L}^{-1}$, with an average of $11.2\text{ mg}\cdot\text{L}^{-1}$. The variance of Cl^- concentration has much relationship with runoff (Figure 6). In spring, the spring flood caused by snowmelt water makes the soil chemical ions into the river, so the concentration of Cl^- is relatively high. Afterwards, with the increase of snowmelt water, glacier meltwater, and precipitation, the runoff has been showing a different amplitudes increase. With the increase of runoff, the dilution effect of ions has also increased, so the concentration of Cl^- decreased. Although groundwater recharged, the dilution effect outweighs the supply effect. During August and September, the runoff has a considerable decrease;

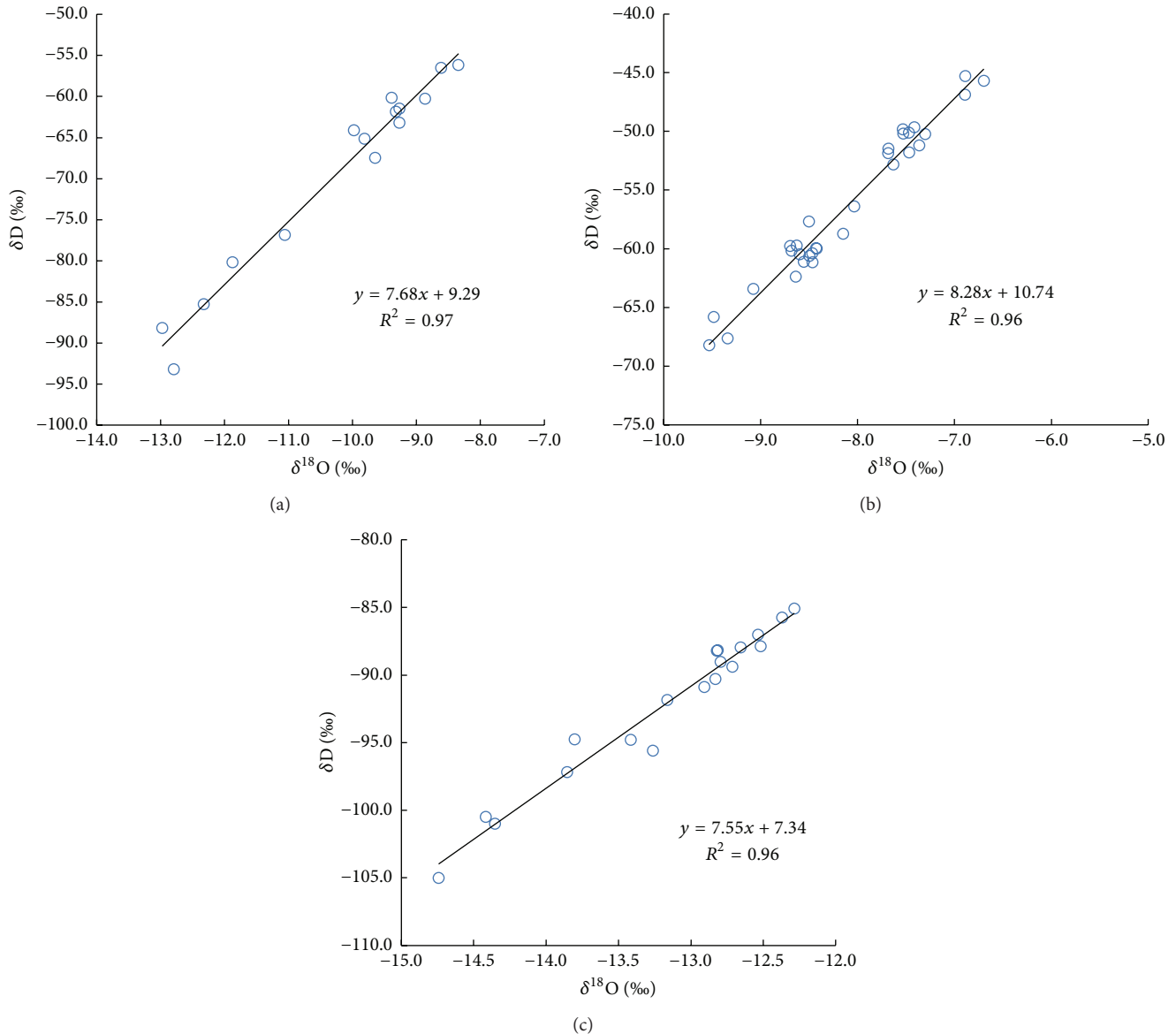


FIGURE 5: Stable isotope (δD and $\delta^{18}O$) compositions of precipitation (a), groundwater (b), and glacial meltwater (c).

the concentration of Cl^- decreased because of the weakening of dilution effect.

4.4. Identification of End Members. Applying the method of geochemical and isotopic tracing, in this paper the runoff characteristics and hydrological law at the Gahé station are investigated at different periods in 2009. We conducted a performance of principal component analysis (PCA) on the concentration data of chloride ion. The results showed that the chemical tracer exhibits conservative behavior, whereas isotopes are geographical source tracers and only change composition due to slow fractionation processes [42]. ^{18}O belongs to the group of stable environmental isotopes occurring naturally in water. It has been widely used to separate

storm flow into proportions of event and pre-event water [1]. As part of the water molecule, ^{18}O behaves conservatively; that is, the combination of chemical and isotopic tracers allows identifying the origin of water pathways.

For the three-component hydrograph separation, the choice of a suitable tracer constellation to explain the chemical changes in discharge during a storm as well as to determine and to identify dominant sources, flow paths, and residence times in the catchment becomes increasingly important. The study suggests that hydrological tracer chlorine concentration and ^{18}O can be used under certain hydrological and lithological conditions. A system of algebraic equations is introduced that enables a three-component hydrograph separation by using ^{18}O and chlorine. These

TABLE 1: Mean, maximum, minimum, and standard deviation values for the concentration of isotope and chloride ion in river water, precipitation, groundwater, and glacial meltwater.

	$\delta^{18}\text{O}$ (‰)				δD (‰)				Cl^- ($\text{mg}\cdot\text{L}^{-1}$)			
	Mean	Max	Min	SD	Mean	Max	Min	SD	Mean	Max	Min	SD
River water	-9.2	-8.5	-9.9	0.36	-62.7	-58.2	-68.9	3.49	11.2	13.4	9.4	1.17
Precipitation	-10.2	-8.3	-13.0	1.56	-69.7	-54.1	-95.1	12.5	0.5	0.8	0.2	0.22
Ground water	-8.1	-6.7	-9.5	0.76	-56.4	-45.3	-68.2	6.44	16.3	19.7	11.0	2.20
Glacial meltwater	-13.2	-12.3	-14.7	0.73	-92.1	-85.1	-105.0	5.63	2.2	3.2	1.2	0.56

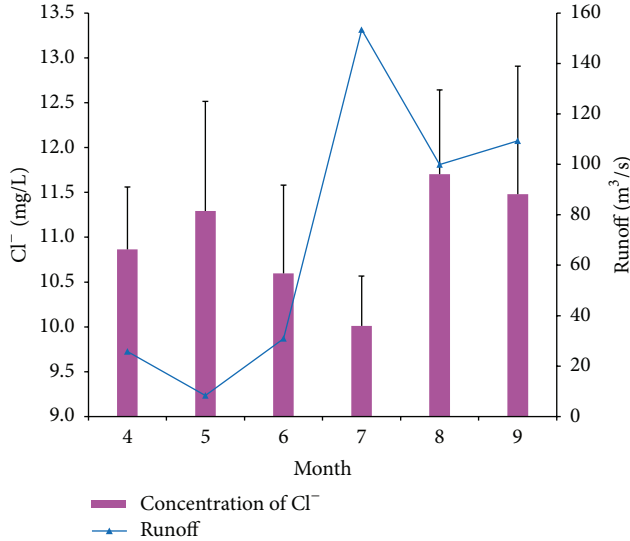


FIGURE 6: Monthly runoff and concentration of Cl^- (with error bars).

alternative tracers should, however, be verified against more conventional tracers before use, as the behavior depends on specific characteristics of solutes.

The basic assumption in EMMA is that the stream water is a discrete mixture of its sources. The sources must therefore be of sufficiently different concentrations compared with the stream water. We projected the average values of tracer chloride ion and ^{18}O of three end members in triangle to test and verify the independence (Figure 7). It shows that most of stream water observations fall into the triangle that is spanned by three end members (precipitation, groundwater, and glacial meltwater). However, there exist some stream water observations that lie outside of the triangle. In many other studies that apply EMMA such a situation has been described [14, 22–24, 35]. These outliers result from a number of factors including (1) uncertainty in field sampling and laboratory analyses, (2) lack of temporal invariance of end members, or (3) the expression of different end member in the mixture as water source areas change temporally. Overall, the result can lead to over- or underprediction of the contributions of each end member to the stream water and should be understood as a source of uncertainty.

4.5. Contribution of End Members to Runoff. Owing to the geological and geomorphological genesis of the study

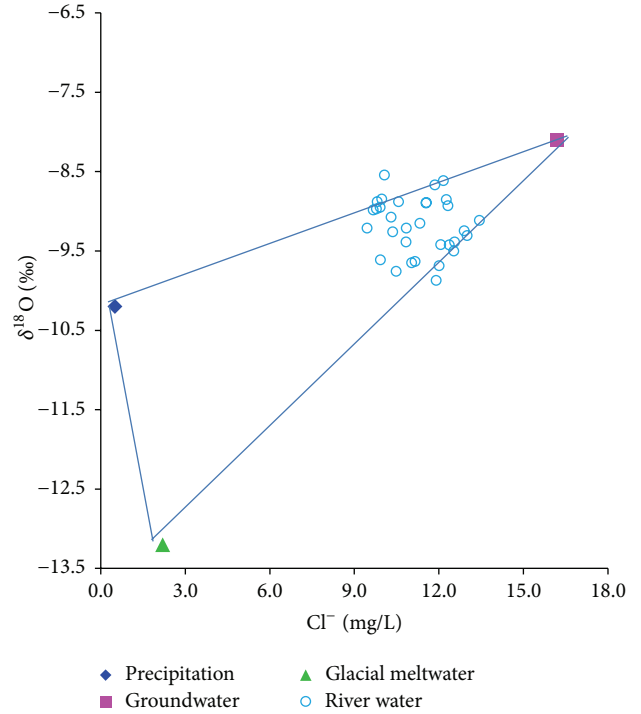


FIGURE 7: Stream water observations and the average values of tracers Cl^- and ^{18}O of three end members that spanned the triangle.

site there are at least three runoff sources having distinct hydrological characteristics. Results obtained by the use of the three-component mixing model are shown in Figure 8. Based on the concentration data of isotope and chloride ion (Table 1), the contributions of each end member to river water were calculated according to the steady-state mass balance equations of water and tracer fluxes (equations (2)). Isotopic hydrograph separation shows that the contribution of groundwater, precipitation, and glacial meltwater is 66.7%, 19.9%, and 13.4%, respectively. The study indicated that groundwater dominated runoff in the headwater area of Shule River Basin. And the roles of glacier meltwater should be significantly noticed in water resource management in this catchment. The glaciers are the headwaters of many rivers and they affect the water discharge of large rivers [43].

Despite the reasonable illustration of the qualitative behavior of runoff components, an exact quantification of runoff components contributing remained difficult and is strongly related to the determination of tracer concentrations

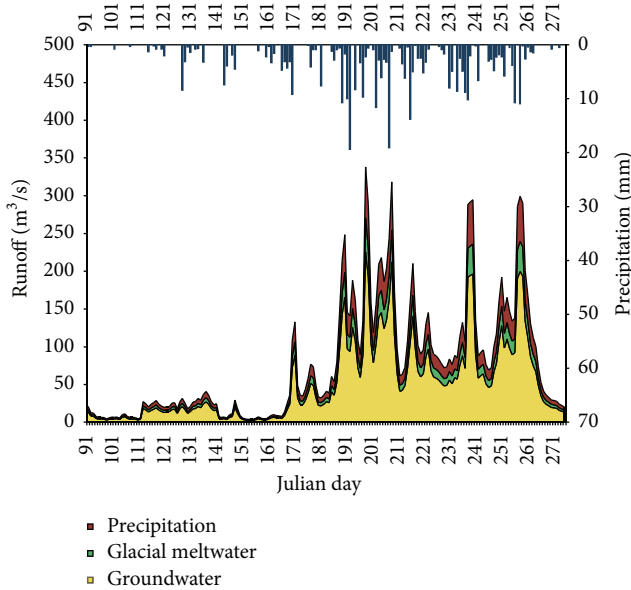


FIGURE 8: The conclusion of hydrograph separation.

in both runoff sources. Owing to the presence of various uncertainties, only qualitative results were achieved. Further experimental investigations are needed to define the tracer concentrations and their variability with greater accuracy. For hydrograph separations in larger scale basins, an extensive consideration of the spatial variability along with the superposition of spatially distributed runoff components is a challenging task for future research. Our results prompt us to focus future work on understanding interannual changes in end member contribution especially in semiarid regions.

5. Discussion and Conclusions

The isotopic and chemical values originate from measurement methods, field data, or the expert knowledge of the investigators. This is reasonable even if the implications of the effects are the same, since all of them cause an uncertain estimation of the end member concentrations and thus of the contribution of different runoff components. So-called end member concentrations need to be defined for every tracer of a specific runoff component for each separation time step in order to calculate the component proportions using mass balance equations for the tracers and the water. However, the determination of these concentrations is often problematic, as it has been shown that they may exhibit high temporal and spatial variability and always include errors caused by the analysis [18, 21]. Therefore, the uncertainty of hydrograph separation results must be addressed. In general, large relative uncertainties must be considered while performing hydrograph separations. Predictive uncertainty is the primary impediment to progress in this area, but continued progress is being made to more fully quantify uncertainty and more fully explore its implications. The importance of reducing errors that have the largest impact on uncertainty is clearly demonstrated. Therefore, future

investigations are needed to define with greater accuracy end member tracer concentrations and their spatial and temporal variability. Moving towards an understanding of uncertainties complexity is a challenging and important task for future research in catchment hydrology.

Assumed values of the uncertainty in isotopic composition were $w_{C_s} = 0.2\text{‰}$, $w_{C_p} = w_{C_e} = 0.4\text{‰}$ [43]. We calculated the uncertainty of tracers itself to be 9%. Analyses suggested that the uncertainty in the measurement method was less important than that in the temporal and spatial variations of tracer concentrations. The uncertainty terms for precipitation were generally higher than 80% of the total uncertainty, indicating that the $\delta^{18}\text{O}$ values of precipitation account for the majority of uncertainty. The uncertainty was sensitive when the difference between mixing components was small. Therefore, the variation of tracers and the difference of mixing components should be considered when hydrograph separation was applied in the basin.

Hydrograph separation shows that the contribution of groundwater, precipitation, and glacial meltwater is $66.7 \pm 6.02\%$, $19.9 \pm 1.79\%$, and $13.4 \pm 1.20\%$, respectively. There are 347 glaciers and the area of glaciers is 29.45 km^2 , which accounts for 0.72% of the headwater area. Under the background of global warming, rising temperature leads to the increase of snowmelt and accelerating the retreat of glaciers, which will have a significant impact on regional runoff. The roles of glacier meltwater should be significantly noticed in water resource management in this catchment. In addition to temporal variability, a superposition of spatial and temporal distributed runoff components needs to be considered. Moving towards an understanding of this complexity is a challenging and important task for future research in catchment hydrology.

Several studies compared the results of two- and three-component separation. Wenninger et al. (2004) showed a difference of 10% in preevent water contributions between the two methods, because the three-component separation accounted for snow and rain inputs together while the two-component separation accounted for rain inputs only [44]. Dense temporal sampling of hydrographs is often challenging especially at remote locations. Therefore studies that investigate runoff generation in alpine catchment are rare. Pionke et al. showed that for a 7.4 km^2 watershed three of four monitored storms were dominated by preevent water (55–94% in total) [45]. DeWalle showed that in a smaller catchment (0.198 km^2) storm runoff was also dominated by preevent water contributions, 90% over the course of the hydrograph [46]. For a 45 km^2 catchment, Buda found more than 80% preevent water contributions to the channel storm flow with 67% during the peak flow in a 6 ha catchment [47]. A similar range of preevent water contributions (80%, 60%) was reported by Munyanzea et al. (2012) for two mesoscale catchments (129.3 km^2 , 257.4 km^2) in Rwanda [48]. Dong et al. have used the recursive digital filter method and smoothed minimum method to separate base flow based on daily runoff data from 1954 to 2009 in the upper reaches of the Shule River Basin, the recursive digital filter and smoothed minimum method were used for base flow separation. The base flow

index is different between the calculation results from the two methods (0.77 and 0.66) [49].

One shortcoming of this study is that the identification of end members is limited to data collected during the vegetation period which comprises only 6 months of the year. Moreover, we only have the isotope data and chemical parameters of one hydrologic section, so we cannot analyze the spatial variability. The importance of reducing errors that have the largest impact is clearly demonstrated; therefore, a targeted sampling strategy is required. In order to fully characterize the range of climatic variability, our results emphasize the need of continued development of the long-term measurement. Our results prompt us to focus future work on understanding interannual changes in end member contribution especially in semiarid regions.

Conflict of Interests

The authors declare that there is no conflict of interests regarding the publication of this paper.

Acknowledgments

This research was financially supported by the National Natural Science Foundation of China (nos. 41130638; 41271085; 41401039). The authors are also grateful to all participants in the field (J. H. Yang, H. Wu) and in the laboratory (R. Xu) for their contribution which allows this study to progress in good conditions.

References

- [1] J. M. Buttle, "Isotope hydrograph separations and rapid delivery of pre-event water from drainage basins," *Progress in Physical Geography*, vol. 18, no. 1, pp. 16–41, 1994.
- [2] M. Bonell, "Selected challenges in runoff generation research in forests from the hillslope to headwater drainage basin scale," *Journal of the American Water Resources Association*, vol. 34, no. 4, pp. 765–785, 1998.
- [3] S. Hoeg, S. Uhlenbrook, and Ch. Leibundgut, "Hydrograph separation in a mountainous catchment—combining hydrochemical and isotopic tracers," *Hydrological Processes*, vol. 14, no. 7, pp. 1199–1216, 2000.
- [4] Z. S. Wang, C. F. Zhou, B. H. Guan et al., "The headwater loss of the western plateau exacerbates China's long thirst," *AMBIO*, vol. 35, no. 5, pp. 271–272, 2006.
- [5] B. G. Mark, "Hot ice: glaciers in the tropics are making the press," *Hydrological Processes*, vol. 16, no. 16, pp. 3297–3302, 2002.
- [6] F. K. Barthold, J. Wu, K. B. Vaché, K. Schneider, H.-G. Frede, and L. Breuer, "Identification of geographic runoff sources in a data sparse region: hydrological processes and the limitations of tracer-based approaches," *Hydrological Processes*, vol. 24, no. 16, pp. 2313–2327, 2010.
- [7] S. Uhlenbrook and S. Hoeg, "Quantifying uncertainties in tracer-based hydrograph separations: a case study for two-, three- and five-component hydrograph separations in a mountainous catchment," *Hydrological Processes*, vol. 17, no. 2, pp. 431–453, 2003.
- [8] J. Cable, K. Ogle, and D. Williams, "Contribution of glacier meltwater to streamflow in the Wind River Range, Wyoming, inferred via a Bayesian mixing model applied to isotopic measurements," *Hydrological Processes*, vol. 25, no. 14, pp. 2228–2236, 2011.
- [9] Y. Kong and Z. Pang, "Evaluating the sensitivity of glacier rivers to climate change based on hydrograph separation of discharge," *Journal of Hydrology*, vol. 434–435, pp. 121–129, 2012.
- [10] T. Pu, Y. He, G. Zhu, N. Zhang, J. Du, and C. Wang, "Characteristics of water stable isotopes and hydrograph separation in Baishui catchment during the wet season in Mt. Yulong region, south western China," *Hydrological Processes*, vol. 27, no. 25, pp. 3641–3648, 2013.
- [11] C. Kendall and T. B. Coplen, "Distribution of oxygen-18 and deuterium in river waters across the United States," *Hydrological Processes*, vol. 15, no. 7, pp. 1363–1393, 2001.
- [12] F. J. Liu, M. Williams, and N. Caine, "Sources waters and flow paths in an alpine catchment, Colorado Front Range, USA," *Water Resources Research*, vol. 40, Article ID W09401, 2004.
- [13] J. J. Gibson, T. W. D. Edwards, S. J. Birks et al., "Progress in isotope tracer hydrology in Canada," *Hydrological Processes*, vol. 19, no. 1, pp. 303–327, 2005.
- [14] C. Wels, R. J. Cornett, and B. D. Lazerte, "Hydrograph separation: a comparison of geochemical and isotopic tracers," *Journal of Hydrology*, vol. 122, no. 1–4, pp. 253–274, 1991.
- [15] P. Durand, M. Neal, and C. Neal, "Variations in stable oxygen isotope and solute concentrations in small sub-mediterranean montane streams," *Journal of Hydrology*, vol. 144, no. 1–4, pp. 283–290, 1993.
- [16] N. C. Christophersen, C. Neal, R. P. Hooper, R. D. Vogt, and S. Andersen, "Modelling streamwater chemistry as a mixture of soilwater end-members—a step towards second-generation acidification models," *Journal of Hydrology*, vol. 116, no. 1–4, pp. 307–320, 1990.
- [17] G. F. Pinder and J. F. Jones, "Determination of the groundwater component of peak discharge from the chemistry of total runoff," *Water Resources Research*, vol. 5, no. 2, pp. 438–445, 1969.
- [18] J. J. McDonnell, M. Bonell, M. K. Stewart, and A. J. Pearce, "Deuterium variations in storm rainfall: implications for stream hydrograph separation," *Water Resources Research*, vol. 26, no. 3, pp. 455–458, 1990.
- [19] W. G. Mook, "Environmental isotopes in the hydrological cycle, principles and applications, Volume III: surface water. International Hydrological Programme," Technical Documents in Hydrology 39, IAEA, Vienna, Austria, 2001.
- [20] P. K. Aggarwal, "Isotope hydrology at the International Atomic Energy Agency," *Hydrological Processes*, vol. 16, no. 11, pp. 2257–2259, 2002.
- [21] N. Christophersen and R. P. Hooper, "Multivariate analysis of stream water chemical data: the use of principal components analysis for the end-member mixing problem," *Water Resources Research*, vol. 28, no. 1, pp. 99–107, 1992.
- [22] F. J. Liu, R. Parmenter, P. D. Brooks, M. H. Conklin, and R. C. Bales, "Seasonal and interannual variation of streamflow pathways and biogeochemical implications in semi-arid, forested catchments in Valles Caldera, New Mexico," *Ecohydrology*, vol. 1, no. 3, pp. 239–252, 2008.
- [23] J. Chaves, C. Neill, S. Germer, S. G. Neto, A. Krusche, and H. Elsenbeer, "Land management impacts on runoff sources in small Amazon watersheds," *Hydrological Processes*, vol. 22, no. 12, pp. 1766–1775, 2008.

- [24] V. Acuña and C. N. Dahm, "Impact of monsoonal rains on spatial scaling patterns in water chemistry of a semiarid river network," *Journal of Geophysical Research G: Biogeosciences*, vol. 112, no. 4, Article ID G04009, 2007.
- [25] B. Ladouche, A. Probst, D. Viville et al., "Hydrograph separation using isotopic, chemical and hydrological approaches (Strengbach catchment, France)," *Journal of Hydrology*, vol. 242, no. 3-4, pp. 255-274, 2001.
- [26] D. Yang, C. Li, B. Ye et al., *Chinese Perspectives on PUB and the Working Group Initiative. Predictions in Ungauged Basins: International Perspectives on the State of the Art and Pathways Forward*, vol. 301, IAHS Publication, 2005.
- [27] J. Klaus and J. J. McDonnell, "Hydrograph separation using stable isotopes: review and evaluation," *Journal of Hydrology*, vol. 505, pp. 47-64, 2013.
- [28] C. H. Leibundgut, "Tracer-based assessment of vulnerability in mountainous headwaters," in *Hydrology, Water Resources and Ecology in Headwaters*, vol. 248, pp. 317-326, 1998.
- [29] Z. Kattan, "Characterization of surface water and groundwater in the Damascus Ghotta basin: hydrochemical and environmental isotopes approaches," *Environmental Geology*, vol. 51, no. 2, pp. 173-201, 2006.
- [30] W. Liu, S. Chen, X. Qin et al., "Storage, patterns, and control of soil organic carbon and nitrogen in the northeastern margin of the Qinghai-Tibetan Plateau," *Environmental Research Letters*, vol. 7, no. 3, Article ID 035401, 2012.
- [31] M. J. Liu, T. D. Han, J. Wang et al., "Variations of the components of radiation in permafrost region of the upstream of Shule River," *Plateau Meteorology*, vol. 32, no. 2, pp. 411-422, 2013.
- [32] Y. Sheng, J. Li, J. C. Wu, B. S. Ye, and J. Wang, "Distribution patterns of permafrost in the upper area of Shule River with the application of GIS technique," *Journal of China University of Mining and Technology*, vol. 39, no. 1, pp. 32-40, 2010.
- [33] X. Xie, G. J. Yang, Z.-R. Wang, and J. Wang, "Landscape pattern change in mountainous areas along an altitude gradient in the upper reaches of Shule River," *Chinese Journal of Ecology*, vol. 29, no. 7, pp. 1420-1426, 2010.
- [34] M. G. Sklash and R. N. Farvolden, "The role of groundwater in storm runoff," *Journal of Hydrology*, vol. 43, no. 1-4, pp. 45-65, 1979.
- [35] M. J. Hinton, S. L. Schiff, and M. C. English, "Examining the contributions of glacial till water to storm runoff using two- and three-component hydrograph separations," *Water Resources Research*, vol. 30, no. 4, pp. 983-993, 1994.
- [36] A. Rodhe, *The origin of streamwater traced by oxygen-18 [Ph.D. thesis]*, Uppsala University, 1987, UNGI Report Series A No. 41.
- [37] D. Genereux, "Quantifying uncertainty in tracer-based hydrograph separations," *Water Resources Research*, vol. 34, no. 4, pp. 915-919, 1998.
- [38] A. L. James and N. T. Roulet, "Investigating the applicability of end-member mixing analysis (EMMA) across scale: a study of eight small, nested catchments in a temperate forested watershed," *Water Resources Research*, vol. 42, no. 8, Article ID W08434, 2006.
- [39] W. Dansgaard, "Stable isotopes in precipitation," *Tellus*, vol. 16, no. 4, pp. 436-468, 1964.
- [40] J. Jouzel, K. Froehlich, and U. Schotterer, "Deuterium and oxygen-18 in present-day precipitation: data and modelling," *Hydrological Sciences Journal*, vol. 42, no. 5, pp. 747-763, 1997.
- [41] J. Wu, Y. Ding, B. Ye, Q. Yang, X. Zhang, and J. Wang, "Spatio-temporal variation of stable isotopes in precipitation in the Heihe River Basin, Northwestern China," *Environmental Earth Sciences*, vol. 61, no. 6, pp. 1123-1134, 2010.
- [42] J. K. Wu, Y. J. Ding, J. H. Yang et al., "Stable isotopes in different waters during melt season in Laohugou Glacial Catchment, Shule River basin, Northwestern China," *Journal of Mountainous Science*. In press.
- [43] T. D. Yao, L. Thompson, W. Yang et al., "Different glacier status with atmospheric circulations in Tibetan Plateau and surroundings," *Nature Climate Change*, vol. 2, pp. 663-667, 2012.
- [44] J. Wenninger, S. Uhlenbrook, N. Tilch, and C. Leibundgut, "Experimental evidence of fast groundwater responses in a hillslope/floodplain area in the Black Forest Mountains, Germany," *Hydrological Processes*, vol. 18, no. 17, pp. 3305-3322, 2004.
- [45] H. B. Pionke, W. J. Gburek, and G. J. Folmar, "Quantifying stormflow components in a Pennsylvania watershed when ^{18}O input and storm conditions vary," *Journal of Hydrology*, vol. 148, no. 1-4, pp. 169-187, 1993.
- [46] D. R. Dewalle and B. R. Swistock, "Differences in oxygen-18 content of throughfall and rainfall in hardwood and coniferous forests," *Hydrological Processes*, vol. 8, no. 1, pp. 75-82, 1994.
- [47] A. R. Buda and D. R. DeWalle, "Dynamics of stream nitrate sources and flow pathways during stormflows on urban, forest and agricultural watersheds in central Pennsylvania, USA," *Hydrological Processes*, vol. 23, no. 23, pp. 3292-3305, 2009.
- [48] O. Munyaneza, J. Wenninger, and S. Uhlenbrook, "Identification of runoff generation processes using hydrometric and tracer methods in a meso-scale catchment in Rwanda," *Hydrology and Earth System Sciences*, vol. 16, no. 7, pp. 1991-2004, 2012.
- [49] W. W. Dong, Y. J. Ding, and X. Wei, "Variation of the base flow and its causes in the upper reaches of the Shule River in the Qilian Mountains," *Journal of Glaciology and Geocryology*, vol. 36, no. 3, pp. 661-669, 2014.

Research Article

Actual Evapotranspiration in Suli Alpine Meadow in Northeastern Edge of Qinghai-Tibet Plateau, China

Jin-kui Wu,¹ Shi-qiang Zhang,^{1,2} Hao Wu,^{1,3} Shi-wei Liu,¹ Yu Qin,¹ and Jia Qin¹

¹State Key Laboratory of Cryospheric Science, Cold and Arid Regions Environmental and Engineering Research Institute, Chinese Academy of Sciences, Lanzhou, Gansu 730000, China

²College of Urban and Environmental Sciences, Northwest University, Xi'an, Shannxi 710127, China

³Yunnan Hydraulic Research Institute, Kunming, Yunnan 650228, China

Correspondence should be addressed to Jin-kui Wu; jkwu@lzb.ac.cn

Received 12 December 2014; Revised 7 April 2015; Accepted 22 April 2015

Academic Editor: Monique Leclerc

Copyright © 2015 Jin-kui Wu et al. This is an open access article distributed under the Creative Commons Attribution License, which permits unrestricted use, distribution, and reproduction in any medium, provided the original work is properly cited.

Actual evapotranspiration was observed by using eddy covariance (EC) technique, calculated by micrometeorological method the Bowen ratio energy balance (BREB) and measured by micro-lysimeter (ML) in the Suli alpine meadow which located in the northeastern edge of Qinghai-Tibet Plateau noted for its high elevation and cold environment during the growing season in 2011. Results showed that the energy balance ratio for half-hour data was 0.74. Without consideration of uncertainty, the evapotranspiration values estimated by BREB, ML, and EC were 270.6 mm, 238.9 mm, and 236.1 mm, respectively. Significant correlation existed between the evapotranspiration results by the three methods. Uncertainties of the evapotranspiration estimation by BREB, ML, and EC were 19.6 mm, 15.6 mm, and 15.1 mm, respectively. Deduced by facts on the natural and vegetation conditions, the value of evapotranspiration should be equal to that of precipitation, that is, about 252 mm. From this point, the evapotranspiration values estimated by the three methods were within a reliable range. The EC method has larger advantage and wider scope for the estimation of evapotranspiration in alpine meadow area.

1. Introduction

Evapotranspiration is one of the major components in the hydrological cycle and an important factor that affects regional water balance and ecosystems [1]. Meanwhile, it is the main form of water consumption in the earth system. Nearly 70% of the precipitation returns into the atmosphere through evapotranspiration and this ratio is up to 90% in arid region [2, 3]. Furthermore, evapotranspiration is an important boundary condition in climate modeling and weather prediction, as it is an important mechanism in the generation of precipitation [4]. Land surface evapotranspiration is closely related to the atmospheric environment, soil environment, and plant ecological and physiological processes. In climatology, agriculture, and above all in hydrology, the calculation of the real evapotranspiration may quantify the climatic water deficit and analyze the aridity of a given

environment in detail [5]. Additionally, it enables hydrologists and resources managers to evaluate water balance at different space and time scales and to define the water reservoir available in a given area for different water uses [6]. Also, its reliable estimation is essential to water resource planning and management [7].

There is a great variety of methods for measuring/estimating ET, such as weighing lysimeters, Bowen ratio energy balance (BREB), eddy covariance (EC), aerodynamic method, remote sensing method, hydrological model, and crop coefficient approach.

Weighting lysimeters, measuring evapotranspiration directly through changes in mass, are the most convenient way to quantify evapotranspiration [8]. Such manual lysimeters have been used to determine periodic water use for a variety of plants grown in small containers [9]. By using a large-scale weighing lysimeter, daily evapotranspiration

of irrigated winter wheat and maize was determined for five seasons between 1995 and 2000 at Luancheng Station in the North China Plain [10]. McKeon et al. [11] developed a hand truck with a load cell for manual measurements of single containers up to 250 kg. Owen et al. [12] automated the process for small containers by connecting top loading balances to a data logger in a nursery setting. Manual lysimeters were also used to measure daily evapotranspiration and evaluate the Penman-Monteith equation at the plateau wetlands in the eastern edge of Qinghai-Tibet Plateau [13].

The two most frequently used methods for estimating the actual evapotranspiration indirectly are the Bowen ratio energy balance (BREB) and the eddy correlation (EC) techniques [14]. BREB-based evapotranspiration rates can be obtained independently of weather conditions. However, any inaccuracy in one of the instruments will have a direct influence on all measured fluxes. Further, the method does not work under Bowen ratio values in the vicinity of -1 . Furthermore, the BREB method is based on the assumption of equal eddy diffusivities for heat and water vapor, conditions which are not always met [15]. On the other hand, in the EC method no assumptions concerning the eddy diffusivities need to be made. The disadvantages of the EC method are dew formation on the instruments during daybreak, which renders the instruments unreliable, and further the fact that the instruments do not work properly under precipitation [14].

Both the BREB and EC methods have been intercompared in a number of field studies. Using four BREB systems and three EC systems in an agricultural field, Dugas et al. [16] found that the sum of EC-based latent and sensible heat fluxes was lower than the BREB-based quantities, with the latent heat flux showing the highest differences. Using both methods in a semiarid environment, Unland et al. [17] indicated that the BREB method is the more adequate method to obtain long records of surface fluxes, basically because EC instruments require more maintenance, but that the EC method is likely to have a higher accuracy over short periods. For grassland and forested areas, Twine et al. [18] gave an overview of the studies in which the BREB and the EC methods have been intercompared. These studies generally show, consistent with the previously mentioned studies over grasslands and agricultural fields, an underestimation of the sum of the EC-based latent and sensible heat fluxes, as compared to the available energy.

Qinghai-Tibet Plateau (QTP) is a vast elevated plateau in Central Asia or East Asia, covering most of the Tibet Autonomous Region and Qinghai Province in western China. With an average elevation exceeding 4500 m and an area of 2500 000 km², the QTP is the world's highest and largest plateau. The QTP is the headwaters of the drainage basins of most of the streams in surrounding regions. The impact of global climate change on the QTP is of intense scientific interest [19]. Comparing to other regions at the same latitude, the atmospheric layer in QTP is thinner and cleaner and has less water vapor and dust. It leads to higher atmospheric

transparency and stronger direct solar radiation [20]. In the context of strong radiation, the regional ecosystem also is exposed to low temperature environment. In addition, the precipitation usually concentrates in May to September, the growing season for plants. Under this unique ecological environment, the evapotranspiration of alpine meadow ecosystem shows its particularity [21].

In this paper, we chose an observation site located in the northeastern edge of the QTP for actual evapotranspiration study. The objectives were to (1) obtain the actual evapotranspiration of the alpine meadow by using different methods, (2) investigate the energy balance rate (EBR), (3) estimate the uncertainty of the evapotranspiration estimation, and (4) compare the results of the actual evapotranspiration from different methods and determine a better one for future observation.

2. Site Description and Measurements

2.1. Site Description. Field measurements were conducted at the Suli Ecological and Environmental Station (38°25'N, 98°19'E; 3885 m a.s.l.), Cold and Arid Regions Environmental and Engineering Research Institute, Chinese Academy of Science. The research station is located in a large valley oriented southeast-northwest and surrounded by the Qilian Mountains, the northeastern edge of the QTP. The average altitude of the mountains is 4200 m and of the valley is 2500–4100 m. The Shulehe River passes to the study area.

The study area belongs to the continental arid desert climate region [22]. It has low average annual temperature, little rainfall, and high evaporation. The mean annual temperature was approximately -5°C and the annual precipitation ranged from 100 to 300 mm [23]. In the growing season of May through September, the plentiful sunshine and rainfall (80% of annual total precipitation) allow plants to grow efficiently.

The landscape is characterized by large mountain ranges with steep valleys and gorges interspersed with relatively level and wide intermountain grassland basins [24]. Our observation tower is set up in a large valley basin. It provides a sufficient upwind fetch of uniform land cover for measuring mass and energy fluxes using tower-based eddy covariance systems.

According to the Chinese soil classification system, the main soil types in this area are frigid calcic soils (Chernozems, Kastanozems) and bog soils (gleysols, histosols, gelic gleysols, gelic histosols, umbric cambisols) [23]. The surface 0.05–0.10 m horizons of the observation site, which are classified as Mat Cry-gelic Cambisols, are wet and high in organic matter.

The study area is in an alpine meadow. The plant community is dominated mainly by *Carex moocroftii* and *Kobresia pygmaea* [25, 26]. The plants start to grow in May, when the air temperature starts rising, and reach maximum aboveground biomass in July and August, when the air temperature and precipitation are in the highest of the year. Their aboveground parts die in October. During the growing season, the plants accumulate photosynthates in belowground storage organs in preparation for the next spring [25, 26]. The study site is grazed by yaks and sheep every winter.

2.2. Measurements

2.2.1. Flux Measurements. The experimental site was equipped with an eddy covariance (EC) system to measure energy, water, and CO₂ fluxes. The EC system was installed at a height of 3.0 m, including a 3D ultrasonic anemometer-thermometer (CSAT-3, Campbell Scientific Inc., Logan, UT, USA) and an open-path infrared gas (CO₂/H₂O) analyzer (IRGA) (LI-7500, LI-COR Inc., Lincoln, NE, USA). The signals were recorded at 10 Hz by a data logger (CR3000, Campbell Scientific Inc., Logan, UT, USA).

2.2.2. Meteorological Measurements. A 10 m tall meteorological tower was established in 2008. A four-component net radiometer (CNR-1, Kipp & Zonen, Delft, Netherlands) was set up at the height of 2.0 m above the ground. Air temperature (T_a) and relative humidity (RH) were measured at four levels (2.0 m, 5.0 m, 7.5 m, and 10.0 m) (HMP45C, Vaisala, Helsinki, Finland). A wind set sensor (020C-1, Met One Inc., OR, USA) was set up at the same four heights to measure horizontal wind speed and wind direction. The data of T_a , RH, and W_s at the height of 2.0 m and 10.0 m above the ground were adopted in this study.

The soil temperature (T_s) profile was measured at six depths (0.05, 0.10, 0.30, 0.50, and 0.70 m) by thermistors (107L, Campbell Scientific Inc., Logan, UT, USA). Soil water content (SWC) profile was measured at five depths (0.10, 0.20, 0.40, 0.60, and 0.80 m) by time domain reflectometry probes (EnviroSMART, Campbell Scientific Inc., Logan, UT, USA). Soil heat flux was measured by two soil heat flux plates (HFP01, Hukseflux Inc., Delft, Netherlands) in separate locations at 0.05 m and 0.10 m below the soil surface. Precipitation was measured using an all-weather precipitation gauge (Geonor T-200B, Norway) without heating above the canopy. All meteorological data was recorded every 2 s, and half-hourly mean data were logged by the data logger (CR1000, Campbell Scientific Inc., Logan, UT, USA).

2.2.3. Micro-Lysimeter. The cylindrical shaped micro-lysimeter was made of metal by 2 mm thick. It was divided into inner barrel and the outer barrel. The inner barrel of each micro-lysimeter, containing isolated volumes of soil and grass mounted flush with or slightly above the soil surface, is 36 cm in diameter with a depth of 40 cm. The micro-lysimeters were weighed twice a day to determine water loss using electronic balances with 0.001 kg precision to meet the measurement requirements. We installed three micro-lysimeters within the study meadow at random.

3. Methods and Data

3.1. Eddy Covariance (EC) Technique. According to the principle of eddy covariance technique, sensible heat flux (H) and latent heat flux (λE) were calculated by the following formula:

$$\begin{aligned} H &= \rho_a c_p \overline{w' \theta'}, \\ \lambda E &= \lambda \rho_a \overline{w' q'}, \end{aligned} \quad (1)$$

where ρ_a is air density (kg m^{-3}) at a given air temperature, c_p is the air specific heat ($\text{J kg}^{-1} \text{K}^{-1}$), λ is the latent heat of vaporization (J kg^{-1}), w' , θ' , and q' denote fluctuations of vertical wind speed (m s^{-1}), air temperature (K), and specific humidity (kg kg^{-1}), respectively, and over bars indicate average over the sampling interval (30 min in this study). Positive scalar fluxes denote the energy transfer from the canopy surface to the atmosphere while negative fluxes signify the reverse.

Software EdiRe was chosen for data correction and quality control in this study. Data processing is mainly referenced by the EC data processing method recommended by FLUX NET [27]. Before the scalar flux computation, spike detection and removal and coordinate rotation were performed. Coordinate rotation was performed to reorient the X-axis parallel to the local main wind direction and to force the mean vertical velocity to zero. In addition, the sonic temperature fluctuations were taken into account to correct the fluxes of sensible heat, and the Webb-Pearman-Leuning (WPL) method was used to correct latent heat fluxes from fluctuations in temperature and water vapor density.

The available data sets were screened to remove any anomalous half-hourly fluxes that resulted from malfunction of the sensors following the criteria: (1) incomplete half-hourly measurement, mainly caused by mechanical conditions such as power failure or infrared gas analyzers (IRGA) calibration, (2) precipitation events, and (3) outliers due to occasional spike in half-hourly flux values for unknown reasons [28].

Roughly 18% of the data obtained from the EC system were discarded in the growing season of 2011, which introduced data gaps. These gaps were filled following the strategies put forward by Falge et al. [29]: (1) linear interpolation was used to fill the gaps that were less than 2 h by calculating an average of the values immediately before and after the data gap; (2) other data gaps were filled using the empirical relationships (look-up tables method); that is, the bin-average values for λE or H in connection with their environmental drivers such as atmospheric vapor pressure deficit (VPD), in cases where those relationships could be established, with three bimonthly look-up tables, were created for the growing season of 2011; and (3) if these relationships could not be established due to missing meteorological data, mean daily variations in the fluxes were used to fill the gaps.

3.2. Bowen Ratio Energy Balance (BREB) Method. The Bowen ratio β can be calculated as

$$\beta = \frac{H}{\lambda E}. \quad (2)$$

We can approximately express β as

$$\beta = \gamma \frac{T_1 - T_2}{e_1 - e_2} = \gamma \frac{\Delta T}{\Delta e} \quad (3)$$

with γ being the psychrometric constant ($\text{kPa } ^\circ\text{C}^{-1}$), T_1 and T_2 being the air temperatures ($^\circ\text{C}$) at levels 1 (2 m in height) and 2 (10.0 m in height), respectively, and e_1 and e_2 being the

water vapor pressures (kPa) at levels 1 and 2, respectively. The psychrometric constant is calculated as

$$\gamma = 0.665 \times 10^{-3} P \quad (4)$$

with P being the atmospheric pressure (kPa). Using the net radiation (R_n , $W m^{-2}$) and the observed ground heat flux (G , $W m^{-2}$), the sensible and latent heat flux can be calculated as

$$\begin{aligned} H &= \frac{\beta (R_n - G)}{1 + \beta}, \\ \lambda E &= \frac{R_n - G}{1 + \beta}. \end{aligned} \quad (5)$$

The ground heat flux at the soil surface (G) was calculated from measurements of the soil heat flux plates by taking into account the energy storage above the plates, which can be estimated using the soil water content and the fluctuations in the soil temperature. In this study, we used two methods as follows.

(1) Using the soil heat flux measured by the soil heat flux plate at the depth of 0.05 m and soil water content at the depth of 0.20 m [30],

$$G = G_5 + C \int_0^z \frac{\partial T}{\partial t} dz, \quad (6)$$

where G is surface soil heat flux ($W m^{-2}$); G_5 is the soil heat flux plate at the depth of 0.05 m ($W m^{-2}$); C is the soil heat capacity ($J m^{-3} ^\circ C^{-1}$); T is temperature of the soil above the plates ($^\circ C$).

(2) Using the soil heat flux measured by the soil heat flux plate at the depth of 0.10 m, surface temperature, ground temperatures at the depth of 0.05 m and 0.10 m, and soil water content at the depth of 0.20 m [31],

$$\begin{aligned} G &= G_{10} \\ &+ C \left(0.01 \times \frac{\partial T_s}{\partial t} + 0.06 \times \frac{\partial T_5}{\partial t} + 0.03 \times \frac{\partial T_{10}}{\partial t} \right), \end{aligned} \quad (7)$$

where G is surface soil heat flux ($W m^{-2}$); G_{10} is the soil heat flux plate at the depth of 0.10 m ($W m^{-2}$); C is the soil heat capacity ($J m^{-3} ^\circ C^{-1}$); T_s , T_5 , and T_{10} are ground temperature at the depth of surface of 0.05 m and 0.10 m ($^\circ C$).

Since the BREB method results in unreliable estimates of the turbulent fluxes when β approaches -1 , data were excluded for Bowen ratios between -0.7 and -1.3 [14]. Further, according to Andreas and Cash [32], data for Bowen ratios larger than 10 or lower than -0.7 (this partly excludes data that were already excluded by the first restriction) and negative or zero vapor pressure gradients were eliminated from the analysis. Overall, 91% of the BREB-based latent heat flux estimates were deemed fit for analysis.

3.3. Micro-Lysimeter (ML) Method. According to the principle of water balance in a lysimeter, the formula for calculating evapotranspiration is as follows:

$$\Delta S = P + W - Q - R - ET, \quad (8)$$

where ΔS is the soil water variation within a lysimeter; P is for precipitation; W is net upward flux of the lower boundary of the soil; Q is for leakage; R is for surface runoff and ET is for evapotranspiration. Units for all variables are in mm.

In this study, the precipitation was directly measured by T200B; the leakage from the lower part of lysimeter was measured by the containers. Considering the fact that the determination depth was less than the water table, the effect of recharge from groundwater was not considered, namely, $W = 0$, in this equation. According to the observations, no leakage occurred during the study period. Due to the small precipitation intensity and flat topography, no runoff generated; thus R was ignored. While no precipitation occurs, the above equation can be expressed as

$$E = \Delta S, \quad (9)$$

where ΔS was calculated directly through changes in mass in mm. The mean values of the 3 micro-lysimeters are used for analysis.

3.4. The Energy Balance Ratio (EBR). The net radiation (R_n) is partitioned into sensible (H), latent (λE), and soil (G) heat fluxes:

$$R_n = H + \lambda E + G. \quad (10)$$

The energy balance ratio (EBR) was used to assess the performance of the EC system [33]. EBR is calculated using the following equation for half-hourly periods where all the data (R_n , H , λE , and G) were available [33]:

$$EBR = \frac{\sum (\lambda E + H)}{\sum (R_n - G)}, \quad (11)$$

where the turbulent energy flux ($\lambda E + H$) is the results from EC method and available energy flux ($R_n - G$) is from the BREB. The advantage of this method is that it gives an overall evaluation of energy balance closure at longer time scales by averaging over random errors in the half-hour measurements [33].

3.5. The Atmospheric Stability (AS). The atmospheric stability (AS) describes the state of the atmospheric turbulence. Usually it is represented by Richard number [34, 35],

$$Ri = \frac{g * \partial \theta / \partial z}{T * (\partial u / \partial z)^2}, \quad (12)$$

where g is acceleration of gravity, $9.8 m s^{-2}$; T is the mean absolute temperature of two layers (K); θ is potential temperature (K); u is the wind speed ($m s^{-1}$); z is the height from the surface (m).

In this study, the two gradient layers used for analyzing were 2 and 10 m as BREB did.

4. Results

4.1. Soil Heat Flux (G). Figure 1 showed the relationship between calculated results of soil heat flux (G) by two

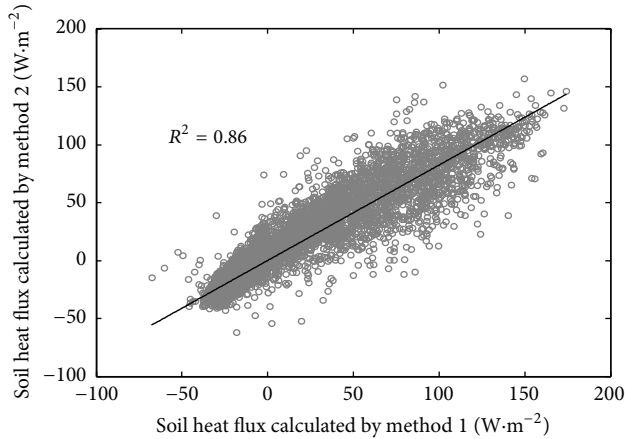


FIGURE 1: The relationship between calculated soil heat fluxes by two methods.

methods by using 30-minute data. As seen from the figure, two scenarios of G had a good agreement with a correlation coefficient of 0.93 (Figure 1) and root mean square error (RMSE) of 16 W m^{-2} . Based on this, the average values of G by 2 methods were used for the following calculations.

4.2. The Energy Balance Ratio (EBR). The EBR for all 30-minute data is 0.74 for the growing season of 2011, falling in the median regions of the reported energy closure, which range from 0.55 to 0.99 for FLUXNET [33] (Figure 2(a)).

During the observational period, daily latent heat flux, daily sensible flux, and daily turbulent energy flux were 71 W m^{-2} , 30 W m^{-2} , and 101 W m^{-2} , respectively, while the daily net radiation, daily soil heat flux, and available energy were 132 W m^{-2} , 12 W m^{-2} , and 120 W m^{-2} , respectively. The turbulent flux by eddy covariance system was less than the available energy by BREB method (Figure 2(b)). The energy balance ratio for daily data was 0.84.

Monthly EBRs were obtained by using observational 30-minute data from May to September 2011. The regression slopes were 0.76, 0.72, 0.75, 0.73, and 0.73 for May, June, July, August, and September, respectively.

4.3. Diurnal Change of Atmospheric Stability. The analysis results of diurnal change atmospheric stability (ζ) at the observation site from May to September 2011 showed the following: during nighttime, $\zeta > 0$, the value of AS varied between 0.2 and 0.3, atmospheric stratification was stable, and the development of turbulence was suppressed, while during daytime, $\zeta < 0$, the atmospheric stratification was unstable, the maximum degree of atmospheric instability occurred around noon ($\zeta = -2.9$), and the turbulent exchange was full; at sunrise (7:00~8:00) and sunset (19:00~20:00) periods, the atmospheric stratification was nearly neutral, namely, $\zeta \approx 0$, and atmospheric stratification was at the transition period from being stable to unstable or unstable to a stable.

4.4. Daily Evapotranspiration Determined by the 3 Methods. Because the observation period of micro-lysimeter was

between 19/6/2011 and 13/9/2011, we had to choose this period for the comparative study of evapotranspiration.

The daily evapotranspiration determined by 3 methods had similar variation trends (Figure 3). Daily evapotranspiration had good relationship with the air temperature as shown in Figure 3. Also, sharp increase of daily evapotranspiration usually connected to relative heavier precipitation (Figure 3). It could be explained that more sufficient water was supplied for evapotranspiration.

Under no consideration of uncertainty, the cumulative evapotranspiration estimated by BREB method was 270.6 mm, 13% higher than that measured by ML method and 15% higher than that estimated by EC method. The cumulative evapotranspiration was 238.9 mm by ML method, nearly the same as 236.1 mm calculated by EC method.

5. Discussion

5.1. The Energy Balance. As this study showed, the EBR at the study site was 0.74. It indicated that the energy was not entirely closed by the results from the eddy covariance method and the energy balance method. In fact, this phenomenon existed in many eddy covariance measurements. By using the flux data across 22 sites and 50 site-years in FLUXNET, a network of eddy covariance sites measuring long-term carbon and energy fluxes in contrasting ecosystems and climates, Wilson et al. [33] found a general inclosure at most sites existing, with a mean imbalance in the order of 20%. Franssen et al. [34, 35] and Li et al. [36] reported their results based on 26 sites (of which 5 were cropland/grassland sites) in Europe and 8 sites (of which 3 were grassland sites) in China, respectively. Both of the analysis results showed that no full energy closure existed in those observational sites. The observation results in alpine meadow in QTP [37–39] also indicated that turbulent energy flux usually was lower than the available energy flux. During the growing season, the latent heat flux was the main part of the turbulent flux. The underestimation of turbulent flux thus led to underestimation of evapotranspiration in those areas.

Li et al. [39] gave a detailed analysis on the causes of inclosure of energy balance from the deviations in samples and instruments, the loss of high frequency and low frequency, the ignorance of some energy items, and loss of advection.

Infrared gas analyzers (IRGA) are widely used around the world for measuring flux exchange of terrestrial ecosystems. However, further comparisons have revealed substantial differences between open- and closed-path designs, especially in cold environments, causing concern in the flux research community [40]. Specifically, carbon dioxide and water vapor density measurements from an open-path IRGA may be biased when the instrument significantly heats the air that it measures, particularly in cold environments [41].

Considering the fact that the study site is in a cold region, the self-heating correction on the sensible and latent heat flux by the LI-7500 open-path is needed. Burba et al. proposed corrections requiring no complementary closed-path measurements, introducing new sensible heat flux terms estimated theoretically and verified experimentally [41]. In

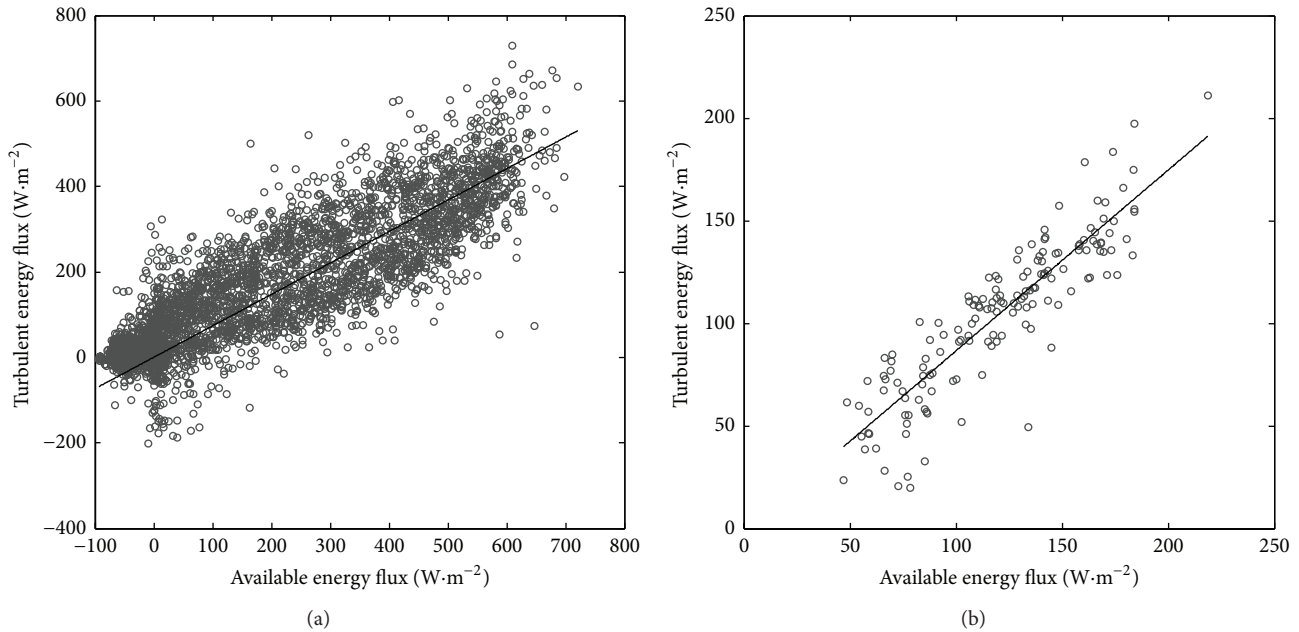


FIGURE 2: Relationship between the turbulent energy flux and available energy flux ((a) 30-minute data; (b) daily data).

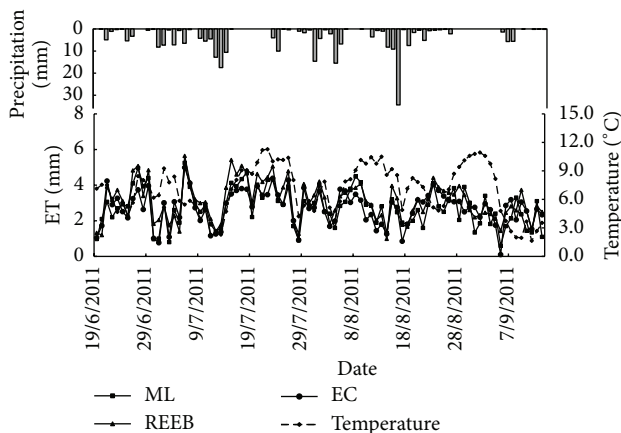


FIGURE 3: Daily variation of air temperature, precipitation, and evapotranspiration (ET) estimated by three methods during the observation period.

this study, we followed this correction method and the parameters for the calculation were derived from Burba et al. [41] and Ji et al. [42].

By using half-hour data, the correction results showed that the mean sensible heat flux correction was 13 W m^{-2} , exceeding the uncorrected mean sensible heat flux by up to 43.3%. The heat exchanges from the bottom window and spars were the main contributor of the correction term of sensible heat flux inside the path with the mean value of 9.5 W m^{-2} and 3.5 W m^{-2} , respectively. Ji et al. [42] reported their results in the Heihe River basin, a neighboring river basin of the Shule River basin, where the mean sensible heat flux correction was about 9 W m^{-2} . Burba et al. [41] found high-frequency temperature measurements inside the

path producing sensible heat flux inside the instrument path exceeding the ambient heat flux by up to 14%. As our study site was colder than other sites, the extent of the correction was larger.

For latent heat flux, the mean correction value was only about 1 W m^{-2} and exceeded the uncorrected mean latent heat flux by up to 1.4%. The magnitude of the correction term was small and negligible. Similar results were found in Burba et al. [41] and Ji et al. [42]. The former reported that the daily correction values of latent heat flux were $-0.14 \sim 0.47 \text{ W m}^{-2}$ and the latter reported a daily correction value of 0.47 W m^{-2} .

5.2. The Comparison of Evapotranspiration Estimated by 3 Methods under No Consideration of Uncertainty. Linear regression analysis was made to determine the relationship between the results of evapotranspiration by eddy covariance method, micro-lysimeter method, and Bowen ratio energy balance method (Figure 4). Generally speaking, the estimated results from 3 methods were in a good agreement.

Though the cumulative evapotranspiration by EC method was very close to that by ML method during the whole observational period as mentioned above, the daily variation of evapotranspiration was not entirely consistent (Figure 3) and had the worst correlation (Figure 4). The daily evapotranspiration measured by micro-lysimeters had a wider fluctuation range due to the measurement errors from the manual weighting. The weighting results were always influenced by human factors and natural factors such as wind. Another research [43] carried out in the Loess Plateau in China also indicated that the cumulative evapotranspiration by EC method and Lysimeter method was nearly the same though the dispersion degree of two daily evapotranspiration series was large. Qi et al. [37] found that evapotranspiration

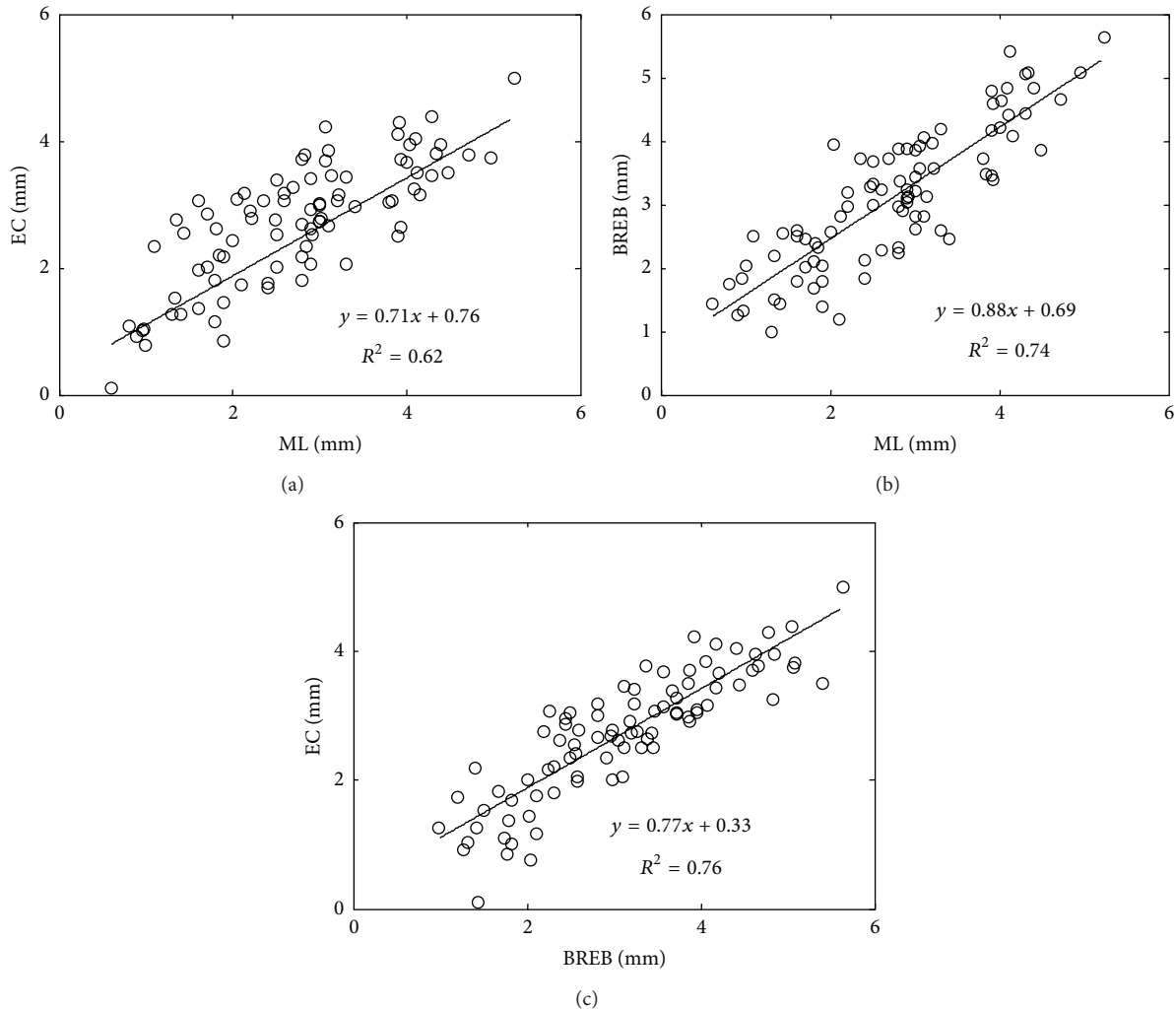


FIGURE 4: Relationship of evapotranspiration between EC, BREB, and ML.

measured by lysimeter (148.7 mm) was 19% larger than that estimated by the eddy covariance method (125.4 mm) in an alpine meadow in QTP.

The cumulative evapotranspiration by BREB method was 13% higher than that by ML method in this study. Qi et al. [37] reported that this percentage was 20% in an alpine meadow in QTP. The observational results in a soybean land indicated that the evapotranspiration by BREB method was basically the same as that by lysimeter measurements in case of nonadvection, while the former was a bit lower than the latter under advection conditions. Qiang et al. [44] found that the evapotranspiration by BREB method was consistent with that by lysimeter measurements in winter wheat field in an irrigation experiment station in northwestern China while Zhu [45] found that the evapotranspiration by BREB method was 20% lower than that by lysimeter measurements in a wheat field in eastern China. The differences between experimental conditions such as irrigation and atmospheric stratification may be the cause of different findings.

Evapotranspiration measured by eddy covariance system was lower than that estimated by BREB method in this area.

It was similar in many studies [37, 44, 46]. By using the data from 4 sets of BREB systems and 3 sets of EC systems in an irrigated spring wheat field, Dugas et al. [16] found that the latent heat flux was underestimated by EC systems and thus the evapotranspiration was underestimated. As discussed above, due to the special environmental conditions as well as the shortage of eddy covariance systems, the turbulent flux was underestimated which led to a lower evapotranspiration.

Evapotranspiration calculated by the BREB method was higher than that estimated by the other two methods. The main reasons for this may be listed as follows.

(1) *Gradient Measurement Errors for BREB Method.* As located in QTP, the observational site got larger solar radiation and wider air temperature variation range. What is more, more precipitation occurred in summer and led to higher soil water content. The atmosphere was in an unstable state and the vertical gradient of the vapor pressure was smaller during daytime. All those factors may lead to higher measurement errors for Bowen ratio system. Meanwhile, for the atmospheric layer was thinner and inverse solar radiation

was smaller on the plateau, the cooling rate was larger at night and in the evening. This led to higher calculated latent and sensible heat fluxes.

(2) *Error Caused by the BREB Basic Assumption.* A basic assumption for BREB was that vapor turbulent exchange coefficient (K_w) was equal to turbulent heat transfer coefficient (K_h), that is, $K_h = K_w$. For underlying surface which was flat, uniform, and stable atmospheric stratification, $K_h \approx K_w$, the error for calculating the evapotranspiration using BREB method was relatively smaller. The air temperature varied violently in sunny days, the convection was obvious during daytime, and the atmosphere was often unstable. All those aspects made it very hard to meet the basic assumption for BREB in QTP.

(3) *The Fluctuation of Bowen Ratio β .* The atmospheric instability on the plateau determined the large fluctuations of Bowen ratio β especially at sunrise (8:00-9:00 in growing season) and sunset (20:00-21:00 in growing season). In this case, the radiation balance and the atmospheric stability were at the negative/positive conversion moment. β value varied around -1 ; LE calculated by BREB method had to be discarded.

5.3. *The Uncertainty in Estimates of Actual Evapotranspiration.* Uncertainty suggests a quantification of the precision of a measurement [47]. There is a growing recognition that more attention needs to be placed on quantifying the uncertainties inherent in the measurements of surface-atmosphere fluxes of carbon and energy at eddy covariance sites [48]. In general, uncertainty sources are classified as either systematic or random [49].

5.3.1. *The Uncertainty Estimation of ML Method.* Lysimeters make direct measurements; therefore a statistical uncertainty analysis should be considered. In this study, root mean square error (RMSE) was taken to evaluate the uncertainty of ML method. The uncertainty was calculated as

$$\text{RMSE} = \sqrt{\frac{1}{n} \sum_{i=1}^n (Z(s) - z(s_i))^2}, \quad (13)$$

where $Z(s)$ is the average value; $z(s_i)$ is the observed value at sampling point s_i ; and n is the number of sample points.

We had 3 sets of micro-lysimeters for the measurement of ET at the experiment site. The results showed that the uncertainty was 15.6 mm at 95% confidence level.

5.3.2. *The Uncertainty Estimation of BREB Method.* Finkelstein and Sims [50] suggested that the random flux measurement error could be characterized if multiple independent observations were made in one place. Hollinger and Richardson [51] developed an alternative method (daily differencing approach) that would enable the estimation of the random uncertainty even when researchers had no second tower. Repeated sampling method [51] was used to calculate the random uncertainty of BREB method in this study. The

random error was quantified in the measured values (x_1, x_2) by determining $\sigma(\delta)$:

$$\sigma(\delta) = \frac{\sigma(x_1, x_2)}{\sqrt{2}}, \quad (14)$$

where x_1 and x_2 are two simultaneous measurements of the same quantity on two successive days and $\sigma(x_1, x_2)$ is the variance of the different measurements.

The estimated random uncertainty of RBEB method was 19.6 mm at 95% confidence level.

5.3.3. *The Uncertainty Estimation of EC Method.* Richardson and Hollinger [52] described a set of methods to quantify the uncertainties in annual net ecosystem exchange (NEE) that were due to both random measurement error and gap filling, including the additional uncertainty that could be attributed to long gaps. Here we used this method to estimate the uncertainty of EC method:

$$\sigma_T(\text{ET}) = \sqrt{\sigma_m^2 + \sigma_g^2}, \quad (15)$$

where σ_T is the total uncertainty and σ_m and σ_g are measurement uncertainty and gap-filling uncertainty, respectively. The detailed calculation of σ_m and σ_g was described in Richardson and Hollinger [52].

The calculated total uncertainty of ET estimated by EC method was 15.1 mm at 95% confidence level.

6. Conclusion

Eddy covariance (EC) technique, Bowen ratio energy balance (BREB) method, and micro-lysimeter (ML) method were used to estimate actual evapotranspiration in alpine meadow in the northeastern edge of Qinghai-Tibet Plateau. The estimated daily results from 3 methods were in a good agreement. The cumulative evapotranspiration estimated by BREB method under no consideration of uncertainty was higher than that estimated by ML method and EC method.

There is still a certain degree of difficulty with accurate measurement of evapotranspiration. The uncertainties of evapotranspiration estimation were calculated by using different methods. Combined with precipitation data, soil moisture conditions, vegetation growth, and other natural conditions over the same period, the evapotranspiration can be determined roughly. During the beginning and end of the observation, the soil water content was nearly the same and no obvious soil water storage or water loss occurred. No surface runoff and no obvious leakage generated during the whole observation period. Furthermore, the vegetation grew well without any irrigation. It inferred that evapotranspiration should be roughly equal to precipitation which was 252 mm during the observation period. Considering the uncertainties, the cumulative evapotranspiration estimated by BREB method, ML method, and EC method was all within a reliable range.

Although evapotranspiration was likely to be underestimated by the eddy covariance method because of the inclosure of the energy balance, the evapotranspiration can

be obtained directly through the latent heat flux from eddy covariance method. Also, long-term and continuous observations for the evapotranspiration in a certain area can be achieved by EC method and this made EC method one of the most important methods to estimate the evapotranspiration. Furthermore, EC method can also be used to determine the CO₂ flux. It has more significance to be used in the grassland regions.

The cost for evapotranspiration by micro-lysimeter method was much lower compared to the other 2 methods. The measurement process was vulnerable to be influenced by manual or natural conditions. Also, heavy labor intensity was always needed. The most obvious disadvantage was that continuous observations were unable to realize by this method.

Compared to the eddy covariance method, Bowen ratio energy balance method had lower equipment costs. Though it usually had a high accuracy for estimating evapotranspiration, BREB method is being replaced by the eddy covariance method.

Conflict of Interests

The authors declare that there is no conflict of interests regarding the publication of this paper.

Acknowledgments

This research was conducted within the Projects of the National Natural Science Foundation of China (nos. 41130638, 41271085), National Scientific and Technological Support Project (2013BAB05B03), and open fund Project of State Key Laboratory of Cryospheric Science (SKLCS-OP-2013-05). The authors are very grateful to the staff who worked in harsh environment for the field observations.

References

- [1] A. Maruyama and T. Kuwagata, "Coupling land surface and crop growth models to estimate the effects of changes in the growing season on energy balance and water use of rice paddies," *Agricultural and Forest Meteorology*, vol. 150, no. 7-8, pp. 919-930, 2010.
- [2] J.-K. Wu, Y.-J. Ding, G.-X. Wang, Y.-P. Shen, Y. Yusuke, and K. Jumpei, "Evapotranspiration of low-lying prairie wetland in middle reaches of heihe river in Northwest China," *Chinese Geographical Science*, vol. 15, no. 4, pp. 325-329, 2005.
- [3] W. Zhao, X. Ji, and H. Liu, "Progresses in evapotranspiration research and prospect in desert oasis evapotranspiration research," *Arid Zone Research*, vol. 28, no. 3, pp. 463-470, 2011.
- [4] S. E. Koch, A. Aksakal, and J. T. McQueen, "The Influence of Mesoscale Humidity and Evapotranspiration Fields on a Model Forecast of a Cold-Frontal Squall Line," *Monthly Weather Review*, vol. 125, no. 3, pp. 384-409, 1997.
- [5] R. J. Donohue, M. L. Roderick, and T. R. McVicar, "On the importance of including vegetation dynamics in Budyko's hydrological model," *Hydrology and Earth System Sciences*, vol. 11, no. 2, pp. 983-995, 2007.
- [6] N. Katerji and G. Rana, "Crop reference evapotranspiration: a discussion of the concept, analysis of the process and validation," *Water Resources Management*, vol. 25, no. 6, pp. 1581-1600, 2011.
- [7] S. Trajkovic, "Testing hourly reference evapotranspiration approaches using lysimeter measurements in a semiarid climate," *Hydrology Research*, vol. 41, no. 1, pp. 38-49, 2010.
- [8] R. C. Beeson Jr., "Weighing lysimeter systems for quantifying water use and studies of controlled water stress for crops grown in low bulk density substrates," *Agricultural Water Management*, vol. 98, no. 6, pp. 967-976, 2011.
- [9] U. K. Schuch and D. W. Burger, "Water use and crop coefficients of woody ornamentals in containers," *Journal of the American Society for Horticultural Science*, vol. 122, no. 5, pp. 727-734, 1997.
- [10] C. Liu, X. Zhang, and Y. Zhang, "Determination of daily evaporation and evapotranspiration of winter wheat and maize by large-scale weighing lysimeter and micro-lysimeter," *Agricultural and Forest Meteorology*, vol. 111, no. 2, pp. 109-120, 2002.
- [11] M. G. McKeon, D. C. Joyce, and R. H. Frith, "A compact and inexpensive mobile weighing device for water relations studies of container-grown trees," *Australian Journal of Botany*, vol. 56, no. 6, pp. 535-538, 2008.
- [12] J. J. S. Owen, S. L. Warren, and T. E. Bilderback, "A gravimetric approach to real-time monitoring of substrate wetness in container grown nursery crops," *Acta Horticulturae*, vol. 819, pp. 317-324, 2009.
- [13] Y. Wang, X. Wang, Q. Zheng, C. Li, and X. Guo, "A comparative study on hourly real evapotranspiration and potential evapotranspiration during different vegetation growth stages in the Zoige Wetland," *Procedia Environmental Sciences*, vol. 13, pp. 1585-1594, 2012.
- [14] V. R. N. Pauwels and R. Samson, "Comparison of different methods to measure and model actual evapotranspiration rates for a wet sloping grassland," *Agricultural Water Management*, vol. 82, no. 1-2, pp. 1-24, 2006.
- [15] A. G. Barr, K. M. King, T. J. Gillespie, G. den Hartog, and H. H. Neumann, "A comparison of Bowen ratio and eddy correlation sensible and latent heat flux measurements above deciduous forest," *Boundary-Layer Meteorology*, vol. 71, no. 1-2, pp. 21-41, 1994.
- [16] W. A. Dugas, L. J. Fritschen, L. W. Gay et al., "Bowen ratio, eddy correlation, and portable chamber measurements of sensible and latent heat flux over irrigated spring wheat," *Agricultural and Forest Meteorology*, vol. 56, no. 1-2, pp. 1-20, 1991.
- [17] H. E. Unland, P. R. Houser, W. J. Shuttleworth, and Z.-L. Yang, "Surface flux measurement and modeling at a semi-arid Sonoran Desert site," *Agricultural and Forest Meteorology*, vol. 82, no. 1-4, pp. 119-153, 1996.
- [18] T. E. Twine, W. P. Kustas, J. M. Norman et al., "Correcting eddy-covariance flux underestimates over a grassland," *Agricultural and Forest Meteorology*, vol. 103, no. 3, pp. 279-300, 2000.
- [19] T. Yao, L. Thompson, W. Yang et al., "Different glacier status with atmospheric circulations in Tibetan Plateau and surroundings," *Nature Climate Change*, vol. 2, no. 9, pp. 663-667, 2012.
- [20] S. Zhou, P. Wu, C. Wang, and J. Han, "Spatial distribution of atmospheric water vapor and its relationship with precipitation in summer over the Tibetan Plateau," *Acta Geographica Sinica*, vol. 66, no. 11, pp. 1466-1478, 2011.
- [21] X. Zhang and M. Yang, "Evapotranspiration in the tibetan plateau based on GAME-Tibet IOP data," *Scientia Geographica Sinica*, vol. 30, no. 6, pp. 929-935, 2010.

- [22] Y. Sheng, J. Li, J.-C. Wu, B.-S. Ye, and J. Wang, "Distribution patterns of permafrost in the upper area of Shule River with the application of GIS technique," *Journal of China University of Mining and Technology*, vol. 39, no. 1, pp. 32–39, 2010.
- [23] W. Liu, S. Chen, X. Qin et al., "Storage, patterns, and control of soil organic carbon and nitrogen in the northeastern margin of the Qinghai-Tibetan Plateau," *Environmental Research Letters*, vol. 7, no. 3, Article ID 035401, 2012.
- [24] X. Xie, G. J. Yang, Z.-R. Wang, and J. Wang, "Landscape pattern change in mountainous areas along an altitude gradient in the upper reaches of Shule River," *Chinese Journal of Ecology*, vol. 29, no. 7, pp. 1420–1426, 2010.
- [25] S. Yi, Z. Zhou, S. Ren et al., "Effects of permafrost degradation on alpine grassland in a semi-arid basin on the Qinghai-Tibetan Plateau," *Environmental Research Letters*, vol. 6, no. 4, Article ID 045403, pp. 454–457, 2011.
- [26] Y. Qin and S. Yi, "Diurnal characteristics of ecosystem respiration of alpine meadow on the Qinghai-Tibetan plateau: implications for carbon budget estimation," *The Scientific World Journal*, vol. 2013, Article ID 289754, 5 pages, 2013.
- [27] X. Lee, W. J. Massman, and B. E. Law, *Handbook of Micrometeorology: A Guide for Surface Flux Measurements*, Kluwer Academic Publishers, Dordrecht, The Netherlands, 2004.
- [28] D. Papale, M. Reichstein, M. Aubinet et al., "Towards a standardized processing of net ecosystem exchange measured with eddy covariance technique: algorithms and uncertainty estimation," *Biogeosciences*, vol. 3, no. 4, pp. 571–583, 2006.
- [29] E. Falge, D. Baldocchi, R. Olson et al., "Gap filling strategies for defensible annual sums of net ecosystem exchange," *Agricultural and Forest Meteorology*, vol. 107, no. 1, pp. 43–69, 2001.
- [30] S. B. Verma, D. D. Baldocchi, D. E. Anderson, D. R. Matt, and R. J. Clement, "Eddy fluxes of CO₂, water vapor, and sensible heat over a deciduous forest," *Boundary-Layer Meteorology*, vol. 36, no. 1-2, pp. 71–91, 1986.
- [31] L. Mahrt, "Flux sampling errors for aircraft and towers," *Journal of Atmospheric and Oceanic Technology*, vol. 15, no. 2, pp. 416–429, 1998.
- [32] E. L. Andreas and B. A. Cash, "A new formulation for the Bowen ratio over saturated surfaces," *Journal of Applied Meteorology*, vol. 35, no. 8, pp. 1279–1289, 1996.
- [33] K. Wilson, A. Goldstein, E. Falge et al., "Energy balance closure at FLUXNET sites," *Agricultural and Forest Meteorology*, vol. 113, no. 1-4, pp. 223–243, 2002.
- [34] Y. Ma and Z. Xu, "The physical characteristics of atmosphere in Qinghai-Tibet plateau," *Acta Meteorologica Sinica*, vol. 45, no. 2, pp. 210–217, 1987.
- [35] H. J. H. Franssen, R. Stöckli, I. Lehner, E. Rotenberg, and S. I. Seneviratne, "Energy balance closure of eddy-covariance data: a multisite analysis for European FLUXNET stations," *Agricultural and Forest Meteorology*, vol. 150, no. 12, pp. 1553–1567, 2010.
- [36] Z. Li, G. Yu, X. Wen, L. Zhang, C. Ren, and Y. Fu, "Energy balance closure at ChinaFLUX sites," *Science in China, Series D: Earth Sciences*, vol. 48, no. 1, pp. 51–62, 2005.
- [37] P.-T. Qi, S. Gu, Y.-H. Tang, M.-Y. Du, L.-B. Wu, and L. Zhao, "Comparison of three methods for measurement of evapotranspiration in an alpine meadow," *Acta Ecologica Sinica*, vol. 28, no. 1, pp. 202–211, 2008.
- [38] S. Gu, Y. Tang, X. Cui et al., "Energy exchange between the atmosphere and a meadow ecosystem on the Qinghai-Tibetan Plateau," *Agricultural and Forest Meteorology*, vol. 129, no. 3-4, pp. 175–185, 2005.
- [39] Q. Li, X.-Z. Zhang, P.-L. Shi, Y.-T. He, L.-L. Xu, and W. Sun, "Study on the energy balance closure of alpine meadow on Tibetan Plateau," *Journal of Natural Resources*, vol. 23, no. 3, pp. 391–399, 2008.
- [40] B. R. Reverter, A. Carrara, A. Fernández et al., "Adjustment of annual NEE and ET for the open-path IRGA self-heating correction: magnitude and approximation over a range of climate," *Agricultural and Forest Meteorology*, vol. 151, no. 12, pp. 1856–1861, 2011.
- [41] G. G. Burba, D. K. McDermitt, A. Grelle, D. J. Anderson, and L. Xu, "Addressing the influence of instrument surface heat exchange on the measurements of CO₂ flux from open-path gas analyzers," *Global Change Biology*, vol. 14, no. 8, pp. 1854–1876, 2008.
- [42] X. Ji, W. Zhao, E. Kang et al., "Effect of the instrument surface heating on CO₂ flux from open-path eddy covariance system at Linze Station," *Plateau Meteorology*, vol. 32, no. 1, pp. 65–77, 2013.
- [43] Q. Zhang, Z. Zhang, X. Wen et al., "Comparisons of observational methods of land surface evapotranspiration and their influence factors," *Advances in Earth Science*, vol. 26, no. 5, pp. 538–547, 2011.
- [44] X. Qiang, H. Cai, and J. Wang, "Comparative study of crop evapotranspiration measured by Bowen ratio and lysimeter," *Transactions of the Chinese Society of Agricultural Engineering*, vol. 25, no. 2, pp. 12–17, 2009.
- [45] Z. Zhu, "Comparative study of crop evapotranspiration measured by Bowen ratio energy balance method and lysimeter," in *Crop Evapotranspiration*, D. Zuo and X. Xie, Eds., pp. 71–79, Meteorological Press, Beijing, China, 1991.
- [46] B. L. Blad and N. J. Rosenberg, "Lysimetric calibration of the Bowen ratio energy balance method for evapotranspiration estimation in the central great plains," *Journal of Applied Meteorology*, vol. 13, no. 2, pp. 227–236, 1974.
- [47] D. P. Billesbach, "Estimating uncertainties in individual eddy covariance flux measurements: a comparison of methods and a proposed new method," *Agricultural and Forest Meteorology*, vol. 151, no. 3, pp. 394–405, 2011.
- [48] A. D. Richardson, D. Y. Hollinger, G. G. Burba et al., "A multi-site analysis of random error in tower-based measurements of carbon and energy fluxes," *Agricultural and Forest Meteorology*, vol. 136, no. 1-2, pp. 1–18, 2006.
- [49] G. Lasslop, M. Reichstein, J. Kattge, and D. Papale, "Influences of observation errors in eddy flux data on inverse model parameter estimation," *Biogeosciences*, vol. 5, no. 5, pp. 1311–1324, 2008.
- [50] P. L. Finkelstein and P. F. Sims, "Sampling error in eddy correlation flux measurements," *Journal of Geophysical Research D: Atmospheres*, vol. 106, no. 4, pp. 3503–3509, 2001.
- [51] D. Y. Hollinger and A. D. Richardson, "Uncertainty in eddy covariance measurements and its application to physiological models," *Tree Physiology*, vol. 25, no. 7, pp. 873–885, 2005.
- [52] A. D. Richardson and D. Y. Hollinger, "A method to estimate the additional uncertainty in gap-filled NEE resulting from long gaps in the CO₂ flux record," *Agricultural and Forest Meteorology*, vol. 147, no. 3-4, pp. 199–208, 2007.

Research Article

Surface Albedo Variation and Its Influencing Factors over Dongkemadi Glacier, Central Tibetan Plateau

Jie Wang,¹ Yuhuan Cui,² Xiaobo He,³ Jian Zhang,³ and Shijiang Yan¹

¹*School of Resources and Environmental Engineering, Anhui University, Hefei 230601, China*

²*School of Science, Anhui Agriculture University, Hefei 230601, China*

³*State Key Laboratory of Cryospheric Sciences, Cold and Arid Regions Environmental and Engineering Research Institute, Chinese Academy of Sciences, Lanzhou 730000, China*

Correspondence should be addressed to Yuhuan Cui; cuiyh@lzb.ac.cn

Received 6 January 2015; Accepted 16 March 2015

Academic Editor: Sven-Erik Gryning

Copyright © 2015 Jie Wang et al. This is an open access article distributed under the Creative Commons Attribution License, which permits unrestricted use, distribution, and reproduction in any medium, provided the original work is properly cited.

Glacier albedo plays a critical role in surface-atmosphere energy exchange, the variability of which influences glacier mass balance as well as water resources. Dongkemadi glacier in central Tibetan Plateau was selected as study area; this research used field measurements to verify Landsat TM-derived albedo and MOD10A1 albedo product and then analyzed the spatiotemporal variability of albedo over the glacier according to them, as well as its influence factors and the relationship with glacier mass balance. The spatial distribution of glacier albedo in winter did not vary with altitude and was determined by terrain shield, whereas, in summer, albedo increased with altitude and was only influenced by terrain shield at accumulation zone. During 2000–2009, albedo in summer decreased at a rate of 0.0052 per year and was influenced by air temperature and precipitation levels, whereas albedo in winter increased at a rate of 0.0045 per year, influenced by the level and frequency of precipitation. The annual variation of albedo in summer during 2000–2012 has the high relative to that of glacier mass balance measurement, which indicates that glacier albedo in the ablation period can be considered as a proxy for glacier mass balance.

1. Introduction

Ice and snow melting is the primary source of water for the inland rivers of western China, and the increased melting of ice and snow is contributing to sea level rise [1]. It is therefore very important to conduct research on glacier mass balance. Under continental climate conditions, glacier mass balance is influenced by surface energy balance processes during the ablation period, and solar radiation provides the primary energy source for glacier melting [2]. Albedo determines the amount of solar radiation energy absorbed by the glacier surface, so it is the key parameter in glacier energy balance models and hydrological models for cold and arid regions. Even small changes in regional climate can cause marked variations of glacier albedo and consequently affect energy balance processes over entire glaciers [3]. Glacier albedo therefore plays a crucial role in glacier mass balance, and variations in albedo caused by changes in climate, as well as

aerosols (e.g., black carbon), could change the rate of ice and snow melting, consequently affecting glacier runoff.

In the past, glacier albedo was measured using instruments placed on the glacier, including automatic weather stations (AWS) [4–8] and portable albedometers [2, 9, 10]. Because of the spatiotemporal variability of glacier albedo, measurements from limited points cannot reflect the variability of albedo over entire glaciers for long period. However, ground-based measurements do provide accurate datasets with high temporal resolution and still have a place in glacial research today.

Satellite-based remote sensing systems can acquire images of entire glaciers at regular intervals over time and are valuable for research into the variation of glacier albedo on a broader spatiotemporal scale [11]. Landsat thematic mapper (TM) data, with a high resolution of 30 meters, have been used to investigate the spatial variation of albedo on single glaciers and ice caps [2, 12, 13]. Landsat TM-derived albedos

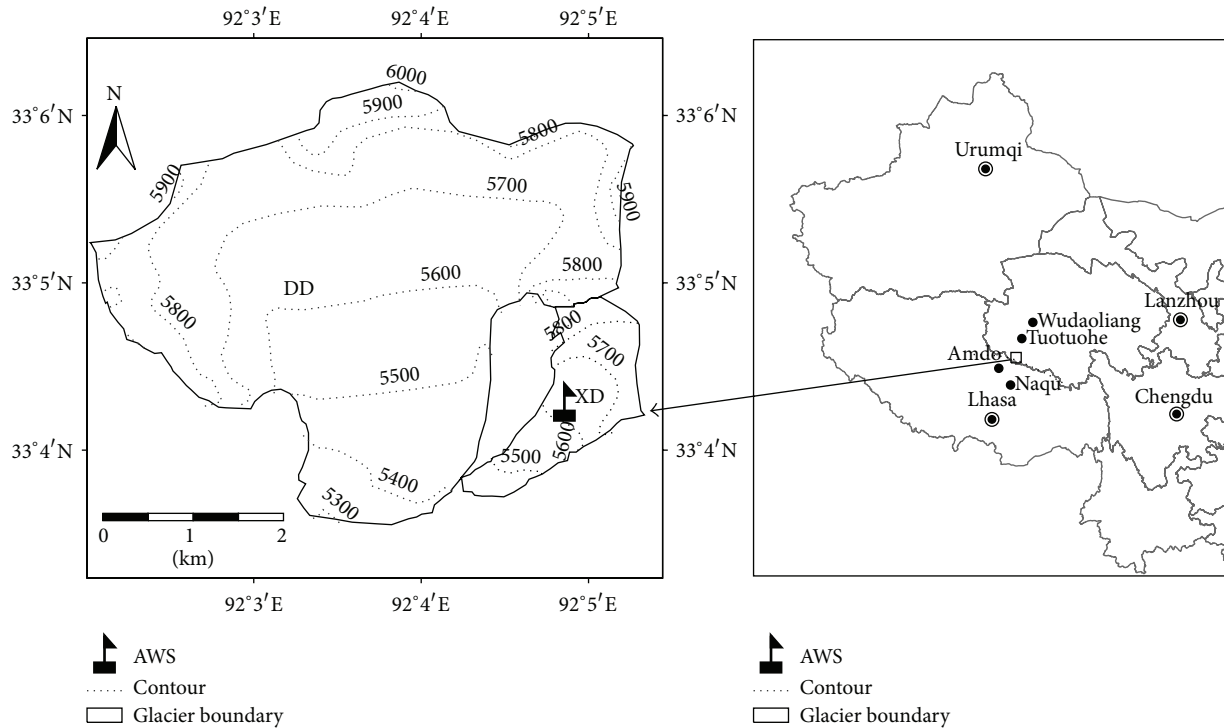


FIGURE 1: The location map of Dongkemadi glacier, indicating the AWS on the glacier and four national weather stations nearby.

have also been incorporated into a distributed mass balance model to calculate mass loss for six glaciers in the European Alps [14]. The high temporal resolution Moderate Resolution Imaging Spectroradiometer (MODIS) albedo product was used to estimate annual anomalies in the surface mass balance of 18 glaciers on Svalbard for the period 2000–2005 [15]. However, there are limitations to the use of remote sensing systems for measuring glacier albedo because the sensors may not be able to acquire data through cloud cover, and data retrieval methods are still being refined. Therefore, it is important to combine ground-based measurements with remote sensing methods for research into the variation of glacier albedo.

The Dongkemadi glacier in the Tanggula Mountains of the central Tibetan Plateau was selected as our study area. We used field measurements on the glacier to verify the accuracy of TM-derived albedo and the beta-test MODIS (MOD10A1) daily albedo product firstly. We then investigated the spatial variation of albedo over the glacier using high spatial resolution TM-derived albedo data and studied the temporal variation of glacier albedo during 2000–2009 using the high temporal resolution MOD10A1 daily albedo product. Lastly, the key factors that affect variation characters of glacier albedo and the influence of glacier albedo on glacier mass balance were further investigated in our research.

2. Materials and Methods

2.1. Study Area. The Dongkemadi glacier in the Tanggula Mountains was selected as a representative glacier in a region

with a semiarid climate. It is a composite glacier formed by the convergence of a trunk glacier stretching southward and a tributary glacier extending toward the southwest (Figure 1). The trunk glacier, named Da Dongkemadi (DD), covers an area of 14.63 km^2 , has a length of 5.4 km, a terminal altitude of 5275 m, an average equilibrium line altitude of 5600 m, and a smooth, even surface. The tributary glacier, named Xiao Dongkemadi (XD), covers an area of 1.77 km^2 , is 2.8 km long and 5926 m high at its peak, has an average equilibrium line altitude of 5620 m, and also has a gently sloping, clean surface without surface moraines [16].

The Dongkemadi is classified as a subcontinental glacier [17], and the annual average temperature and precipitation levels are around -8.4°C and 659 mm, respectively. One mass balance year can be divided into two periods: the summer season and the winter season. During the summer season, from May to September, the glacier is under the control of the Indian monsoon, with warm temperatures and high precipitation. During the winter season, from October to April, the weather is under the control of the Westerly Circulation and is sunny, dry, and cold [18].

2.2. Field Observation. In August 2007, an AWS was installed at $33^\circ 04' 14.24''\text{N}$, $92^\circ 04' 53.41''\text{E}$, and 5620 m a.s.l. near the equilibrium line of Xiao Dongkemadi glacier. The AWS was equipped with sensors for temperature, air pressure, humidity, wind speed, and wind direction. It was also equipped with a net radiometer (with upward- and downward-facing pyranometers), and the recording interval was set at 10 min.

TABLE 1: The difference between TM-derived albedo and AWS-measured albedo.

Date acquired	Path/row	TM-derived values	Measured values	Bias
2008-2-2	137/37	0.6283	0.6705	-0.0422
2008-3-5	137/37	0.8308	0.8507	-0.0199
2008-6-16	138/37	0.6613	0.6231	0.0382
2008-10-22	138/37	0.8217	0.7596	0.0670
2008-10-31	137/37	0.6737	0.6383	0.0354
2008-11-16	137/37	0.7113	0.6877	0.0236
2008-11-23	138/37	0.7713	0.7159	0.0554
2008-12-9	138/37	0.6730	0.6628	0.0101
2009-3-8	137/37	0.6538	0.5885	0.0653
2009-4-16	138/37	0.7096	0.6695	0.0400
2009-4-25	137/37	0.6866	0.6497	0.0369
2009-5-2	138/37	0.6211	0.5469	0.0743
2009-5-18	138/37	0.6750	0.7182	-0.0431
2009-8-31	137/37	0.5418	0.5425	-0.0007

The solar radiation flux measured by the net radiometer was used to calculate the surface albedo at the AWS location, and the distance between the net radiometer and the glacier surface remained close to 1.2 m throughout the ablation period.

2.3. Validation of Remote Sensing Albedo Products

2.3.1. TM-Derived Albedo. Landsat TM images have the advantage of high spatial resolution in the shortwave range of 0.3–4.0 μm [19–21]. Therefore TM-derived albedo data can be used to analyze the spatial distribution of albedo over entire glaciers. The process of deriving albedo data from the original images consists of four steps: radiometric calibration, topographic correction, atmospheric correction, and narrowband to broadband conversion. For the last step, the formula developed by Knap et al. [11] is used:

$$\alpha_{\text{short}} = 0.726 * \alpha_2 - 0.322 * \alpha_2^2 - 0.051 * \alpha_4 + 0.581 * \alpha_4^2. \quad (1)$$

Here, α_{short} represents the shortwave albedo and α_2 and α_4 represent the spectral albedo in bands TM 2 and TM 4, respectively.

To verify the accuracy of the above method for retrieving albedo from Landsat TM images, 14 Landsat ETM+ scenes, all acquired around noon and covering the entire glacier, were downloaded from the USGS website (<http://glovis.usgs.gov/>) during 2008–2009. Shortwave albedo images were retrieved from the downloaded ETM+ scenes according to the above method, and the results were compared with noontime AWS-measured albedo values by extracting pixel values at the AWS location. Results are shown in Table 1.

The difference between the albedo values retrieved from Landsat TM images (TM-derived albedo) and AWS-measured values ranged from -0.05 to 0.07 (average error (AE) = 0.024, RMSE = 0.046, and $R^2 = 0.74$). The discrepancy

was mainly a result of the atmospheric correction process because, to account for the lack of actual atmospheric parameters when the Landsat TM images were acquired, we used a standard atmospheric model proposed by the 6S code (the middle latitude summer/winter model) to estimate atmospheric effects (gaseous absorption by water vapor, carbon dioxide, oxygen, and ozone, and scattering by molecules and aerosols). For use in climate models, the accuracy of surface albedo needs to be ± 0.05 [22]. Therefore, we found that albedo results retrieved from TM images were accurate enough to be used for research on the spatial variation of albedo.

2.3.2. MOD10A1 Daily Albedo Product. Since February 2000, the MOD10A1 daily product, with a spatial resolution of 500 m, has been distributed by the National Snow and Ice Data Center (NSIDC). The product generates valid shortwave albedo values when a pixel is covered by ice or snow and is cloud-free [8]. Compared with the MCD43A3 albedo product that contains 16 d of data, the daily MOD10A1 product has the advantage of higher temporal resolution. However, the MOD10A1 daily albedo product is a beta-test product and may contain unsubstantiated errors, especially in output from mountainous regions. It was therefore necessary to verify the product's accuracy over the Dongkemadi glacier.

To account for spatial heterogeneity on the glacier surface, we used spatial scaling transformation technology to upscale high resolution images to moderate resolution, as described by Liang et al. [23]. To determine the accuracy of the MOD10A1 daily albedo product, TM-derived albedo data were first calibrated using ground-based measurements and then aggregated to the MODIS resolution (Figure 2(a)). The difference between calibrated TM-derived albedo and the MOD10A1 daily albedo product is shown in Figure 2(b). The average error was less than 0.05 (AE = 0.019, RMSE = 0.05, $R^2 = 0.67$), and the correlation coefficient was higher than 0.8, so the MOD10A1 albedo product was also accurate

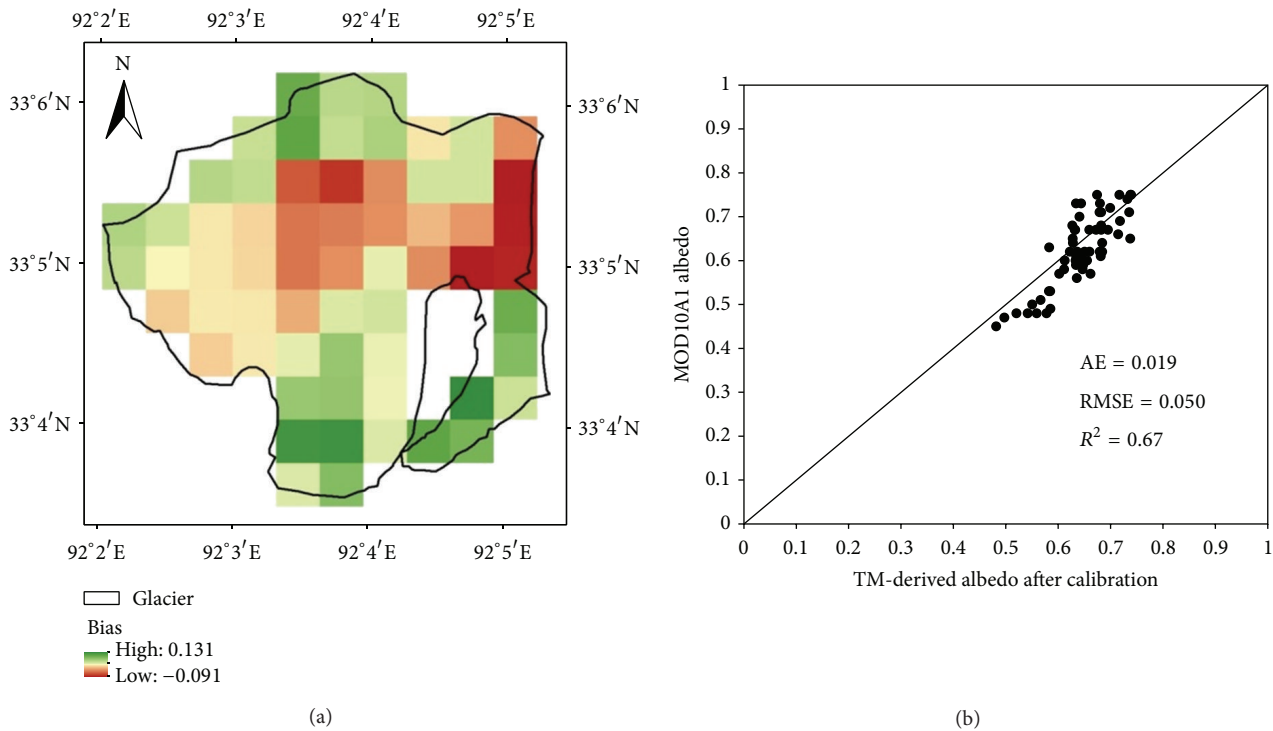


FIGURE 2: Comparison between calibrated TM-derived albedo and MOD10A1 albedo. (a) The difference; (b) the scatter diagram (date acquired: 2007-4-28).

enough to be used for research on the variation of glacier albedo.

3. Results

3.1. Spatial Variation of Albedo on the Dongkemadi Glacier. Field measurements show that albedo at single points on a glacier changes constantly over time, and this underlies the variation in spatial distribution of albedo over an entire glacier in one year. To investigate the spatial distribution of albedo on the Dongkemadi glacier over one year, we acquired six Landsat TM scenes between October 2006 and September 2007 (three winter scenes and three summer scenes). The glacier albedo was retrieved from the images using the method described in Section 2.3.1, and the retrieved albedo values were divided into four levels (0.0–0.3, 0.3–0.5, 0.5–0.7, and 0.7–1.0) (Figure 3).

Figure 3 shows that the spatial distribution of albedo on the Dongkemadi glacier varied markedly in one mass balance year, and the variation was more complex over the lower part of the glacier than the upper.

In early winter (2006-10-2), the albedo of the glacier did not vary obviously with altitude, with most values between 0.7 and 0.8, because fresh snow covers the glacier surface at this time of year. There were several albedo values less than 0.7 recorded at high altitude and at the terminal end of the glacier, caused by terrain shield and slight subglacial melting, respectively. In midwinter (2006-12-5), glacier albedo values

were similar to those recorded in early winter, and again values did not vary obviously with altitude. Most values were higher than 0.7, and the low albedo values observed were caused by terrain shield. Compared with October, the albedo values did decrease slightly with altitude because the snowpack becomes older with less snowfall. In late winter (2007-4-28), glacier albedo was lower across the entire surface, but, with most values between 0.5 and 0.7, variation with altitude was still not obvious.

In early summer (2007-6-22), glacier albedo was only slightly lower than in late winter, with values between 0.5 and 0.7, and there was little variation with altitude. In midsummer (2007-8-2), glacier albedo values were lower across the entire glacier, but values were clearly related to altitude. Values were higher than 0.5 above 5650 m a.s.l. and lower than 0.3 below 5580 m a.s.l.; spatial variation in the upper glacier was caused by terrain shield. Spatial variation was also obvious in late summer (2007-9-19), with values higher than 0.7 above 5500 m a.s.l. and lower than 0.5 below 5350 m a.s.l., and albedo also increased with altitude over the lower glacier.

3.2. Annual Variation of Albedo on the Dongkemadi Glacier. It is difficult to conduct field observations on glaciers, and it is therefore difficult to obtain ground-based albedo datasets on glaciers over long period. The long-term albedo datasets provided by the MOD10A1 product make it possible to investigate the annual variation of glacier albedo. We studied the annual variation of albedo on the Dongkemadi glacier

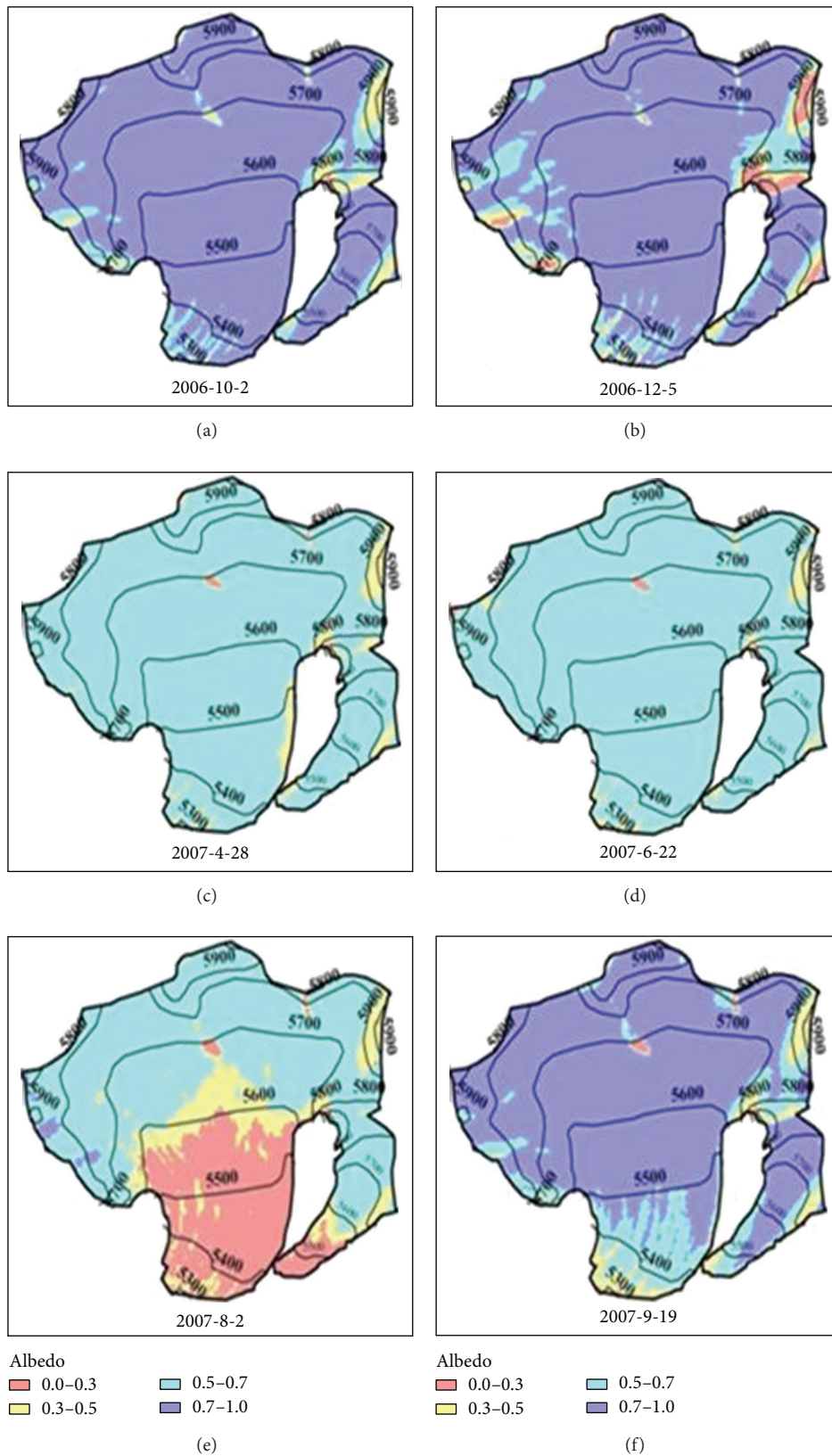


FIGURE 3: The spatial distribution of albedo on the Dongkemadi glacier in one mass balance year from October 2006 to September 2007. Where the solid lines represent the contour lines, and the numbers represent the altitude values of the contour lines (units: meters a.s.l.).

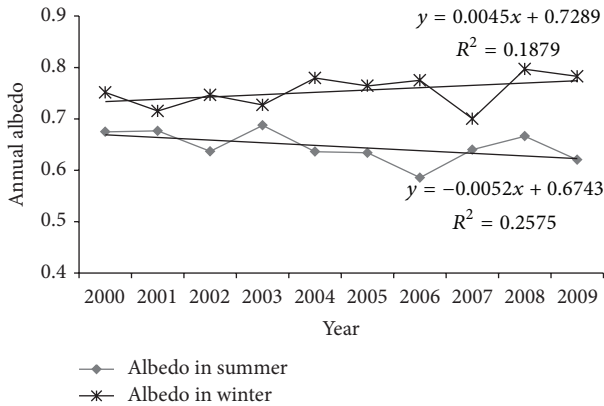


FIGURE 4: Annual variation of albedo on the Dongkemadi glacier from 2000 to 2009.

over the last decade using MOD10A1 daily albedo products from 2000–2009 and also analyzed the influence of climate change (air temperature and precipitation) on the annual variation of albedo.

Variations in albedo differ across the year; therefore, we divided one mass balance year into summer and winter periods as described above. The annual variation of glacier albedo during these two periods is shown in Figure 4. The figure shows that the annual variation of glacier albedo for the summer period between 2000 and 2009 decreased at a rate of 0.0052 per year, while the variation for the winter period over the same period increased slightly at a rate of 0.0045 per year.

4. Discussion

4.1. Influence of Terrain Factors on Spatial Variation of Glacier Albedo. The above results in Section 3.1 showed that the spatial distribution of glacier albedo varied obviously in a mass balance year, using TM-derived albedo datasets. In order to analyze the influence of terrain factors on spatial variation of Glacier albedo, this research divided the glacier into several altitude zones at 50 m intervals using ASTER GDEM with the resolution of 30 meters; then albedo variations with altitude for the different seasons are analyzed in Figure 5.

Figure 5 shows that glacier albedo increases with altitude generally in the ablation period (2007-8-2, 2007-9-19) and displaying a steep gradient in the center of the glacier, relatively constant above certain altitudes, while glacier albedo in the accumulation period (2006-10-2, 2006-12-5, 2007-10-28) presents a fluctuation around the constant values, not relatively to altitude.

Aim to further study on the reason for the fluctuation at the accumulation zone (the part above annual equilibrium line altitude), terrain shield, represents the influence of rugged terrain on sunshine hours, was introduced into our research, and was calculated by ArcGIS software using solar incident angle and Aster GDEM [24, 25]. The glacier was also divided into several terrain shield zones at 0.1 intervals. Figure 6 shows albedo variations with terrain shield for the

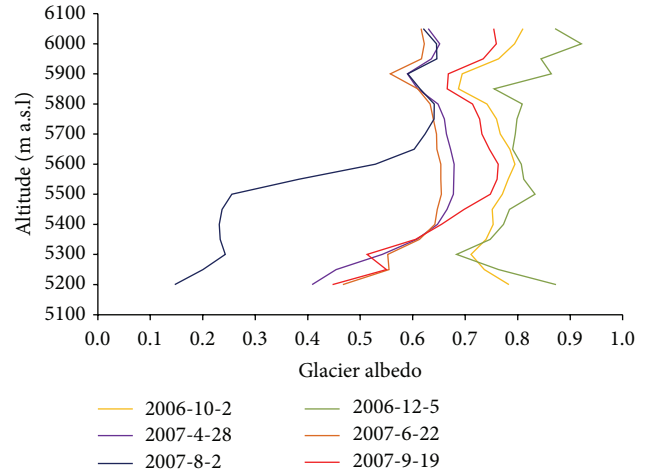


FIGURE 5: Albedo variations with altitude for the different seasons in the period of 2006-2007.

accumulation zone and the ablation zone (the part below annual equilibrium line altitude) on the different months in 2006-2007. From the figure, it can be seen that glacier albedo decreases with terrain shield in accumulation zone, while that in ablation zone is not obvious. The above results indicated that glacier albedo varied little with altitude at the accumulation zone, and terrain shield was the main factor underlying spatial variation. However, glacier albedo clearly increased with altitude at the ablation zone, and terrain shield again influenced the spatial distribution of albedo.

4.2. Annual Variation of Glacier Albedo Responses to Climate Change. Air temperature and precipitation are the main factors controlling the glacier mass balance. The temporal variation of albedo on glaciers is mainly affected by air temperature, snowfall, and the black carbon content in the snow pack [9, 26].

In our study, air temperature and precipitation for the Dongkemadi glacier during 2000–2009 were rebuilt using the datasets from four nearby national weather stations (Amdo, Wudaoliang, Tuotuohe, and Nakchu, shown in Figure 1), based on the relationships of air temperature, precipitation between AWS on the glacier and these four national weather stations as described by Gao et al. [27]. Annual variation of glacier albedo was displayed based on the long-term albedo datasets provided by MOD10A1 daily product in the period of 2000–2009.

The annual variations of air temperature, precipitation levels, frequency of precipitation, and glacier albedo in summer and winter are shown in Figures 7 and 8, respectively. The figures show that annual variation of glacier albedo in summer from 2000 to 2009 followed an opposite trend to that of air temperature and a similar trend to that of precipitation levels, but there was no obvious relationship to the frequency of precipitation. The annual variation of glacier albedo in winter from 2000 to 2009 followed a similar trend to precipitation levels and frequency of precipitation,

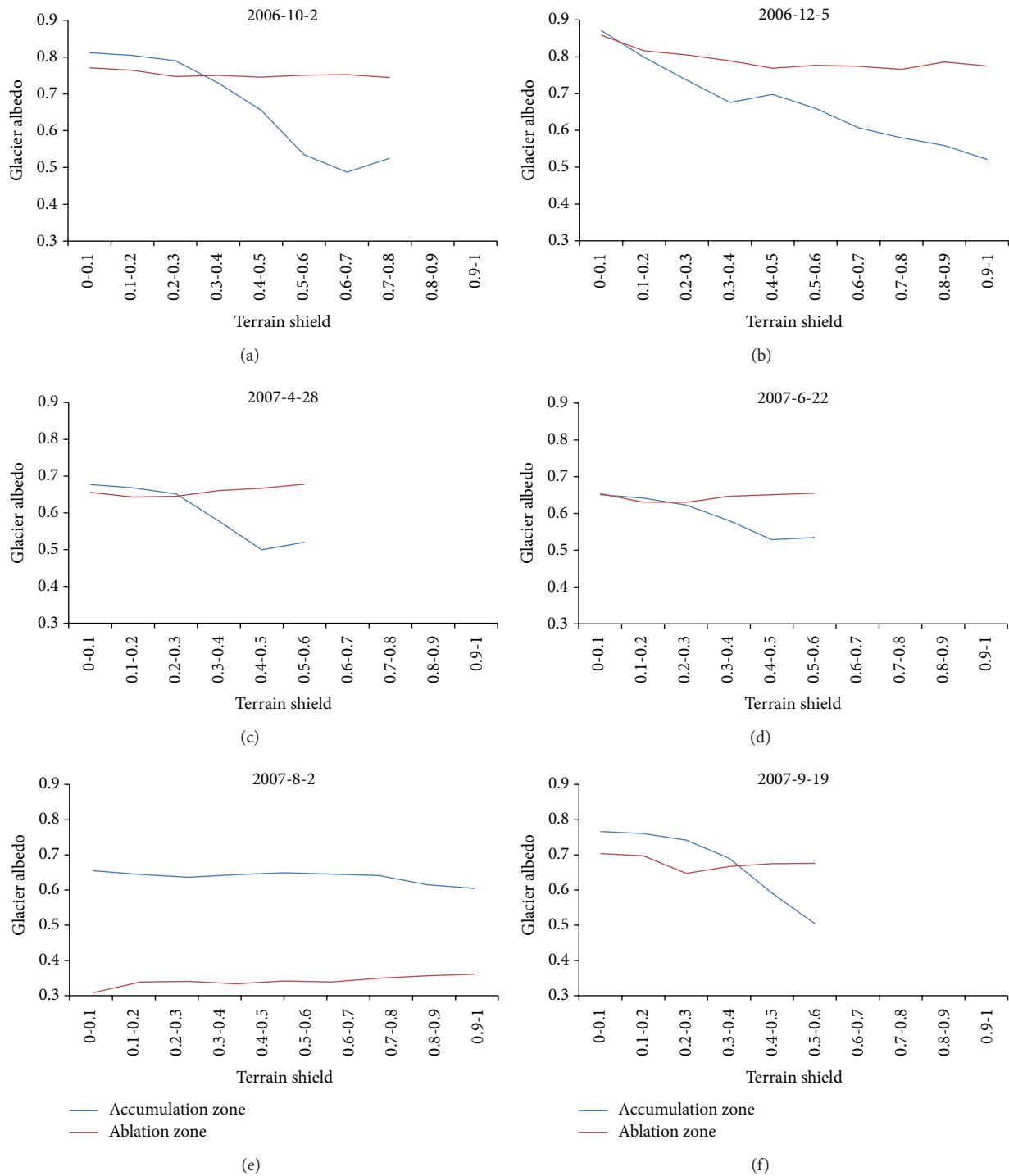


FIGURE 6: Albedo variations with terrain shield for the accumulation zone and ablation zone on the different months in 2006-2007.

but there was no obvious relationship to air temperature. These results suggest that the annual variation of albedo in summer is influenced by annual changes in air temperature and precipitation levels, while in winter the variation is influenced by the annual change of precipitation levels and the frequency of precipitation.

4.3. Influence of Glacier Albedo on Glacier Mass Balance. As the controlling factor in energy budget on land surface, glacier albedo at the ablation period influences the snow/ice melt rate and then influences glacier mass balance [26, 28]. Aiming at investigating the influence of glacier albedo on glacier mass balance, we compare the averaged glacier albedo

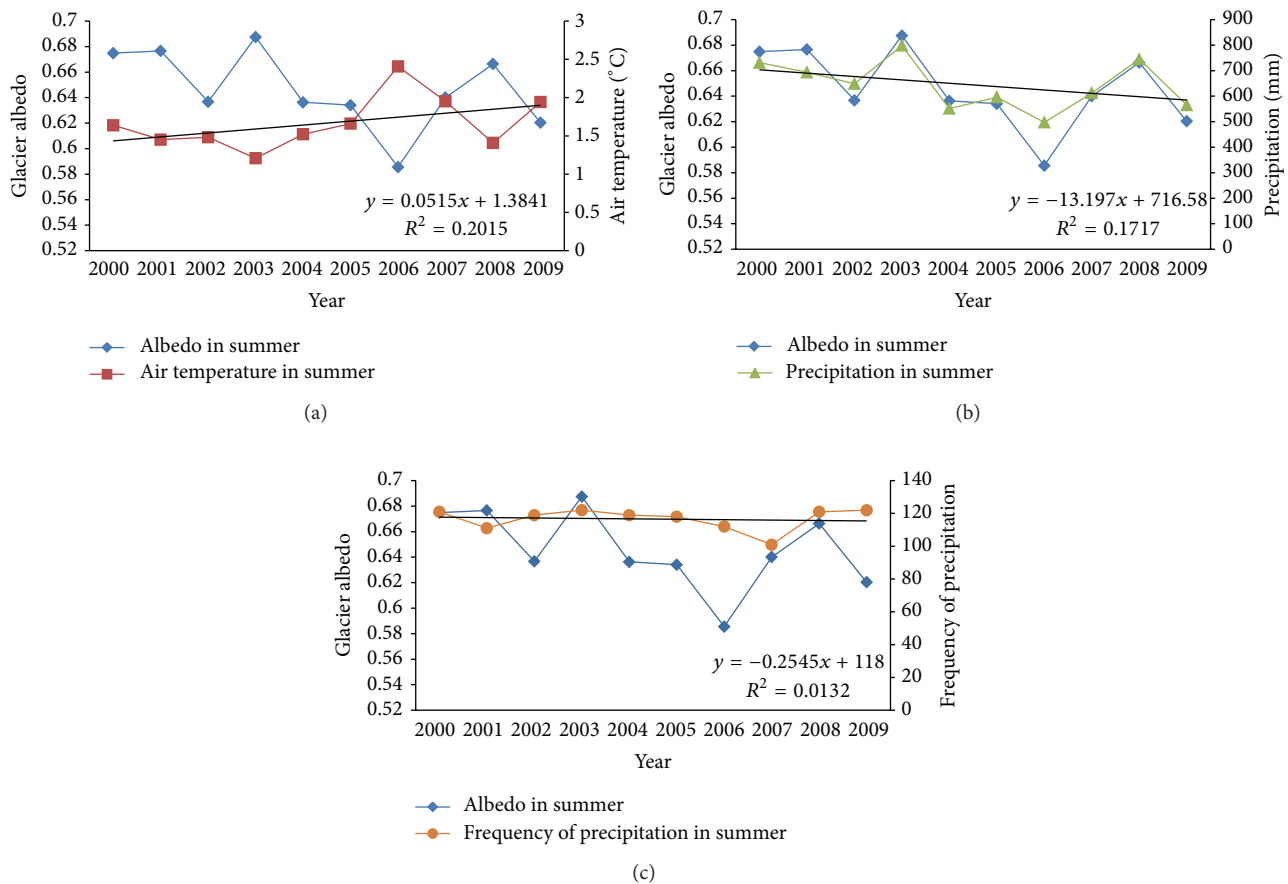


FIGURE 7: Annual variations of glacier albedo and meteorological factors in summer during 2000–2009. (a) Air temperature. (b) Precipitation levels. (c) Frequency of precipitation.

in summer to annual mass balance measured by the stakes located on the glacier (shown as Figure 9). Annual variation of glacier albedo was displayed based on the albedo datasets provided by MOD10A1 daily product during the period of 2000–2012.

As shown in Figure 9, the annual variation of albedo in summer was high relative to that of glacier mass balance ($r = 0.85$, $P < 0.05$). The compared result indicates that glacier albedo in summer can be considered as a proxy for glacier mass balance, so glacier albedo from the remote-sensing products can be used to monitor the trend of glacier mass balance over a long period.

5. Conclusions

Monitoring the variations of mass balance on the glaciers in western China is an important task of the glaciological community. Glacier albedo has a dominant impact on simulating the mass balance of glaciers, as well as on meltwater resources. In this study, we validated the effectiveness of two remote sensing products, Landsat TM-derived albedo and the MOD10A1 albedo product. We then analyzed the spatial variation of albedo on the Dongkemadi glacier in one mass

balance year and investigated the factors influencing this variation. We also investigated annual variation of albedo on the Dongkemadi glacier in the last decade and analyzed its influencing factors and the relationship with glacier mass balance.

Both TM-derived albedo and the MOD10A1 albedo product used on the Dongkemadi glacier have reasonable accuracy (RMSE = 0.046, $R^2 = 0.74$, and RMSE = 0.050, $R^2 = 0.67$, resp.), and they can therefore be used for research on the variation of glacier albedo. The spatial distribution of glacier albedo in the accumulation period did not vary obviously with altitude and was influenced by terrain shield while in summer albedo increased with altitude and was influenced by terrain shield at the accumulation zone.

During the period 2000–2009, annual variation of albedo in the ablation period decreased at a rate of 0.0052 per year and was related to the annual change in air temperature and precipitation levels, while the annual variation of albedo in the accumulation period increased at a rate of 0.0045 per year and was influenced by the annual change in precipitation levels and the frequency of precipitation. The annual variation of albedo in summer was high relative to that of glacier mass balance measurement, which indicates that glacier albedo in

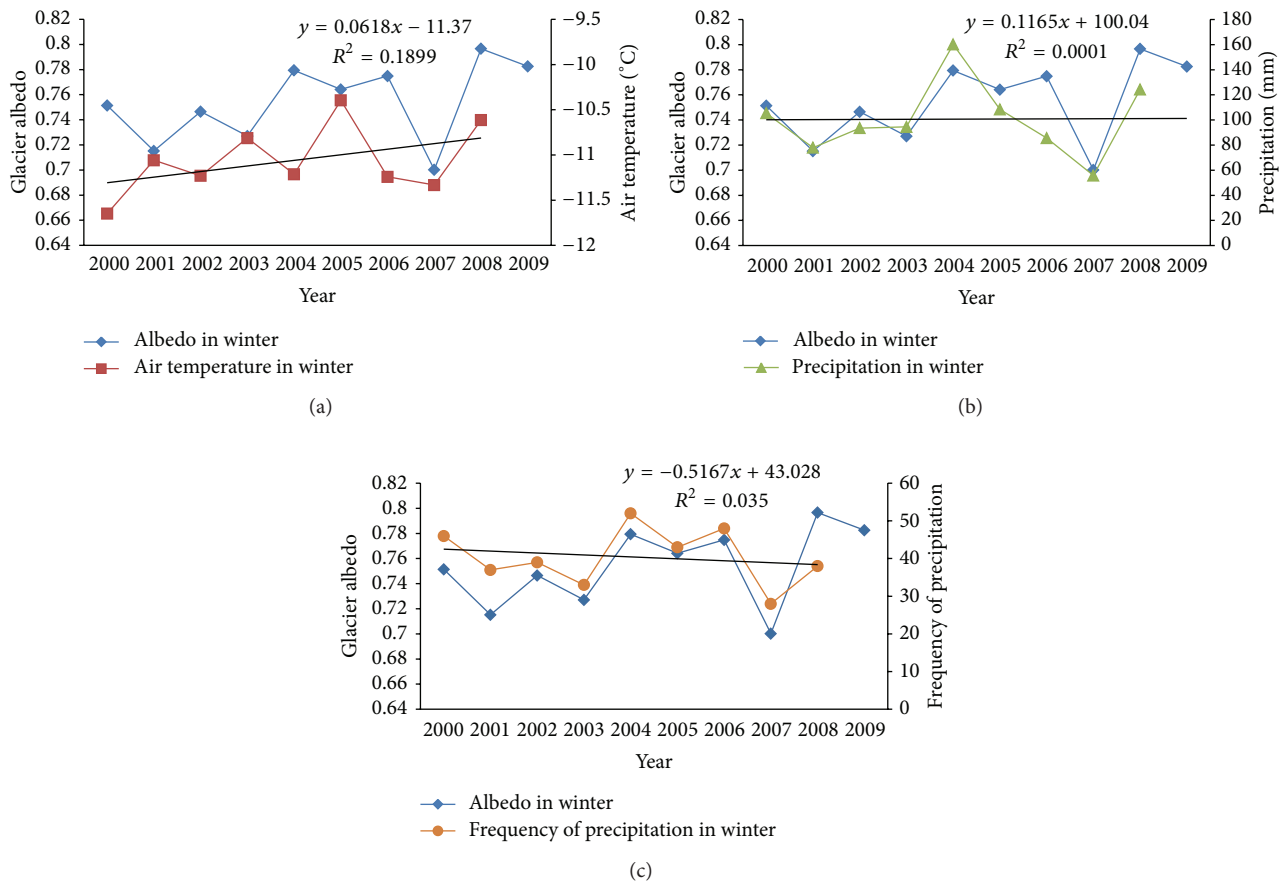


FIGURE 8: Annual variations of glacier albedo, meteorological factors in winter during 2000–2009. (a) Air temperature. (b) Precipitation levels. (c) Frequency of precipitation.

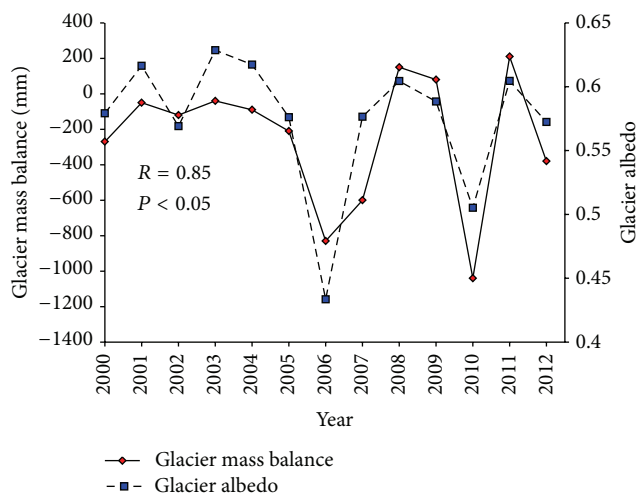


FIGURE 9: Annual variations of glacier mass balance, glacier albedo in summer during 2000–2012.

the ablation period can be considered as a proxy for glacier mass balance.

Conflict of Interests

The authors declare that there is no conflict of interests regarding to the publication of this paper.

Acknowledgments

The work was financially supported by the China National Natural Science Foundation (Grants nos. 41401022, 41301422, and 41471001), the Foundation for Young Talents in College of Anhui Province (no. 2013KJT010022), and the Doctoral Research Start-up Funds Projects of Anhui University (no. 32030068). The authors would like to thank Professor Jian Wang and Shiqiang Zhang for their helpful comments and suggestions. Finally, the authors are grateful to the National Snow and Ice Data Center and the United States Geological Survey for the provision of the MOD10A1 product and Landsat TM/ETM+ images.

References

[1] IPCC, *Climate Change 1995: The Science of Climate Change*, Cambridge University Press, Cambridge, UK, 1995.

- [2] C. H. Reijmer, W. H. Knap, and J. Oerlemans, "The surface albedo of the Vatnajökull ice cap, Iceland: a comparison between satellite-derived and ground-based measurements," *Boundary-Layer Meteorology*, vol. 92, no. 1, pp. 125–144, 1999.
- [3] J. Xi, W. Ninglian, P. Jianchen et al., "The Albedo on the Qiyi Glacier in Qilian Mountains during the ablation period," *Journal of Glaciology and Geocryology*, vol. 30, no. 5, pp. 752–760, 2008.
- [4] R. C. Hubley, "Measurements of diurnal variations in snow albedo on lemon creek glacier, Alaska," *Journal of Glaciology*, vol. 2, no. 18, pp. 560–563, 1955.
- [5] H. Mannstein, "The interpretation of Albedo measurements on a snowcovered slope," *Archives for Meteorology, Geophysics, and Bioclimatology Series B*, vol. 36, no. 1, pp. 73–81, 1985.
- [6] P. M. Cutler and D. S. Munro, "Visible and near-infrared reflectivity during the ablation period on Peyto Glacier, Alberta, Canada," *Journal of Glaciology*, vol. 42, no. 141, pp. 333–340, 1996.
- [7] U. Strasser, J. Corripio, F. Pellicciotti, P. Burlando, B. Brock, and M. Funk, "Spatial and temporal variability of meteorological variables at Haut Glacier d'Arolla (Switzerland) during the ablation season 2001: measurements and simulations," *Journal of Geophysical Research*, vol. 109, Article ID D03103, 2004.
- [8] J. C. Stroeve, J. E. Box, and T. Haran, "Evaluation of the MODIS (MOD10A1) daily snow albedo product over the Greenland ice sheet," *Remote Sensing of Environment*, vol. 105, no. 2, pp. 155–171, 2006.
- [9] B. Zhongyuan and T. Ohata, "Variations of albedo on the glacier No.1 at the headwater of Urumqi river, Tianshan mountains, during the summer ablation period," *Journal of Glaciology and Geocryology*, vol. 11, no. 4, pp. 311–324, 1989.
- [10] A. E. Tekeli, A. Şensoy, A. Şorman, Z. Akyürek, and Ü. Şorman, "Accuracy assessment of MODIS daily snow albedo retrievals with *in situ* measurements in Karasu basin, Turkey," *Hydrological Processes*, vol. 20, no. 4, pp. 705–721, 2006.
- [11] W. H. Knap, C. H. Reijmer, and J. Oerlemans, "Narrowband to broadband conversion of landsat TM glacier albedos," *International Journal of Remote Sensing*, vol. 20, no. 10, pp. 2091–2110, 1999.
- [12] R. Koelemeijer, J. Oerlemans, and S. Tjemkes, "Surface reflectance of Hintereisferner, Austria, from Landsat 5 TM imagery," *Annals of Glaciology*, vol. 17, pp. 17–22, 1993.
- [13] E. J. Klok, W. Greuell, and J. Oerlemans, "Temporal and spatial variation of the surface albedo of Morteratschgletscher, Switzerland, as derived from 12 Landsat images," *Journal of Glaciology*, vol. 49, no. 167, pp. 491–502, 2004.
- [14] F. Paul, H. Machguth, and A. Kääb, "On the impact of glacier albedo under conditions of extreme glacier melt: the summer of 2003 in the ALPS," *EARSeL eProceedings*, vol. 4, no. 2, pp. 139–149, 2005.
- [15] W. Greuell, J. Kohler, F. Obleitner et al., "Assessment of interannual variations in the surface mass balance of 18 Svalbard glaciers from the Moderate Resolution Imaging Spectroradiometer/Terra albedo product," *Journal of Geophysical Research D: Atmospheres*, vol. 112, no. 7, Article ID D07105, 2007.
- [16] Y. Zhang, T. Yao, J. Pu et al., "The features of hydrological processes in the Dongkemadi River Basin, Tanggula Pass, Tibetan Plateau," *Journal of Glaciology and Geocryology*, vol. 19, no. 3, pp. 214–222, 1997.
- [17] Y. Shi and S. Liu, "Estimation on the response of glaciers in China to the global warming in the 21st century," *Chinese Science Bulletin*, vol. 45, no. 7, pp. 668–672, 2000.
- [18] J. Pu, T. Yao, and Y. Zhang, "Study on the relationship between mass balance and climatic factors on the Xiao Dongkemadi Glacier," *The Cryosphere*, vol. 2, pp. 59–62, 1996.
- [19] T. Hilker, M. A. Wulder, N. C. Coops et al., "A new data fusion model for high spatial- and temporal-resolution mapping of forest disturbance based on Landsat and MODIS," *Remote Sensing of Environment*, vol. 113, no. 8, pp. 1613–1627, 2009.
- [20] C. Doña, N. B. Chang, V. Caselles et al., "Integrated satellite data fusion and mining for monitoring lake water quality status of the Albufera de Valencia in Spain," *Journal of Environmental Management*, vol. 151, pp. 416–426, 2015.
- [21] Y. M. Shuai, J. G. Masek, F. Gao et al., "An approach for the long-term 30-m land surface snow-free albedo retrieval from historic Landsat surface reflectance and MODIS-based a priori anisotropy knowledge," *Remote Sensing of Environment*, vol. 152, pp. 467–479, 2014.
- [22] J. Wang and G. Feng, "Discussion on the problems on land surface albedo retrieval by remote sensing data," *Remote Sensing Technology and Application*, vol. 19, no. 5, pp. 295–300, 2004.
- [23] S. Liang, H. Fang, M. Chen et al., "Validating MODIS land surface reflectance and albedo products: methods and preliminary results," *Remote Sensing of Environment*, vol. 83, no. 1–2, pp. 149–162, 2002.
- [24] R. Chen, E. Kang, X. Ji, J. Yang, and J. Wang, "An hourly solar radiation model under actual weather and terrain conditions: a case study in Heihe river basin," *Energy*, vol. 32, no. 7, pp. 1148–1157, 2007.
- [25] W.-L. Lee, K. N. Liou, and A. Hall, "Parameterization of solar fluxes over mountain surfaces for application to climate models," *Journal of Geophysical Research*, vol. 116, pp. 01101–01113, 2011.
- [26] J. Pu, T. Yao, M. Yang et al., "Rapid decrease of mass balance observed in the Xiao (Lesser) Dongkemadi glacier, in the central Tibetan Plateau," *Hydrological Processes*, vol. 22, no. 16, pp. 2953–2958, 2008.
- [27] H. Gao, X. He, B. Ye, and J. Pu, "Modeling the runoff and glacier mass balance in a small watershed on the Central Tibetan Plateau, China, from 1955 to 2008," *Hydrological Processes*, vol. 26, no. 11, pp. 1593–1603, 2012.
- [28] W. Greuell, J. Kohler, F. Obleitner et al., "Assessment of inter-annual variations in the surface mass balance of 18 Svalbard glaciers from the moderate resolution imaging spectroradiometer /terra albedo product," *Journal of Geophysical Research D: Atmospheres*, vol. 112, no. 7, Article ID D07105, 2007.

Research Article

Evaluation of Water Storage Change of Inland Cryosphere in Northwestern China

Min Xu,¹ Shichang Kang,^{1,2} and Jiazhen Li¹

¹State Key Laboratory of Cryospheric Science, Cold and Arid Regions Environmental and Engineering Research Institute, Chinese Academy of Sciences, Lanzhou 730000, China

²CAS Center for Excellence in Tibetan Plateau Earth Sciences, Chinese Academy of Sciences, Beijing 100101, China

Correspondence should be addressed to Min Xu; careerigis@163.com

Received 25 December 2014; Revised 14 March 2015; Accepted 14 March 2015

Academic Editor: Hiroyuki Hashiguchi

Copyright © 2015 Min Xu et al. This is an open access article distributed under the Creative Commons Attribution License, which permits unrestricted use, distribution, and reproduction in any medium, provided the original work is properly cited.

The Gravity Recovery and Climate Experiment (GRACE) satellite mission provides measurements of Earth's static and time-variable gravity fields with monthly resolution. In this study, changes of water storage in northwestern China were determined by GRACE monthly gravity field data obtained from 2003 to 2010. Comparisons of water storage change (WSC) simulated by a four-dimensional assimilation model (Noah) and observed by GRACE revealed similar patterns of change and a correlation coefficient of 0.71 ($P < 0.05$). Trend analysis indicated significant changes in the spatiotemporal variation of WSC in northwestern China during the 8-year study period, which were stronger in the east than in the west and more pronounced in the south than in the north. The most pronounced increase in water storage occurred in Gansu and Qinghai provinces, but, overall, water storage increased by 0.61 mm/a over northwestern China during the study period. Clear seasonal variations of WSC and precipitation were found, because glacial meltwater and precipitation are the main sources of water in the hydrosphere; meanwhile, the distributions of glaciers and permafrost also affect the spatial distribution of WSC.

1. Introduction

The cryosphere is an important component of the global water cycle, and its sensitivity to climate change has been a subject of much concern. In particular, since the 1980s, the global cryosphere has undergone significant changes due to global warming, which have important consequences with regard to the global water cycle [1]. It has been in the principal cryospheric region of northwestern China, including Xinjiang (XJ), Gansu (GS), Ningxia (NX), and Qinghai (QH) provinces and Tibet, where these changes in the water cycle have been most pronounced [1]. Therefore, the study of the spatiotemporal variation of water storage change (WSC) in these areas has importance regarding the understanding of the water cycle, climate change, agricultural production, and natural disasters.

In northwestern China water sources are mainly melting snow and ice and groundwater recharge. For example, mountain runoff is the only source that recharges surface and subsurface runoff in the basin of the Xinjiang Plain

[2]. The socioeconomic development of northwestern China has led to increased water demand, overexploitation of water resources, and consequent water shortages that have become a major restriction to the ongoing development of the region [3, 4]. WSC is an important measure that reflects the changes of regional water resources, which have become one of the most important issues regarding socioeconomic development in China.

It is difficult to estimate WSC using traditional long-term water balance calculations and estimations of the water resources of a watershed/region, and, therefore, it is often considered as zero on the annual scale. However, ignoring WSC could have significant impact on the estimated elements of the water balance under climate change scenarios. In estimating the water balance in the source region of the Yellow River, Xu et al. [5] showed that average evaporation calculated by the Sib2 model is 978.2 mm, but when considering WSC, the average evaporation is 507.4 mm. These results suggest that an assessment of WSC is crucial for understanding the changes of the water balance in northwestern China.

WSC can be derived by calculating the difference between precipitation, evapotranspiration, surface runoff, and soil exchange of moisture and groundwater in the water cycle [6]. However, it is difficult to obtain an accurate estimation of the WSC of a region/watershed because of the lack of observational data and the high cost of the measurement methods. Some researchers have used satellite-derived gravity data to monitor long-term WSC and they have made considerable advances [7–9]. The advantage of satellite-based methods is their ability to reflect uniform region/basin-scale observations of water storage variations. Traditional remote sensing satellites can be used to detect the soil moisture of the land surface to depths of only tens of centimeters, and the spatial distribution of field stations for verification purposes is poor. However, to a certain extent, the Gravity Recovery and Climate Experiment (GRACE) satellite can compensate for such disadvantages, and it offers a new opportunity for the quantitative study of regional land WSC.

The variation in the gravity field detected by GRACE is mainly due to land WSC, ice masses (e.g., polar ice sheets, alpine glaciers ice cap), and other geophysical signals (e.g., postglacial rebound and deformation caused by earthquakes). Interference signals in the GRACE data are caused by the atmosphere and ocean mass variations, which can be removed using numerical simulation [10], and, therefore, following the removal of the geophysical signals, the WSC can be determined. Results show that the GRACE satellite can monitor the water equivalent change of the ground to about 0.9 cm and the precision can reach 1–1.5 cm [11, 12]. Some researchers have compared the results retrieved by GRACE with those calculated using global land surface process models. The two methods produce results that are similar in most areas, but there are also discrepancies related to difficulties in obtaining precise input data in some areas. GRACE data can overcome such problems and, thus, can provide a reference for the improvement of the accuracy of global land surface process models [13–16]. Strassberg et al. [17] used GRACE data to estimate the WSC over about 450,000 km² of the American High Plains region and found good correlation ($R = 0.95$) between the WSC retrieved by GRACE and the measured soil moisture and groundwater data. In addition, WSC retrieved by GRACE has been used in cryospheric-related research on permafrost activities and WSC in the Arctic. The results showed that WSC increased at a rate of 1.15 km³/a on the coast of Alaska, whereas it showed a rate of decline of 7.44 km³/a in the Yukon basin. Changes of the permafrost active layer might be an important reason behind the variation of WSC, and the results of the study suggest that GRACE satellite data could be used to analyze the variation of WSC in permafrost regions [18]. Chinese research on this subject has concentrated mainly on large areas, such as the Chinese continental region, Xinjiang and the surrounding mountainous area, and northern, northeastern, and southern regions of China [4, 15, 16, 19]. Generally, these researches have involved regional quantitative descriptions of WSC, and they have established that different regions exhibit different variational features. Some studies have used GRACE satellite data to analyze the magnitude of WSC in the Three Gorges

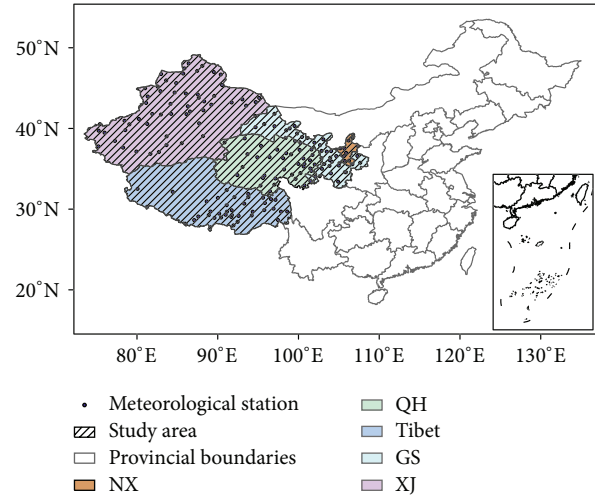


FIGURE 1: Study area.

Reservoir area and the Yangtze River and Heihe River basins. The amplitude of annual variation of WSC in the Yangtze River basin was up to 3.4 cm equivalent water height with the maximum value appearing in spring and early autumn. The root-mean-square error (RMSE) of the variation of WSC of the Three Gorges Reservoir was 1.3 cm, for the amplitude of the annual variation of 0.1 cm. In addition, the WSC of the Heihe River basin increased yearly from 2002 to 2008 [20–24]. These studies reveal that applications of GRACE data are lacking in depth and breadth, although they do indicate that GRACE satellite data could enhance the understanding of WSC, and provide a basis for better predictions of drought and changes in global water resources due to climate change. However, a comprehensive study of the WSC of the cryosphere and of its causes in northwestern China has not been reported previously. In this study, gravity information derived from GRACE satellite observations was used to retrieve monthly WSC, which was compared with results simulated by the Noah model to analyze WSC in northwestern China from 2003 to 2010. This work expands the spatiotemporal scale of the analysis of WSC in northwestern China, by considering the water resources of five provinces (Xinjiang, Gansu, Ningxia, Tibet, and Qinghai) and the Qinghai–Tibet Plateau and by discussing the effects on WSC of glaciers and the underlying permafrost.

2. Study Area

The study area incorporates Tibet and Gansu (GS), Qinghai (QH), Ningxia (NX), and Xinjiang (XJ) provinces with an area of about 2,808,000 km² (Figure 1). The climate is mainly influenced by monsoon and westerlies, and precipitation declines from the east to the west and from the south to the north. Annual precipitation is about 400 mm in the east, which decreases to 200 mm in the west or 50 mm below. The main topographic features of the area are plateaus, basins, and mountains, including the Loess and Qinghai–Tibet Plateaus, the Tarim, Zhungeer, and Qaidam basins, and the Tianshang,

Qianlian, Karakorum, and Kunlun Mountains. The Qinghai-Tibet Plateau, sometimes referred to as the world's "third pole," is the largest glacial resource in China. The total ice volume is 2798 km³, which accounts for 50% of the ice reserves. The ice covers about 32320 km², which accounts for 54.4% of the entire area. There are 22468 glaciers within this region, and the permafrost area extends over about 1.3 × 10⁶ km² [25, 26]. There are 18311 glaciers in XJ, accounting for 46.8% of the total number of glaciers in China, covering an area of 24721.93 km². The total of ice reserves are 2623.4 km³, and the water storage of the glaciers is 23611.2 × 10⁸ m³ [27].

3. Materials and Methods

3.1. Precipitation Data and Spatial Interpolation Method. Precipitation data from 2003 to 2010 were obtained from national meteorological stations within the study area and corrected for the influence of wind [28]. Furthermore, to improve the surface accuracy of precipitation within the study area, the data were interpolated using Kriging with consideration of elevation [29]. This method uses precipitation and site elevation data to perform a linear regression. The spatial P_r was calculated using the formula for linear regression; the residuals (regressed precipitation minus measured precipitation) were interpolated using the Kriging spatial interpolation method, and then the spatial P_r was added to the spatial residuals, which provides the spatial distribution of precipitation:

$$P_{\text{result}} = P_r + P_{\text{residual}}, \quad (1)$$

where P_{result} is the spatial precipitation, P_r is the rasterized precipitation regressed by elevation, and P_{residual} is the spatial residual (units of precipitation: mm).

3.2. Change of Precipitation. Precipitation is the main source of land surface water and changes in precipitation affect evaporation, runoff, and WSC. In this study, the change of precipitation was calculated using the following formula:

$$P_c = P_i - P_{i-1}, \quad (2)$$

where P_c is the change of precipitation, P_i is the precipitation in month i , P_{i-1} is the precipitation in the preceding month, and i is the month (from 1 to 12).

3.3. Retrieval Method for WSC Data. This study used Release-04 (R4) Level-3 grids provided by the GRACE Science Team centers. The global grids comprise 1-arc-degree water equivalent mass change complete to degree and order 60 [8, 12]. The GRACE R4 Level-3 (300 km Gauss-smoothing kernel) land and ocean monthly grids from 2003 to 2008 were combined to provide global coverage [20, 23]. Glacial isostatic adjustment or solid mass flow within Earth's mantle, following the decay of the Pleistocene Laurentide and Cordilleran ice sheets in North America and Scandinavia, was applied to the GRACE grids [30].

3.4. Soil Moisture Simulated by Model. WSC represents a vertically integrated measure of variation of water storage that includes soil moisture, groundwater, surface water, snow and ice, and biomass. A previous study of WSC in the High Plains of the United States showed that soil moisture and groundwater are the primary contributors to terrestrial water storage variability and that the variations due to snow and ice, biomass, and surface water are relatively minor [31]. Hydrological models can be divided into two categories based on global and continental scales: land surface models (LSMs) and water budget models. A land surface process model describes the composition of WSC, which includes groundwater, surface water, water exchange, and storage.

In this study, in order to compare the results retrieved by GRACE, the Noah LSM was used to simulate soil moisture. The Noah model was developed by the Research Applications Laboratory of the National Center for Atmospheric Research (NCAR), and a four-dimensional assimilation system was used to calculate the simulated results. The unsaturated zone of the soil was divided into four layers, the thicknesses of which from the soil surface to the bottom were 0.1, 0.3, 0.6, and 1.0 m. Model input data included precipitation, solar radiation, surface air pressure, humidity, and surface wind speed. The shortwave and longwave radiation data were provided by the Air Force Weather Agency agrometeorological simulation system (AGMET), and all other data were obtained from national meteorological stations. Model output included four layers of soil moisture change with temporal resolution of 1 month and spatial resolution of 1° × 1°. It is important to note that model simulations are ineffective in permafrost zones.

3.5. WSC Cycle. To study the extent and period of WSC within study area quantitatively, the least-squares method was used to calculate the cycle and amplitude of regional WSC:

$$y(t) = A \cdot \sin \left[\frac{2\pi \cdot (t - \phi)}{\omega} \right], \quad (3)$$

where A is amplitude, ϕ is phase, and ω is the cycle. Amplitude represents the intensity of WSC and the cycle represents the length of WSC in the time series.

4. Results and Discussion

4.1. Results of WSC Retrieved by GRACE and Simulated by Noah. The results of WSC retrieved by GRACE and simulated by Noah for representative periods of summer (August 2007) and winter (December 2008) are shown in Figure 2. It can be seen that over a large area the two results have similarities. For example, the WSC exhibits a state of loss in the west of XJ and NX, whereas it shows a state of gain in the middle of GS and the Qilian Mountains. However, in some small parts, they exhibit differences. Overall, the WSC retrieved by GRACE demonstrates better continuity than that simulated by Noah.

A comparison of the two results as time series (Figure 3) reveals that both exhibit seasonal change and demonstrate

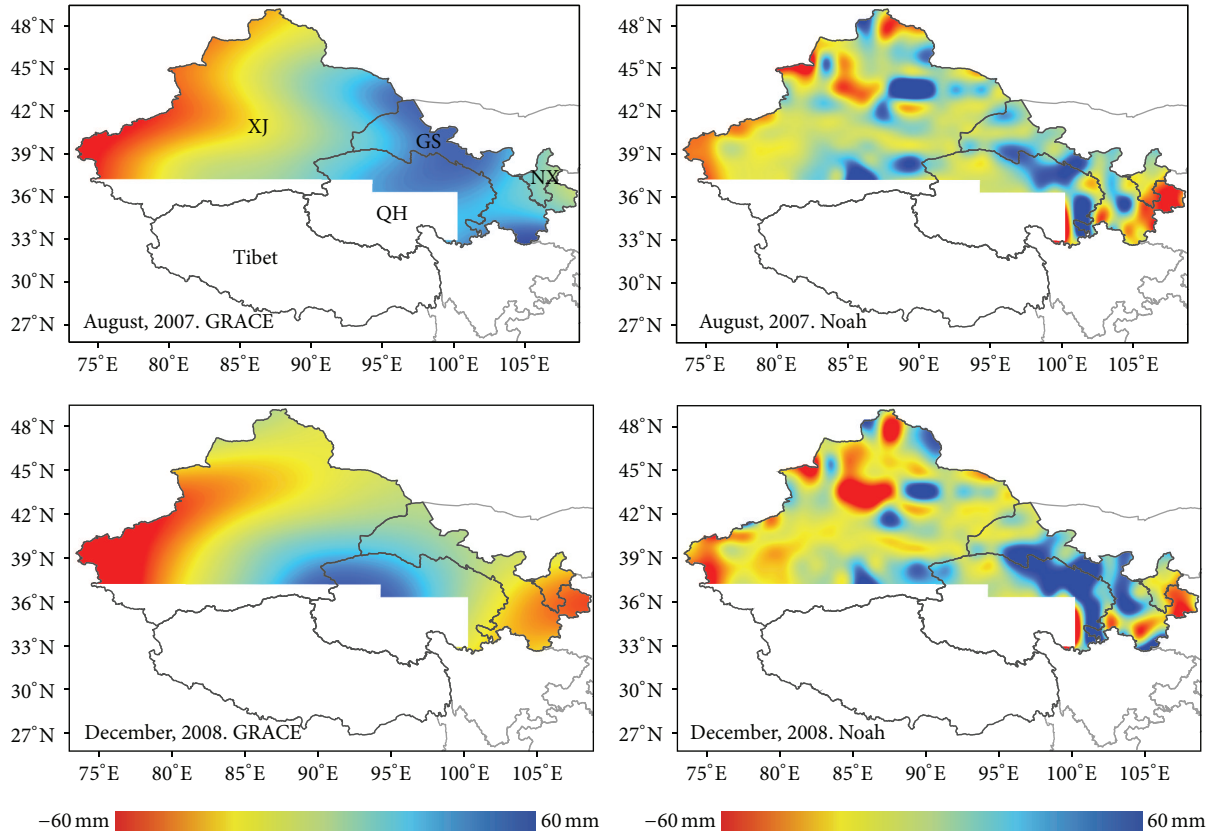


FIGURE 2: Results of WSC retrieved by GRACE and simulated by Noah.

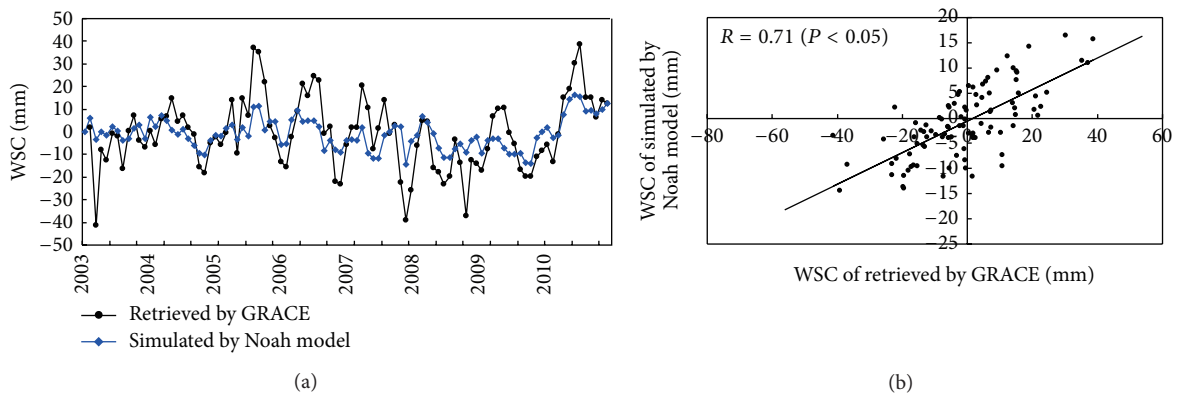


FIGURE 3: Correlation of WSC retrieved by GRACE and simulated by Noah as time series.

a fluctuating feature (correlation between them is 0.71). However, as can be seen, the range of the values retrieved by GRACE is much larger than that simulated by Noah. One reason for this is that GRACE data can reflect deeper soil water equivalent.

It should be pointed out that although the two results coincide, they have differences in scale, and there are two reasons for this. The first is that the expressions of the two results are different; Noah only reflects changes of soil humidity, whereas GRACE reflects soil, surface water, glaciers, and frozen soil moisture. The other reason is that

the distribution of the stations is sparse, which limits the results simulated by the model.

4.2. Temporal and Spatial Patterns of WSC and Precipitation over Northwestern China. WSC was retrieved from GRACE satellite data from 2003 to 2010 over northwestern China, and the distributions of the average WSC and of the average change of precipitation, calculated using formulas (1) and (2), are shown in Figures 4(a) and 4(b), respectively. As can be seen, there is much less change in the south than in the north and much more change in the east than in the west.

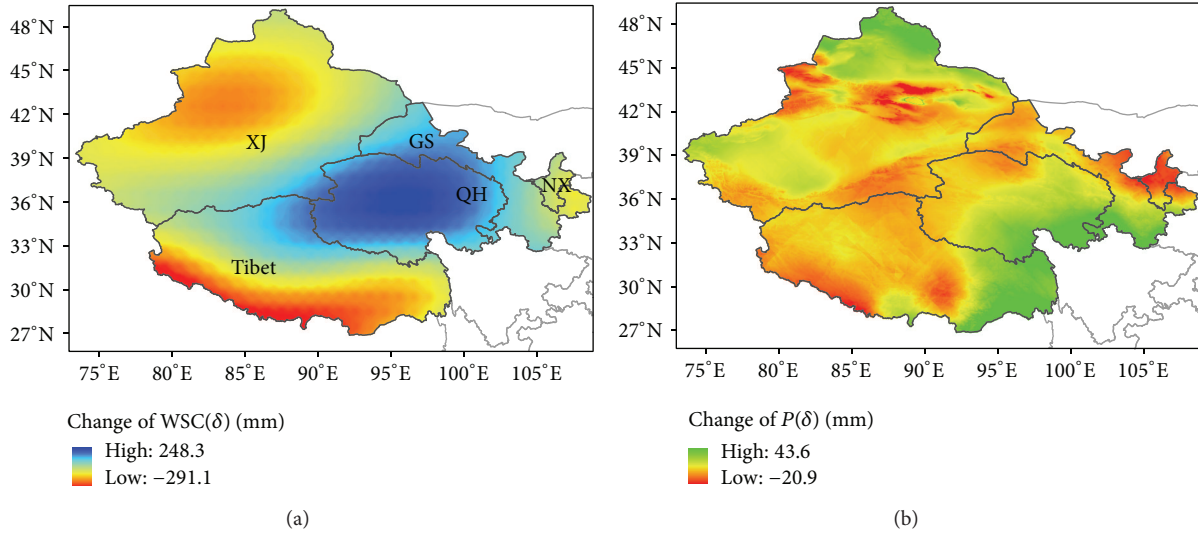


FIGURE 4: Temporal and spatial patterns of average annual WSC and precipitation over northwestern China from 2003 to 2010.

WSC is in a surplus state in QH and GS, but precipitation does not coincide with the distribution of WSC in this area, which means that the spatial distribution of precipitation is not the only factor driving the spatial distribution of WSC. Precipitation is the main source of WSC, but degradation of the permafrost and increased thickening of the active layer of seasonally frozen soil also increase the storage capacity of the area [5]. WSC is in a state of loss in most parts of XJ, especially in western regions where the largest loss value reaches -175 mm. The WSC shows an intense state of loss in the Himalayas where the value is about -291.1 mm. This is consistent with research that claims there has been glacial mass balance loss in this area and where the retreat has been faster in the middle and west of the region [32, 33]. However, WSC shows gains in the Karakorum region and the Altai Mountains, which could corroborate research that has shown that glaciers in these areas have exhibited mass stability or even expansion. As can be seen, the precipitation has increased in these areas and previous studies have shown that snowfall is less sensitive to warming [34]. The WSC shows serious losses in XJ, except in the north. There are 18311 glaciers in XJ with a total area of 24721.93 km^2 , but most of the glaciers in XJ are retreating [35, 36], which means that the water resource has decreased. Across the entire study area, WSC is between -291.1 and 248.3 mm. As shown in Figure 4(b), the range of variation of precipitation is -20.9 to 43.6 mm with the distribution showing the characteristic of a decrease from southeast to northwest. Precipitation shows a reduction in most of the region, although it shows an increase in northern XJ, eastern Tibet, and QH. The distributions of WSC and precipitation have spatial differences, but they do show localized consistency (such as southeastern QH).

It can be seen from Figure 5 that the amplitude of variation of WSC across the study area is -36.4 to 55.9 mm. This means that the maximum value of increased water is about 55.9 mm equivalent water height, and the minimum value is -36.4 mm equivalent water height. Monthly

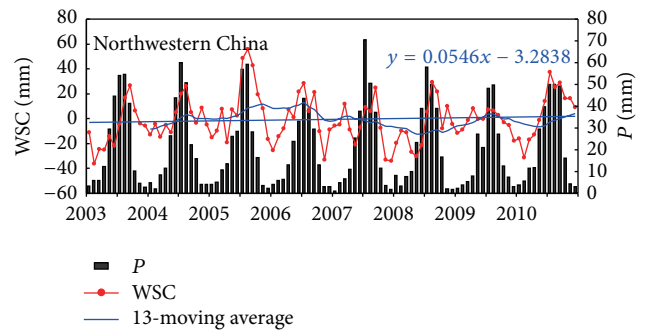


FIGURE 5: Time series of WSC and precipitation (P) over northwestern China from 2003 to 2010.

precipitation is about 1.1 – 70.5 mm. Generally, WSC shows a slight upward trend, but the difference between inflow and outflow is increasingly small. WSC and precipitation have obvious seasonal variation and consistent change processes. The study area is located in inland areas of the mid-latitude westerly belt, where sources of water vapor depend mainly on the zonal westerly circulation and the Indian Ocean monsoon [37, 38]. Rainfall is concentrated mainly from May to September, which is when the WSC generally increases and the peak value appears in this period. Precipitation is relatively small from December to March, but evaporation is large, and, therefore, the WSC is at a loss. The characteristics of variation of precipitation have a dominant effect on WSC in the time series. In northwestern China, the WSC increases slightly year by year from 2003 to 2010; the average rate of increase is about 0.61 mm/a , and the total increase in the quantity of water is about $1.47 \times 10^{10} \text{ m}^3$.

4.3. Monthly Average WSC from 2003 to 2010. The distributions of monthly average WSC indicate differences during the years for which it was retrieved by GRACE (Figure 6). It can

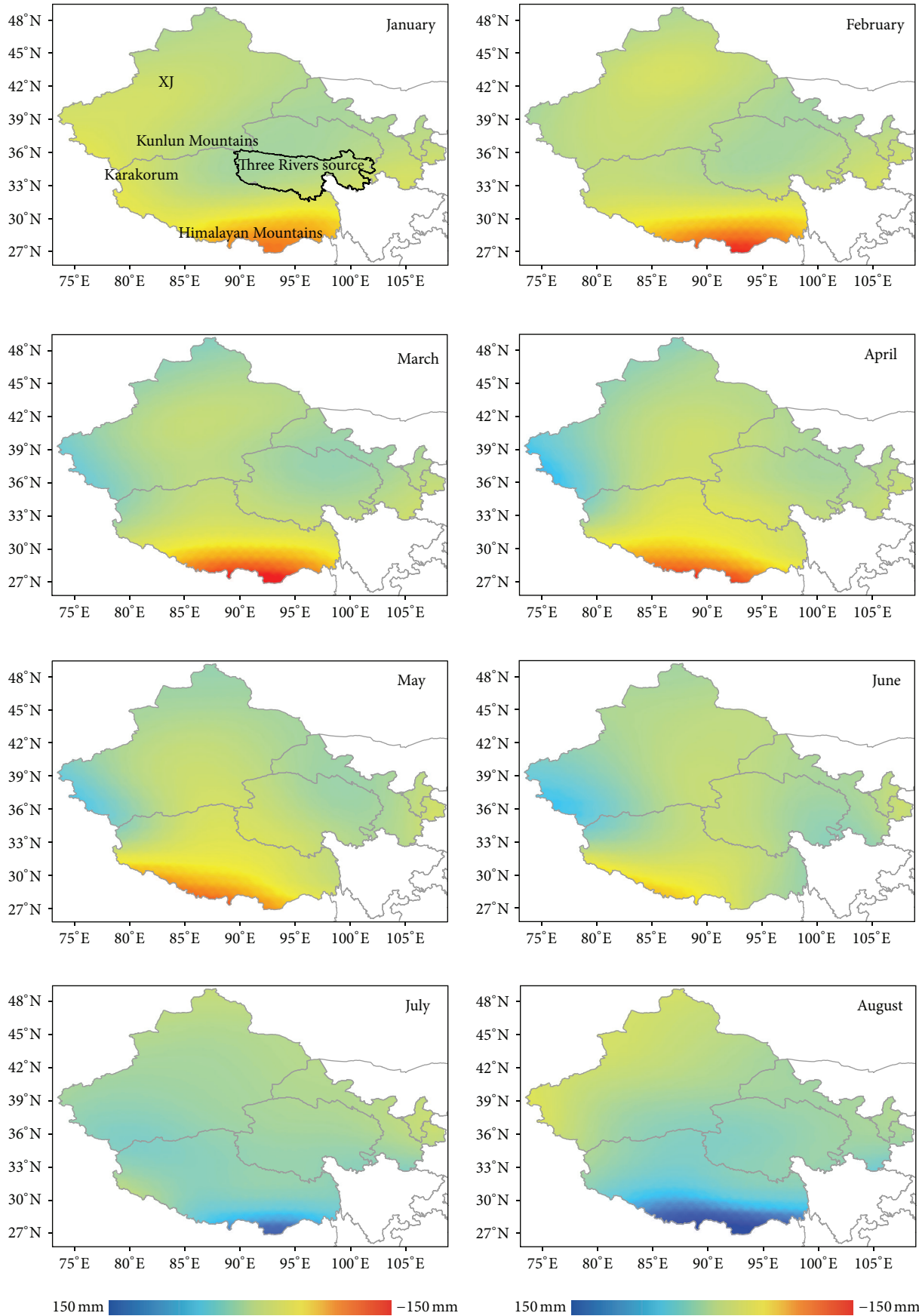


FIGURE 6: Continued.

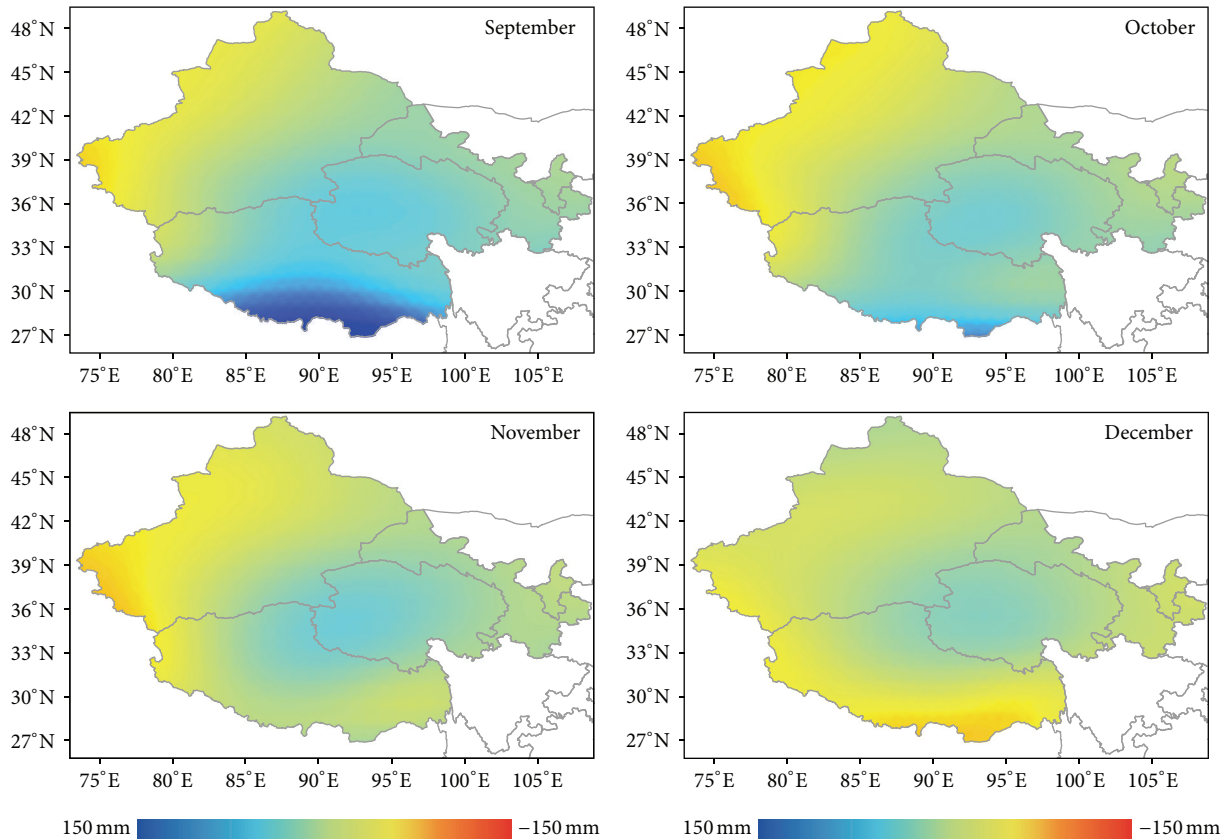


FIGURE 6: Monthly averages of WSC from 2003 to 2010.

be seen that the WSC is in a state of loss in the Himalayan region from January to June and in December, with particularly serious losses in February and March. However, it is in a state of gain from July to November, although as the months proceed, the state of gain weakens. That pattern is due to the low precipitation and high evaporation during spring and winter and greater precipitation brought in summer by the Indian monsoon, which brings much more water vapor [39, 40]. The XJ region is influenced by the westerly circulation, which brings increased levels of water vapor and a state of gain in western parts from March to July. This state is particularly evident in the Karakorum and Kunlun Mountains; the state of gain moves west to middle. The WSC is in a state of gain from January to March in the Three Rivers source area, because spring snowmelt runoff begins, which results in a state of loss from April to June. This area is influenced by the rainy season as well as by glacial meltwater supply during July, which means that the WSC is in a state of gain from July to February of the following year.

4.4. Annual Distribution of WSC from 2003 to 2010. We also calculated the annual distribution of WSC (Figure 7). It can be seen from the figure that the WSC is in a state of gain from March to July in XJ but that it is in a state of loss for the rest of the year. The maximum value (about 13.5 mm) appears in July and the minimum value (about -28.2 mm) is in October. The WSC of GS shows a state of loss in January,

February, and December, whereas it is in a state of gain for the other months and the maximum value (about 21.6 mm) occurs in September. The WSC is in a state of loss in QH from April to June, principally because the area includes the Three Rivers source area and the runoff of spring snowmelt leads to supplementary losses. In the other months, WSC is in a state of gain and the maximum value (about 44.4 mm) occurs in September. The WSC is irregular in NX, showing a state of gain in March and April and from August to December, but is in a state of loss in the other months; the maximum and minimum values occur in September and December, respectively. The WSC is more consistent in Tibet and on the Qinghai-Tibet Plateau. It is in a state of gain from July to November but in a state of loss in the other months. The maximum value appears in September and the minimum in April.

4.5. Process of WSC in Northwestern China. We calculated the WSC and precipitation during 2003–2010 in XJ, GS, QH, NX, and Tibet and on the Qinghai-Tibet Plateau (Figure 8). It can be seen that regional WSC exhibits strong seasonal fluctuations, but changes in precipitation are not obvious. The WSC increases in GS and QH and on the Qinghai-Tibet Plateau from 2003 to 2010, at rates of 3.63, 9.68, and 2.49 mm/a, respectively. The WSC decreases in XJ, NX, and Tibet at rates of -1.49, -2.54, and -3.05 mm/a, respectively.

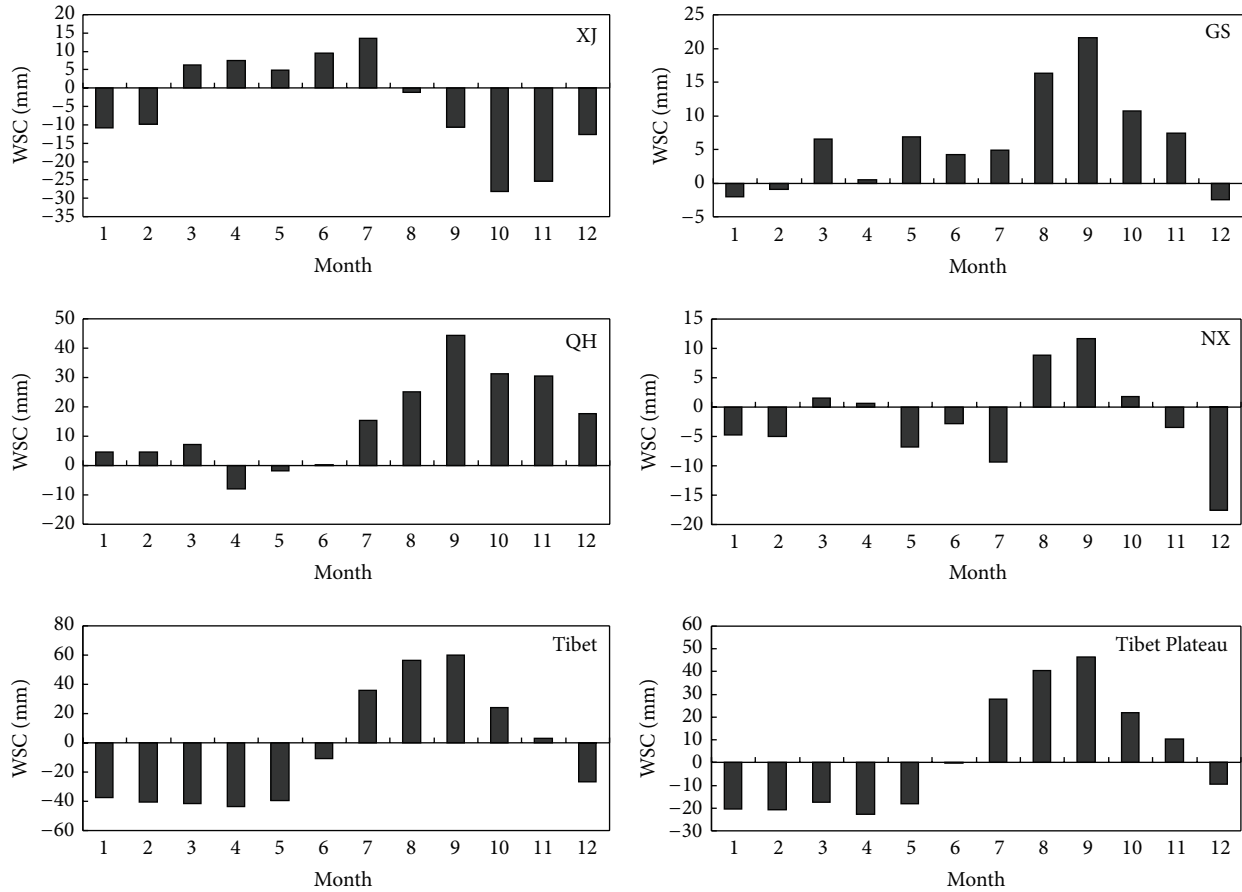


FIGURE 7: Annual distributions of WSC from 2003 to 2010.

TABLE 1: Amount of WSC over northwestern China from 2003 to 2010.

Region	Rate of change (mm/a)	2003–2010 WSC (10^9 m^3)
XJ	-1.49	-195
GS	3.63	117
NX	-2.54	-10.3
QH	9.68	555
Tibet	-3.05	-294
Qinghai–Tibet Plateau	2.49	506

The total amount of water increased by about $555 \times 10^9 \text{ m}^3$ in QH and it decreased by about $294 \times 10^9 \text{ m}^3$ in Tibet (Table 1).

The trends of WSC retrieved by GRACE are in line with the normal patterns and we analyzed the cycles using (3). The amplitude of the land surface water resource reflects the intensity of the hydrological cycle, and the cycle represents the duration of the cycle of WSC. As can be seen from Table 2, the smallest intensity of WSC is 3.4 mm in QH, which means that the WSC is in a steady state in this area. The largest amplitude is 11.5 mm in GS, indicating that the change of water resource in this area has greater complexity and uncertainty and that although the WSC of the area has

TABLE 2: Cycle of WSC over northwestern China.

Region	Amplitude (mm)	Cycle (month)
XJ	4.1	18
GS	11.5	21
QH	3.4	20
NX	7.8	25
Tibet	7.9	20
Qinghai–Tibet Plateau	3.2	22

increased overall, the distribution of WSC is unequal. The largest cycle of WSC is in NX, which is about 25 months, and the smallest is in XJ, which is about 18 months. This reflects the greater development of agriculture and industry in XJ, which accelerates the speed of the water cycle. Whether on temporal or spatial scales, the distribution of WSC in northwestern China is shown to be heterogeneous.

4.6. Influence of Glaciers and Permafrost on WSC. The distributions of glaciers, permafrost, and talik (a layer of ground that remains unfrozen year-round) affect the characteristics of surface drainage and groundwater storage changes in northwestern China [5]. The dynamics of permafrost, talik, and the active layer exert significant influences on surface

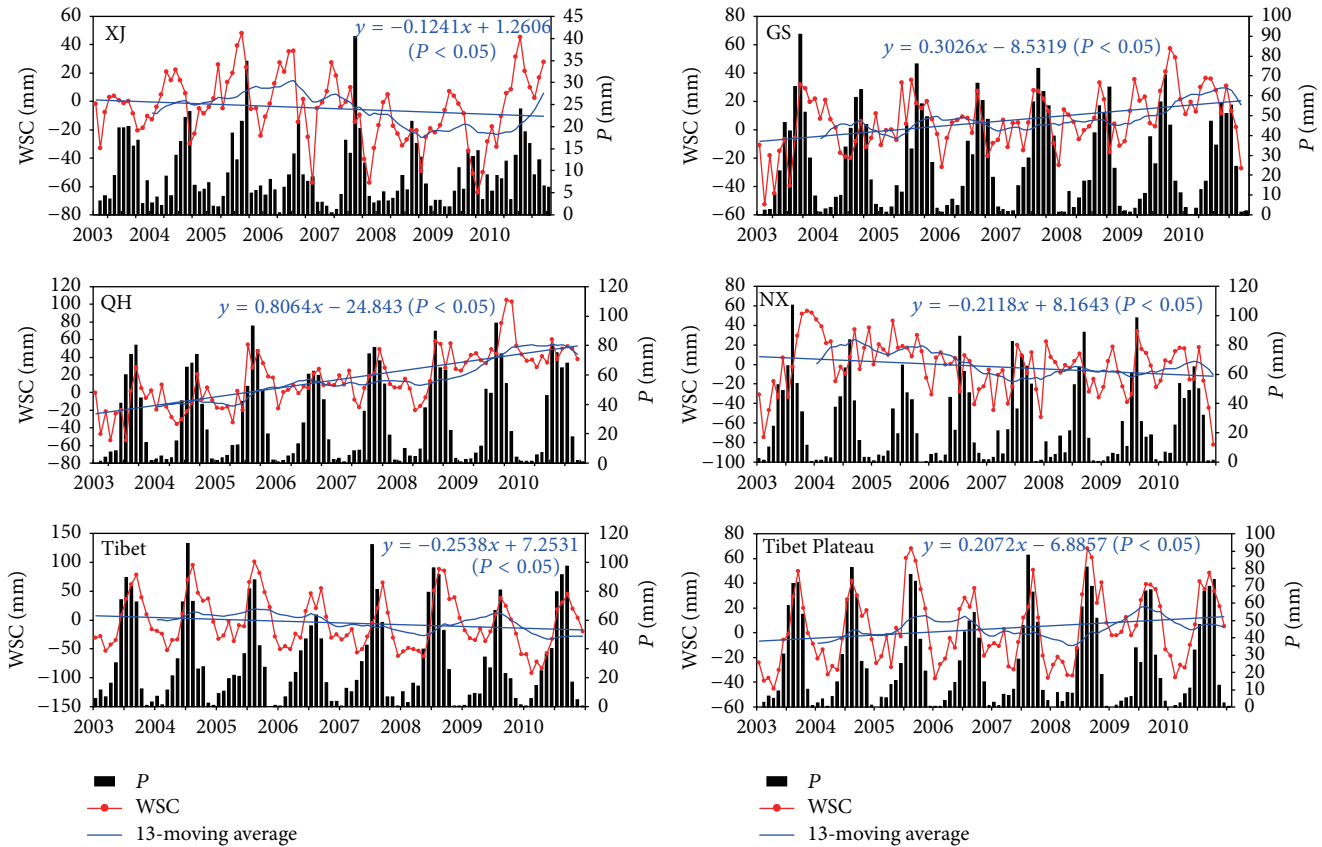


FIGURE 8: Time series of WSC and precipitation (P) over each of the study areas from 2003 to 2010.

and groundwater hydrology and geomorphology in area A of Figure 9. Area A is a region of numerous and sometimes quite large thermokarst thaw ponds, lakes, and drained thaw-lake basins [39, 40]. Area B has a large number of glaciers that have retreated considerably [36]. Glacial meltwater flows into area B from the northern slopes of the Himalayas. However, between areas A and B, a considerable amount of predominantly continuous permafrost prevents movement of the surface water into the groundwater. Thus, the active layer increases and thickens, which leads to greater infiltration of surface water into the groundwater, which results in increased water storage in area A. The GRACE monthly water equivalent changes capture the changes of the base flow from groundwater and surface water in the permafrost area of the Qinghai–Tibet Plateau. In related research, GRACE-derived WSC has been found to increase in the watershed of the Lena and Yenisei rivers [41]. These watersheds encompass large areas of both continuous and discontinuous permafrost zones and talik.

Glaciers have exhibited mass stability or even expansion in area D of Figure 9 [42–44]. The results retrieved by GRACE also reflect that the WSC has increased in this area. Research has indicated that the Karakorum seasonal cycle is dominated by nonmonsoonal winter precipitation, which has uniquely protected it from reductions in annual snowfall under climate warming during the early part of the 21st

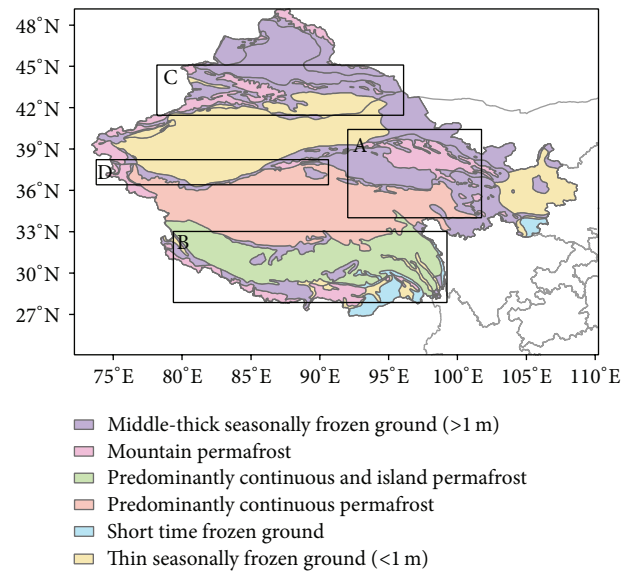


FIGURE 9: Distribution of frozen soil types over northwestern China.

century [34]. Glacial mass loss has occurred across areas C and A in Figure 9 [35]. Since the early 2000s, the trend of precipitation has not changed much [45, 46], whereas the

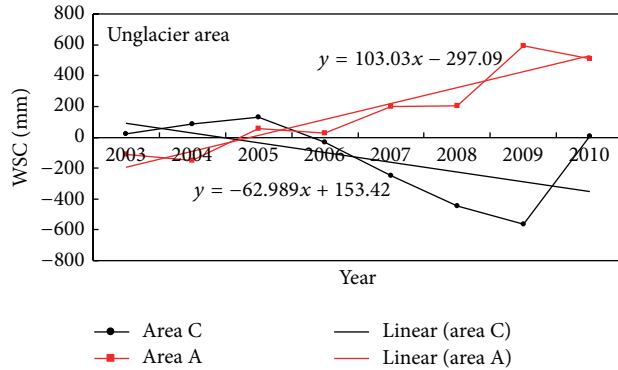


FIGURE 10: WSC of nonglaciater areas of A and C.

WSC exhibits large differences (Figure 4(a)). The WSC in the Tianshan Mountains part of area C has decreased, whereas it has increased in the Qilian Mountains part of area A. The total area of the Tianshan Mountains is 270,000 km², and the area of glaciers is approximately 9225 km², which accounts for 3.41% of the total area. The area of permafrost is about 63,000 km², which accounts for 23% of the total area. The area of the Qilian Mountains is 198,000 km² and the area of glaciers is approximately 1931 km², which accounts for about 1% of the total area. The area of permafrost is about 100,000 km², which accounts for 50% of the total area. Both regions rely mainly on the supplement of meltwater runoff from the mountains. However, the WSC is in a state of loss in area C, which shows that the glacial meltwater flows out this area but that less surface water infiltrates into the groundwater. Furthermore, area A has a greater distribution of permafrost, and thus the thickened active layer as well as more ponds might store more water which caused an increase of WSC (Figure 10).

5. Conclusions

- (1) The WSC in the northwestern China was retrieved using GRACE data and the results were compared with the simulations of the Noah model. The total amount of WSC in northwestern China was calculated and analyzed and discussed based on the regional WSC of five provinces and the Qinghai-Tibet Plateau. The retrieved results agree well with the simulations by Noah; the correlation coefficient is 0.71 ($P < 0.05$). And retrieved results reflect the seasonal change, interannual variation, and spatial distribution of the total water resource within the study area.
- (2) The interannual variability of WSC was found to have decreased in XJ, NX, and Tibet but increased in GS and QH and on the Qinghai-Tibet Plateau. The study area encompasses the principal regions of glaciers and permafrost in China, which have an effect on the annual regional differences in WSC in XJ, GS, QH, NX, Tibet, and the Qinghai-Tibet Plateau. Seasonal changes of WSC were clear, but the seasonal differences and cycles and annual magnitudes of change

reflect the imbalance of water resource distribution in northwestern China.

- (3) Recent warming leads to the degradation of permafrost and retreat of glaciers. Permafrost plays an important role in the water cycle, and the increase and thickening of the active layer can lead to greater infiltration of surface water into the groundwater, which can result in increased water storage and changes in the regional water balance.

Conflict of Interests

The authors declare that there is no conflict of interests regarding the publication of this paper.

Acknowledgments

This study was supported by the National Key Program for Developing Basic Sciences in China (no. 2013CBA01806), Chinese Academy of Sciences (KJZD-EW-G03-04), National Natural Science Foundation of China (41121001, 41225002, and 41471060), and the Foundation for Young Talents in Cold and Arid Regions Environmental and Engineering Research Institute of CAS (no. Y451191001). The authors would like to thank the editors and the anonymous reviewers for their crucial comments, which improved the quality of this paper.

References

- [1] B. Ye, Y. Ding, K. Jiao, and J. Zhang, "Cold runoff response to climate change," *Quaternary Sciences*, vol. 32, pp. 103–110, 2012.
- [2] C. Xi, *Physical Geography of Arid Land in China*, Science Press, Beijing, China, 2010.
- [3] G. Zhu, *Investigations on Time-Variation of Continental Water Storage with GRACE Gravity Models*, Chinese Academy of Surveying and Mapping, Beijing, China, 2007.
- [4] M. Zhong, J. Duan, H. Xu, P. Peng, H. Yan, and Y. Zhu, "Trend of China land water storage redistribution at medium and large-spatial scales in recent five years by satellite gravity observations," *Chinese Science Bulletin*, vol. 54, no. 5, pp. 816–821, 2009.
- [5] M. Xu, B. Ye, Q. Zhao, S. Zhang, and J. Wang, "Estimation of water balance in the source region of the Yellow River based on GRACE satellite data," *Journal of Arid Land*, vol. 5, no. 3, pp. 384–395, 2013.
- [6] Y. Ding and R. Shou, *Northwest China Region Climate and Ecological Environment*, China Meteorological Press, Beijing, China, 2001.
- [7] J. Wahr, M. Molenaar, and F. Bryan, "Time variability of the Earth's gravity field: hydrological and oceanic effects and their possible detection using GRACE," *Journal of Geophysical Research B: Solid Earth*, vol. 103, no. 12, pp. 30205–30229, 1998.
- [8] B. D. Tapley, S. Bettadpur, J. C. Ries, P. F. Thompson, and M. M. Watkins, "GRACE measurements of mass variability in the Earth system," *Science*, vol. 305, no. 5683, pp. 503–505, 2004.
- [9] S. B. Luthcke, H. J. Zwally, W. Abdalati et al., "Recent Greenland ice mass loss by drainage system from satellite gravity observations," *Science*, vol. 314, no. 5803, pp. 1286–1289, 2006.

- [10] S. Bettadpur, *GRACE level-2 Gravity Field Product User Handbook*, Center for Space Research, The University of Texas at Austin, Austin, Tex, USA, 2003.
- [11] O. B. Andersen and J. Hinderer, "Global inter-annual gravity changes from GRACE: early results," *Geophysical Research Letters*, vol. 32, no. 1, pp. 1–4, 2005.
- [12] G. Ramillien, A. Cazenave, and O. Brunau, "Global time variations of hydrological signals from GRACE satellite gravimetry," *Geophysical Journal International*, vol. 158, no. 3, pp. 813–826, 2004.
- [13] A. Güntner, "Improvement of global hydrological models using GRACE data," *Surveys in Geophysics*, vol. 29, no. 4-5, pp. 375–397, 2008.
- [14] D. D. Rowlands, S. B. Luthcke, S. M. Klosko et al., "Resolving mass flux at high spatial and temporal resolution using GRACE intersatellite measurements," *Geophysical Research Letters*, vol. 32, no. 4, article L4310, 2005.
- [15] D. Jianbin, Z. Min, Y. Haoming, and J. Min, "Recovery of land water storage variations in Chinese Mainland by use of GRACE data," *Journal of Geodesy and Geodynamics*, vol. 27, no. 3, pp. 68–71, 2007.
- [16] X. Su, J. Ping, and Q. Ye, "Study on water storage change using GRACE data in North China," *Chinese Science (Earth Science)*, vol. 42, pp. 917–922, 2012.
- [17] G. Strassberg, B. R. Scanlon, and D. Chambers, "Evaluation of groundwater storage monitoring with the GRACE satellite: case study of the high plains aquifer, Central United States," *Water Resources Research*, vol. 45, no. 5, Article ID W054102009, 2009.
- [18] R. R. Muskett and V. E. Romanovsky, "Alaskan permafrost groundwater storage changes derived from GRACE and ground measurements," *Remote Sensing*, vol. 3, no. 2, pp. 378–397, 2011.
- [19] S.-H. Ye, X.-L. Su, J.-S. Ping, and Q. Huang, "Land water storage variations in China and adjacent areas revealed by the GRACE gravity mission," *Journal of Jilin University*, vol. 41, no. 5, pp. 1580–1586, 2011.
- [20] X. G. Hu, J. Chen, Y. Zhou, C. Huang, and X. H. Miao, "GRACE space gravity measurements to monitor the use of the Yangtze River seasonal changes in water storage," *Science in China: Earth Science*, vol. 36, pp. 225–232, 2006.
- [21] H.-S. Wang, Z.-Y. Wang, X.-D. Yuan, P. Wu, and E. Rangelova, "Water storage changes in Three Gorges water systems area inferred from GRACE time-variable gravity data," *Chinese Journal of Geophysics*, vol. 50, no. 3, pp. 730–736, 2007.
- [22] L. Xing, H. Li, D. Liu, and X. Zhou, "Monthly water distribution in China and its adjacent area from time-variation gravity of GRACE," *Journal of Geodesy and Geodynamics*, vol. 27, pp. 35–38, 2007.
- [23] Y. Yang, E. Dongchen, D. Chao, and H. Wang, "Seasonal and inter-annual change in land water storage from GRACE," *Chinese Journal of Geophysics*, vol. 52, pp. 298–299, 2009.
- [24] Y. Cao and Z. Nan, "Monitoring water storage variations in the heihe river basin by the GRACE gravity satellite," *Remote Sensing Technology and Application*, vol. 26, no. 6, pp. 719–727, 2011.
- [25] P. Xu and W. Zhang, "Inversion of terrestrial water storage changes in recent years for Qinghai-Tibetan plateau and Yarlung Zangbo River basin by GRACE," *Journal of Water Resources & Water Engineering*, vol. 24, pp. 23–29, 2013.
- [26] R. Jiawen, Y. Baisheng, D. Yongjian, and L. Shiyin, "Preliminary estimates the potential contribution of cryospheric changes to sea level rise in China," *Chinese Science Bulletin*, vol. 56, pp. 1084–1087, 2013.
- [27] Z. Li, K. Li, and L. Wang, "Recent glacier change and its impact on water resources in Xinjiang," *Quaternary Sciences*, vol. 30, pp. 96–106, 2010.
- [28] Y. Ding, D. Yang, B. Ye, and N. Wang, "Effects of bias correction on precipitation trend over China," *Journal of Geophysical Research D: Atmospheres*, vol. 112, no. 13, Article ID D13116, 2007.
- [29] M. Xu, Y. Wang, Z. Y. Zhou, S. H. Yi, and B. S. Ye, "Discussion of methods on spatial interpolation for monthly temperature data in Yangtze River basin," *Resources and Environment in the Yangtze Basin*, vol. 21, pp. 327–334, 2012.
- [30] I. Velicogna and J. Wahr, "Measurements of time-variable gravity show mass loss in Antarctica," *Science*, vol. 311, no. 5768, pp. 1754–1756, 2006.
- [31] G. Strassberg, B. R. Scanlon, and M. Rodell, "Comparison of seasonal terrestrial water storage variations from GRACE with groundwater-level measurements from the High Plains Aquifer (USA)," *Geophysical Research Letters*, vol. 34, no. 14, Article ID L14402, 2007.
- [32] Z. Qidong, X. Cunde, and Q. Dahe, "In recent decades the Himalayan glacier change and its impact on water resources," *Journal of Glaciology and Geocryology*, vol. 31, pp. 885–895, 2009.
- [33] H. Lv, *Nearly 40 Years in Response to Fluctuations in the Himalayan Glaciers to Climate Change*, Lanzhou University, Lanzhou, China, 2013.
- [34] S. B. Kapnick, T. L. Delworth, M. Ashfaq, S. Malyshev, and P. C. Milly, "Snowfall less sensitive to warming in Karakoram than in Himalayas due to a unique seasonal cycle," *Nature Geoscience*, vol. 7, no. 11, pp. 834–840, 2014.
- [35] S. Yongping, S. Hongchao, and W. Guoya, "The responses of glaciers and snow cover to climate change in Xinjiang(1): hydrological effect," *Journal of Glaciology and Geocryology*, vol. 35, pp. 513–527, 2013.
- [36] T. Yao, L. Thompson, W. Yang et al., "Different glacier status with atmospheric circulations in Tibetan Plateau and surroundings," *Nature Climate Change*, vol. 2, no. 9, pp. 663–667, 2012.
- [37] L. Cheng and Y. Qu, *Water and Land Resources and Their Rational Development and Utilization in the Hexi Region*, Science Press, Beijing, China, 1992.
- [38] J. Yang, Z. Jiang, and X. Liu, "Influence research on spring vegetation of Eurasia to summer drought-wetness over the northwest China," *Arid Land Geography*, vol. 35, pp. 1–9, 2012.
- [39] W.-W. Qi, B.-P. Zhang, Y. Pang, F. Zhao, and S. Zhang, "TRMM-data-based spatial and seasonal patterns of precipitation in the Qinghai-Tibet plateau," *Scientia Geographica Sinica*, vol. 33, no. 8, pp. 999–1005, 2013.
- [40] D. Zhang, *The Temporal and Spatial Variations of Water Resource over the Tibet Plateau*, Lan Zhou University, 2013.
- [41] R. R. Muskett and V. E. Romanovsky, "Groundwater storage changes in arctic permafrost watersheds from GRACE and in situ measurements," *Environmental Research Letters*, vol. 4, no. 4, Article ID 045009, 2009.
- [42] T. Bolch, A. Kulkarni, A. Kääb et al., "The state and fate of Himalayan glaciers," *Science*, vol. 336, no. 6079, pp. 310–314, 2012.
- [43] K. Hewitt, "The Karakoram anomaly? Glacier expansion and the 'elevation effect,' Karakoram Himalaya," *Mountain Research and Development*, vol. 25, no. 4, pp. 332–340, 2005.
- [44] J. Gardelle, E. Berthier, and Y. Arnaud, "Slight mass gain of Karakoram glaciers in the early twenty-first century," *Nature Geoscience*, vol. 5, no. 5, pp. 322–325, 2012.

- [45] M. Xu, B. Ye, and Q. Zhao, "Temporal and spatial patterns of water storage change of Tianshan in the last 8 years based on GRACE," *Arid Zone Research*, vol. 30, pp. 404–411, 2013.
- [46] M. Xu, S. Zhang, J. Wang, Q. Zhao, and C. Zhao, "Temporal and spatial patterns of water storage change of Qilian Mountains in recent 8 years based on GRACE," *Arid Land Geography*, vol. 37, pp. 458–467, 2014.

Research Article

Validation of the Accuracy of Different Precipitation Datasets over Tianshan Mountainous Area

Chuanheng Zhao,^{1,2} Shuxia Yao,² Shiqiang Zhang,³ Haidong Han,¹
Qiudong Zhao,¹ and Shuhua Yi¹

¹State Key Laboratory of Cryospheric Sciences, Cold and Arid Regions Environmental and Engineering Research Institute, Chinese Academy of Sciences, Lanzhou 730000, China

²Lanzhou City University, Lanzhou 730070, China

³College of Urban and Environmental Science, Northwest University, Xi'an 710127, China

Correspondence should be addressed to Shuxia Yao; yaoshuxia@163.com

Received 5 November 2014; Revised 26 February 2015; Accepted 26 February 2015

Academic Editor: Hann-Ming H. Juang

Copyright © 2015 Chuanheng Zhao et al. This is an open access article distributed under the Creative Commons Attribution License, which permits unrestricted use, distribution, and reproduction in any medium, provided the original work is properly cited.

Precipitation is one of the important water supplies in the arid and semiarid regions of northwestern China, playing a vital role in maintaining the fragile ecosystem. In remote mountainous area, it is difficult to obtain an accurate and reliable spatialization of the precipitation amount at the regional scale due to the inaccessibility, the sparsity of observation stations, and the complexity of relationships between precipitation and topography. Furthermore, accurate precipitation is important driven data for hydrological models to assess the water balance and water resource for hydrologists. Therefore, the use of satellite remote sensing becomes an important means over mountainous area. Precipitation datasets based on station data or pure satellite data have been increasingly available in spite of several weaknesses. This paper evaluates the usefulness of three precipitation datasets including TRMM 3B43_V6, 3B43_V7, and Asian Precipitation Highly Resolved Observational Data Integration Towards Evaluation with rain gauge data over Tianshan mountainous area where precipitation data is scarce. The results suggest that precipitation measurements only provided accurate information on a small scale, while the satellite remote sensing of precipitation had obvious advantages in basin scale or large scale especially over remote mountainous area.

1. Introduction

Mountainous areas play a critical role in maintaining water resource supply in the arid and semiarid regions [1, 2]. However, due to the inaccessibility, the sparsity of observation stations, and the complexity of relationships between precipitation and topography, little data has generally been collected in mountainous areas, and it is difficult to obtain an accurate and reliable spatialization of precipitation amount at the regional scale [3–5]. Many researchers have indicated that in the arid and semiarid regions, including the northwest of China, mountainous areas contribute 40–85% of total runoff, while in subhumid areas the contribution only varies from 20% to 50% [6–10]. As one important input parameter for hydrological and ecological models, how to obtain high resolution precipitation data in remote mountainous areas is a true challenge for researchers [11, 12].

In general, precipitation data is mainly obtained by rain gauge measurement, estimation, and modeling. Because of complex terrain, the density of rain gauge networks is seriously limited in mountainous area, and the distribution is unreasonable and even practically impossible in high mountainous area. Hence, accurate understanding of the distribution and characteristics of mountainous precipitation is particularly difficult. In recent decades, with the development of remote sensing techniques, precipitation data with relatively uniform and consistent information with temporal and spatial coverage has become available in some remote regions lacking data. On the basis of this, the precipitation datasets based on satellite remote sensing in hydrological and meteorological stations have increased significantly in the past few decades [13–15]. However, there are always different types of error such as inherent measurement and retrieval

errors and sampling uncertainty. In order to obtain accurate data, the precipitation datasets based on satellite need to be calibrated or verified by comparison with ground-based rain gauge data [16–18].

There are a number of precipitation datasets with distinct characteristics at different temporal and spatial scales, and they are helpful to study global warming, the hydrological cycle, and economic activities at large scale. These datasets include Climate Research Unit (CRU) precipitation datasets [19], Global Precipitation and Climatology Project (GPCP) One-Degree Daily [20], and CPC Merged Analysis of Precipitation (CMAP) [21]. These datasets can be divided into two categories: one provides high resolution to meet spatial resolution requirement but lacks time series, and the other displays great stability for year long-term but sacrifices temporal and spatial resolution [22, 23]. The CRU precipitation datasets can originate station measurement using thin-plate splines interpolation with up to 14500 stations and provide precipitation data of all continents except Antarctica at $0.5^\circ \times 0.5^\circ$ resolution from the period 1901 to 2001. The GPCP One-Degree Daily precipitation datasets can adjust the satellite estimation to the gauge bias and then combine multisatellites with rain gauge through inverse error-variance weighting, which can provide precipitation data globally at $1^\circ \times 1^\circ$ resolution from October 1996 forward. The CMAP datasets can merge different kinds of information sources with different characteristics, including gauge observations, estimates from a variety of satellite observations, and the NCEP-NCAR reanalysis, and provide global precipitation monthly at $2.5^\circ \times 2.5^\circ$ resolution from 1979 onwards. Besides, the datasets can reduce random errors by linearly combining satellite estimates using the maximum likelihood method and give an inversely proportional weight to the linear combination coefficients in relation to the square of the random error of the individual sources [23].

The Tianshan mountainous area is located in the northwest of China, stretched from west to east, and divides Xinjiang into two parts, that is, Southern Xinjiang and Northern Xinjiang [24–26]. This area is situated in the hinterland of Eurasian continent far away from the ocean, and precipitation is the main source of surface water for river runoff, farm irrigation, and urban water consumption. The west wind current owing to the prevailing westerlies is the major vapor resource over Tianshan mountainous area, and the dry and cold current from the Arctic Ocean is the second resource, whose vapor content is equal to 25–33% of that of the west wind current [26]. As a result, the Tianshan mountainous area presents more precipitation in the north than in the south, more in the west than in the east, more in the mountainous area than in the plain area, and more on the windward slope than on the leeward slope [27]. Zonal vertical distribution of mountainous precipitation is very obvious [25].

To address this, this paper tries to point out the similarities and discrepancies over the Tianshan mountainous area from 1998 to 2007 by virtue of comparing the monthly precipitation datasets of TRMM 3B43_V6, the new version of 3B43_V7, and APHRODITE with rain gauge data. According to the results, the applicability of these datasets for hydrological and ecological models in mountainous area is evaluated

to provide some suggestions for decision makers including agriculturalists, emergency managers, and industrialists.

2. Data and Methodology

2.1. Data Collection. The Tropical Rainfall Measuring Mission (TRMM) is a joint US-Japan program to monitor tropical and subtropical rainfall, which provides the hourly, daily, and monthly precipitation datasets of the NASA Goddard Space Flight Centre with high resolution. The datasets have shown good performance in different regions around the world including Asian region [28–30]. TRMM 3B43_V6 is a monthly precipitation dataset with spatial resolution of $0.25^\circ \times 0.25^\circ$ covering 50°N – 50°S from 1998 onwards [31]. This dataset combines the estimates generated by the TRMM 3B42 with other satellite datasets and calibrates against globally gridded monthly rain gauge data to scale the estimates. On May 22, 2012, the new version of TRMM, 3B43_V7, was implemented, and the functions of TRMM were further enhanced. Notably, although the TRMM algorithm ensures every grid box has the best possible estimate, it can also result in statistically heterogeneous datasets [32].

APHRODITE precipitation datasets are produced using a modified version of the distance-weighting interpolation method to interpolate rain gauge observations from meteorological stations generated by the Asian Precipitation Highly Resolved Observational Data Integration Towards Evaluation (APHRODITE) of Water Resources project [33]. The datasets use daily precipitation climatology to interpolate the ratio of the daily precipitation to the climatology with a resolution of 0.05 degrees and then multiply each gridded ratio by each gridded climatology value day-by-day. APHRODITE has released several daily precipitation datasets since 2008 over Monsoon Asia (MA), Middle East (ME), and Russia (RU) with resolution of $0.25^\circ \times 0.25^\circ$ and $0.5^\circ \times 0.5^\circ$, which were considered as “ground-truth” precipitation datasets throughout the region [34]. Thereinto, the APHRODITE_V1003R1 is a daily dataset released in 2010 and monthly data used in this research is cumulated on daily data obtained from this dataset.

Monthly precipitation was used for 32 stations in the Tianshan mountainous area (Figure 1). Quality of the datasets was firmly controlled and homogeneity tests were also performed before its release [35]. Most stations were distributed in low elevations from 35 to 3539 m as presented in Table 1, and no stations were distributed in high mountains over 4000 m. The series of datasets were different in this research, and comparisons were made over a 10-year period from 1998 to 2007.

2.2. Methodology. The same resolution was set for TRMM 3B43_V6, 3B43_V7, and APHRODITE_V1003R1, and the precipitation datasets were quantitatively compared on a cell-by-cell basis to avoid losing fine details when the datasets were aggregated and assessed [36]. The nearly gridded data was selected to be compared with station data because of the resolution difference of station data with TRMM 3B43_V6, 3B43_V7, and APHRODITE_V1003R1. The quantitative accuracy of precipitation datasets was assessed by the root-mean

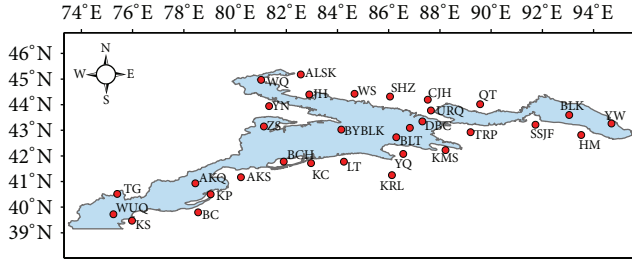


FIGURE 1: Location of the study area and distribution of meteorological stations.

square error (RMSE), the root-mean square factor (RMSF), and correlation coefficient (R).

The RMSE is a common accuracy measure that is usually used as the measure of magnitude of errors in time series [37, 38], which can be calculated as follows:

$$\text{RMSE} = \sqrt{\frac{1}{n} \sum_{i=1}^n (x_i - y_i)^2}, \quad (1)$$

where n is the length of datasets in time series and x_i and y_i stand for two compared datasets at time i for each grid, respectively. However, the RMSE mainly emphasizes the differences resulting from erroneous data and only provides limited information for further research. Whereas the RMSF has been found to provide more information than the RMSE, the RMSF comparing the two datasets is also calculated as follows:

$$\text{RMSF} = \exp \left\{ \frac{1}{n} \sum_{i=1}^n \left[\ln \left(\frac{x_i}{y_i} \right)^2 \right] \right\}^{1/2}. \quad (2)$$

The closer the RMSF value is to 1, the more accurate the two compared datasets.

3. Results

Before comparing different precipitation databases, a general description of the mean annual precipitation field of 3B43_V6, 3B43_V7, and APHRODITE_V1003R1 is given. The mean annual precipitation over the Tianshan mountainous area displays a well-known pattern of more mean annual precipitation in the north than in the south and more in the west than in the east during the period 1998 to 2007. Figure 2 illustrates the mean annual precipitation distribution of the three different databases. It can be seen that the mean annual precipitation of APHRODITE_V1003R1 varies from 54 to 684 mm, that of 3B43_V6 from 77 to 590 mm, and that of 3B43_V7 from 68 to 786 mm. The spatial distribution of these datasets is basically similar over the whole study areas, while the 3B43_V6 shows lower values in northern Ili Valley. Considering the amount, the patterns displayed by the APHRODITE_V1003R1 and 3B43_V7 are better than that of 3B43_V6.

TABLE 1: Geographical coordinates of the meteorological stations of Tianshan mountainous area.

Weather station	Longitude (°E)	Latitude (°N)	Elevation (m)
Aksu (AKS)	80.23	41.17	1104
Baicheng (BCH)	81.9	41.78	1229
Kuche (KC)	82.97	41.72	1082
Keping (KP)	79.05	40.5	1162
Baluntai (BLT)	86.3	42.73	1739
Bayanbulak (BYB)	84.15	43.03	2458
Yanqi (YQ)	86.57	42.08	1055
Luntai (LT)	84.25	41.78	976
Korla (KRL)	86.13	41.25	932
Alashankou (ALSK)	82.57	45.18	336
Wenquan (WQ)	81.02	44.97	1358
Jinghe (JH)	82.9	44.4	320
Caijiahu (CJH)	87.53	44.2	440
Qitai (QT)	89.57	44.02	794
Shijianfang (SSJF)	91.73	43.22	721
Balikun (BLK)	93.05	43.6	1677
Yiwu (YW)	94.7	43.27	1728
Hami (HM)	93.52	42.82	737
Kashgar (KS)	75.98	39.47	1289
Bachu (BC)	78.56	39.8	1117
Torugart (TG)	75.4	40.52	3504
Wuqia (WUQ)	75.25	39.72	2175
Akqi (AKQ)	78.45	40.93	1985
Shihezi (SHZ)	86.05	44.32	442
Wusu (WS)	84.67	44.43	478
Kumishi (KMS)	88.22	42.23	922
Turpan (TRP)	89.2	42.93	35
Urumqi (URQ)	87.65	43.78	935
Daxigou (DXG)	86.83	43.1	3539
Dabancheng (DBC)	87.32	43.35	1104
Yining (YN)	81.33	43.95	663
Zhaosu (ZS)	81.13	43.15	1851

3.1. *TRMM 3B43_V6 and APHRODITE_V1003R1*. The statistics of R , RMSE, and RMSF are first calculated between the APHRODITE_V1003R1 and TRMM 3B43_V6, as shown in Figure 3. It is obvious that the description of the interpolation data highlights the existence of similarities and discrepancies with satellite-based data, not only in terms of temporal and spatial distribution, but also in terms of total amount of precipitation. The spatial distribution of correlation value provides a more complete picture that the value is higher in the south than in the north and higher in the east than in the west (Figure 3(a)). In the middle and west parts of Tianshan mountainous area, the value of correlation coefficient is higher than 0.85, which indicates a good performance between the two databases, while in the north and west parts of the region, the value is lower than 0.2, which indicates that the two databases work badly at the position where the precipitation amount is high, especially in the Ili Valley. In the whole study area, the spatial distribution of RMSE is

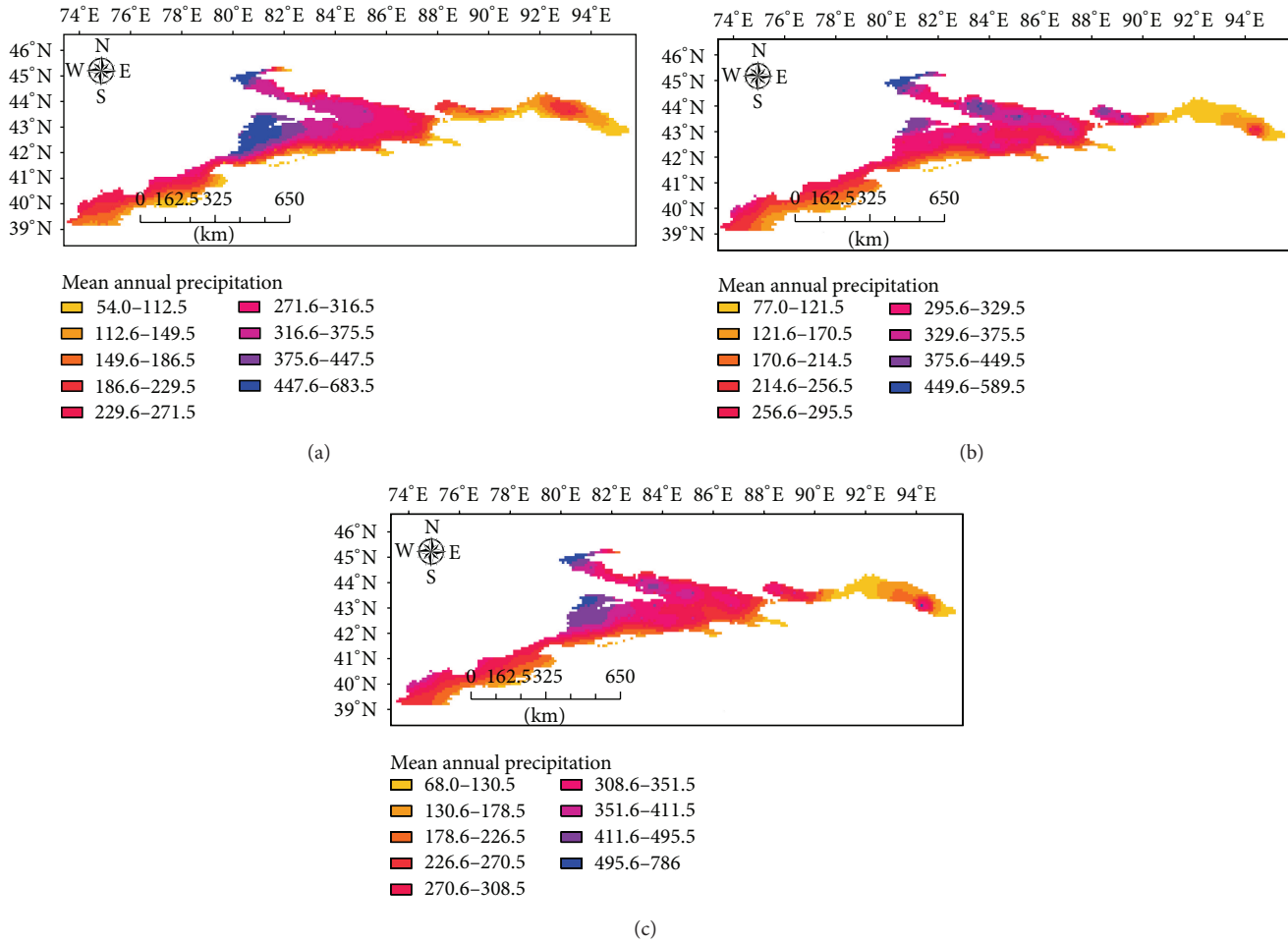


FIGURE 2: Spatial distribution of mean annual precipitation during 1998~2007. (a) APHRODITE_V1003R1, (b) 3B43_V6, and (c) 3B43_V7.

reverse to that of correlation coefficient (Figure 3(b)); namely, higher RMSE can be obtained over the high precipitation area while correlation coefficient would be lower. On the contrary, the spatial distribution of RMSF presents good consistency with that of correlation coefficient (Figure 3(c)), which means the two databases work well in low mountainous area but fail in the area where orographic precipitation has a greater influence on the amount of precipitation.

3.2. TRMM 3B43_V7 and APHRODITE_V1003R1. Figure 4 shows the spatial distribution of R , RMSE, and RMSF between the APHRODITE_V1003R1 and TRMM 3B43_V7. It can be seen that the value of correlation coefficient (Figure 4(a)) has been greatly improved compared with Figure 3(a) in the whole study area, which means the two databases have good consistency in most grid cells. In the middle of Tianshan mountainous area especially the Ili Valley, the improvement is most obvious relative to those in the east and west. The RMSE and RMSF have also been significantly improved (Figures 4(b) and 4(c)). The spatial distribution in Figures 4(b) and 4(c) is identical to that in Figures 3(b) and 3(c); the relationship is reverse between RMSE and R but consistent between RMSF and R . In general,

the higher the precipitation, the lower the value of R and RMSF and the higher the value of RMSE.

3.3. Validation of the Rain Gauge and Precipitation Datasets. Considering sparse rain gauge distribution in Tianshan mountainous area, the accuracy evaluation on the satellite-based database, and the calculation of R , RMSE, and RMSF are carried out only in 32 grids containing stations for annual precipitation between TRMM 3B43_V6, 3B43_V7, APHRODITE_V1003R1, and rain gauge data.

3.3.1. TRMM 3B43_V6 and Rain Gauge Data. The patterns of TRMM 3B43_V6 and rain gauge are showing that the correlation coefficients are statistically significant across much of Tianshan mountainous area. The value of correlation coefficient is greater in the south than in the north and greater in the west than in the east. The value is less than 0.1 among WQ, WS, ZS, and SSJF, while being up to 0.9 for many stations in the south slope. The RMSE value follows reverse spatial patterns of the correlation coefficients and reaches its maximum of above 250 mm in the Ili Valley. The RMSF follows similar spatial patterns to the RMSE, which is lower

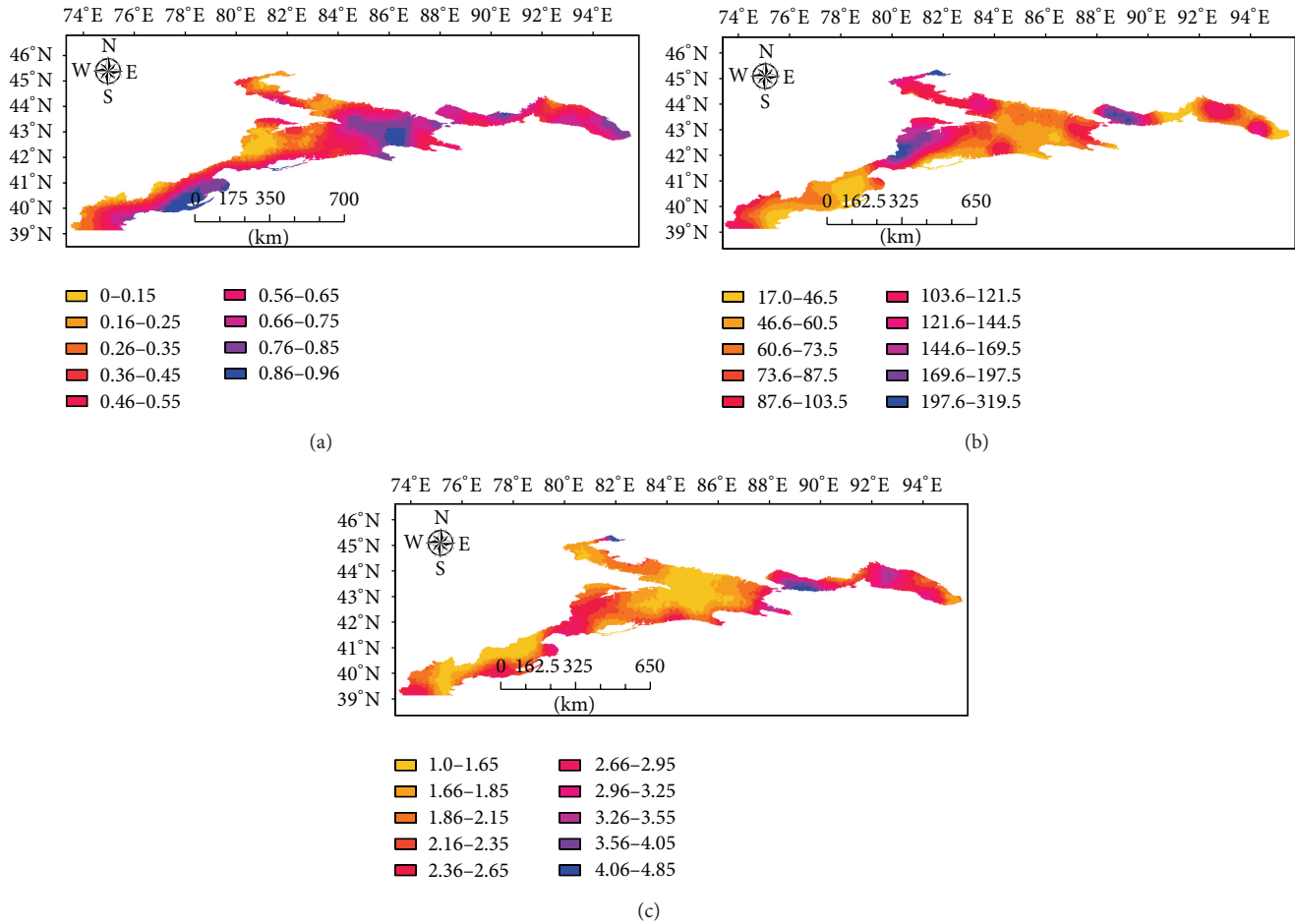


FIGURE 3: Spatial distribution of annual precipitation during 1998~2007 produced by APHRODITE_V1003R1 and TRMM 3B43_V6. (a) Correlation coefficient, (b) RMSE, and (c) RMSE.

in the south than in the north and lower in the west than in the east, with its maximum in the TRP. The results indicate that the two databases are well matched in the west and the middle compared with the east of Tianshan mountainous area.

The spatial distributions of correlation coefficient of TRMM 3B43_V6 against rain gauge have shown obvious seasonal characteristics. During winter, the correlation coefficient between TRMM 3B43_V6 and rain gauge is above 0.5 except individual stations, while correlation coefficient is declining with elevation rising which stations are above 2000 m. In spring, the relationship between elevation and correlation coefficient is relatively complex. Firstly, the correlation coefficient is increasing with station elevation rising about 1100 m. After this point, the correlation coefficient is decreasing with station elevation rising. This pattern is also reflected in the fall. In summer, the correlation coefficient is increasing with station elevation rising. Therefore, the relationship between precipitation and terrain can be portrayed in TRMM 3B43_V6 datasets.

3.3.2. TRMM 3B43_V7 and Rain Gauge Data. The pattern of correlation coefficient indicates the significant improvement

between TRMM 3B43_V7 and rain gauge data at almost all stations over whole study area, while the spatial distribution characteristic of correlation value follows similar patterns to TRMM 3B43_V6 and rain gauge, where the correlation value is greater in the south than in the north. The minimum value of correlation is larger than 0.34 in SSJF and HM of the east parts of Tianshan mountainous area, and the greater error with RMSE exceeding 100 mm is observed in the east center and Ili Valley. The spatial distribution characteristic of RMSE is reverse to that of RMSE, where the value is lower except the east center and Ili Valley. The results indicate that the TRMM 3B43_V7 database matches with rain gauge data better over Tianshan mountainous area than the TRMM 3B43_V6 database does.

3.3.3. APHRODITE_V1003R1 and Rain Gauge Data. As the APHRODITE precipitation datasets are produced by interpolation using rain gauge observations, the results are well matched with rain gauge data in most grid cells compared with the two versions of TRMM. Figure 5 depicts the monthly variations of precipitation of the selected stations and grid boxes for rain gauge and APHRODITE with correlation

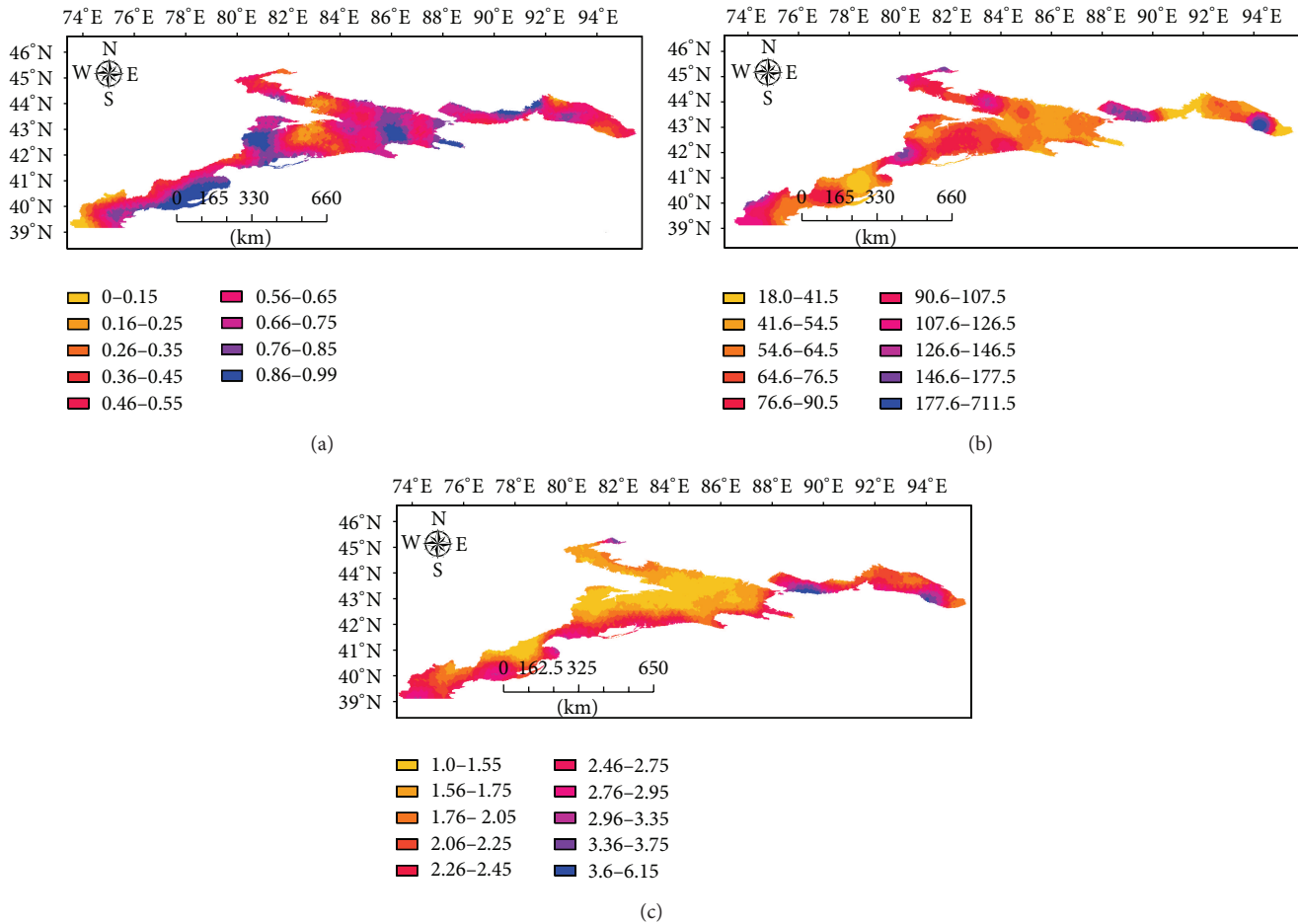


FIGURE 4: Spatial distribution of annual precipitation during 1998~2007 produced by APHRODITE_V1003R1 and TRMM 3B43_V7. (a) Correlation coefficient, (b) RMSE, and (c) RMSE.

coefficient 0.59 (YW), 0.8 (TRP), and 0.95 (BLT), respectively, during the period 1998–2007. Generally, it is apparent that the rain gauge data is greater than the APHRODITE data (see Figures 5(a) and 5(c)), while correlation coefficient is 0.59 and 0.95, respectively. However, as a Global Telecommunication System station used in the interpolation, The APHRODITE, may be overestimated, is higher than rain gauge with correlation coefficient 0.8 in TRP which is lower than BLT. During the drought in winter, the rain gauge data has shown good consistency with APHRODITE data. On the contrary, the more the monthly precipitation, the more significant, the difference between rain gauges with APHRODITE, especially in summer. Thus, the validation of APHRODITE datasets is necessary especially in mountainous areas.

4. Discussion and Conclusions

4.1. Discussion. Except the altitude, the variability and distribution of precipitation were affected by elevation, mountains toward, vapor source, and so forth. The elevation is the most significant impact among them, especially in the mountainous area. Thus, the quality of precipitation data can be reflected by the relationship between the precipitation

data and elevation. As for the consistency, the each grid cell contained at least one station has been selected, and elevation of each grid cell is extracted by using the digital elevation model. The correlation coefficients of the annual mean precipitation between APHRODITE, TRMM 3B43_V6, TRMM 3B43_V7, rain gauge, and elevation are calculated, respectively (Figure 6). Obviously, the correlation coefficient between rain gauge and elevation is the highest among them, while it is not significant difference in the relationship between APHRODITE, TRMM 3B43_V6, TRMM 3B43_V7, and elevation. As for the stations or grid cells below the 1500 m, part of the stations or grid cells are located in the north slope of Tianshan mountainous area which is windward, especially the Ili River Valley, and other stations or grid cells are located in the south of the piedmont Gobi; the relationship between precipitation and elevation is affected by these stations or grid cells. However, above 1500 m, the relationship between precipitation and elevation is more significant.

The correlation coefficients of the average monthly precipitation between APHRODITE, TRMM 3B43_V6, TRMM 3B43_V7, rain gauge, and elevation are analyzed. The results have shown that the relationship between the rain gauge

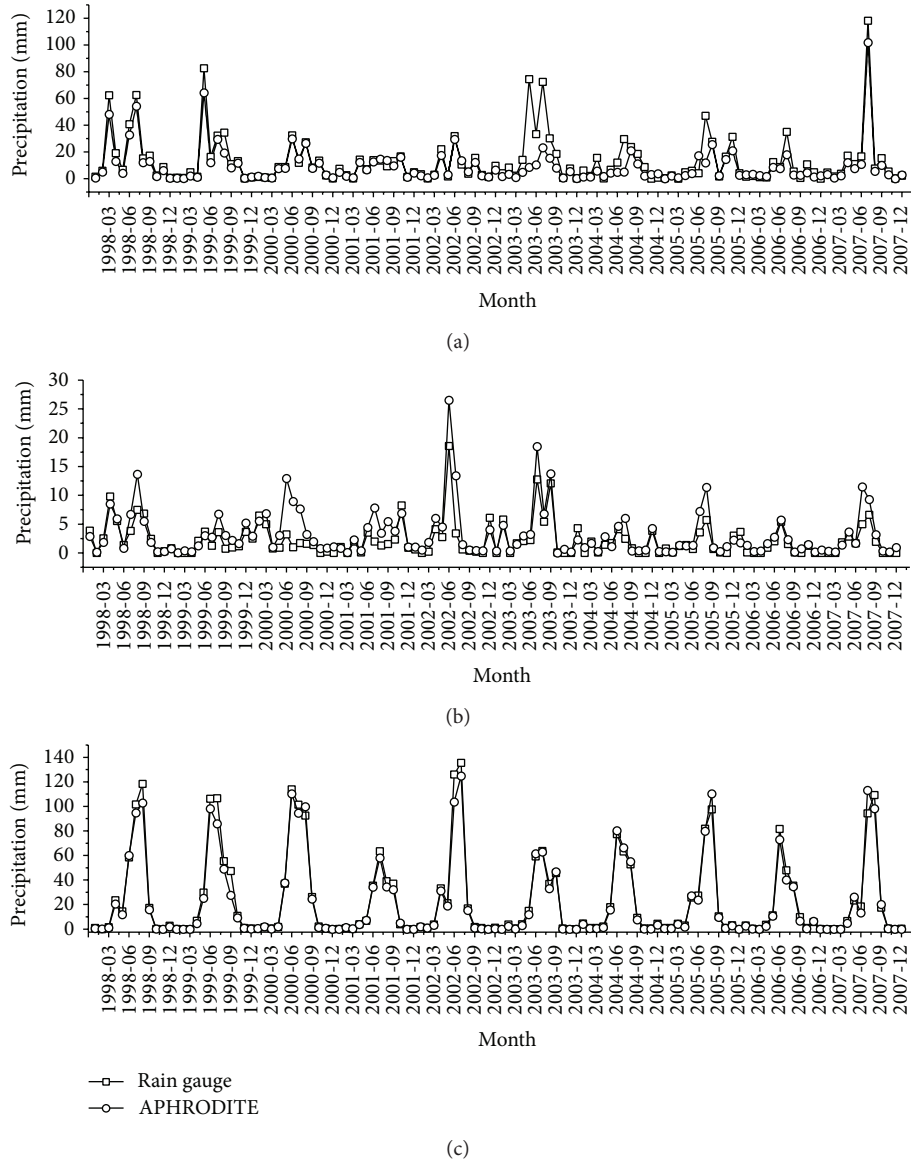


FIGURE 5: Average monthly precipitation of the 3 selected stations and grid boxes, respectively ((a) YW, $R = 0.59$; (b) TRP, $R = 0.8$; and (c) BLT, $R = 0.95$).

and elevation is still the best, but poor between the TRMM 3B43.V6 and elevation. Overall, the relationship between precipitation and elevation presented negative correlation in January and February; the correlation coefficient is low and did not pass the test of significance. But this relationship is reversed in March. The relationship between precipitation and elevation has exhibited weak positive correlation in March and April and has shown a significant positive correlation from May to September, passing the test of significance. With the increase in precipitation, the correlation coefficient is increased. However, the relationship is reversed in October; the correlation is not significant. The main reason is that rainy season is from April to September over Tianshan mountainous area and amount of precipitation from April to September accounts for 80% of annual precipitation,

and most of precipitation is liquid easily observed. The precipitation is solid and is greatly influenced by the wind; the accuracy is not high, especially for the remote datasets in January, February, November, and December. It is obvious that the relationship between precipitation and elevation has influence on this factor.

4.2. Conclusions. The comparison between several kinds of precipitation datasets has shown good agreement over the Tianshan mountainous area but rather poor agreement in some regions. Similar precipitation patterns have been identified according to the results of all datasets, which perform well over the whole study area except the east center and Ili Valley. Compared with APHRODITE, it is obvious that TRMM 3B43.V7 performs better than TRMM 3B43.V6

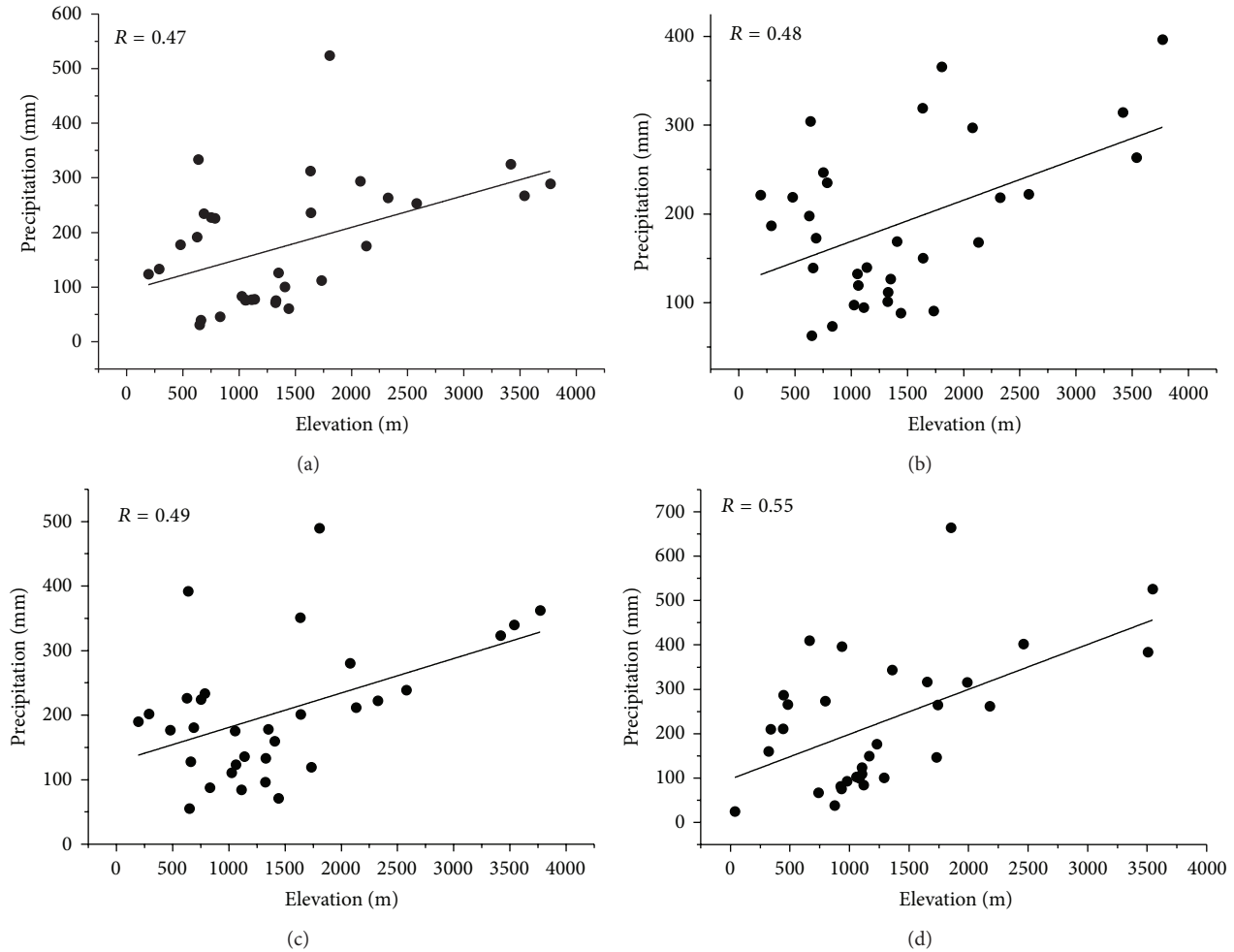


FIGURE 6: The correlation coefficient of annual mean precipitation and elevation. (a) Correlation coefficient of APHRODITE and elevation, (b) correlation coefficient of TRMM_V6 and elevation, (c) correlation coefficient of TRMM_V7 and elevation, and (d) correlation coefficient of rain gauge and elevation, respectively.

over the whole study areas. Compared with observations, the TRMM 3B43_V7 and APHRODITE perform better than TRMM 3B43_V6 in the low or middle mountainous regions, while all datasets perform badly in high mountainous area in the case of sparse data. Several kinds of precipitation data can be depicted from the relationship between precipitation and elevation, and the higher the monthly precipitation, the more significant the correlation.

The intricate variation and correlation of climatic, topographic, and environmental variables over Tianshan mountainous area mean that detecting spatial variation in precipitation is extremely complex. Fortunately, with the improvement of accuracy, the precipitation datasets based on satellite remote sensing will provide wide prospects over remote mountainous areas for researchers.

Conflict of Interests

The authors declare that there is no conflict of interests regarding the publication of this paper.

Acknowledgments

This study was supported by the National Science Foundation of China (NSFC) under Grants no. 41130641, 41130638, 41361013, 31300388, the Knowledge Innovation Program of the Chinese Academy of Sciences (no. KZCX2-YW-GJ04), and Lanzhou City University Ph.D. Research Fund (LZCU-BS2013-09, LZCU-BS2013-12). The authors also would like to acknowledge the helpful comments and suggestions from anonymous referees.

References

- [1] C. de Jong, D. Lawler, and R. Essery, "Mountain hydroclimatology and snow seasonality—perspectives on climate impacts, snow seasonality and hydrological change in mountain environments," *Hydrological Processes*, vol. 23, no. 7, pp. 955–961, 2009.
- [2] J. I. López-Moreno, S. M. Vicente-Serrano, E. Morán-Tejada, J. Lorenzo-Lacruz, A. Kenawy, and M. Beniston, "Effects of the North Atlantic Oscillation (NAO) on combined temperature and precipitation winter modes in the Mediterranean

- mountains: observed relationships and projections for the 21st century,” *Global and Planetary Change*, vol. 77, no. 1-2, pp. 62–76, 2011.
- [3] X. Zhang and R. Srinivasan, “GIS-based spatial precipitation estimation using next generation radar and raingauge data,” *Environmental Modelling and Software*, vol. 25, no. 12, pp. 1781–1788, 2010.
 - [4] M. Li and Q. X. Shao, “An improved statistical approach to merge satellite rainfall estimates and raingauge data,” *Journal of Hydrology*, vol. 385, no. 1-4, pp. 51–64, 2010.
 - [5] F. Gottardi, C. Obled, J. Gailhard, and E. Paquet, “Statistical reanalysis of precipitation fields based on ground network data and weather patterns: application over French mountains,” *Journal of Hydrology*, vol. 432-433, pp. 154–167, 2012.
 - [6] D. Viviroli, H. H. Dürr, B. Messerli, M. Meybeck, and R. Weingartner, “Mountains of the world, water towers for humanity: typology, mapping, and global significance,” *Water Resources Research*, vol. 43, no. 7, Article ID W07447, 2007.
 - [7] Z. Ma, S. Z. Kang, L. Zhang, L. Tong, and X. Su, “Analysis of impacts of climate variability and human activity on streamflow for a river basin in arid region of northwest China,” *Journal of Hydrology*, vol. 352, no. 3-4, pp. 239–249, 2008.
 - [8] O. Olsson, M. Gassmann, K. Wegerich, and M. Bauer, “Identification of the effective water availability from streamflows in the Zerafshan river basin, Central Asia,” *Journal of Hydrology*, vol. 390, no. 3-4, pp. 190–197, 2010.
 - [9] B. F. Li, Y. N. Chen, Z. S. Chen, and W. H. Li, “Trends in runoff versus climate change in typical rivers in the arid region of Northwest China,” *Quaternary International*, vol. 282, pp. 87–95, 2012.
 - [10] Y. Luo, J. Arnold, S. Y. Liu, X. Wang, and X. Chen, “Inclusion of glacier processes for distributed hydrological modeling at basin scale with application to a watershed in Tianshan Mountains, northwest China,” *Journal of Hydrology*, vol. 477, pp. 72–85, 2013.
 - [11] C. S. Ngongondo, “An analysis of long-term rainfall variability, trends and groundwater availability in the Mulunguzi river catchment area, Zomba mountain, Southern Malawi,” *Quaternary International*, vol. 148, no. 1, pp. 45–50, 2006.
 - [12] C. A. Velasco-Forero, D. Sempere-Torres, E. F. Cassiraga, and J. Jaime Gómez-Hernández, “A non-parametric automatic blending methodology to estimate rainfall fields from rain gauge and radar data,” *Advances in Water Resources*, vol. 32, no. 7, pp. 986–1002, 2009.
 - [13] A. Milewski, M. Sultan, E. Yan et al., “A remote sensing solution for estimating runoff and recharge in arid environments,” *Journal of Hydrology*, vol. 373, no. 1-2, pp. 1–14, 2009.
 - [14] W. W. Immerzeel, P. Droogers, S. M. de Jong, and M. F. P. Bierkens, “Large-scale monitoring of snow cover and runoff simulation in Himalayan river basins using remote sensing,” *Remote Sensing of Environment*, vol. 113, no. 1, pp. 40–49, 2009.
 - [15] U. Germann, M. Berenguer, D. Sempere-Torres, and M. Zappa, “REAL-ensemble radar precipitation estimation for hydrology in a mountainous region,” *Quarterly Journal of the Royal Meteorological Society*, vol. 135, no. 639, pp. 445–456, 2009.
 - [16] D. A. Vila, L. G. G. de Goncalves, D. L. Toll, and J. R. Rozante, “Statistical evaluation of combined daily gauge observations and rainfall satellite estimates over continental South America,” *Journal of Hydrometeorology*, vol. 10, no. 2, pp. 533–543, 2009.
 - [17] A. Aghakouchak, E. Habib, and A. Bárdossy, “A comparison of three remotely sensed rainfall ensemble generators,” *Atmospheric Research*, vol. 98, no. 2-4, pp. 387–399, 2010.
 - [18] S. Javanmard, A. Yatagai, M. I. Nodzu, J. Bodaghjamali, and H. Kawamoto, “Comparing high-resolution gridded precipitation data with satellite rainfall estimates of TRMM_3B42 over Iran,” *Advances in Geosciences*, vol. 25, pp. 119–125, 2010.
 - [19] M. New, M. Hulme, and P. Jones, “Representing twentieth-century space-time climate variability. Part II: development of 1901–96 monthly grids of terrestrial surface climate,” *Journal of Climate*, vol. 13, no. 13, pp. 2217–2238, 2000.
 - [20] G. J. Huffman, R. F. Adler, D. T. Bolvin et al., “The TRMM multisatellite precipitation analysis (TMPA),” in *Satellite Rainfall Applications for Surface Hydrology*, pp. 3–22, Springer, Dordrecht, The Netherlands, 2010.
 - [21] P. P. Xie and P. A. Arkin, “Global precipitation: a 17-year monthly analysis based on gauge observations, satellite estimates, and numerical model outputs,” *Bulletin of the American Meteorological Society*, vol. 78, no. 11, pp. 2539–2558, 1997.
 - [22] C. Kidd and G. Huffman, “Global precipitation measurement,” *Meteorological Applications*, vol. 18, no. 3, pp. 334–353, 2011.
 - [23] F. J. Tapiador, F. J. Turk, W. Petersen et al., “Global precipitation measurement: methods, datasets and applications,” *Atmospheric Research*, vol. 104-105, pp. 70–97, 2012.
 - [24] Z. Wu, H. Zhang, C. M. Krause, and N. S. Cobb, “Climate change and human activities: a case study in Xinjiang, China,” *Climatic Change*, vol. 99, no. 3, pp. 457–472, 2010.
 - [25] X. Li, F. Jiang, L. Li, and G. Wang, “Spatial and temporal variability of precipitation concentration index, concentration degree and concentration period Xinjiang, China,” *International Journal of Climatology*, vol. 31, no. 11, pp. 1679–1693, 2011.
 - [26] H. B. Ling, H. L. Xu, J. Y. Fu, Q. Q. Zhang, and X. W. Xu, “Analysis of temporal-spatial variation characteristics of extreme air temperature in Xinjiang, China,” *Quaternary International*, vol. 282, pp. 14–26, 2012.
 - [27] C. C. Xu, Y. N. Chen, Y. H. Yang, X. Hao, and Y. Shen, “Hydrology and water resources variation and its response to regional climate change in Xinjiang,” *Journal of Geographical Sciences*, vol. 20, no. 4, pp. 599–612, 2010.
 - [28] T. Dinku, P. Ceccato, E. Grover-Kopec, M. Lemma, S. J. Connor, and C. F. Ropelewski, “Validation of satellite rainfall products over East Africa’s complex topography,” *International Journal of Remote Sensing*, vol. 28, no. 7, pp. 1503–1526, 2007.
 - [29] Q. Liu and Y. F. Fu, “An examination of summer precipitation over Asia based on TRMM/TMI,” *Science in China, Series D: Earth Sciences*, vol. 50, no. 3, pp. 430–441, 2007.
 - [30] F. G. Su, Y. Hong, and D. P. Lettenmaier, “Evaluation of TRMM multisatellite precipitation analysis (TMPA) and its utility in hydrologic prediction in the La Plata Basin,” *Journal of Hydrometeorology*, vol. 9, no. 4, pp. 622–640, 2008.
 - [31] G. J. Huffman, D. T. Bolvin, E. J. Nelkin et al., “The TRMM Multisatellite Precipitation Analysis (TMPA): quasi-global, multi-year, combined-sensor precipitation estimates at fine scales,” *Journal of Hydrometeorology*, vol. 8, no. 1, pp. 38–55, 2007.
 - [32] M. Kizza, I. Westerberg, A. Rodhe, and H. K. Ntale, “Estimating areal rainfall over Lake Victoria and its basin using ground-based and satellite data,” *Journal of Hydrology*, vol. 464-465, pp. 401–411, 2012.
 - [33] A. Yatagai, K. Kamiguchi, O. Arakawa, A. Hamada, N. Yasutomi, and A. Kitoh, “APHRODITE: constructing a long-term daily gridded precipitation dataset for Asia based on a dense network of rain gauges,” *Bulletin of the American Meteorological Society*, vol. 93, no. 9, pp. 1401–1415, 2012.

- [34] A. Yatagai, O. Arakawa, K. Kamiguchi, H. Kawamoto, M. I. Nodzu, and A. Hamada, "A 44-year daily gridded precipitation dataset for Asia based on a dense network of rain gauges," *SOLA*, vol. 5, pp. 137–140, 2009.
- [35] Y. Ding, Z. Wang, and Y. Sun, "Inter-decadal variation of the summer precipitation in East China and its association with decreasing Asian summer monsoon. Part I: observed evidences," *International Journal of Climatology*, vol. 28, no. 9, pp. 1139–1161, 2008.
- [36] J. M. A. Duncan and E. M. Biggs, "Assessing the accuracy and applied use of satellite-derived precipitation estimates over Nepal," *Applied Geography*, vol. 34, pp. 626–638, 2012.
- [37] L. Spadavecchia and M. Williams, "Can spatio-temporal geostatistical methods improve high resolution regionalisation of meteorological variables?" *Agricultural and Forest Meteorology*, vol. 149, no. 6-7, pp. 1105–1117, 2009.
- [38] J. W. Karl, "Spatial predictions of cover attributes of rangeland ecosystems using regression kriging and remote sensing," *Rangeland Ecology and Management*, vol. 63, no. 3, pp. 335–349, 2010.